POLITECNICO DI MILANO
DEPARTMENT OF ARCHITECTURE, BUILT ENVIRONMENT AND CONSTRUCTION ENGINEERING
DOCTORAL PROGRAM IN STRUCTURAL MECHANICS

Kinematic Equilibrium Black Box Analysis and the Characterization of Dry-Stack Masonry Arches

Doctoral Dissertation of:
Gabriel Lee Stockdale

Supervisor:
Prof. Gabriele Milani

Tutor:
Prof. Marco Vincenzo Valente

The Chair of the Doctoral Program:
Prof. Marco Scaioni

Year 2020 – Cycle XXXII

Acknowledgements

I would first like to thank my PhD supervisor Professor Gabriele Milani for his guidance, conversations and technical debates that helped define and strengthen my research. A big thank you is also sent to Dr. Vasilis Sarhosis for his invaluable support in the development of this research and to the staff at Newcastle University for their insight and expertise in the area of experimental testing. I would also like to thank Christian Malone for providing the space and equipment for constructing and performing the full-scale arch experimentation. Additionally, a big thank you is sent to the external reviewers, Professor Bahman Ghiassi and Professor Francesco Clementi for both their critical and complementary comments. Last but not least, I would like to thank my wife Dayana Stockdale and our children Octavia and Olympia for their continued encouragement and support, without which none of this would have been possible.

Abstract

STRUCTURAL masonry and its supporting stability-based design techniques have the potential to become a viable and advantageous method for new constructions. This technique however requires a modernization of the design and an accessibility to the analysis for engineers and other practitioners. Sudden failure must be removed. Simplified engineering equations and procedures must be established, and the model must be economically competitive. Limiting the conversation to the masonry arch, this research presents a black box analysis approach for dry-stack masonry arches. Through the application of kinematic equations of equilibrium and the kinematic admissibility of their solutions, a simple and effective strategy is developed for the analysis of dry-stack masonry arches subjected to mechanical joint control. The kinematic equations of equilibrium are established through the inclusion of an applied loading variable into the free-body diagram that defines the kinematic condition which generates a determinant system and a single solution. The results of the solution are then used to establish the resulting thrust line that represents the theoretical concentration of compressive forces through the system. This thrust line is then evaluated against the boundaries of the defined kinematic state to establish admissibility of the combined kinematic and loading conditions.

Incorporating this approach into the developed Kinematic Collapse Load Calculator (KCLC) establishes an accessibility and efficiency to the analysis through the visual representation of the condition under analysis and its solution with a back-end isolation of the supporting mathematics. Expanding beyond the traditional four hinged mechanism, the KCLC is adapted to incorporate limiting condition assessments for multi-mechanism analyses introduced from the inclusion of slip-joints. The inclusion of slip is accomplished through the incorporation of the coefficient of static friction. The inclusion of friction is balanced with a moment at the slip joint and the relationship between normal and parallel reactions at the mechanical joint. The resulting thrust lines from kinematically admissible statically unstable conditions are then evaluated against an arch geometry to establish the required joint reinforcements to maintain rigid elements between mechanical joints. The reinforcement magnitudes are calculated by determining the required moment or surface tension necessary to shift the thrust line back to the boundary of the arch. The accessibility and efficiency are then further expanded through the incorporation of a CAD based data extraction technique that allows the analysis structure to be applied to any

drawn arch model. Lastly for the black box analysis structure, the single degree of freedom motion of the kinematic condition is incorporated to evaluate mechanical deformations and their effect on capacity. This expands the kinematic equilibrium to static deformations and allows for the evaluation of conditions such as a hinge stiffness from a non-ideal joint reinforcement.

The transformation from the focus of stability to kinematic admissibility also allows the characterization of an arch to be established. This characterization is demonstrated by the development of collapse load diagrams (CLDs) and the adaptation of the analysis model to experimental conditions. CLDs are developed from calculating the minimum mechanisms for the admissible configurations of the base hinges for a given arch and plotting the capacities against the negative tangent of the angle between the base hinges. These diagrams establish a first-order assessment strategy for comparing arches and establishing quantitative values for project development stages of construction. This family of mechanisms also highlights the behavior between capacity and hinge sets. This behavior provides the comparison structure necessary to establish a capacity adjustment equation that directly adjust the theoretical model to a real arch. This process was repeated with two experimental campaigns, one for an in-scale arch and the other for a full-scale arch, both subjected to a tilting plane.

Lastly, the evaluation of statically deformed conditions is expanded into a seismic modelling structure. The kinematic equilibrium of mechanical deformations combined with the equivalent single point representation of deformation establishes required work-paths necessary to propagate the kinematic arch to collapse. The definition of conservative work then links these work-paths with kinetic energy for accelerations that exceed the static limit, or when the arch is in a kinematic state. The spatial establishment of kinetic energy in turn allows the formation of the time domain for the kinematic condition. This establishes the time-step propagation of position and kinetic energy through an acceleration sequence.

Therefore, this work establishes an analysis foundation that addresses both the static and dynamic conditions of dry-stack masonry arches subjected to hinge control. It formulates a single theoretical structure that can be employed for every stage of a project's development from inception and selection to contract execution. It links design with structural analysis and maintains a simplicity that can extend masonry arch analysis from the academic to practicing engineer. From this point the modernization of masonry has begun.

Author's Note

THIS work is a collimation of research rooted in the discovery of why structural masonry is not used in modern construction. My initial investigation began as an independent study during my Master's studies in civil structural engineering at the University of Hawaii. That time was also my first introduction into structural engineering which was an ignorant attempt to combine my construction past with my physics education. I remember repeatedly being confused by the constants created to simplify concrete and steel, and simultaneously the simplicity and elegance I saw with the masonry arch was not reciprocated with my peers. So, after discovering why structural masonry is no longer used or taught to the practicing engineer, I switched my focus from the discovery of why to the question of how. How can structural masonry enter the halls of modern construction methods? The focus of this work is to establish the foundation of a simple, efficient and effective theory for the structural analysis of dry-stack arches. Utilizing the fundamental principles of statics and the transformation of state that defines their traditional failure, this work presents a black box analysis approach designed from arches for arches.

This work utilizes ideas and figures that have previously appeared in the following journal articles and conference proceedings:

1. Stockdale, G. L., Sarhosis, V., & Milani, G. (2019). Seismic capacity and multi-mechanism analysis for dry-stack masonry arches subjected to hinge control. Bulletin of Earthquake Engineering, https://doi.org/10.1007/s10518-019-00583-7
2. Stockdale, G., & Milani, G. (2019). Diagram based assessment strategy for first-order analysis of masonry arches. Journal of Building Engineering, 22, 122–129. https://doi.org/10.1016/J.JOBE.2018.12.002
3. Stockdale, G., Tiberti, S., Camilletti, D., Sferrazza Papa, G., Basshofi Habieb, A., Bertolesi, E., … Casolo, S. (2018). Kinematic collapse load calculator: Circular arches. SoftwareX. https://doi.org/10.1016/j.softx.2018.05.006
4. Stockdale, G. (2016). Reinforced stability-based design: a theoretical introduction through a mechanically reinforced masonry arch. International Journal of Masonry Research and Innovation, 1(2), 101–142. https://doi.org/10.1504/IJMRI.2016.077469
5. Stockdale G., Milani G., & Sarhosis V. (2019). Increase in Seismic Resistance for a Full-Scale Dry Stack Masonry Arch Subjected to Hinge Control, Key Engineering Materials, Vol 817, pp. 221-228

6. Stockdale G, Sarhosis, V and Milani G (2019) Finite Hinge Stiffness and its Effect on the Capacity of a Dry-Stack Masonry Arch Subjected to Hinge Control, Key Engineering Materials, Vol. 817, pp. 259-266
7. Stockdale G, Milani G and Sarhosis V (2019) Irrevocable Collapse Time for a Fixed-Hinge Dry-Stack Arch Under Constant Horizontal Acceleration, AIP Conference Proceedings, Vol. 2186:1, pp. 1-4
8. Stockdale, G., Sarhosis, V., & Milani, G. (2018). Increase in seismic resistance for a dry joint masonry arch subjected to hinge contro. In 10th IMC Conference Proceedings (pp. 968–981). International Masonry Society.
9. Stockdale, G., & Milani, G. (2018). Interactive MATLAB-CAD limit analysis of horizontally loaded masonry arches. In 10th IMC Conference Proceedings (pp. 298–306). Milan: International Masonry Society.
10. Stockdale G., Milani G., & Sarhosis V. (under review). Work-Path Approach Seismic Modelling of Hinge-Controlled Masonry Arches. Structures and Buildings, pp. 1-16 (Submitted on 29/9/2019)
11. Stockdale G., Milani G., & Sarhosis V. (under review). Dynamic Modelling Structure of Hinge-Controlled Masonry Arches and 2D Accelerations. International Journal of Masonry Research and Innovation, pp. 1-29 (Submitted on 4/12/2019)

Table of Contents

List of Tables

List of Figures

CHAPTER 1

INTRODUCTION

List of Abbreviations and Symbols

BVP	—	Boundary value problem
DOF	—	Degree of freedom
FBG	—	Fiber Bragg grating sensor
FRP	—	Fiber reinforced polymer
KCLC	—	Kinematic collapse load calculator
LA	—	Limit analysis
RSBD	—	Reinforced stability-based design
SBD	—	Stability-based design
SHM	—	Structural health monitoring
TRM	—	Textile reinforced mortar

Sustainability is a fundamental concept that must be integrated into the practices of architects, engineers, scientists, and all other disciplines that support the health and wellbeing of societies and their populations. It is only as a collective that the issues of resource exhaustion and climate change can be combated. Each and every discipline must find their unique ways to contribute to this collective. For structural engineers and architects, significantly increasing the lifespan of new structures is one method.

Currently reinforced concrete is the most common building method used. With cheap materials and quick construction this is a favored method, but the corrosive behavior of steel, which is the primary material used to withstand tension, compromises its longevity. Techniques that replace steel with alternative composite materials, and pre-stressing methods are continuously being developed to increase the lifespan of these structures. Their fundamental lifespan however is short and extending it is cumbersome. Another method for lifespan extension is the implementation of sensors for continuous performance monitoring. This instrumentation is termed structural health monitoring (SHM).

Appropriately applied SHM systems allow for corrective measures to be implemented at the onset of a problem. SHM systems applied to reinforced concrete structures face significant challenges from the high degree of approximations and assumptions incorporated into the standard design and construction practices [1]. These approximations and assumptions, which are applied conservatively to ensure safety and design efficiency, result in the inability to know the behavior of the structure prior to instrumentation. Consequently, the effective application of SHM systems to reinforced concrete structures require multi-step campaigns and long calibration periods that ultimately render their application uneconomical for all but the most critical and complex structures.

Creating a more sustainable model through the concept of longevity can also be accomplished by starting with a construction method that has a proven track record, in terms of longevity, and adapting it to satisfy modern structural standards. One such design method that meets this criterion is the Stability-Based Design (SBD) techniques used for constructing unreinforced masonry structures. The potential longevity of SBD is realized through the existence of structures built in the Greek through Gothic times. Unfortunately, the lack of structural interest that was observed during the Renaissance resulted in the near extinction of this design method. When the interest of structural design reemerged in the nineteenth century it was coupled with the integration of iron as a tensile material [2].

Structural design's reemergence was in the form of graphical analysis as formalized by Culmann in **DIE GRAPHISCHE STATIK** [3]. Graphical statics became the dominant method used in determining structural equilibrium for the end of the nineteenth and beginning of the twentieth centuries, but this method was replaced by the theory of elasticity by 1920 [4]. The theory of elasticity had two distinct advantages to graphical statics: one being its closed-form analytical solutions that increased design efficiency and the other being the removal of the drawing skills required by its counterpart. The theory of elasticity continued to dominate, and as iron turned into steel and then reinforced concrete, graphical analysis methods were abandoned, and are now no longer taught to the young engineer. Graphic analysis worked very well for the analysis of SBD structures, but the same could not be said for the theory of elasticity and its corresponding mathematics. Additionally, traditional SBD (i.e. unreinforced masonry) structures and their inability to withstand tensile forces produces collapse failures that are both sudden and potentially without warning. This sudden collapse is further exacerbated in seismic regions. Consequently, the development of the theory of elasticity, coupled with the inability for SBD to adapt and the possibility of a sudden collapse, resulted in SBD's extinction for the modern engineer. However, the understanding of the technique has not been lost. Its focus and understanding has been directed by engineers towards the preservation, restoration, and rehabilitation of historical structures.

1.1 Modernization of Masonry

The reintroduction of SBD techniques requires modernization of the design to satisfy current safety and structural standards. Additionally, a successful reintroduction requires that the modernization is done in a manner that is palatable to the practicing engineer. For this to occur, the sudden failure needs to be removed from the system, simplified engineering equations and procedures must be established, and the model must be economically competitive.

1.1.1 Removal of Sudden Collapse

The removal of the sudden collapse and assumption of no slippage between blocks has been proposed through the concept of Reinforced Stability-Based Design RSBD [5]. This RSBD technique is developed on the principle of maintaining the traditional SBD behavior under normal service conditions and designing a reinforcement system that “activates” after the loss of stability. The theoretical investigation into this behavior for a semi-circular arch produced a linear relationship between the applied load and mechanical hinge rotation for small angles. This linearity is transferred into a linear strength problem through the application of a linearly elastic tensile material. The proposed methodology to achieve this behavior is through the application of a woven reinforcement that removes the no-slip assumption without compromising the ability to rotate, and then applying external reinforcement only anchored to the weave (see Figure 1). In this manner, the rigid block motion is reinforced with negligible effects to the stable system.

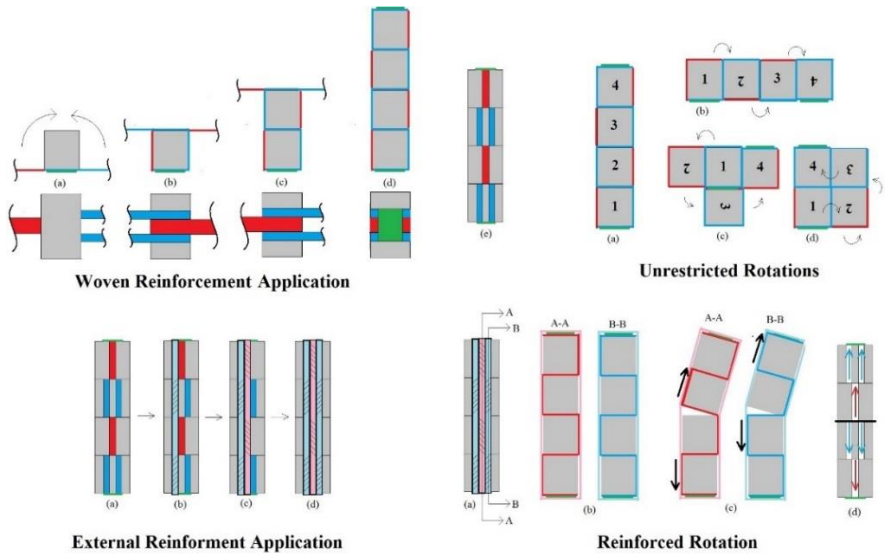

Figure 1. Diagrams showing the woven reinforcement application to four blocks, the demonstration of no hinge restrictions from the weave, the external application of reinforcement attached to the weave and the resulting hinge reinforcement.

1.1.1.1 RSBD and Structural Health Monitoring

The decoupling of the masonry and reinforcement in the RSBD approach allows for the piecewise analysis of the pre- and post-stable systems. If the loss of stability is defined as failure, then the two systems can be isolated into serviceability and safety respectively. Additionally, the inert behavior of the of the reinforcement under service conditions creates a natural switch condition.

It has already been shown that the combination of Fiber Bragg Grating (FBG) sensors and Fiber Reinforced Polymers (FRPs) can be used to produce a set of limit states that can be immediately monitored regardless of their application [6]. Thus, if FRPs are the RSBD reinforcing material, the switch condition can be coupled with the generalized FGB/FRP system to create an element based SHM structure that requires minimal calibration and no elaborate statistical analysis or excessive data manipulation. Furthermore, the geometric mechanization requirements for the failure of curved masonry elements such as arches creates the potential to not only identify the onset of failure, but also a finite set of conditions that would cause the failure. This in turn accelerates the rehabilitation while minimizing labor costs.

1.1.2 Assessment Versus Design

RSBD addresses the fundamental flaw preventing the reintroduction of structural masonry and presents an advantageous SHM structure for efficient long-term management [5]. Now the focus must turn to the efficiency and accessibility of the structural analysis. In the presentation of RSBD, it was argued that the decoupling of the stable and mechanical systems allows for the utilization of the wealth of existing knowledge. This knowledge, which is discussed in Chapter 2, has primarily collimated in the 21st century: long after structural masonry's demise. Consequently, and understandably so, the wealth of existing knowledge aims at the assessment of existing system and the minimum problem.

The process of assessment is a passive process which for civil engineers focuses on the evaluation of something that exists and whether or not it is safe and functioning correctly. Intervention is performed out of necessity and must account for the physical and cultural complexities that exist. Design, however, is an active process focused on the development of something new. For civil engineers, this means that the quantification of failure is directly considered in defining the assembly of an engineered system. While it is often the case that processes used for assessment and design overlap, it is not guaranteed.

The nature of unreinforced masonry discretizes the system and holds the potential for the formation of a hinge at any joint. This generates many kinematic hinge-set combinations that can potentially exist. Within the assessment context, the focus becomes the identification the hinge-set that produce a minimum capacity mechanism condition. Under the context of design, the focus is on optimizing the defined failure condition based upon the anticipated demands of the structure. This requires the ability to examine more than the minimum condition.

1.1.3 Strength Versus Stability

For masonry arches, there exists a strong understanding of reinforcement and retrofitting strategies, and of those strategies FRPs and Textile Reinforced Mortars (TRMs) have shown adeptness for reinforcing flexural hinges and the ease of their installation [7], [8], [17], [9]–[16]. The application of these systems however has primarily focused on strengthening existing systems. This has resulted in the direct transformation of the arche's failure from the SBD driven mechanism to a material strength problem (i.e. delamination, crushing or rupture) [9], [10], [12], [13], [15], [18]–[21]. This full strengthening drives the narrative towards the material properties which are as diverse and complex as the ancient structures being assessed. When combined with the curved nature of arches, the quantitative establishment of retrofitting standards becomes almost impossible as can be seen in the standardized Italian CNR recommendations for the external FRP strengthening of existing structures [22].

It is widely accepted that stable dry-stack masonry imposes at most one-tenth of the material's compressive capacity upon mechanization. This allows the utilization of the mechanism as a defined and recoverable failure point if it is structurally defined. The ability to efficiently create the structural definition does not exist.

1.2 Problem Statement

The successful reintroduction of curved structural masonry requires an efficient and accessible design and analysis methodology. That methodology must be derived around the control and optimization of the system. Existing unreinforced masonry arch analysis has focused on the assessment of the minimum mechanism while the rehabilitation strategies focus on maximizing capacity. This assessment-strength duality is understandable and reasonable in the context of retrofitting and rehabilitation, but not for controlling the system. Namely, what happens if only the minimum mechanism is reinforced, or more importantly what is required to physically define a mechanism?

RSBD introduces a simple linear condition to the post-stable strengthening of a dry-sack masonry arch and addresses the issue of sudden collapse and no slippage. Its structure however is limited to the post-stable system. The success of masonry, and more specifically masonry arches' reintroduction as a modern structural element requires a simplicity and efficiency to analysis of both the pre- and post-stable systems.

Lastly, SBD analysis is a Boundary Value Problem (BVP) who's capacity is defined by the onset of a mechanism. This mechanism creation is a physical phenomenon that arises from the system's transformation from a stable to kinematic state. Figure 2 shows the stable state and a kinematic state defined by the inclusion of four hinges to a masonry arch. Under traditional structural analysis and statics, the four-pinned arch can be idealized into three pin-connected elements shown in Figure 3a. This generates a geometrically unstable condition because there are fewer reactive forces than equations of equilibrium, and the idealized arch will collapse as shown in Figure 3b under

self-weight. The collapse propagation however results in an oscillatory motion of the element $\overline{CD}$ which can be resisted through the application of an external force such as that seen if Figure 3c. This generates a kinematic state that is in equilibrium. Superimposing the four-pinned masonry arch to the idealized kinematic system (see Figure 3d) then highlights that the unstable failure under self-weight is directly resisted by the thickness of the blocks. Therefore, the equilibrium condition of the idealized kinematic state is the transition point between the stable four-pinned masonry arch and its mechanical failure. Unfortunately, the discussion provided to the budding engineer is a statement of avoidance for any system that is classified as unstable in the evaluation of determinacy [23].

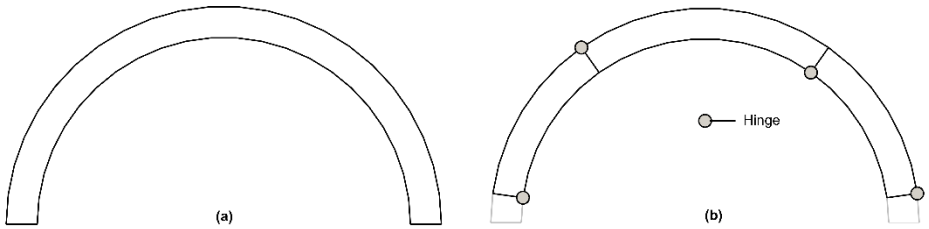

Figure 2. Boundary representation of an arch in a (a) stable state and a (b) kinematic state defined by four hinges

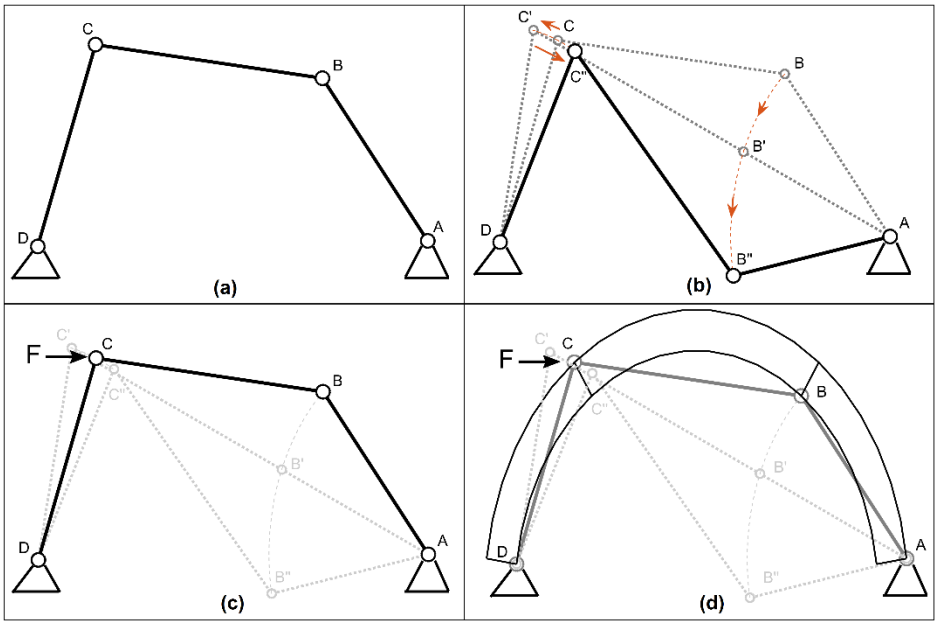

Figure 3. A (a) four-pinned truss arch, its (b) kinematic failure propagation under self-weight, the (c) establishment of equilibrium through an applied force, and (d) the superposition of the four-pinned masonry arch to the equilibrium condition

1.3 Objectives

The objectives of this work are to create the foundation and blueprint of an efficient and accessible structural analysis methodology and software to support the reintroduction of curved masonry as a modern construction method. The foundation of this methodology is kinematic equilibrium. The blueprint is the black box analysis structure used for the formation of the software and the characterization strategies developed for first-order assessments and the synchronization of the theoretical model with experimental observations.

Kinematic equilibrium is defined as:

> **Kinematic Equilibrium**[1] – The static equilibrium analysis of a kinematic state superimposed on a stable condition through the incorporation of at least one external loading variable to the free-body diagram and corresponding equations of equilibrium that define the structure.

In other words, kinematic equilibrium incorporates an applied force-mechanism pair into the free-body diagrams and equations of equilibrium used in standard statics evaluations. This formulates a database structure to the equations of equilibrium for the variations in force-mechanism pairs.

The aim of the black box analysis is to access this database structure of developed kinematic equilibrium conditions, combine them with user defined arches, evaluate the admissibility of the combined system and display the results. A black box condition is defined as a sequence of operations that generates an output from a user's input without requiring the users explicit understanding of the sequence employed: such as a calculator or voltage regulator. The terminology is employed here to emphasize that the complexities of the masonry arch analysis can be contained within a structure that does not require the explicit knowledge or involvement of the practicing engineer in order to obtain the information necessary for structural design.

Lastly, the objective of the characterization strategies is to demonstrate the application of the analysis structure, highlight its adaptability, and its ability to incorporate all aspects of structural analysis from conception to creation. This process is accomplished through the analysis of a family of mechanisms for a given arch subjected to hinge control, and then through the expansion of the analysis structure into dynamic modelling.

For masonry arches this static-kinematic transformation presents a singularity into a system that otherwise has infinite solutions. For stable masonry arches, the traditional mechanism is the result of the release of four degrees of freedom (DOF) in the form of hinges and an asymmetrically applied loading condition. The location of these hinges and the loading geometry generate five input parameters that must be applied to the arch geometry in order to obtain a determinant system of equations. As a compression only system the solution to

[1] Kinematic refers to the failure mechanism a priori assigned, then at least one external load variable is applied to guarantee equilibrium is satisfied under self-weight.

the determinant system must also abide by the rules of motion and the validity of the resulting thrust line. The thrust line is the line that represents the flow of compressive forces and was originally defined from the tension only system of a hanging chain [4]. In fact, the hanging chain itself is in a kinematic equilibrium condition as any additional load would result in motion through deformation. Therefore, the application of the input parameters to the arch to define a singularity condition and the admissibility of the resulting mechanical state generates a black box condition where the input and output are linked through equilibrium and admissibility.

The novelty of this work begins with the formal establishment of kinematic equilibrium and its application to masonry arches subjected to mechanical joint control, and its use in all the developed static and dynamic analysis procedures, methodologies and software. All the work presented in this thesis, including theory, software and experimentation are original works developed over the course of the PhD program.

1.3.1 Outline

This thesis is divided into seven chapters beginning with the Introduction in Chapter 1 where the motivation, the problem and the objectives are discussed. Chapter 2 presents a literature review aimed at summarizing the current understanding of masonry. The development of the kinematic free-body diagrams are derived in Chapter 3. The derived equations include various loading geometries and the 70 potential mechanisms that exist from the inclusion of translational DOF releases that arises from the inclusion of friction. Chapter 4 develops the black box structure through the kinematic admissibility of the solutions obtained from the kinematic equilibrium sets. After the assessment of admissibility, the Kinematic Collapse Load Calculator (KCLC) is introduced. The KCLC is a graphical user interface that connects the user input with the output of the black box analysis. The incorporation of multi-mechanism analysis to the KCLC is presented for a discrete set of mechanisms and followed by the limiting condition evaluation of the mechanism set. Then the KCLC's ability to analyze generic arch geometries through a CAD based data extraction technique is presented. After the detailed discussion of the KCLC, the capacity compensation requirements for non-stable kinematically admissible conditions is formulated and added to the KCLC. Lastly in Chapter 4, the mechanical deformation of the four-hinged mechanism is derived and used to evaluate the kinematic equilibrium of static deformations, establish equivalent systems through parametric plotting, and is combined with the capacity compensation requirements to evaluate finite hinge stiffness from non-ideal reinforcement. Chapter 5 applies this black box analysis to create characterization strategies first through the development of Collapse Load Diagrams, and then carries the theoretical model through two experimental results to characterize physical arches and customize the analysis model to them. Chapter 6 then expands the analysis to the kinematic state for 2D seismic modelling through the development of required work paths from combining the kinematic equilibrium of static deformations with the equivalent systems discussed in Chapter 4. These work paths establish kinetic energy equations from the path independence of

conservative work and allow the formulation of the time domain for constant accelerations in excess of the static limit. Lastly, this work is concluded in Chapter 7.

CHAPTER 2

LITERATURE REVIEW

List of Abbreviations and Symbols

ENT — Elastic-no-tension

FE — Finite element

LA — Limit analysis

ML — Masonry-like

RNT — Rigid-no-tension

SBD — Stability-based design

TNM — Thrust network method

For the field of masonry structures and especially historical ones, the breadth of existing work is broad and spans multiple scientific disciplines. With regards to analyzing and modeling however, a cohesion and consolidation of literary work has begun. The primary focus of this chapter is to present a general schematic of the current understanding of unreinforced masonry and SBD as discussed in two of these consolidations. An overview of masonry mechanics is first presented. Next, the computation methods for vaults are discussed and then followed by a brief discussion on the continued developments.

2.1 Mechanics of Masonry Structures

The cohesion and consolidation of literary work on masonry mechanics can be seen in the book titled **MECHANICS OF MASONRY STRUCTURES** [24]. In this work the basic facts of masonry materials are discussed and the simple and refined modelling methods are introduced [25].

The simple model approach is developed through the consideration of the macroscopic system. Constructed from the traditional no-tension assumption formulated from the “pioneering work of Heyman” [26], the simple model comprises three simplified uniaxial models. The models are named for the number of parameters required for their definition (i.e. zero, one, and two) [25]. An evolution-type approach to the refinement of the uniaxial masonry-like

behavior model has been constructed with these three models. Model zero is the Rigid No Tension (RNT) material approximation established from the traditional assumptions: infinite compressive strength, zero tensile strength, and perfectly rigid elements. Model one replaces the perfect rigidity in model zero with a finite stiffness and is termed the Elastic No Tension (ENT) material. Model two imposes a limit to the compressive stress capacity of the masonry material. This removal of the infinite compressive strength assumption creates the Masonry-Like (ML) material [25]. Following the establishment of the simplified behavior models, a rigorous and detailed introduction to the mathematics behind the ML material and limit analysis is provided through the utilization of an extensive set of mechanical and mathematical tools [27]. The constitutive equations are then explicitly determined the for isotropic ML materials, a numerical method for solving the equilibrium boundary value problem for ML solids is established, and the explicit and numerical solutions are compared [28]. The simple model is then concluded through an extensive presentation on the practical application of the three developed unilateral models, including the development of a numerical approach and the comparison of that approach to analytical solutions and test results [29].

The refined model approach for masonry structures is developed through the restriction of the mechanical system to specific masonry types where the materials are the combination of units (i.e. bricks, blocks, etc.) and joints (i.e. mortar, glue, etc.) arranged such that a periodic repetition of the microstructure exists [25]. The introduction to the refined model approach briefly presents four common techniques: (1) micro-modeling, where direct consideration of the geometry of units and joints is given and the constitutive laws are experimentally obtained; (2) macro-modelling, which maintains the experimentally obtained constitutive laws, but the units and joints are smeared out in the continuum; (3) homogenization, where geometry and material data are used to mathematically represent the micro-structure to obtain a smeared continuum model; and (4) structural component models, where the internal forces directly provide the constitutive laws of the structural elements. The introduction to the refined model is then ended with a presentation of the mechanical properties of unit and mortar, the interface, and the masonry through the homogenization technique [25]. Next, the ideas and methodologies for modeling the interfaces of masonry structures is presented through the phenomological modeling approach and the deductive modeling approach [30]. Experimental results are provided for brick-brick and brick-mortar interactions, dry friction masonry is modelled, and the phenomological model of adhesion for two interface models as well as numerical results is discussed [30]. After presenting the interface modelling, the micromechanical, multiscale, and macro-mechanical modeling approaches are presented: including details for various recently developed models framed in the 2D small strain and displacement approach [31]. Finally, an in-depth look into the homogenization theory and assumptions, including its ability to couple with finite element (FE) analysis codes and extend to the structural level, is presented [32]. The **MECHANICS OF MASONRY STRUCTURES** is then conclude with considerations of seismic assessment, including case studies utilizing static (pushover) analysis, time integration analysis, and macro-block analysis

techniques [24], [32]. It is also worth noting that in the introduction to the refined model, reference is made to Lourenço [33] for a comprehensive review on the structural analysis of masonry structures, as well as Marques and Lourenço [34] and Lourenço et al. [35] for the seismic analysis of masonry with and without box behavior respectively.

2.2 Computational Methods for Masonry Vaults

Another example of the cohesion and consolidation of scientific literature on the analysis of masonry structures is in the paper **COMPUTATIONAL METHODS FOR MASONRY VAULTS: A REVIEW OF RECENT RESULTS** [36]. In this paper a critical review of the current methods and models used in the analysis of masonry vaults up to their collapse is organized into, (a) the development of the modern vault theory, and (b) computational methods. Note that prior to the development of those two sections Huerta [37], [38] and Benvenuto [39] are referenced with regards to obtaining the appropriate knowledge to understand the behavior of historical constructions.

For the modern vault theory it is stated that a "sound theoretical framework exists," referencing Huerta [38] and Como [40], and it is acknowledged that the modern theory of LA, primarily founded by Heyman [26], is the most reliable tool for the analysis of curved masonry structures [36]. Establishing the traditional conditions of the RNT material, the static (lower bound) and kinematic (upper bound) theorems are introduced. The static theorem states that if a statically admissible state of equilibrium can be found then the structure will not collapse. The only analysis technique presented is thrust line analysis for the explanation and examination of stability in 1D structures. The kinematic theory states that the arch will collapse if a kinematically admissible mechanism resulting in positive or zero work from external forces is found. Como [40] is once again referenced, this time for finding 1D equilibrium solutions for the different types of vaults through manual analysis methods. Fanning and Boothby [41] are cited for their critical overview of more complex analysis methods for masonry arches and vaults as well. The remaining discussion on the kinematic theorem is focused on the essentials of the materials used for masonry as highlighted by Huerta [37] (i.e. heterogeneity; minimal tensile resistance and good compressive strength; high friction coefficient; and the importance of geometry in establishing equilibrium). These essentials along with an extensive list of existing literature is presented for the development of the statements that masonry is a composite heterogeneous material that exhibits a non-isotropic behavior in both the elastic and collapse range [42]–[45]; tensile strength varies, but it can be modeled in the interface between mortar and brick [44], [46], [47]; the friction coefficient for historical masonry is between 0.4 and 0.6, but its inclusion in the system results in a loss of normality, a non-associate flow rule, an inability to apply limit analysis theorems, and complicates linear programming methods [48]–[50]; and finally that the overall geometry [51]–[54], inclusion of infill material [55]–[64], and inclusion of existing cracks are all variables that have significant impact on the structure's performance [36].

The computational methods discussed by Tralli et al. [36] are divided into three categories: (1) thrust network methods (TNM); (2) FE method developed for non-linear incremental analysis; and (3) FE models developed for limit analysis. TNM addresses extending the thrust line to spatial structures. Several approaches are presented including the use of 3D funicular force networks introduced by O'Dwyer [65] and built upon by Block and co-workers [66]–[68], a 3D equilibrium analysis using Gaudi-inspired funicular networks [69], [70], funicular networks from a specific 3D extension of the lumped stress method [71], [72] including significant case studies [73], [74], a solving algorithm developed from the lumped stress method and thrust networks [75], and finally an approach involving membrane stress selection and a no tension constitutive equation [76], [77]. For FE methods using incremental non-linear analysis, two programs are listed that have developed specific software for studying masonry curved structures, NOSA CNUCE by CNR Pisa [78], developed from the constitutive assumption of no tension material, and DIANA by TNO Delft [79] which arose from an accurate modelling of the masonry mechanical behavior. It is also noted that some commercial FE programs designed for steel and concrete have been used in studies published since 2000, and the combination of the constructed techniques of analysis and sound engineering reasoning appear to be adequate as can be seen in numerous examples [54], [61], [80]–[84], but heterogeneity is not accounted for and isotropic behavior is assumed for both the elastic field and collapse. In comparison FE methods using limit analysis allow for the consideration of heterogeneity and anisotropy through homogenization [44], [45], [51]–[53], infill [55], [62], [63], and discrete and realistic crack patterns, but computational problems involving convergence of the no tension solution and friction's violation of the limit analysis theorems do exist. Additionally, the adoption of rigid elements and homogenized interfaces, used to limit computational effort, produces the inability to provide displacements during the deformation process. Efforts to circumvent this limitation have begun [85].

2.3 Continued Development

In Sections 2.1 and 2.2 an existing understanding and analysis of masonry mechanics and vaults was presented to demonstrate the coupling of the wealth of knowledge that exists and its consolidation for masonry as a whole. Further works of consolidation have developed with respect to the assessments and experimental investigations of masonry arch bridges [86], [87]. Furthermore, continued success and advancements are observed with the development and application of numerical modelling strategies [88], [89], [98]–[106], [90]–[97] and LA approaches [95], [107], [116], [117], [108]–[115]. This also includes additional consolidation efforts for both reinforced and unreinforced systems [118]–[120], but as previously mentioned these works aim at the assessment, and rehabilitation of existing and historical systems.

It is also clear that this comprehensive understanding of masonry and more specifically arches exists today and that the ability to analyze most situations exists, but what can also be observed is that the accessibility of the information and understanding is limited to academic experts. The information and

approaches are not structed for the practicing engineer. Additionally, the LA approaches are limited to the onset of a mechanization and cannot predict the post-stable response of the system which may recover before collapse [121]–[123], while the numerical approaches require a high level of expertise and are computationally expensive [87].

CHAPTER 3

KINEMATIC EQUILIBRIUM

List of Abbreviations and Symbols

- a_x — Horizontal component of an applied acceleration
- a_y — Vertical component of an applied acceleration
- α_i — Angle relationship between the reaction vector, the i^{th} joint line, and the friction angle (see Figure 19)
- [BC] — Balance matrix component of the equations of equilibrium
- C_i — Identifier for combined slip-hinge joint at the i^{th} joint
- CM — Center of mass
- $\Delta x_{i,j}$ — Horizontal lever arm between points i and j (i.e. $x_i - x_j$)
- $\Delta y_{i,j}$ — Vertical lever arm between points i and j (i.e. $y_i - y_j$)
- e_i — Thrust line eccentricity from the i^{th} hinge position along the joint line
- F_h — Net equivalent horizontal force from a distributed load
- F_v — Net equivalent vertical force from a distributed load
- f_{gj} — Gravitation body force of the j^{th} element
- f_{hj} — Net equivalent horizontal force component acting on the j^{th} element
- f_{vj} — Net equivalent vertical force component acting on the j^{th} element
- g — Gravitational acceleration constant
- H_i — Identifier for the i^{th} hinge
- h_i — Horizontal reaction force at the i^{th} hinge
- LA — Limit analysis
- λ_a — Collapse multiplier for uniform acceleration

λ_d	—	Collapse multiplier for the net equivalent force of a distributed load
λ_p	—	Collapse multiplier for an applied point load
M_i	—	Moment at i^{th} mechanical joint from slip condition (i.e. N_i*e_i)
μ_s	—	Coefficient of static friction
N_i	—	Normal reaction force at the i^{th} mechanical joint
P_i	—	Parallel reaction force at the i^{th} mechanical joint
P_x	—	Horizontal component of an applied point load
P_y	—	Vertical component of an applied point load
{q}	—	Constants vector component of the equations of equilibrium
RNT	—	Rigid-no-tension model
RSBD	—	Reinforced stability-based design
{r}	—	Reaction vector component of the equations of equilibrium
SBD	—	Stability-based design
S_i	—	Identifier for a slip-joint at the i^{th} hinge
$\sum F_x$	—	Algebraic sum of horizontal forces
$\sum F_y$	—	Algebraic sum of vertical forces
$\sum M_O$	—	Algebraic sum of moments taken about the point O
θ_a	—	Polar angle of an acceleration vector
θ_d	—	Polar angle of the net equivalent force vector from a distributed load
θ_i	—	Slope angle of the i^{th} mechanical joint line (see Figure 19)
θ_p	—	Polar angle of a point load vector
θ_s	—	Static friction angle
θ_w	—	Polar angle of an arch segment
v_i	—	Vertical reaction force at the i^{th} hinge
$\omega(x,y)$	—	Distributed load function
(x_h,y_h)	—	Cartesian coordinates of a net equivalent horizontal force
(x_P,y_P)	—	Cartesian coordinates of a point load
(x_v,y_v)	—	Cartesian coordinates of a net equivalent vertical force

The modern theory of LA is argued as the most reliable tool for the analysis of curved masonry [26], [36]. Limit analysis for masonry arches is initially built on the conditions of infinite compressive strength, no slippage between blocks, and no tensile strength (the RNT model) and can be evaluated through the lower bound or upper bound theorems. The RTN model establishes the foundation of SBD and masonry analysis and is important for any kind of masonry [105], [116]. The lower bound theorem, also known as the static approach, states that if there exists a statically admissible state of equilibrium, then the arch will not collapse. The upper bound theorem, also known as the kinematic approach, states that the arch will not collapse as long as there are no kinematically admissible mechanisms that produce zero or positive work from external forces.

In the context of structural analysis, the kinematic theorem addresses the beginning of the kinematic condition that propagates the arch towards collapse, whereas the lower bound theorem evaluates the maximum limit of stability. While both conditions are focused on quantifying the static-kinematic transformation point, the kinematic state carries the arch to collapse. For this reason, the kinematic theorem is the best suited for structural analysis and design. Traditionally this analysis method is performed through the principle of virtual powers. The principle of virtual powers is extrapolated from the principle of virtual work that is used to analyze redundant systems under elastic modelling and beam theory. Kinematic equilibrium however focuses directly on the equilibrium requirements of a defined kinematic state. Since it is assumed that the system is stable under normal loading conditions, the formation of a kinematic condition requires an external loading condition, and thus the loading condition can be paired with the kinematic condition. This allows the analysis to be directly structured into a “determinate” equilibrium problem that does not require the application of virtual conditions.

In this chapter the equilibrium problem of the kinematic condition of an arch is derived. The derived systems are formatted into equations of equilibrium. Each paired kinematic and loading condition requires the formation of its own equations of equilibrium. Therefore, this chapter derives a comprehensive set of loading and kinematic conditions. It is the objective of this chapter to establish a database and quick reference structure of kinematic free-body diagrams and their associated equations of equilibrium. From these variations of equations of equilibrium some conclusions are made on the potential to simplify the process of establishing additional equations of equilibrium not directly addressed in this chapter.

3.1 Equilibrium Problem

From statics it is known that a structure or its members are in equilibrium when they maintain a balance of forces and moments. When the principle load carrying portions lie on a single plane, it reduces the equations of equilibrium to

$$\begin{aligned} \sum F_x &= 0 \\ \sum F_y &= 0 \\ \sum M_O &= 0 \end{aligned} \tag{1}$$

where $\sum F_x$ and $\sum F_y$ are the algebraic sums of the cartesian components of the forces and $\sum M_O$ is the sum of the moments about the point O.

For the RNT masonry arch, a traditional kinematically admissible mechanism consists of the development of four hinges that alternate between the intrados and extrados across the span of the arch (see Figure 4). A hinge develops when the loading conditions result in the concentration of the normal forces near a curved boundary (i.e. the intrados or extrados) and can be idealized by the placement of concentrated point loads at the boundary. By assuming perfect hinges, the kinematic arch can be expressed as three rigid pin connected elements as shown in Figure 5.

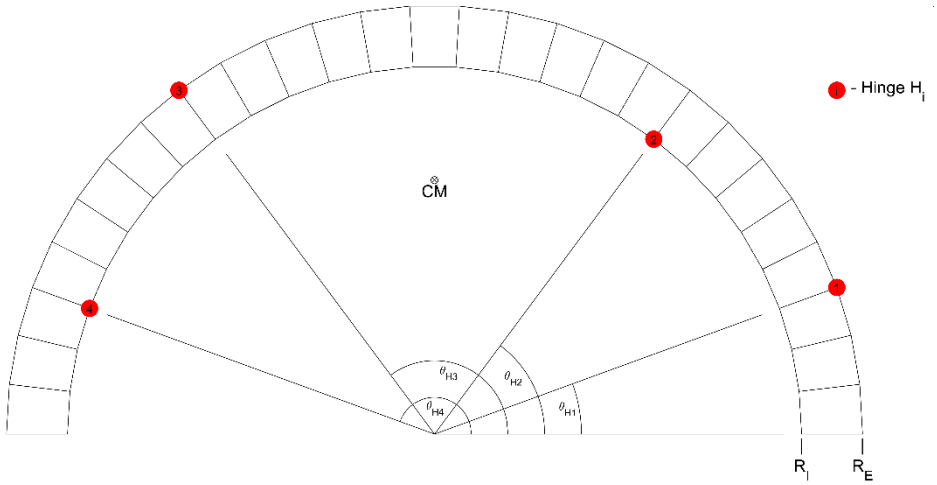

Figure 4. An example of a kinematically admissible hinge set.

A pin connection between blocks removes the ability to carry a moment at the joint. Decomposing Figure 5 into the three rigid elements as seen in Figure 6 allows the standard static equilibrium equations (i.e. Eqn. 1) to be constructed for the three element system. For the self-weight condition and summing the moments of elements 1, 2 and 3 at hinges 1, 2 and 3 respectively, the equilibrium equations are (in matrix form)

$$\begin{bmatrix} -1 & 0 & 1 & 0 & 0 & 0 & 0 & 0 \\ 0 & 1 & 0 & -1 & 0 & 0 & 0 & 0 \\ 0 & 0 & -\Delta y_{2,1} & \Delta x_{1,2} & 0 & 0 & 0 & 0 \\ 0 & 0 & -1 & 0 & 1 & 0 & 0 & 0 \\ 0 & 0 & 0 & 1 & 0 & 1 & 0 & 0 \\ 0 & 0 & 0 & 0 & \Delta y_{3,2} & \Delta x_{2,3} & 0 & 0 \\ 0 & 0 & 0 & 0 & -1 & 0 & 1 & 0 \\ 0 & 0 & 0 & 0 & 0 & -1 & 0 & 1 \\ 0 & 0 & 0 & 0 & 0 & 0 & \Delta y_{3,4} & -\Delta x_{3,4} \end{bmatrix} \begin{bmatrix} h_1 \\ v_1 \\ h_2 \\ v_2 \\ h_3 \\ v_3 \\ h_4 \\ v_4 \end{bmatrix} = \begin{bmatrix} 0 \\ f_{g1} \\ -f_{g1}\Delta x_{1,CM1} \\ 0 \\ f_{g2} \\ f_{g2}\Delta x_{2,CM2} \\ 0 \\ f_{g3} \\ -f_{g3}\Delta x_{3,CM3} \end{bmatrix} \quad (2)$$

where, v_i and h_i are the vertical and horizontal reactions at the ith hinge respectively, and f_{gj} is the body force of the jth element applied at the element's center of mass. The moments were calculated by the cartesian forces multiplied by their respective vertical, Δy and horizontal Δx, lever arms. The subscripts of, Δx, and Δy, in Eqn. 2 denote the hinges or center of mass locations used to construct the lever arms (i.e. $\Delta y_{2,1}$ is $(y_2 - y_1)$ and $\Delta x_{1,CM1}$ is $(x_1 - x_{CM1})$, see Figure 6). The format of Eqn. 2 is the repeat of Eqn. 1 for each of the three elements of the arch: the first three rows correspond to the equations of equilibrium for Element 1, the next three for Element 2 and the last three for Element 3.

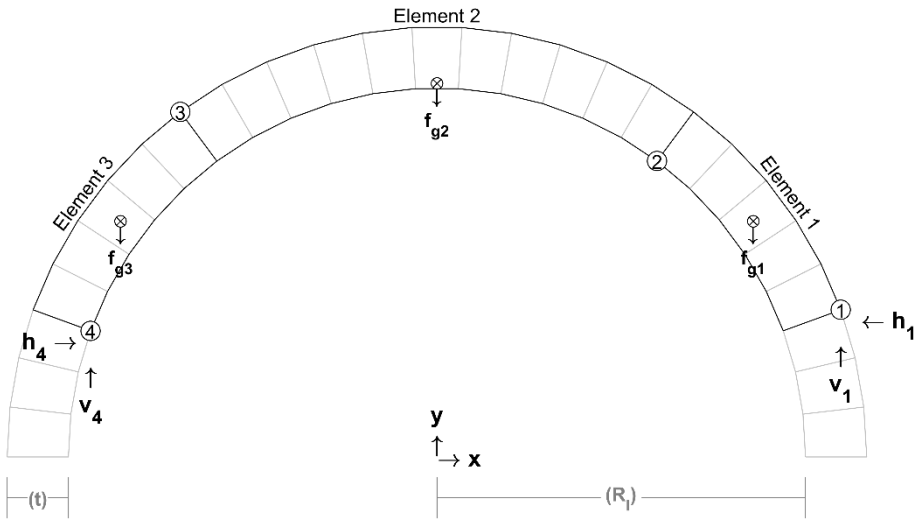

Figure 5. Free-body diagram for a four-pinned arch under self-weight.

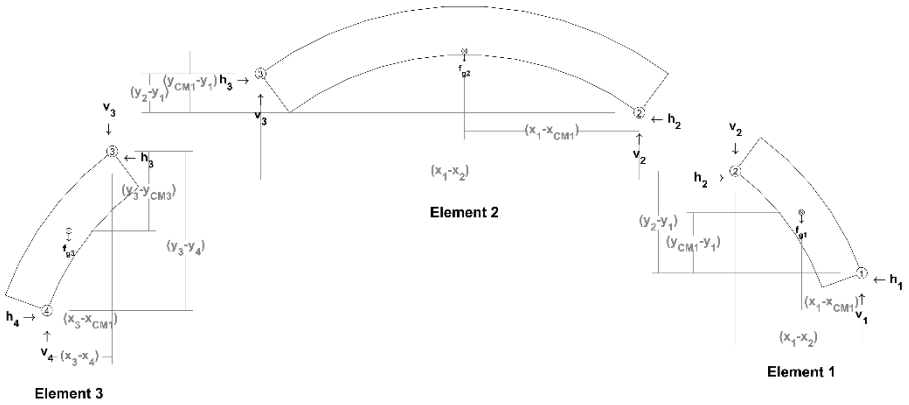

Figure 6. Element based forces, reactions, and lever arms used in the development of the equilibrium equations for the kinematic arch under self-weight.

The three-element representation of the arch generates nine equilibrium equations (three per element), but under its self-weight only eight unknowns exist due to the zero moment at the pin connections. In the traditional sense of statics, the condition of the four-pinned arch is unstable, which is true since the formation of the kinematic system is by definition concurrent with the loss of stability. In the context of mathematics and equilibrium, the four-pinned arch results in a system with infinite solutions. A ninth variable is required to create a determinate system, and with it a single solution. This ninth variable can either be a restriction of motion through the removal of a pin connection (i.e. the three-pinned arch) for the static condition, or the inclusion of an applied force that imposes equilibrium for the kinematic state.

Assuming the arch is stable under its self-weight therefore requires the application of an external load to generate a kinematic condition. Thus, the loading condition can be assigned a variable and incorporated into the equations of equilibrium to construct a kinematically determinant system with a singular solution.

Expressing Eqn. 2 in matrix form generates

$$[BC]\{r\} = \{q\} \tag{3}$$

where ***BC*** is the balance matrix, ***r*** is the reaction vector, and ***q*** is the constants vector. The addition of a loading condition and the accompanying loading variable into the formation of the equations of equilibrium generates a non-zero determinant for ***BC,*** allowing the reaction variables to be obtained by

$$\{r\} = [BC]^{-1}\{q\} \tag{4}$$

In the following sections, the *equations of equilibrium* are the combined balance matrix, reaction vector and constants vector group required to solve Eqn. 4.

3.2 Loading Conditions

To introduce the loading condition as a variable in the equations of equilibrium a multiplier is added to the geometry of the loading condition being analyzed. The choice of the multiplier depends on the conditions under evaluation. For example, seismic assessments typically include the multiplier as a factor of the gravitational constant g, while multipliers for capacity evaluations from external loading are applied to the unity condition of the loading geometry. Maintaining the traditional four-hinge mechanism, this section presents various loading conditions and the resulting balance matrix, reaction vector and constants vector that establish the equations of equilibrium.

3.2.1 Uniform Accelerations

Uniform accelerations are often used to perform simplified seismic assessments. The forces are thus driven by the density of the blocks and as such the load multiplier, λ_a, is expressed as a multiplier of *g*.

The simplest uniform acceleration is horizontal where the gravity and the added acceleration vectors are perpendicular. This isolates the vectors onto the *(x,y)* basis of the cartesian coordinate system which simplifies the analysis. The perpendicular behavior is not required however, and the uniform acceleration can also be applied generally as a 2D vector. This diagonal consideration of acceleration adds an additional variable and can be expressed in polar coordinates as (λ_a*g,θ_a), where θ_a is the polar angle of the acceleration vector. The cartesian accelerations become

$$\begin{aligned} a_x &= \lambda_a \cdot g \cdot \cos(\theta_a) \\ a_y &= \lambda_a \cdot g \cdot \sin(\theta_a) \end{aligned} \tag{5}$$

The linear set of equations utilized in the kinematic equilibrium approach requires the linearity of the variables. This requires the predefinition of either the angle or the magnitude of the acceleration vector prior to calculating the reaction vector. If the acceleration angle is defined, then the variable included in the reaction vector is set as λ_a. If the multiplier if fixed the evaluation can be utilized to determine the rotation angle of collapse. This can represent a tilting plane evaluation of capacity by determining an acceleration angle that generates a unit multiplier. The free-body diagram and equations of equilibrium for both horizontal acceleration and generic 2D accelerations applied to the standard four-hinge mechanism are presented.

3.2.1.1 Horizontal Acceleration

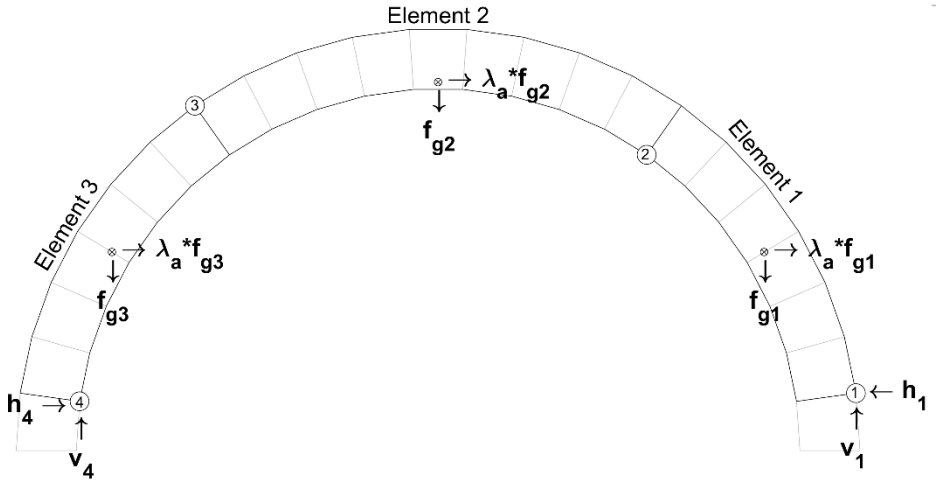

Figure 7. Free-body diagram for constant horizontal acceleration.

The equations of equilibrium for the condition shown in Figure 7 is

$$[BC] = \begin{bmatrix} -1 & 0 & 1 & 0 & 0 & 0 & 0 & 0 & f_{g1} \\ 0 & 1 & 0 & -1 & 0 & 0 & 0 & 0 & 0 \\ 0 & 0 & -\Delta y_{2,1} & \Delta x_{1,2} & 0 & 0 & 0 & 0 & -f_{g1}\Delta y_{CM1,1} \\ 0 & 0 & -1 & 0 & 1 & 0 & 0 & 0 & f_{g2} \\ 0 & 0 & 0 & 1 & 0 & 1 & 0 & 0 & 0 \\ 0 & 0 & 0 & 0 & \Delta y_{3,2} & \Delta x_{2,3} & 0 & 0 & f_{g2}\Delta y_{2,CM2} \\ 0 & 0 & 0 & 0 & -1 & 0 & 1 & 0 & f_{g3} \\ 0 & 0 & 0 & 0 & 0 & -1 & 0 & 1 & 0 \\ 0 & 0 & 0 & 0 & 0 & 0 & \Delta y_{3,4} & -\Delta x_{3,4} & f_{g3}\Delta y_{3,CM3} \end{bmatrix}$$

$$\{r\} = \begin{bmatrix} h_1 \\ v_1 \\ h_2 \\ v_2 \\ h_3 \\ v_3 \\ h_4 \\ v_4 \\ \lambda_a \end{bmatrix} \qquad \{q\} = \begin{bmatrix} 0 \\ f_{g1} \\ -f_{g1}\Delta x_{1,CM1} \\ 0 \\ f_{g2} \\ f_{g2}\Delta x_{2,CM2} \\ 0 \\ f_{g3} \\ -f_{g3}\Delta x_{3,CM3} \end{bmatrix} \tag{6}$$

3.2.1.2 2D Acceleration

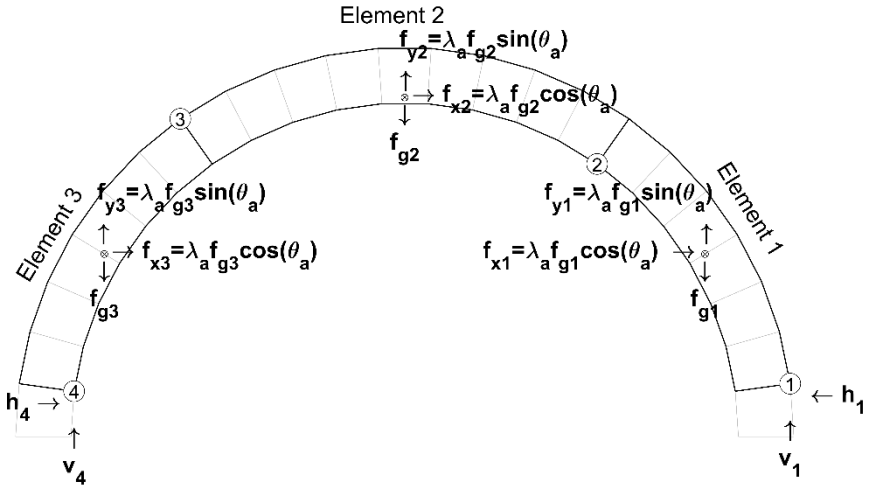

Figure 8. Free-body diagram for constant 2D acceleration.

The equations of equilibrium for the condition shown in Figure 8 is

$$[BC]=\begin{bmatrix} -1 & 0 & 1 & 0 & 0 & 0 & 0 & 0 & f_{x1} \\ 0 & 1 & 0 & -1 & 0 & 0 & 0 & 0 & f_{y1} \\ 0 & 0 & \Delta y_{2,1} & \Delta x_{1,2} & 0 & 0 & 0 & 0 & f_{x1}\Delta y_{CM1,1}-f_{y1}\Delta x_{1,CM1} \\ 0 & 0 & -1 & 0 & 1 & 0 & 0 & 0 & f_{x2} \\ 0 & 0 & 0 & 1 & 0 & 1 & 0 & 0 & f_{y2} \\ 0 & 0 & 0 & 0 & \Delta y_{3,2} & -\Delta x_{2,3} & 0 & 0 & f_{x2}\Delta y_{CM2,2}-f_{y2}\Delta x_{2,CM2} \\ 0 & 0 & 0 & 0 & -1 & 0 & 1 & 0 & f_{x3} \\ 0 & 0 & 0 & 0 & 0 & -1 & 0 & 1 & f_{y3} \\ 0 & 0 & 0 & 0 & 0 & 0 & \Delta y_{3,4} & -\Delta x_{3,4} & f_{x3}\Delta y_{3,CM3}+f_{y2}\Delta x_{3,CM3} \end{bmatrix}$$

$$\{r\}=\begin{bmatrix} h_1 \\ v_1 \\ h_2 \\ v_2 \\ h_3 \\ v_3 \\ h_4 \\ v_4 \\ \lambda_a \end{bmatrix} \qquad \{q\}=\begin{bmatrix} 0 \\ f_{g1} \\ -f_{g1}\Delta x_{1,CM1} \\ 0 \\ f_{g2} \\ f_{g2}\Delta x_{2,CM2} \\ 0 \\ f_{g3} \\ -f_{g3}\Delta x_{3,CM3} \end{bmatrix} \tag{7}$$

3.2.2 Point Loads

Asymmetric point loads represent the simplest external loading condition, and vertical point loads are often used for experimental testing. Typically, the collapse multiplier, λ_P, is attached to a downward unity load applied on the extrados of the arch. Under traditional assessment conditions the location of the vertical point load defines the position of hinge H_3 which develops at or near its location when unrestricted. The defining of the mechanism and subsequent rigid elements removes this relationship.

The point load can be defined by the polar pair, (λ_P, θ_p), which becomes

$$\begin{aligned} P_x &= \lambda_P \cdot \cos(\theta_P) \\ P_y &= \lambda_P \cdot \sin(\theta_P) \end{aligned} \tag{8}$$

The unbound positioning of the point load and mechanism requires three equations of equilibrium to address the interaction of the point load with each individual element. The point load's position, (x_P, y_P), thus determines the equations of equilibrium to evaluate and the hinge H_i used to establish the lever arm lengths $\Delta x_{P,i}$ and $\Delta y_{P,i}$. Also note that as with the uniform acceleration, the polar loading angle is a defined variable in the evaluation of an equations of equilibrium. Investigations into the effects of the polar loading angle require an iterative application of the equilibrium evaluation.

3.2.2.1 Point Load at Element 1

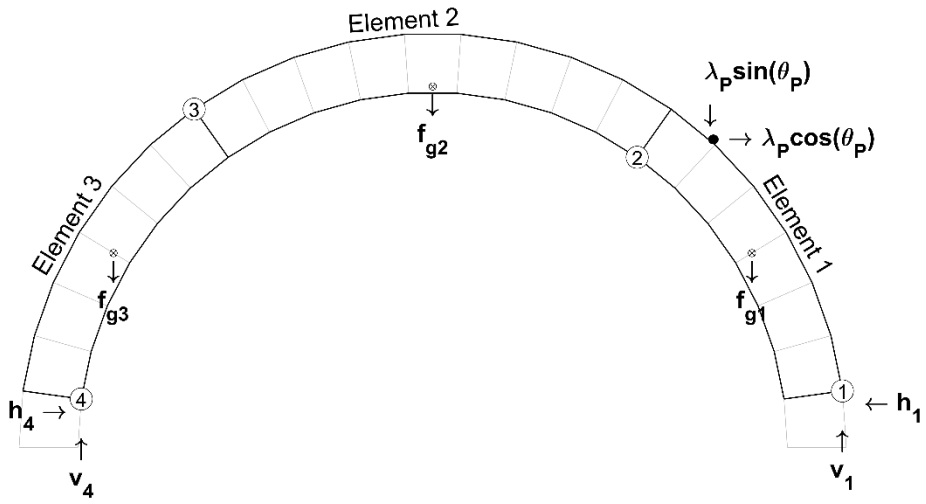

Figure 9. Free-body diagram for a point load at Element 1

The equations of equilibrium for the condition shown in Figure 9 is

$$[BC] = \begin{bmatrix} -1 & 0 & 1 & 0 & 0 & 0 & 0 & 0 & \cos(\theta_P) \\ 0 & 1 & 0 & -1 & 0 & 0 & 0 & 0 & -\sin(\theta_P) \\ 0 & 0 & -\Delta y_{2,1} & \Delta x_{1,2} & 0 & 0 & 0 & 0 & -\Delta x_{2,P}\sin(\theta_P) + \Delta y_{2,P}\sin(\theta_P) \\ 0 & 0 & -1 & 0 & 1 & 0 & 0 & 0 & 0 \\ 0 & 0 & 0 & 1 & 0 & 1 & 0 & 0 & 0 \\ 0 & 0 & 0 & 0 & \Delta y_{3,2} & \Delta x_{2,3} & 0 & 0 & 0 \\ 0 & 0 & 0 & 0 & -1 & 0 & 1 & 0 & 0 \\ 0 & 0 & 0 & 0 & 0 & -1 & 0 & 1 & 0 \\ 0 & 0 & 0 & 0 & 0 & 0 & \Delta y_{3,4} & -\Delta x_{3,4} & 0 \end{bmatrix}$$

$$\{r\} = \begin{bmatrix} h_1 \\ v_1 \\ h_2 \\ v_2 \\ h_3 \\ v_3 \\ h_4 \\ v_4 \\ \lambda_p \end{bmatrix} \qquad \{q\} = \begin{bmatrix} 0 \\ f_{g1} \\ -f_{g1}\Delta x_{1,CM1} \\ 0 \\ f_{g2} \\ f_{g2}\Delta x_{2,CM2} \\ 0 \\ f_{g3} \\ -f_{g3}\Delta x_{3,CM3} \end{bmatrix} \tag{9}$$

3.2.2.2 Point Load at Element 2

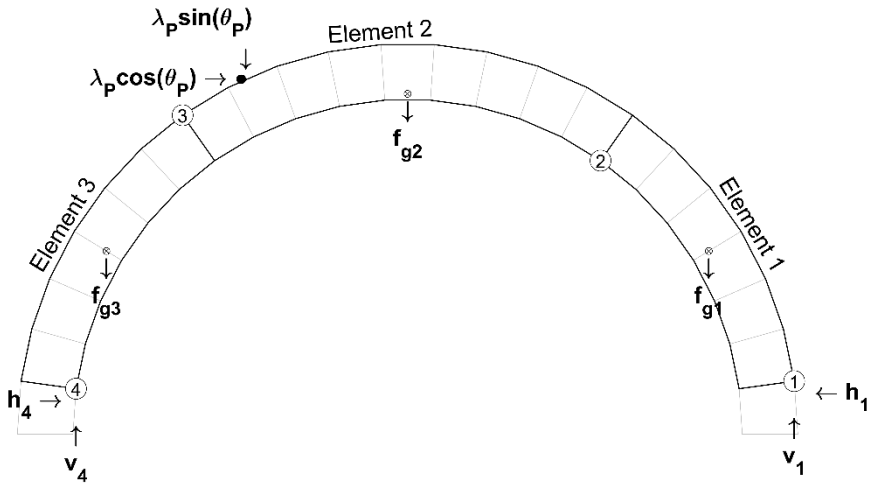

Figure 10. Free-body diagram for a point load at Element 2

The equations of equilibrium for the condition shown in Figure 10 is

$$[BC] = \begin{bmatrix} -1 & 0 & 1 & 0 & 0 & 0 & 0 & 0 & 0 \\ 0 & 1 & 0 & -1 & 0 & 0 & 0 & 0 & 0 \\ 0 & 0 & -\Delta y_{2,1} & \Delta x_{1,2} & 0 & 0 & 0 & 0 & 0 \\ 0 & 0 & -1 & 0 & 1 & 0 & 0 & 0 & \cos(\theta_P) \\ 0 & 0 & 0 & 1 & 0 & 1 & 0 & 0 & -\sin(\theta_P) \\ 0 & 0 & 0 & 0 & \Delta y_{3,2} & \Delta x_{2,3} & 0 & 0 & -\Delta x_{2,P}\sin(\theta_P) + \Delta y_{2,P}\sin(\theta_P) \\ 0 & 0 & 0 & 0 & -1 & 0 & 1 & 0 & 0 \\ 0 & 0 & 0 & 0 & 0 & -1 & 0 & 1 & 0 \\ 0 & 0 & 0 & 0 & 0 & 0 & \Delta y_{3,4} & -\Delta x_{3,4} & 0 \end{bmatrix}$$

$$\{r\} = \begin{bmatrix} h_1 \\ v_1 \\ h_2 \\ v_2 \\ h_3 \\ v_3 \\ h_4 \\ v_4 \\ \lambda_p \end{bmatrix} \qquad \{q\} = \begin{bmatrix} 0 \\ f_{g1} \\ -f_{g1}\Delta x_{1,CM1} \\ 0 \\ f_{g2} \\ f_{g2}\Delta x_{2,CM2} \\ 0 \\ f_{g3} \\ -f_{g3}\Delta x_{3,CM3} \end{bmatrix} \tag{10}$$

3.2.2.3 Point Load at Element 3

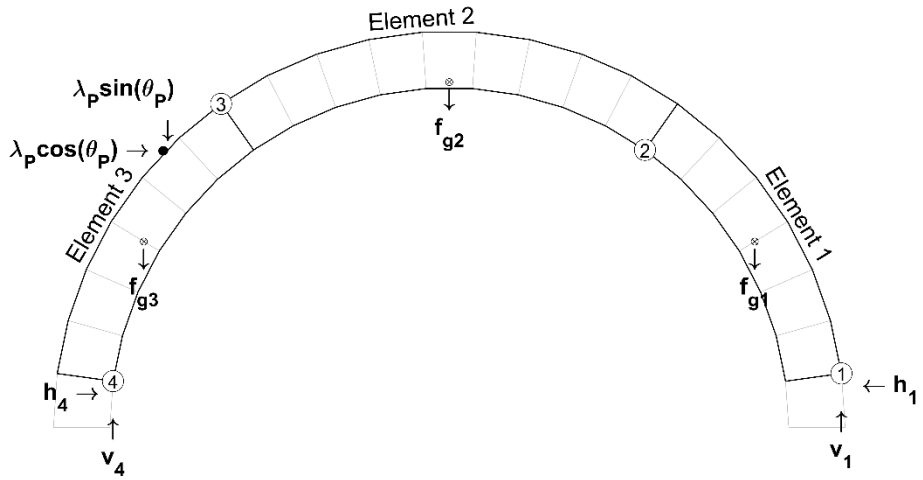

Figure 11. Free-body diagram for a point load at Element 3

The equations of equilibrium for the condition shown in Figure 11 is

$$[BC] = \begin{bmatrix} -1 & 0 & 1 & 0 & 0 & 0 & 0 & 0 & 0 \\ 0 & 1 & 0 & -1 & 0 & 0 & 0 & 0 & 0 \\ 0 & 0 & -\Delta y_{2,1} & \Delta x_{1,2} & 0 & 0 & 0 & 0 & 0 \\ 0 & 0 & -1 & 0 & 1 & 0 & 0 & 0 & 0 \\ 0 & 0 & 0 & 1 & 0 & 1 & 0 & 0 & 0 \\ 0 & 0 & 0 & 0 & \Delta y_{3,2} & \Delta x_{2,3} & 0 & 0 & 0 \\ 0 & 0 & 0 & 0 & -1 & 0 & 1 & 0 & \cos(\theta_P) \\ 0 & 0 & 0 & 0 & 0 & -1 & 0 & 1 & -\sin(\theta_P) \\ 0 & 0 & 0 & 0 & 0 & 0 & \Delta y_{3,4} & -\Delta x_{3,4} & -\Delta x_{3,P}\sin(\theta_P) + \Delta y_{3,P}\sin(\theta_P) \end{bmatrix}$$

$$\{r\} = \begin{bmatrix} h_1 \\ v_1 \\ h_2 \\ v_2 \\ h_3 \\ v_3 \\ h_4 \\ v_4 \\ \lambda_p \end{bmatrix} \qquad \{q\} = \begin{bmatrix} 0 \\ f_{g1} \\ -f_{g1}\Delta x_{1,CM1} \\ 0 \\ f_{g2} \\ f_{g2}\Delta x_{2,CM2} \\ 0 \\ f_{g3} \\ -f_{g3}\Delta x_{3,CM3} \end{bmatrix} \tag{11}$$

3.2.3 Distributed Loads

The final primary loading condition is distributed loads. Ranging from non-ideal point loads to full infill conditions, distributed loads are the most common loading condition applied to arches. As with the application of the point load, the structure of the equations of equilibrium used to evaluate capacity depends upon the elements on which the load is applied. The evaluation of stable capacity also depends on the distribution of the load itself.

Beginning with the definition of pin-connected rigid elements allows the application of equivalent force systems to establish concentrated forces acting on the elements from the applied distributed load. For a given load distribution geometry, ω(x,y), the horizontal position of the net vertical component, F_v, and the vertical position of the net horizontal component, F_h, of the equivalent concentrated forces are

$$x_v = \frac{\int_{x_1}^{x_2} \omega(x,y) x dx}{\int_{x_1}^{x_2} \omega(x,y) dx} \tag{12}$$

and

$$y_h = \frac{\int_{y_1}^{y_2} \omega(x,y) y dy}{\int_{y_1}^{y_2} \omega(x,y) dy} \tag{13}$$

respectively. The corresponding coordinate values for vertical, y_v, and horizontal x_h, force components are obtained from the extrados boundary of the arch under evaluation. Setting the total force to unity and multiplying by the load multiplier, λ_d, establishes the force variable and the polar form, (λ_d, θ_d), of the equivalent concentrated force with

$$\theta_d = \tan^{-1}\left(\frac{F_v}{F_h}\right) \tag{14}$$

As with the other loading conditions, the polar angle or force multiplier must be defined to obtain a solution to the reactions vector. Also, distributed loads that do not cross the boundaries of an element will result in a zero applied force on that element, and distributed loads themselves are decomposed into their element based net equivalent horizontal forces, f_{hi}, and vertical forces, f_{vi}.

3.2.3.1 Left Horizontal Distribution

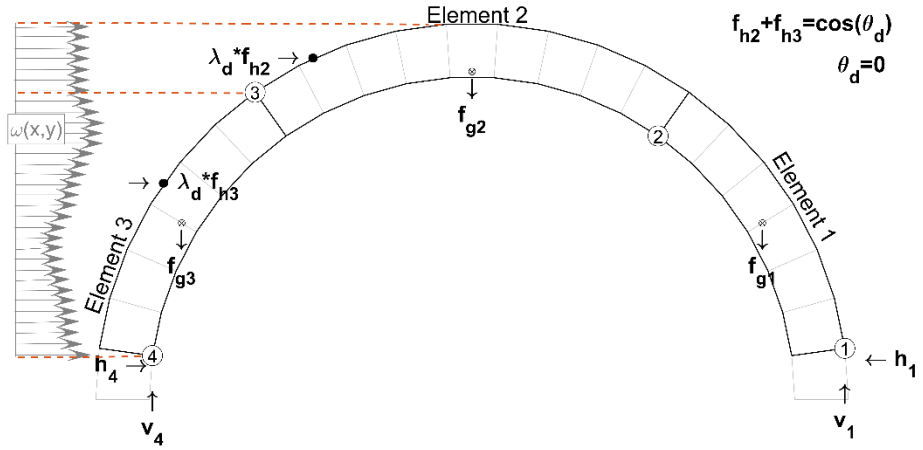

Figure 12. Free-body diagram for a left horizontal distributed load

The equations of equilibrium for the condition shown in Figure 12 is

$$[BC] = \begin{bmatrix} -1 & 0 & 1 & 0 & 0 & 0 & 0 & 0 & 0 \\ 0 & 1 & 0 & -1 & 0 & 0 & 0 & 0 & 0 \\ 0 & 0 & -\Delta y_{2,1} & \Delta x_{1,2} & 0 & 0 & 0 & 0 & 0 \\ 0 & 0 & -1 & 0 & 1 & 0 & 0 & 0 & f_{h2} \\ 0 & 0 & 0 & 1 & 0 & 1 & 0 & 0 & 0 \\ 0 & 0 & 0 & 0 & \Delta y_{3,2} & \Delta x_{2,3} & 0 & 0 & f_{h2}\Delta y_{h2,2} \\ 0 & 0 & 0 & 0 & -1 & 0 & 1 & 0 & f_{h3} \\ 0 & 0 & 0 & 0 & 0 & -1 & 0 & 1 & 0 \\ 0 & 0 & 0 & 0 & 0 & 0 & \Delta y_{3,4} & -\Delta x_{3,4} & f_{h3}\Delta y_{3,h3} \end{bmatrix}$$

$$\{r\} = \begin{bmatrix} h_1 \\ v_1 \\ h_2 \\ v_2 \\ h_3 \\ v_3 \\ h_4 \\ v_4 \\ \lambda_d \end{bmatrix} \qquad \{q\} = \begin{bmatrix} 0 \\ f_{g1} \\ -f_{g1}\Delta x_{1,CM1} \\ 0 \\ f_{g2} \\ f_{g2}\Delta x_{2,CM2} \\ 0 \\ f_{g3} \\ -f_{g3}\Delta x_{3,CM3} \end{bmatrix} \tag{15}$$

3.2.3.2 Right Horizontal Distribution

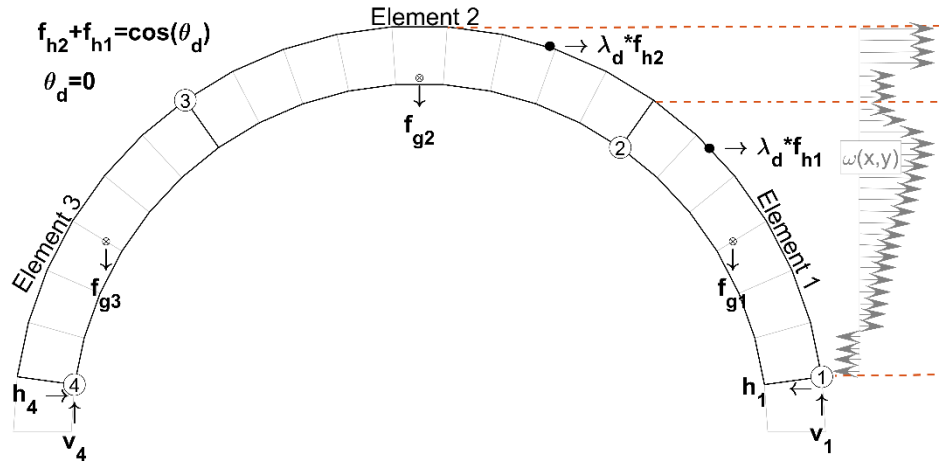

Figure 13. Free-body diagram for a right horizontal distributed load

The equations of equilibrium for the condition shown in Figure 13 is

$$[BC] = \begin{bmatrix} -1 & 0 & 1 & 0 & 0 & 0 & 0 & 0 & f_{h1} \\ 0 & 1 & 0 & -1 & 0 & 0 & 0 & 0 & 0 \\ 0 & 0 & -\Delta y_{2,1} & \Delta x_{1,2} & 0 & 0 & 0 & 0 & f_{h1}\Delta y_{h1,1} \\ 0 & 0 & -1 & 0 & 1 & 0 & 0 & 0 & f_{h2} \\ 0 & 0 & 0 & 1 & 0 & 1 & 0 & 0 & 0 \\ 0 & 0 & 0 & 0 & \Delta y_{3,2} & \Delta x_{2,3} & 0 & 0 & f_{h2}\Delta y_{h2,2} \\ 0 & 0 & 0 & 0 & -1 & 0 & 1 & 0 & 0 \\ 0 & 0 & 0 & 0 & 0 & -1 & 0 & 1 & 0 \\ 0 & 0 & 0 & 0 & 0 & 0 & \Delta y_{3,4} & -\Delta x_{3,4} & 0 \end{bmatrix}$$

$$\{r\} = \begin{bmatrix} h_1 \\ v_1 \\ h_2 \\ v_2 \\ h_3 \\ v_3 \\ h_4 \\ v_4 \\ \lambda_d \end{bmatrix} \qquad \{q\} = \begin{bmatrix} 0 \\ f_{g1} \\ -f_{g1}\Delta x_{1,CM1} \\ 0 \\ f_{g2} \\ f_{g2}\Delta x_{2,CM2} \\ 0 \\ f_{g3} \\ -f_{g3}\Delta x_{3,CM3} \end{bmatrix} \tag{16}$$

3.2.3.3 Vertical Distribution

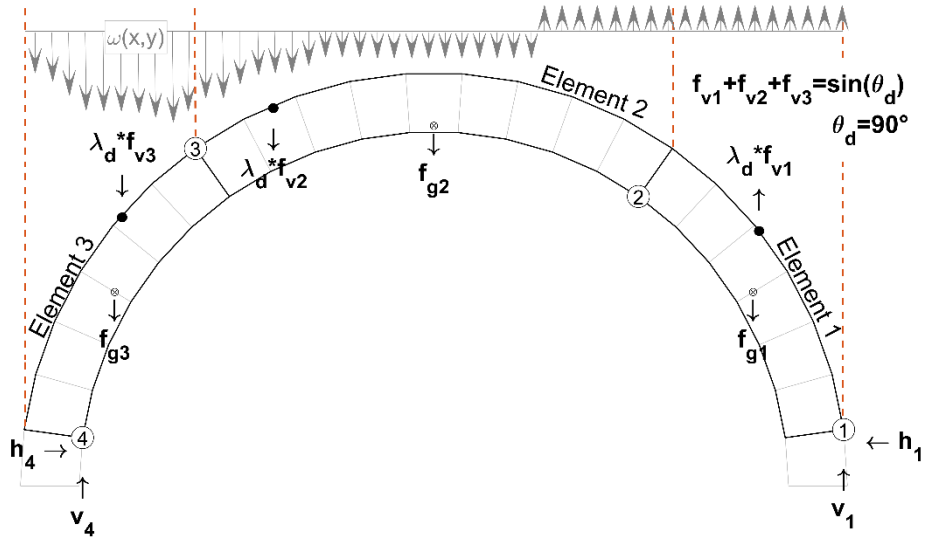

Figure 14. Free-body diagram for a vertical distributed load

The equations of equilibrium for the condition shown in Figure 14 is

$$[BC]=\begin{bmatrix} -1 & 0 & 1 & 0 & 0 & 0 & 0 & 0 & 0 \\ 0 & 1 & 0 & -1 & 0 & 0 & 0 & 0 & f_{v1} \\ 0 & 0 & -\Delta y_{2,1} & \Delta x_{1,2} & 0 & 0 & 0 & 0 & f_{v1}\Delta x_{1,v1} \\ 0 & 0 & -1 & 0 & 1 & 0 & 0 & 0 & 0 \\ 0 & 0 & 0 & 1 & 0 & 1 & 0 & 0 & f_{v2} \\ 0 & 0 & 0 & 0 & \Delta y_{3,2} & \Delta x_{2,3} & 0 & 0 & f_{v2}\Delta x_{2,v2} \\ 0 & 0 & 0 & 0 & -1 & 0 & 1 & 0 & 0 \\ 0 & 0 & 0 & 0 & 0 & -1 & 0 & 1 & f_{v3} \\ 0 & 0 & 0 & 0 & 0 & 0 & \Delta y_{3,4} & -\Delta x_{3,4} & f_{v3}\Delta x_{3,v3} \end{bmatrix}$$

$$\{r\}=\begin{bmatrix} h_1 \\ v_1 \\ h_2 \\ v_2 \\ h_3 \\ v_3 \\ h_4 \\ v_4 \\ \lambda_d \end{bmatrix} \qquad \{q\}=\begin{bmatrix} 0 \\ f_{g1} \\ -f_{g1}\Delta x_{1,CM1} \\ 0 \\ f_{g2} \\ f_{g2}\Delta x_{2,CM2} \\ 0 \\ f_{g3} \\ -f_{g3}\Delta x_{3,CM3} \end{bmatrix} \tag{17}$$

3.2.4 Combining Loads

For all the examined loading conditions, the incorporation of the load multiplier on the equations of equilibrium is isolated to a single column of ***BC*** as highlighted in Figure 15. If a loading condition exists and is not associated with the collapse multiplier, then the constants vector is subtracted by the appropriate load variable column times the known multiplier. In this manner equations of equilibrium can be efficiently established for any loading condition.

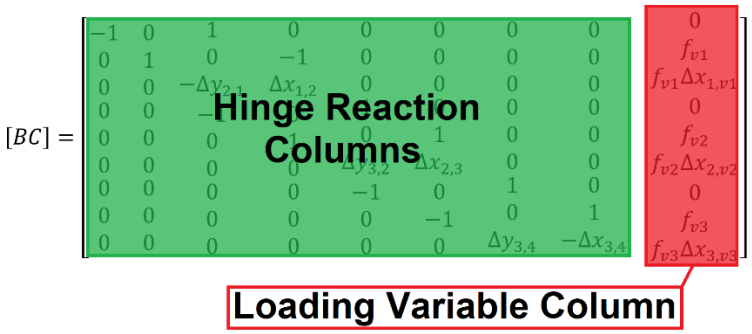

Figure 15. Isolated columns of the balance condition matrix

3.2.4.1 Combined Loads Example

Consider the arch-hinge-loading condition shown in Figure 16. The arch is subjected to a point load, a distributed load and a constant acceleration. The point load, λ_P, is vertical and applied on Element 2 near hinge H_3. The distributed load $\omega(x,y)$ is applied radially across the extrados of the arch segment θ_ω starting from Hinge H_1. The constant acceleration is applied horizontally.

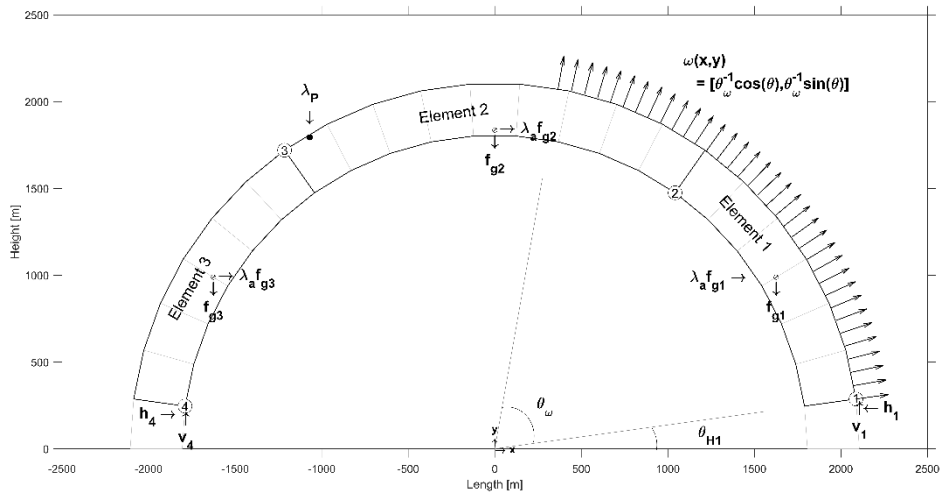

Figure 16. Free-body diagram for combined loading condition

The net force of the distributed load sums to unity with a vector angle θ_d that is half the span angle plus the hinge H_1 offset θ_{H1}. Utilizing Section 3.2.3, allows for the decomposition of the distributed load and the inclusion of the multiplier, λ_d, in the equivalent force structure. Figure 17 shows this decomposition for the final geometry used in the kinematic equilibrium evaluations.

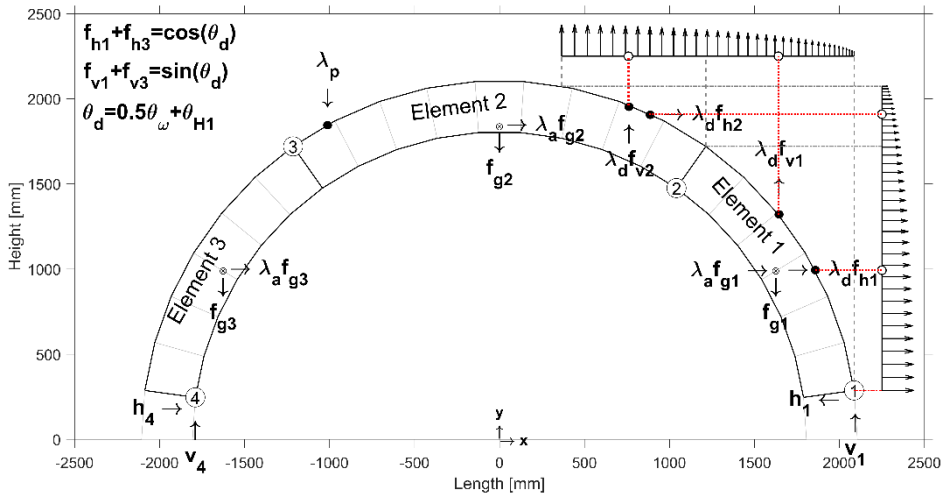

Figure 17. Free-body diagram for establishing combined equations of equilibrium

Utilizing Eqns. 6, 10, 16, and 17, and assigning the acceleration as the loading variable generates the equations of equilibrium

$$[BC] = \begin{bmatrix} -1 & 0 & 1 & 0 & 0 & 0 & 0 & 0 & f_{g1} \\ 0 & 1 & 0 & -1 & 0 & 0 & 0 & 0 & 0 \\ 0 & 0 & -\Delta y_{2,1} & \Delta x_{1,2} & 0 & 0 & 0 & 0 & -f_{g1}\Delta y_{CM1,1} \\ 0 & 0 & -1 & 0 & 1 & 0 & 0 & 0 & f_{g2} \\ 0 & 0 & 0 & 1 & 0 & 1 & 0 & 0 & 0 \\ 0 & 0 & 0 & 0 & \Delta y_{3,2} & \Delta x_{2,3} & 0 & 0 & f_{g2}\Delta y_{2,CM2} \\ 0 & 0 & 0 & 0 & -1 & 0 & 1 & 0 & f_{g3} \\ 0 & 0 & 0 & 0 & 0 & -1 & 0 & 1 & 0 \\ 0 & 0 & 0 & 0 & 0 & 0 & \Delta y_{3,4} & -\Delta x_{3,4} & f_{g3}\Delta y_{3,CM3} \end{bmatrix}$$

$$\{r\} = \begin{bmatrix} h_1 \\ v_1 \\ h_2 \\ v_2 \\ h_3 \\ v_3 \\ h_4 \\ v_4 \\ \lambda_a \end{bmatrix} \qquad \{q\} = \begin{bmatrix} \lambda_d f_{h1} \\ f_{g1} + \lambda_d f_{v1} \\ -f_{g1}\Delta x_{1,CM1} + \lambda_d\left(f_{h1}\Delta y_{h1,1} + f_{v1}\Delta x_{1,v1}\right) \\ \lambda_d f_{h2} \\ f_{g2} + \lambda_P + \lambda_d f_{v2} \\ f_{g2}\Delta x_{2,CM2} - \lambda_P \Delta x_{2,P} + \lambda_d\left(f_{h2}\Delta y_{h2,2} + f_{v2}\Delta x_{2,v2}\right) \\ 0 \\ f_{g3} \\ -f_{g3}\Delta x_{3,CM3} \end{bmatrix} \qquad (18)$$

Switching the point load with the acceleration variables creates

$$[BC] = \begin{bmatrix} -1 & 0 & 1 & 0 & 0 & 0 & 0 & 0 & 0 \\ 0 & 1 & 0 & -1 & 0 & 0 & 0 & 0 & 0 \\ 0 & 0 & -\Delta y_{2,1} & \Delta x_{1,2} & 0 & 0 & 0 & 0 & 0 \\ 0 & 0 & -1 & 0 & 1 & 0 & 0 & 0 & 0 \\ 0 & 0 & 0 & 1 & 0 & 1 & 0 & 0 & 1 \\ 0 & 0 & 0 & 0 & \Delta y_{3,2} & \Delta x_{2,3} & 0 & 0 & -\Delta x_{2,P} \\ 0 & 0 & 0 & 0 & -1 & 0 & 1 & 0 & 0 \\ 0 & 0 & 0 & 0 & 0 & -1 & 0 & 1 & 0 \\ 0 & 0 & 0 & 0 & 0 & 0 & \Delta y_{3,4} & -\Delta x_{3,4} & 0 \end{bmatrix}$$

$$\{r\} = \begin{bmatrix} h_1 \\ v_1 \\ h_2 \\ v_2 \\ h_3 \\ v_3 \\ h_4 \\ v_4 \\ \lambda_P \end{bmatrix} \qquad \{q\} = \begin{bmatrix} \lambda_a f_{g1} + \lambda_d f_{h1} \\ f_{g1} + \lambda_d f_{v1} \\ -f_{g1}\Delta x_{1,CM1} + \lambda_a f_{g1}\Delta y_{CM1,1} + \lambda_d\left(f_{h1}\Delta y_{h1,1} + f_{v1}\Delta x_{1,v1}\right) \\ \lambda_a f_{g2} + \lambda_d f_{h2} \\ f_{g2} + \lambda_d f_{v2} \\ f_{g2}\Delta x_{2,CM2} + \lambda_a f_{g2}\Delta y_{CM2,2} + \lambda_d\left(f_{h2}\Delta y_{h2,2} + f_{v2}\Delta x_{2,v2}\right) \\ \lambda_a f_{g3} \\ f_{g3} \\ -f_{g3}\Delta x_{3,CM3} + \lambda_a f_{g3}\Delta y_{3,CM3} \end{bmatrix} \quad (19)$$

Lastly, assigning the distributed load as the loading variable creates the equations of equilibrium

$$[BC] = \begin{bmatrix} -1 & 0 & 1 & 0 & 0 & 0 & 0 & 0 & f_{h1} \\ 0 & 1 & 0 & -1 & 0 & 0 & 0 & 0 & f_{v1} \\ 0 & 0 & -\Delta y_{2,1} & \Delta x_{1,2} & 0 & 0 & 0 & 0 & f_{h1}\Delta y_{h1,1} + f_{v1}\Delta x_{1,v1} \\ 0 & 0 & -1 & 0 & 1 & 0 & 0 & 0 & f_{h2} \\ 0 & 0 & 0 & 1 & 0 & 1 & 0 & 0 & f_{v2} \\ 0 & 0 & 0 & 0 & \Delta y_{3,2} & \Delta x_{2,3} & 0 & 0 & -\Delta x_{2,P} \\ 0 & 0 & 0 & 0 & -1 & 0 & 1 & 0 & f_{h2}\Delta y_{h2,2} + f_{v2}\Delta x_{2,v2} \\ 0 & 0 & 0 & 0 & 0 & -1 & 0 & 1 & 0 \\ 0 & 0 & 0 & 0 & 0 & 0 & \Delta y_{3,4} & -\Delta x_{3,4} & 0 \end{bmatrix}$$

$$\{r\} = \begin{bmatrix} h_1 \\ v_1 \\ h_2 \\ v_2 \\ h_3 \\ v_3 \\ h_4 \\ v_4 \\ \lambda_d \end{bmatrix} \qquad \{q\} = \begin{bmatrix} \lambda_a f_{g1} \\ f_{g1} \\ -f_{g1}\Delta x_{1,CM1} + \lambda_a f_{g1}\Delta y_{CM1,1} \\ \lambda_a f_{g2} \\ f_{g2} + \lambda_P \\ f_{g2}\Delta x_{2,CM2} + \lambda_a f_{g2}\Delta y_{CM2,2} \\ \lambda_a f_{g3} \\ f_{g3} \\ -f_{g3}\Delta x_{3,CM3} + \lambda_a f_{g3}\Delta y_{3,CM3} \end{bmatrix} \quad (20)$$

Equations 18-20 highlight the simplicity and efficiency of constructing equations of equilibrium for the kinematic equilibrium analysis approach with multiple applied loads. While not presented here, it is also important to note that the relationship of loading conditions can be further expanded by constructing collapse multipliers that define relationships between different loads. This more

complex consideration is outside the current scope of work but will play an important role as the technique of designing safety factors for RSBD is explored.

3.3 Mechanisms

The previous section focused on the development of the equations of equilibrium for determining kinematic equilibrium of an arch subjected to different loading conditions. Each of these loading conditions was combined with the traditional four-hinge mechanism that forms under the assumption of no slippage. The removal of the no-slip assumption however introduces additional mechanisms. For instance, the replacement of a hinge rotation with a slip translation as shown in Figure 18 was experimentally observed and numerically validated (see Chapter 5) [124], [125]. Additionally, in the context of structural design and detailing it is imperative that all potential failure mechanisms are considered to ensure that the desired mechanism controls. Therefore, it is necessary to establish the equations of equilibrium for all the potential mechanism types that exist from the removal of the no slip assumption.

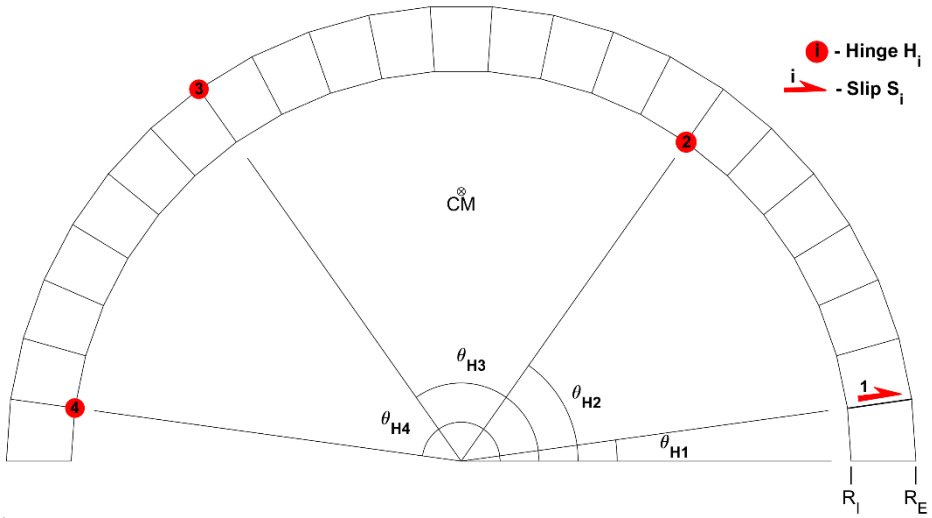

Figure 18. Admissible mechanism with a slip joint

The inclusion of slip is performed through the inclusion of an additional variable to the system, static friction, at the mechanical joints. This results in three potential conditions at each mechanical joint: hinge rotation, slip translation, or a combination of the two. Note that the combination of slip and rotation at a single joint results in two degrees of freedom and thus requires the removal of a different mechanical joint for the system to be balanced. Consequently, the total number of potential mechanisms becomes 70 including the standard. These 70 mechanisms, identified as Type I through Type LXX, can be divided into six groups by their similarities. These mechanism groups are the Standard, Slip-Hinge, Combined-Hinge, Combined-Hinge-Slip, Combined-Slip, and Combined. Limiting the loading condition to constant horizontal accelerations, this section

derives the inclusion of slip into the free-body diagrams and establishes the equations of equilibrium for the 70 potential mechanisms.

For the reference of the 70 mechanism types, H_i, S_i and C_i indicate a standard hinge rotation, a slip translation, and a hinge-slip combination for the i^{th} mechanical joint respectively.

3.3.1 Slip Replacement

The replacement of a hinge rotation with a slip translation at a joint has the consequence of removing the singularity of the thrust line boundary condition at that joint. Remember that the thrust line is the line that represents the flow of concentrated forces. The development of a hinge fixes the thrust line at the hinge, but the slip condition releases that restraint. Without the knowledge of the thrust line location at the slip joint, an additional variable must be added to the free-body diagram. That variable is a moment and is defined as

$$M_i = e_i \cdot N_i \tag{21}$$

for the i^{th} mechanical joint. The eccentricity, e_i , is taken as the distance from the standard hinge location and the reaction force, N_i, is the normal force at the mechanical joint.

The inclusion of the moment into the reaction variables creates an indeterminate system. Thus, the inclusion of static friction through the relationships

$$P_i = F_{Ni} \cdot \mu_S \tag{22}$$

and

$$\theta_S = \tan^{-1}(\mu_S) \tag{23}$$

re-establishes a determinate system. In Eqns. 22 and 23 P_i is the parallel reaction force at the i^{th} joint, μ_S is the coefficient of static friction and θ_S is the friction angle. In terms of cartesian coordinates, the relationship between the horizontal and vertical reactions becomes

$$v_i = h_i \tan(\alpha_i) \tag{24}$$

where α_i is established through the reaction vector condition and the mechanical joint angle. Eqn. 24 provides the addition to ***BC*** required to balance the addition of M_i to ***r***.

For slip joints S_1, S_2, S_3 and S_4 the geometric relationships between the joint angle, the friction angle and the reaction vectors are shown in Figure 19.

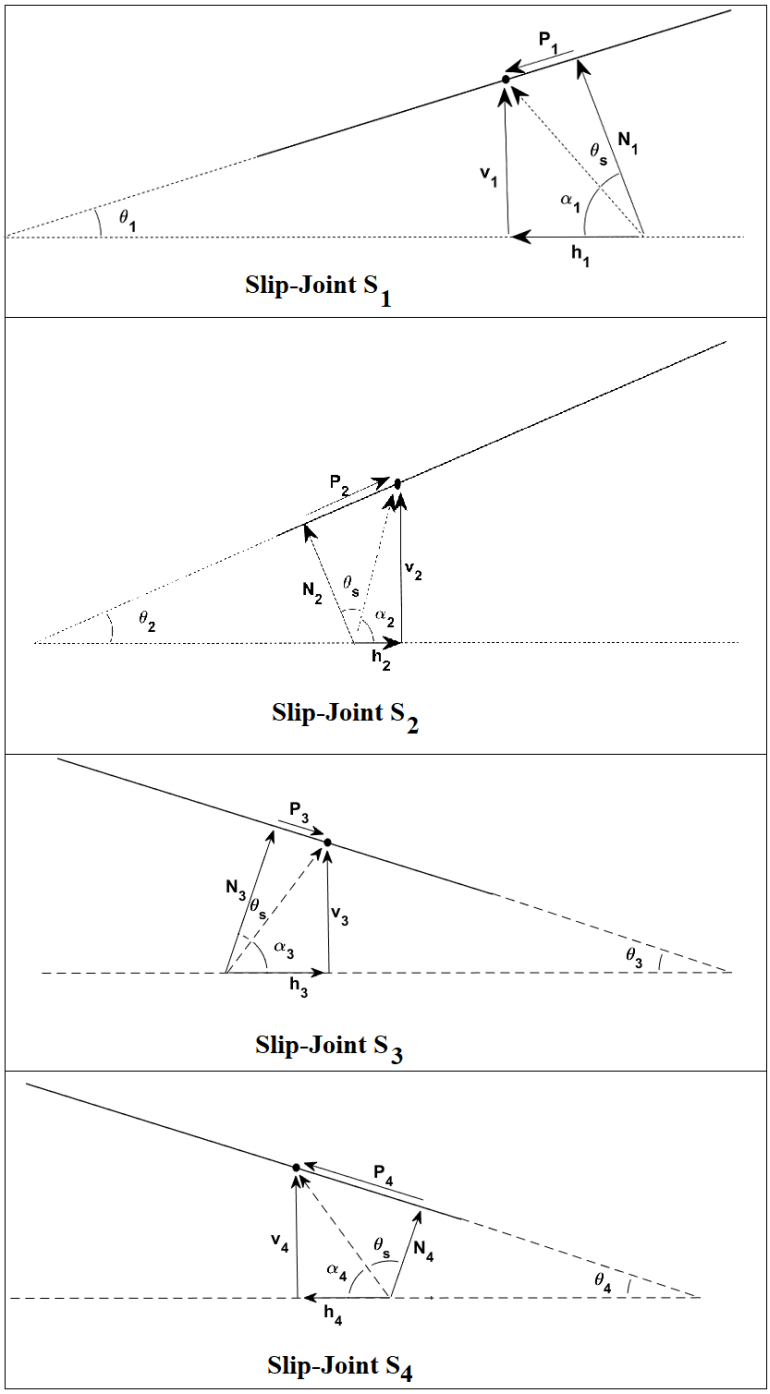

Figure 19. Geometric relationships between the joint angle, friction angle, and reaction vectors for the slip-joints used in the slip replacement mechanisms

3.3.2 Standard Mechanism

3.3.2.1 Type I – H_1 H_2 H_3 H_4

Refer to Section 3.2 for the free-body diagram and equations of equilibrium of the standard four-hinge mechanism.

3.3.3 Slip-Hinge Mechanisms

The slip-hinge mechanisms include the all the potential mechanisms that replace hinge rotations with slip translations. Mechanisms Type II through Type V replace a single hinge with a slip joint, Type VI through Type XI replace two hinges with slip joints, Type XII through Type XV replace three hinges with slip joints, and Type XVI replaces all four hinges with slip joints.

Note that for each slip joint introduced to the system, an additional variable is added to the equations of equilibrium. This results in the expansion of the original nine variables up to thirteen variables for the condition of four slip joints. As previously stated, the added variable is the moments at the mechanical joints which are balanced with friction relationship defined in Eqn. 24. Additionally, from Figure 19 it can be seen that

$$\alpha_1 = \frac{\pi}{2} - \theta_1 - \theta_S \tag{25}$$

$$\alpha_2 = \frac{\pi}{2} - \theta_2 - \theta_S \tag{26}$$

$$\alpha_3 = \frac{\pi}{2} - \theta_3 - \theta_S \tag{27}$$

and

$$\alpha_4 = \frac{3\pi}{2} - \theta_4 - \theta_S \tag{28}$$

for mechanisms that include slip joints S_1, S_2, S_3 and S_4 respectively.

3.3.3.1 Type II – S_1 H_2 H_3 H_4

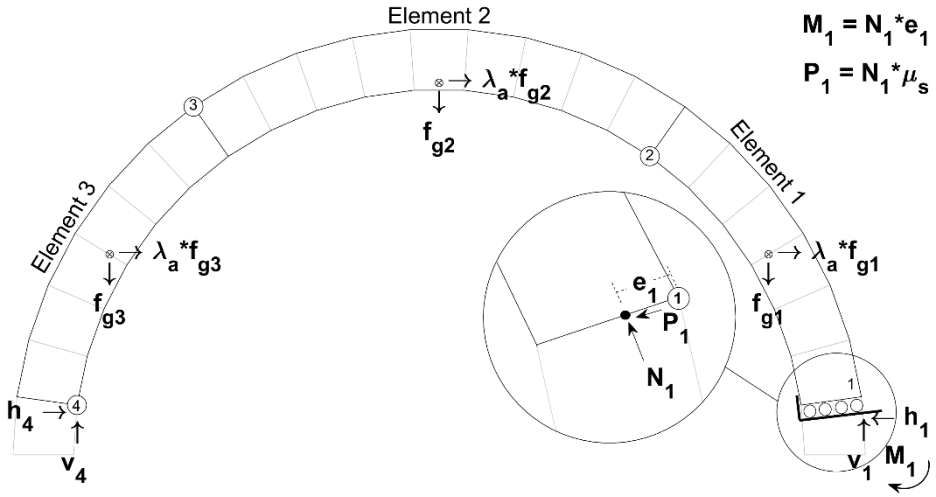

Figure 20. Free-body diagram for the Type II mechanism

The Equilibrium Set for the condition shown in Figure 20 is

$$[BC] = \begin{bmatrix} -1 & 0 & 1 & 0 & 0 & 0 & 0 & 0 & f_{g1} & 0 \\ 0 & 1 & 0 & -1 & 0 & 0 & 0 & 0 & 0 & 0 \\ 0 & 0 & -\Delta y_{2,1} & \Delta x_{1,2} & 0 & 0 & 0 & 0 & -f_{g1}\Delta y_{CM1,1} & -1 \\ 0 & 0 & -1 & 0 & 1 & 0 & 0 & 0 & f_{g2} & 0 \\ 0 & 0 & 0 & 1 & 0 & 1 & 0 & 0 & 0 & 0 \\ 0 & 0 & 0 & 0 & \Delta y_{3,2} & \Delta x_{2,3} & 0 & 0 & f_{g2}\Delta y_{2,CM2} & 0 \\ 0 & 0 & 0 & 0 & -1 & 0 & 1 & 0 & f_{g3} & 0 \\ 0 & 0 & 0 & 0 & 0 & -1 & 0 & 1 & 0 & 0 \\ 0 & 0 & 0 & 0 & 0 & 0 & \Delta y_{3,4} & -\Delta x_{3,4} & f_{g3}\Delta y_{3,CM3} & 0 \\ \tan(\alpha_1) & -1 & 0 & 0 & 0 & 0 & 0 & 0 & 0 & 0 \end{bmatrix}$$

$$\{r\} = \begin{bmatrix} h_1 \\ v_1 \\ h_2 \\ v_2 \\ h_3 \\ v_3 \\ h_4 \\ v_4 \\ \lambda_a \\ M_1 \end{bmatrix} \qquad \{q\} = \begin{bmatrix} 0 \\ f_{g1} \\ -f_{g1}\Delta x_{1,CM1} \\ 0 \\ f_{g2} \\ f_{g2}\Delta x_{2,CM2} \\ 0 \\ f_{g3} \\ -f_{g3}\Delta x_{3,CM3} \\ 0 \end{bmatrix} \tag{29}$$

3.3.3.2 Type III – H_1 S_2 H_3 H_4

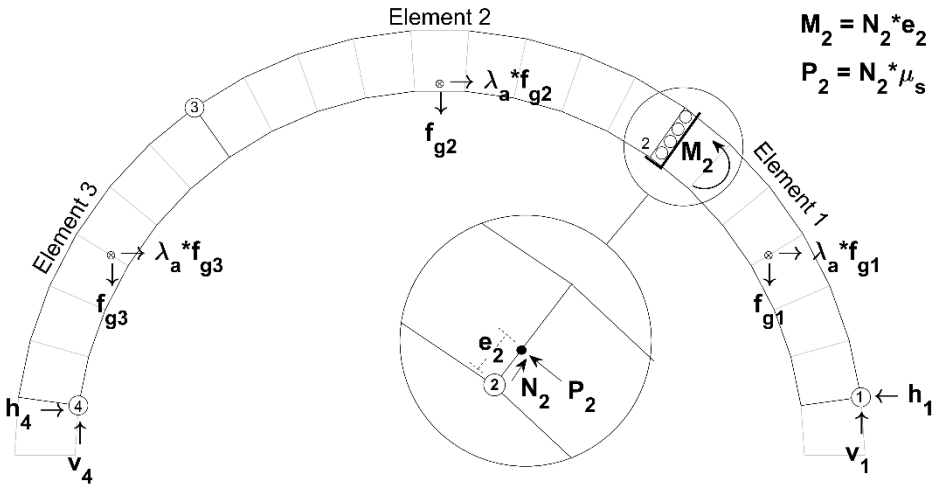

Figure 21. Free-body diagram for the Type III mechanism

The Equilibrium Set for the condition shown in Figure 21 is

$$[BC] = \begin{bmatrix} -1 & 0 & 1 & 0 & 0 & 0 & 0 & 0 & f_{g1} & 0 \\ 0 & 1 & 0 & -1 & 0 & 0 & 0 & 0 & 0 & 0 \\ 0 & 0 & -\Delta y_{2,1} & \Delta x_{1,2} & 0 & 0 & 0 & 0 & -f_{g1}\Delta y_{CM1,1} & -1 \\ 0 & 0 & -1 & 0 & 1 & 0 & 0 & 0 & f_{g2} & 0 \\ 0 & 0 & 0 & 1 & 0 & 1 & 0 & 0 & 0 & 0 \\ 0 & 0 & 0 & 0 & \Delta y_{3,2} & \Delta x_{2,3} & 0 & 0 & f_{g2}\Delta y_{2,CM2} & 1 \\ 0 & 0 & 0 & 0 & -1 & 0 & 1 & 0 & f_{g3} & 0 \\ 0 & 0 & 0 & 0 & 0 & -1 & 0 & 1 & 0 & 0 \\ 0 & 0 & 0 & 0 & 0 & 0 & \Delta y_{3,4} & -\Delta x_{3,4} & f_{g3}\Delta y_{3,CM3} & 0 \\ 0 & 0 & \tan(\alpha_2) & -1 & 0 & 0 & 0 & 0 & 0 & 0 \end{bmatrix}$$

$$\{r\} = \begin{bmatrix} h_1 \\ v_1 \\ h_2 \\ v_2 \\ h_3 \\ v_3 \\ h_4 \\ v_4 \\ \lambda_a \\ M_2 \end{bmatrix} \qquad \{q\} = \begin{bmatrix} 0 \\ f_{g1} \\ -f_{g1}\Delta x_{1,CM1} \\ 0 \\ f_{g2} \\ f_{g2}\Delta x_{2,CM2} \\ 0 \\ f_{g3} \\ -f_{g3}\Delta x_{3,CM3} \\ 0 \end{bmatrix} \tag{30}$$

3.3.3.3 Type IV – H_1 H_2 S_3 H_4

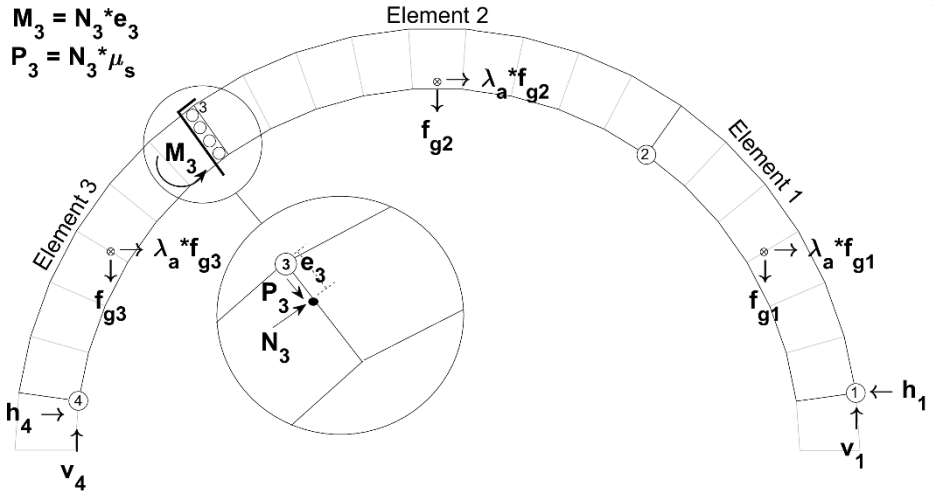

Figure 22. Free-body diagram for the Type IV mechanism

The Equilibrium Set for the condition shown in Figure 22 is

$$[BC] = \begin{bmatrix} -1 & 0 & 1 & 0 & 0 & 0 & 0 & 0 & f_{g1} & 0 \\ 0 & 1 & 0 & -1 & 0 & 0 & 0 & 0 & 0 & 0 \\ 0 & 0 & -\Delta y_{2,1} & \Delta x_{1,2} & 0 & 0 & 0 & 0 & -f_{g1}\Delta y_{CM1,1} & 0 \\ 0 & 0 & -1 & 0 & 1 & 0 & 0 & 0 & f_{g2} & 0 \\ 0 & 0 & 0 & 1 & 0 & 1 & 0 & 0 & 0 & 0 \\ 0 & 0 & 0 & 0 & \Delta y_{3,2} & \Delta x_{2,3} & 0 & 0 & f_{g2}\Delta y_{2,CM2} & 1 \\ 0 & 0 & 0 & 0 & -1 & 0 & 1 & 0 & f_{g3} & 0 \\ 0 & 0 & 0 & 0 & 0 & -1 & 0 & 1 & 0 & 0 \\ 0 & 0 & 0 & 0 & 0 & 0 & \Delta y_{3,4} & -\Delta x_{3,4} & f_{g3}\Delta y_{3,CM3} & -1 \\ 0 & 0 & 0 & 0 & \tan(\alpha_3) & -1 & 0 & 0 & 0 & 0 \end{bmatrix}$$

$$\{r\} = \begin{bmatrix} h_1 \\ v_1 \\ h_2 \\ v_2 \\ h_3 \\ v_3 \\ h_4 \\ v_4 \\ \lambda_a \\ M_3 \end{bmatrix} \qquad \{q\} = \begin{bmatrix} 0 \\ f_{g1} \\ -f_{g1}\Delta x_{1,CM1} \\ 0 \\ f_{g2} \\ f_{g2}\Delta x_{2,CM2} \\ 0 \\ f_{g3} \\ -f_{g3}\Delta x_{3,CM3} \\ 0 \end{bmatrix} \tag{31}$$

3.3.3.4 Type V – H_1 H_2 H_3 S_4

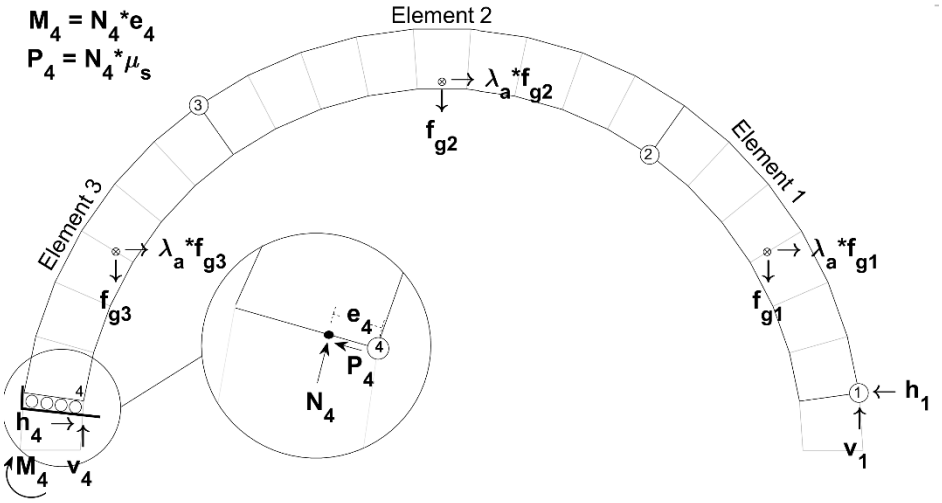

Figure 23. Free-body diagram for the Type V mechanism

The Equilibrium Set for the condition shown in Figure 23 is

$$[BC] = \begin{bmatrix} -1 & 0 & 1 & 0 & 0 & 0 & 0 & 0 & f_{g1} & 0 \\ 0 & 1 & 0 & -1 & 0 & 0 & 0 & 0 & 0 & 0 \\ 0 & 0 & -\Delta y_{2,1} & \Delta x_{1,2} & 0 & 0 & 0 & 0 & -f_{g1}\Delta y_{CM1,1} & 0 \\ 0 & 0 & -1 & 0 & 1 & 0 & 0 & 0 & f_{g2} & 0 \\ 0 & 0 & 0 & 1 & 0 & 1 & 0 & 0 & 0 & 0 \\ 0 & 0 & 0 & 0 & \Delta y_{3,2} & \Delta x_{2,3} & 0 & 0 & f_{g2}\Delta y_{2,CM2} & 0 \\ 0 & 0 & 0 & 0 & -1 & 0 & 1 & 0 & f_{g3} & 0 \\ 0 & 0 & 0 & 0 & 0 & -1 & 0 & 1 & 0 & 0 \\ 0 & 0 & 0 & 0 & 0 & 0 & \Delta y_{3,4} & -\Delta x_{3,4} & f_{g3}\Delta y_{3,CM3} & -1 \\ 0 & 0 & 0 & 0 & 0 & 0 & tan(\alpha_4) & -1 & 0 & 0 \end{bmatrix}$$

$$\{r\} = \begin{bmatrix} h_1 \\ v_1 \\ h_2 \\ v_2 \\ h_3 \\ v_3 \\ h_4 \\ v_4 \\ \lambda_a \\ M_4 \end{bmatrix} \qquad \{q\} = \begin{bmatrix} 0 \\ f_{g1} \\ -f_{g1}\Delta x_{1,CM1} \\ 0 \\ f_{g2} \\ f_{g2}\Delta x_{2,CM2} \\ 0 \\ f_{g3} \\ -f_{g3}\Delta x_{3,CM3} \\ 0 \end{bmatrix} \tag{32}$$

3.3.3.5 Type VI – S_1 S_2 H_3 H_4

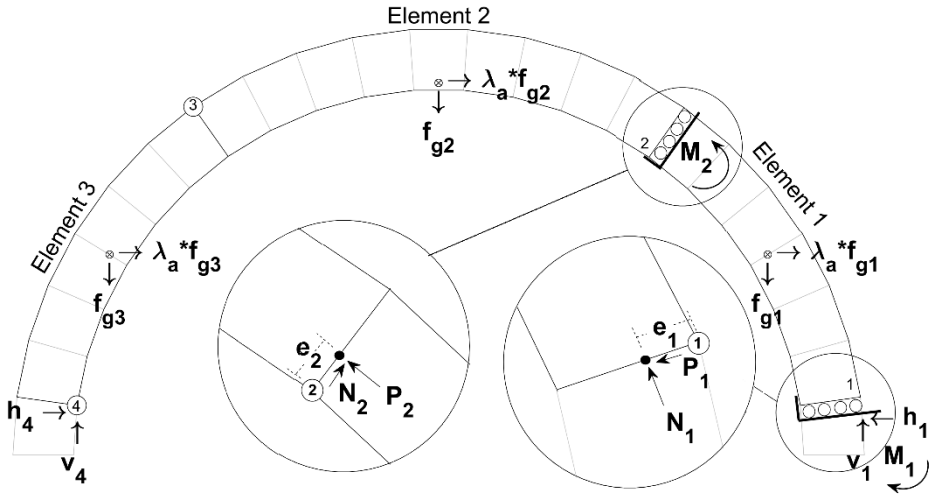

Figure 24. Free-body diagram for Type VI mechanism

The equations of equilibrium for the condition shown in Figure 24 is

$$[BC] = \begin{bmatrix} -1 & 0 & 1 & 0 & 0 & 0 & 0 & 0 & f_{g1} & 0 & 0 \\ 0 & 1 & 0 & -1 & 0 & 0 & 0 & 0 & 0 & 0 & 0 \\ 0 & 0 & -\Delta y_{2,1} & \Delta x_{1,2} & 0 & 0 & 0 & 0 & -f_{g1}\Delta y_{CM1,1} & -1 & -1 \\ 0 & 0 & -1 & 0 & 1 & 0 & 0 & 0 & f_{g2} & 0 & 0 \\ 0 & 0 & 0 & 1 & 0 & 1 & 0 & 0 & 0 & 0 & 0 \\ 0 & 0 & 0 & 0 & \Delta y_{3,2} & \Delta x_{2,3} & 0 & 0 & f_{g2}\Delta y_{2,CM2} & 0 & 1 \\ 0 & 0 & 0 & 0 & -1 & 0 & 1 & 0 & f_{g3} & 0 & 0 \\ 0 & 0 & 0 & 0 & 0 & -1 & 0 & 1 & 0 & 0 & 0 \\ 0 & 0 & 0 & 0 & 0 & 0 & \Delta y_{3,4} & -\Delta x_{3,4} & f_{g3}\Delta y_{3,CM3} & 0 & 0 \\ \tan(\alpha_1) & -1 & 0 & 0 & 0 & 0 & 0 & 0 & 0 & 0 & 0 \\ 0 & 0 & \tan(\alpha_2) & -1 & 0 & 0 & 0 & 0 & 0 & 0 & 0 \end{bmatrix}$$

$$\{r\} = \begin{bmatrix} h_1 \\ v_1 \\ h_2 \\ v_2 \\ h_3 \\ v_3 \\ h_4 \\ v_4 \\ \lambda_a \\ M_1 \\ M_2 \end{bmatrix} \qquad \{q\} = \begin{bmatrix} 0 \\ f_{g1} \\ -f_{g1}\Delta x_{1,CM1} \\ 0 \\ f_{g2} \\ f_{g2}\Delta x_{2,CM2} \\ 0 \\ f_{g3} \\ -f_{g3}\Delta x_{3,CM3} \\ 0 \\ 0 \end{bmatrix} \tag{33}$$

3.3.3.6 Type VII – S_1 H_2 S_3 H_4

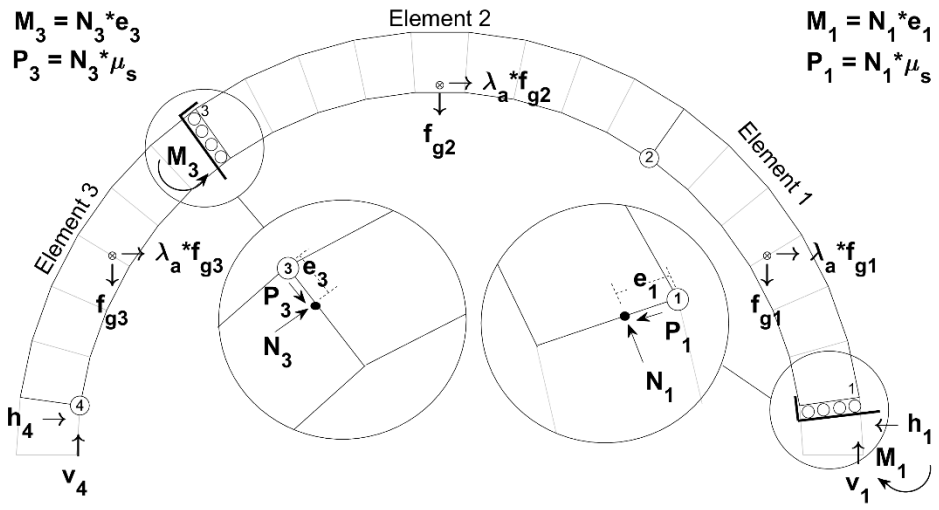

Figure 25. Free-body diagram for Type VII mechanism

The equations of equilibrium for the condition shown in Figure 25 is

$$[BC] = \begin{bmatrix} -1 & 0 & 1 & 0 & 0 & 0 & 0 & 0 & f_{g1} & 0 & 0 \\ 0 & 1 & 0 & -1 & 0 & 0 & 0 & 0 & 0 & 0 & 0 \\ 0 & 0 & -\Delta y_{2,1} & \Delta x_{1,2} & 0 & 0 & 0 & 0 & -f_{g1}\Delta y_{CM1,1} & -1 & 0 \\ 0 & 0 & -1 & 0 & 1 & 0 & 0 & 0 & f_{g2} & 0 & 0 \\ 0 & 0 & 0 & 1 & 0 & 1 & 0 & 0 & 0 & 0 & 0 \\ 0 & 0 & 0 & 0 & \Delta y_{3,2} & \Delta x_{2,3} & 0 & 0 & f_{g2}\Delta y_{2,CM2} & 0 & 1 \\ 0 & 0 & 0 & 0 & -1 & 0 & 1 & 0 & f_{g3} & 0 & 0 \\ 0 & 0 & 0 & 0 & 0 & -1 & 0 & 1 & 0 & 0 & 0 \\ 0 & 0 & 0 & 0 & 0 & 0 & \Delta y_{3,4} & -\Delta x_{3,4} & f_{g3}\Delta y_{3,CM3} & 0 & -1 \\ \tan(\alpha_1) & -1 & 0 & 0 & 0 & 0 & 0 & 0 & 0 & 0 & 0 \\ 0 & 0 & 0 & 0 & \tan(\alpha_3) & -1 & 0 & 0 & 0 & 0 & 0 \end{bmatrix}$$

$$\{r\} = \begin{bmatrix} h_1 \\ v_1 \\ h_2 \\ v_2 \\ h_3 \\ v_3 \\ h_4 \\ v_4 \\ \lambda_a \\ M_1 \\ M_3 \end{bmatrix} \qquad \{q\} = \begin{bmatrix} 0 \\ f_{g1} \\ -f_{g1}\Delta x_{1,CM1} \\ 0 \\ f_{g2} \\ f_{g2}\Delta x_{2,CM2} \\ 0 \\ f_{g3} \\ -f_{g3}\Delta x_{3,CM3} \\ 0 \\ 0 \end{bmatrix} \tag{34}$$

3.3.3.7 Type VIII – S_1 H_2 H_3 S_4

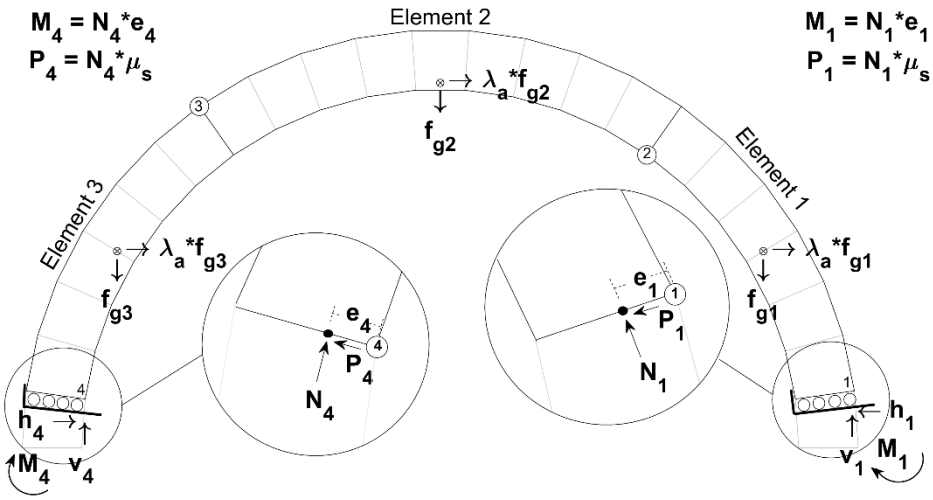

Figure 26. Free-body diagram for the Type VIII mechanism

The equations of equilibrium for the condition shown in Figure 26 is

$$[BC] = \begin{bmatrix} -1 & 0 & 1 & 0 & 0 & 0 & 0 & 0 & f_{g1} & 0 & 0 \\ 0 & 1 & 0 & -1 & 0 & 0 & 0 & 0 & 0 & 0 & 0 \\ 0 & 0 & -\Delta y_{2,1} & \Delta x_{1,2} & 0 & 0 & 0 & 0 & -f_{g1}\Delta y_{CM1,1} & -1 & 0 \\ 0 & 0 & -1 & 0 & 1 & 0 & 0 & 0 & f_{g2} & 0 & 0 \\ 0 & 0 & 0 & 1 & 0 & 1 & 0 & 0 & 0 & 0 & 0 \\ 0 & 0 & 0 & 0 & \Delta y_{3,2} & \Delta x_{2,3} & 0 & 0 & f_{g2}\Delta y_{2,CM2} & 0 & 0 \\ 0 & 0 & 0 & 0 & -1 & 0 & 1 & 0 & f_{g3} & 0 & 0 \\ 0 & 0 & 0 & 0 & 0 & -1 & 0 & 1 & 0 & 0 & 0 \\ 0 & 0 & 0 & 0 & 0 & 0 & \Delta y_{3,4} & -\Delta x_{3,4} & f_{g3}\Delta y_{3,CM3} & 0 & -1 \\ \tan(\alpha_1) & -1 & 0 & 0 & 0 & 0 & 0 & 0 & 0 & 0 & 0 \\ 0 & 0 & 0 & 0 & 0 & 0 & \tan(\alpha_4) & -1 & 0 & 0 & 0 \end{bmatrix}$$

$$\{r\} = \begin{bmatrix} h_1 \\ v_1 \\ h_2 \\ v_2 \\ h_3 \\ v_3 \\ h_4 \\ v_4 \\ \lambda_a \\ M_1 \\ M_4 \end{bmatrix} \qquad \{q\} = \begin{bmatrix} 0 \\ f_{g1} \\ -f_{g1}\Delta x_{1,CM1} \\ 0 \\ f_{g2} \\ f_{g2}\Delta x_{2,CM2} \\ 0 \\ f_{g3} \\ -f_{g3}\Delta x_{3,CM3} \\ 0 \\ 0 \end{bmatrix} \tag{35}$$

3.3.3.8 Type IX – $H_1\ S_2\ S_3\ H_4$

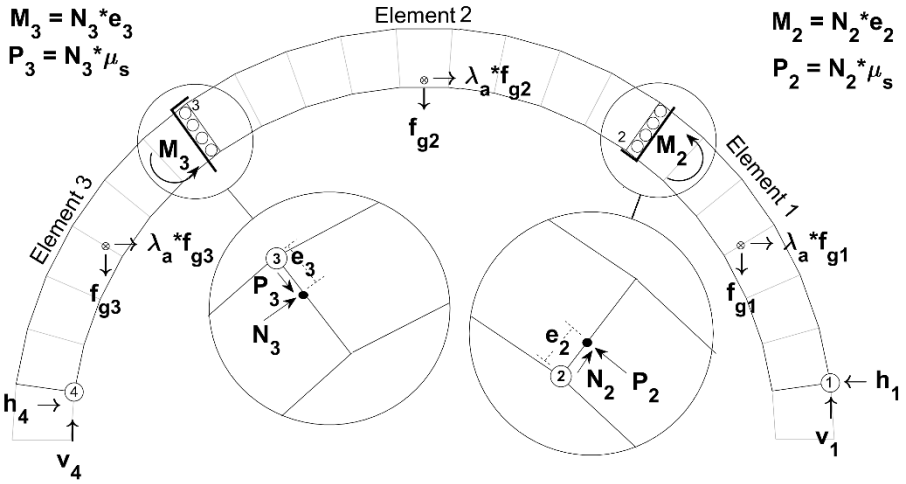

Figure 27. Free-body diagram for the Type IX mechanism

The equations of equilibrium for the condition shown in Figure 27 is

$$[BC] = \begin{bmatrix} -1 & 0 & 1 & 0 & 0 & 0 & 0 & 0 & f_{g1} & 0 & 0 \\ 0 & 1 & 0 & -1 & 0 & 0 & 0 & 0 & 0 & 0 & 0 \\ 0 & 0 & -\Delta y_{2,1} & \Delta x_{1,2} & 0 & 0 & 0 & 0 & -f_{g1}\Delta y_{CM1,1} & -1 & 0 \\ 0 & 0 & -1 & 0 & 1 & 0 & 0 & 0 & f_{g2} & 0 & 0 \\ 0 & 0 & 0 & 1 & 0 & 1 & 0 & 0 & 0 & 0 & 0 \\ 0 & 0 & 0 & 0 & \Delta y_{3,2} & \Delta x_{2,3} & 0 & 0 & f_{g2}\Delta y_{2,CM2} & 1 & -1 \\ 0 & 0 & 0 & 0 & -1 & 0 & 1 & 0 & f_{g3} & 0 & 0 \\ 0 & 0 & 0 & 0 & 0 & -1 & 0 & 1 & 0 & 0 & 0 \\ 0 & 0 & 0 & 0 & 0 & 0 & \Delta y_{3,4} & -\Delta x_{3,4} & f_{g3}\Delta y_{3,CM3} & 0 & 1 \\ 0 & 0 & \tan(\alpha_2) & -1 & 0 & 0 & 0 & 0 & 0 & 0 & 0 \\ 0 & 0 & 0 & 0 & \tan(\alpha_3) & -1 & 0 & 0 & 0 & 0 & 0 \end{bmatrix}$$

$$\{r\} = \begin{bmatrix} h_1 \\ v_1 \\ h_2 \\ v_2 \\ h_3 \\ v_3 \\ h_4 \\ v_4 \\ \lambda_a \\ M_2 \\ M_3 \end{bmatrix} \qquad \{q\} = \begin{bmatrix} 0 \\ f_{g1} \\ -f_{g1}\Delta x_{1,CM1} \\ 0 \\ f_{g2} \\ f_{g2}\Delta x_{2,CM2} \\ 0 \\ f_{g3} \\ -f_{g3}\Delta x_{3,CM3} \\ 0 \\ 0 \end{bmatrix} \tag{36}$$

3.3.3.9 Type X – H_1 S_2 H_3 S_4

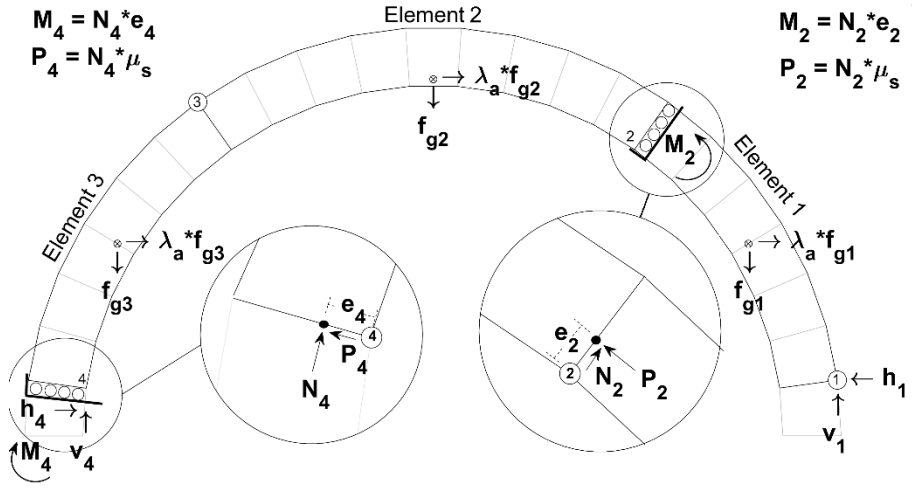

Figure 28. Free-body diagram for the Type X mechanism

The equations of equilibrium for the condition shown in Figure 28 is

$$[BC] = \begin{bmatrix} -1 & 0 & 1 & 0 & 0 & 0 & 0 & 0 & f_{g1} & 0 & 0 \\ 0 & 1 & 0 & -1 & 0 & 0 & 0 & 0 & 0 & 0 & 0 \\ 0 & 0 & -\Delta y_{2,1} & \Delta x_{1,2} & 0 & 0 & 0 & 0 & -f_{g1}\Delta y_{CM1,1} & -1 & 0 \\ 0 & 0 & -1 & 0 & 1 & 0 & 0 & 0 & f_{g2} & 0 & 0 \\ 0 & 0 & 0 & 1 & 0 & 1 & 0 & 0 & 0 & 0 & 0 \\ 0 & 0 & 0 & 0 & \Delta y_{3,2} & \Delta x_{2,3} & 0 & 0 & f_{g2}\Delta y_{2,CM2} & 1 & 0 \\ 0 & 0 & 0 & 0 & -1 & 0 & 1 & 0 & f_{g3} & 0 & 0 \\ 0 & 0 & 0 & 0 & 0 & -1 & 0 & 1 & 0 & 0 & 0 \\ 0 & 0 & 0 & 0 & 0 & 0 & \Delta y_{3,4} & -\Delta x_{3,4} & f_{g3}\Delta y_{3,CM3} & 0 & -1 \\ 0 & 0 & \tan(\alpha_1) & -1 & 0 & 0 & 0 & 0 & 0 & 0 & 0 \\ 0 & 0 & 0 & 0 & 0 & 0 & \tan(\alpha_4) & -1 & 0 & 0 & 0 \end{bmatrix}$$

$$\{r\} = \begin{bmatrix} h_1 \\ v_1 \\ h_2 \\ v_2 \\ h_3 \\ v_3 \\ h_4 \\ v_4 \\ \lambda_a \\ M_2 \\ M_4 \end{bmatrix} \qquad \{q\} = \begin{bmatrix} 0 \\ f_{g1} \\ -f_{g1}\Delta x_{1,CM1} \\ 0 \\ f_{g2} \\ f_{g2}\Delta x_{2,CM2} \\ 0 \\ f_{g3} \\ -f_{g3}\Delta x_{3,CM3} \\ 0 \\ 0 \end{bmatrix} \tag{37}$$

3.3.3.10 Type XI – H_1 H_2 S_3 S_4

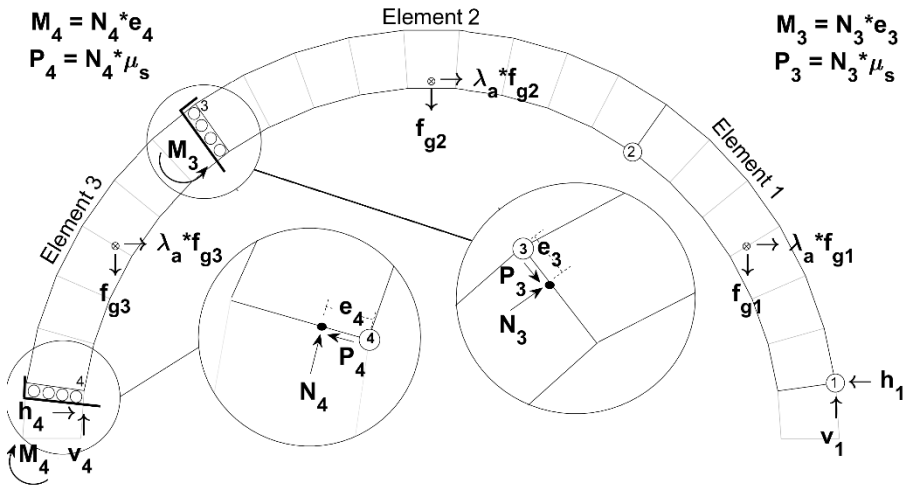

Figure 29. Free-body diagram for the Type XI mechanism

The equations of equilibrium for the condition shown in Figure 29 is

$$[BC] = \begin{bmatrix} -1 & 0 & 1 & 0 & 0 & 0 & 0 & 0 & f_{g1} & 0 & 0 \\ 0 & 1 & 0 & -1 & 0 & 0 & 0 & 0 & 0 & 0 & 0 \\ 0 & 0 & -\Delta y_{2,1} & \Delta x_{1,2} & 0 & 0 & 0 & 0 & -f_{g1}\Delta y_{CM1,1} & 0 & 0 \\ 0 & 0 & -1 & 0 & 1 & 0 & 0 & 0 & f_{g2} & 0 & 0 \\ 0 & 0 & 0 & 1 & 0 & 1 & 0 & 0 & 0 & 0 & 0 \\ 0 & 0 & 0 & 0 & \Delta y_{3,2} & \Delta x_{2,3} & 0 & 0 & f_{g2}\Delta y_{2,CM2} & -1 & 0 \\ 0 & 0 & 0 & 0 & -1 & 0 & 1 & 0 & f_{g3} & 0 & 0 \\ 0 & 0 & 0 & 0 & 0 & -1 & 0 & 1 & 0 & 0 & 0 \\ 0 & 0 & 0 & 0 & 0 & 0 & \Delta y_{3,4} & -\Delta x_{3,4} & f_{g3}\Delta y_{3,CM3} & 1 & -1 \\ 0 & 0 & 0 & 0 & \tan(\alpha_3) & -1 & 0 & 0 & 0 & 0 & 0 \\ 0 & 0 & 0 & 0 & 0 & 0 & \tan(\alpha_4) & -1 & 0 & 0 & 0 \end{bmatrix}$$

$$\{r\} = \begin{bmatrix} h_1 \\ v_1 \\ h_2 \\ v_2 \\ h_3 \\ v_3 \\ h_4 \\ v_4 \\ \lambda_a \\ M_3 \\ M_4 \end{bmatrix} \qquad \{q\} = \begin{bmatrix} 0 \\ f_{g1} \\ -f_{g1}\Delta x_{1,CM1} \\ 0 \\ f_{g2} \\ f_{g2}\Delta x_{2,CM2} \\ 0 \\ f_{g3} \\ -f_{g3}\Delta x_{3,CM3} \\ 0 \\ 0 \end{bmatrix} \tag{38}$$

3.3.3.11 Type XII – S_1 S_2 S_3 H_4

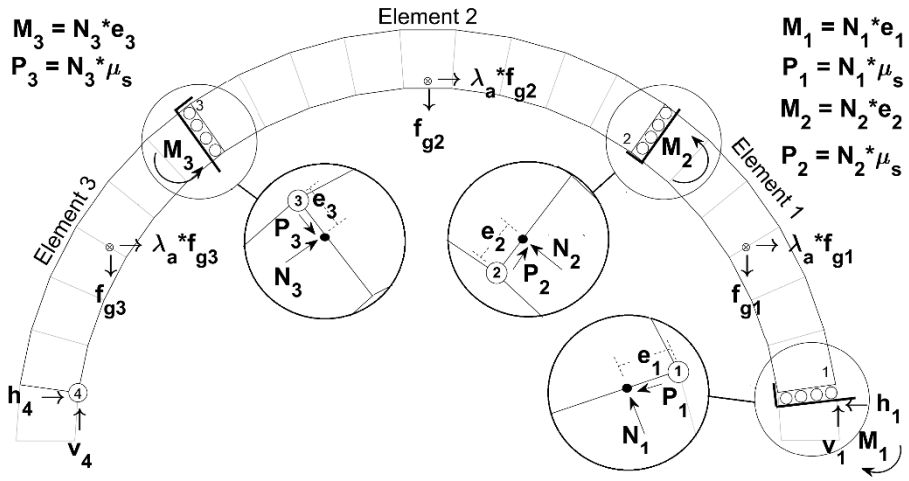

Figure 30. Free-body diagram for the Type XII mechanism

The equations of equilibrium for the condition shown in Figure 30 is

$$[BC] = \begin{bmatrix} -1 & 0 & 1 & 0 & 0 & 0 & 0 & 0 & f_{g1} & 0 & 0 & 0 \\ 0 & 1 & 0 & -1 & 0 & 0 & 0 & 0 & 0 & 0 & 0 & 0 \\ 0 & 0 & -\Delta y_{2,1} & \Delta x_{1,2} & 0 & 0 & 0 & 0 & -f_{g1}\Delta y_{CM1,1} & -1 & -1 & 0 \\ 0 & 0 & -1 & 0 & 1 & 0 & 0 & 0 & f_{g2} & 0 & 0 & 0 \\ 0 & 0 & 0 & 1 & 0 & 1 & 0 & 0 & 0 & 0 & 0 & 0 \\ 0 & 0 & 0 & 0 & \Delta y_{3,2} & \Delta x_{2,3} & 0 & 0 & f_{g2}\Delta y_{2,CM2} & 0 & 1 & 1 \\ 0 & 0 & 0 & 0 & -1 & 0 & 1 & 0 & f_{g3} & 0 & 0 & 0 \\ 0 & 0 & 0 & 0 & 0 & -1 & 0 & 1 & 0 & 0 & 0 & 0 \\ 0 & 0 & 0 & 0 & 0 & 0 & \Delta y_{3,4} & -\Delta x_{3,4} & f_{g3}\Delta y_{3,CM3} & 0 & 0 & -1 \\ \tan(\alpha_1) & -1 & 0 & 0 & 0 & 0 & 0 & 0 & 0 & 0 & 0 & 0 \\ 0 & 0 & \tan(\alpha_2) & -1 & 0 & 0 & 0 & 0 & 0 & 0 & 0 & 0 \\ 0 & 0 & 0 & 0 & \tan(\alpha_3) & -1 & 0 & 0 & 0 & 0 & 0 & 0 \end{bmatrix}$$

$$\{r\} = \begin{bmatrix} h_1 \\ v_1 \\ h_2 \\ v_2 \\ h_3 \\ v_3 \\ h_4 \\ v_4 \\ \lambda_a \\ M_1 \\ M_2 \\ M_3 \end{bmatrix} \qquad \{q\} = \begin{bmatrix} 0 \\ f_{g1} \\ -f_{g1}\Delta x_{1,CM1} \\ 0 \\ f_{g2} \\ f_{g2}\Delta x_{2,CM2} \\ 0 \\ f_{g3} \\ -f_{g3}\Delta x_{3,CM3} \\ 0 \\ 0 \\ 0 \end{bmatrix} \tag{39}$$

3.3.3.12 Type XIII – S_1 S_2 H_3 S_4

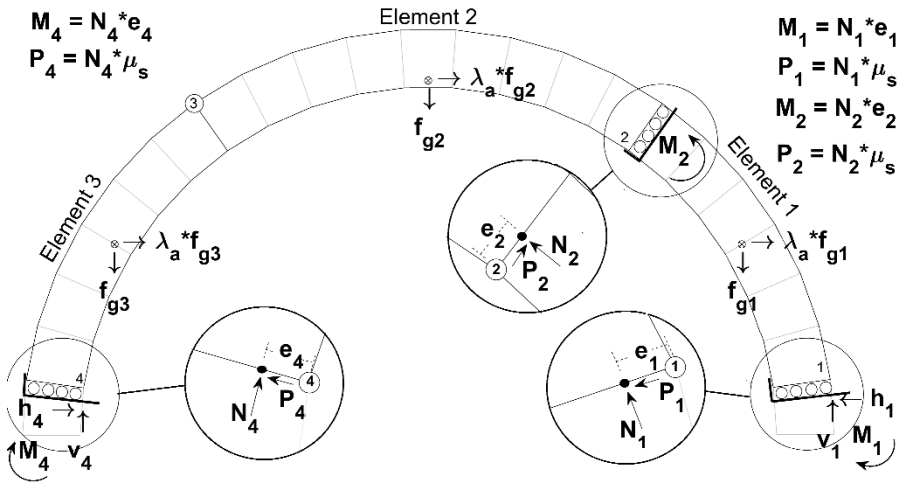

Figure 31. Free-body diagram for the Type XIII mechanism

The equations of equilibrium for the condition shown in Figure 31 is

$$[BC] = \begin{bmatrix} -1 & 0 & 1 & 0 & 0 & 0 & 0 & 0 & f_{g1} & 0 & 0 & 0 \\ 0 & 1 & 0 & -1 & 0 & 0 & 0 & 0 & 0 & 0 & 0 & 0 \\ 0 & 0 & -\Delta y_{2,1} & \Delta x_{1,2} & 0 & 0 & 0 & 0 & -f_{g1}\Delta y_{CM1,1} & -1 & -1 & 0 \\ 0 & 0 & -1 & 0 & 1 & 0 & 0 & 0 & f_{g2} & 0 & 0 & 0 \\ 0 & 0 & 0 & 1 & 0 & 1 & 0 & 0 & 0 & 0 & 0 & 0 \\ 0 & 0 & 0 & 0 & \Delta y_{3,2} & \Delta x_{2,3} & 0 & 0 & f_{g2}\Delta y_{2,CM2} & 0 & 1 & 0 \\ 0 & 0 & 0 & 0 & -1 & 0 & 1 & 0 & f_{g3} & 0 & 0 & 0 \\ 0 & 0 & 0 & 0 & 0 & -1 & 0 & 1 & 0 & 0 & 0 & 0 \\ 0 & 0 & 0 & 0 & 0 & 0 & \Delta y_{3,4} & -\Delta x_{3,4} & f_{g3}\Delta y_{3,CM3} & 0 & 0 & -1 \\ \tan(\alpha_1) & -1 & 0 & 0 & 0 & 0 & 0 & 0 & 0 & 0 & 0 & 0 \\ 0 & 0 & \tan(\alpha_2) & -1 & 0 & 0 & 0 & 0 & 0 & 0 & 0 & 0 \\ 0 & 0 & 0 & 0 & 0 & 0 & \tan(\alpha_4) & -1 & 0 & 0 & 0 & 0 \end{bmatrix}$$

$$\{r\} = \begin{bmatrix} h_1 \\ v_1 \\ h_2 \\ v_2 \\ h_3 \\ v_3 \\ h_4 \\ v_4 \\ \lambda_a \\ M_1 \\ M_2 \\ M_4 \end{bmatrix} \qquad \{q\} = \begin{bmatrix} 0 \\ f_{g1} \\ -f_{g1}\Delta x_{1,CM1} \\ 0 \\ f_{g2} \\ f_{g2}\Delta x_{2,CM2} \\ 0 \\ f_{g3} \\ -f_{g3}\Delta x_{3,CM3} \\ 0 \\ 0 \\ 0 \end{bmatrix} \tag{40}$$

3.3.3.13 Type XIV – S_1 H_2 S_3 S_4

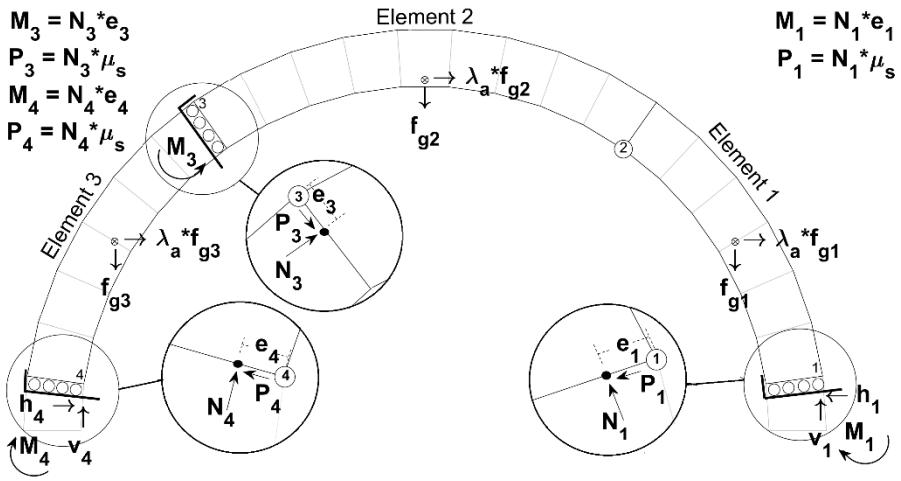

Figure 32. Free-body diagram for the Type XIV mechanism

The equations of equilibrium for the condition shown in Figure 32 is

$$[BC] = \begin{bmatrix} -1 & 0 & 1 & 0 & 0 & 0 & 0 & 0 & f_{g1} & 0 & 0 & 0 \\ 0 & 1 & 0 & -1 & 0 & 0 & 0 & 0 & 0 & 0 & 0 & 0 \\ 0 & 0 & -\Delta y_{2,1} & \Delta x_{1,2} & 0 & 0 & 0 & 0 & -f_{g1}\Delta y_{CM1,1} & -1 & 0 & 0 \\ 0 & 0 & -1 & 0 & 1 & 0 & 0 & 0 & f_{g2} & 0 & 0 & 0 \\ 0 & 0 & 0 & 1 & 0 & 1 & 0 & 0 & 0 & 0 & 0 & 0 \\ 0 & 0 & 0 & 0 & \Delta y_{3,2} & \Delta x_{2,3} & 0 & 0 & f_{g2}\Delta y_{2,CM2} & 0 & -1 & 0 \\ 0 & 0 & 0 & 0 & -1 & 0 & 1 & 0 & f_{g3} & 0 & 0 & 0 \\ 0 & 0 & 0 & 0 & 0 & -1 & 0 & 1 & 0 & 0 & 0 & 0 \\ 0 & 0 & 0 & 0 & 0 & 0 & \Delta y_{3,4} & -\Delta x_{3,4} & f_{g3}\Delta y_{3,CM3} & 0 & 1 & -1 \\ \tan(\alpha_1) & -1 & 0 & 0 & 0 & 0 & 0 & 0 & 0 & 0 & 0 & 0 \\ 0 & 0 & 0 & 0 & \tan(\alpha_3) & -1 & 0 & 0 & 0 & 0 & 0 & 0 \\ 0 & 0 & 0 & 0 & 0 & 0 & \tan(\alpha_4) & -1 & 0 & 0 & 0 & 0 \end{bmatrix}$$

$$\{r\} = \begin{bmatrix} h_1 \\ v_1 \\ h_2 \\ v_2 \\ h_3 \\ v_3 \\ h_4 \\ v_4 \\ \lambda_a \\ M_1 \\ M_3 \\ M_4 \end{bmatrix} \qquad \{q\} = \begin{bmatrix} 0 \\ f_{g1} \\ -f_{g1}\Delta x_{1,CM1} \\ 0 \\ f_{g2} \\ f_{g2}\Delta x_{2,CM2} \\ 0 \\ f_{g3} \\ -f_{g3}\Delta x_{3,CM3} \\ 0 \\ 0 \\ 0 \end{bmatrix} \tag{41}$$

3.3.3.14 Type XV – H_1 S_2 S_3 S_4

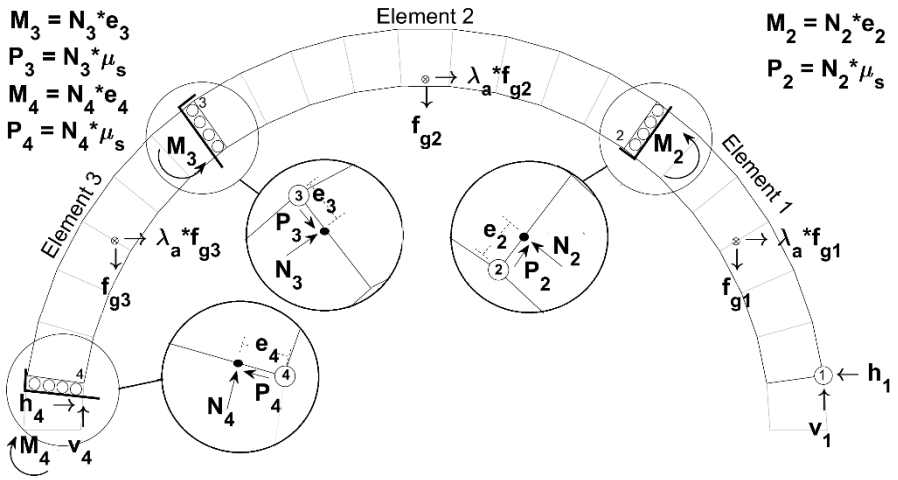

Figure 33. Free-body diagram for the Type XV mechanism

The equations of equilibrium for the condition shown in Figure 33 is

$$[BC] = \begin{bmatrix} -1 & 0 & 1 & 0 & 0 & 0 & 0 & 0 \\ 0 & 1 & 0 & -1 & 0 & 0 & 0 & 0 \\ 0 & 0 & -\Delta y_{2,1} & \Delta x_{1,2} & 0 & 0 & 0 & 0 \\ 0 & 0 & -1 & 0 & 1 & 0 & 0 & 0 \\ 0 & 0 & 0 & 1 & 0 & 1 & 0 & 0 \\ 0 & 0 & 0 & 0 & \Delta y_{3,2} & \Delta x_{2,3} & 0 & 0 \\ 0 & 0 & 0 & 0 & -1 & 0 & 1 & 0 \\ 0 & 0 & 0 & 0 & 0 & -1 & 0 & 1 \\ 0 & 0 & 0 & 0 & 0 & 0 & \Delta y_{3,4} & -\Delta x_{3,4} \\ 0 & 0 & \tan(\alpha_2) & -1 & 0 & 0 & 0 & 0 \\ 0 & 0 & 0 & 0 & \tan(\alpha_3) & -1 & 0 & 0 \\ 0 & 0 & 0 & 0 & 0 & 0 & \tan(\alpha_4) & -1 \end{bmatrix} \begin{bmatrix} f_{g1} \\ 0 \\ -f_{g1}\Delta y_{CM1,1} \\ f_{g2} \\ 0 \\ f_{g2}\Delta y_{2,CM2} \\ f_{g3} \\ 0 \\ f_{g3}\Delta y_{3,CM3} \\ 0 \\ 0 \\ 0 \end{bmatrix} \begin{bmatrix} 0 & 0 & 0 \\ 0 & 0 & 0 \\ -1 & 0 & 0 \\ 0 & 0 & 0 \\ 0 & 0 & 0 \\ 0 & -1 & 0 \\ 0 & 0 & 0 \\ 0 & 0 & 0 \\ 0 & 1 & -1 \\ 0 & 0 & 0 \\ 0 & 0 & 0 \\ 0 & 0 & 0 \end{bmatrix}$$

$$\{r\} = \begin{bmatrix} h_1 \\ v_1 \\ h_2 \\ v_2 \\ h_3 \\ v_3 \\ h_4 \\ v_4 \\ \lambda_a \\ M_2 \\ M_3 \\ M_4 \end{bmatrix} \qquad \{q\} = \begin{bmatrix} 0 \\ f_{g1} \\ -f_{g1}\Delta x_{1,CM1} \\ 0 \\ f_{g2} \\ f_{g2}\Delta x_{2,CM2} \\ 0 \\ f_{g3} \\ -f_{g3}\Delta x_{3,CM3} \\ 0 \\ 0 \\ 0 \end{bmatrix} \tag{42}$$

3.3.3.15 Type XVI – S_1 S_2 S_3 S_4

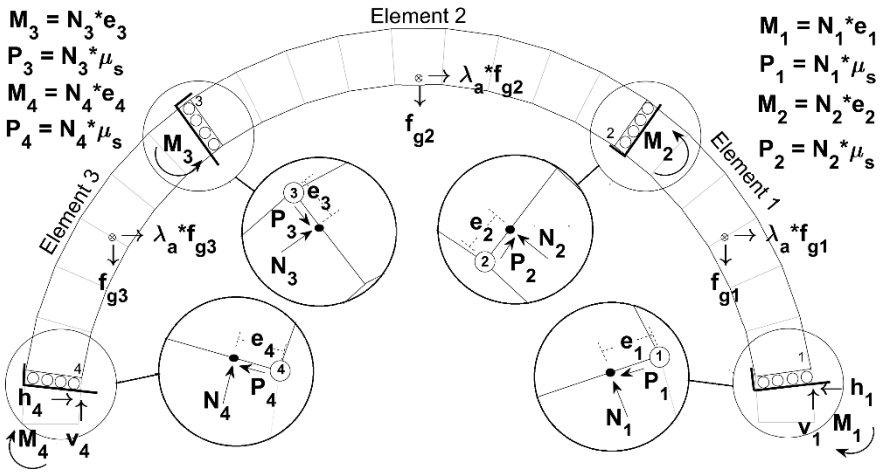

Figure 34. Free-body diagram for the Type XVI mechanism

The equations of equilibrium for the condition shown in Figure 34 is

$$[BC] = \begin{bmatrix} -1 & 0 & 1 & 0 & 0 & 0 & 0 & 0 \\ 0 & 1 & 0 & -1 & 0 & 0 & 0 & 0 \\ 0 & 0 & -\Delta y_{2,1} & \Delta x_{1,2} & 0 & 0 & 0 & 0 \\ 0 & 0 & -1 & 0 & 1 & 0 & 0 & 0 \\ 0 & 0 & 0 & 1 & 0 & 1 & 0 & 0 \\ 0 & 0 & 0 & 0 & \Delta y_{3,2} & \Delta x_{2,3} & 0 & 0 \\ 0 & 0 & 0 & 0 & -1 & 0 & 1 & 0 \\ 0 & 0 & 0 & 0 & 0 & -1 & 0 & 1 \\ 0 & 0 & 0 & 0 & 0 & 0 & \Delta y_{3,4} & -\Delta x_{3,4} \\ \tan(\alpha_2) & -1 & 0 & 0 & 0 & 0 & 0 & 0 \\ 0 & 0 & \tan(\alpha_2) & -1 & 0 & 0 & 0 & 0 \\ 0 & 0 & 0 & 0 & \tan(\alpha_3) & -1 & 0 & 0 \\ 0 & 0 & 0 & 0 & 0 & 0 & \tan(\alpha_4) & -1 \end{bmatrix} \begin{bmatrix} f_{g1} \\ 0 \\ -f_{g1}\Delta y_{CM1,1} \\ f_{g2} \\ 0 \\ f_{g2}\Delta y_{2,CM2} \\ f_{g3} \\ 0 \\ f_{g3}\Delta y_{3,CM3} \\ 0 \\ 0 \\ 0 \\ 0 \end{bmatrix} \begin{bmatrix} 0 & 0 & 0 & 0 \\ 0 & 0 & 0 & 0 \\ -1 & 1 & 0 & 0 \\ 0 & 0 & 0 & 0 \\ 0 & 0 & 0 & 0 \\ 0 & -1 & 1 & 0 \\ 0 & 0 & 0 & 0 \\ 0 & 0 & 0 & 0 \\ 0 & 0 & -1 & -1 \\ 0 & 0 & 0 & 0 \\ 0 & 0 & 0 & 0 \\ 0 & 0 & 0 & 0 \\ 0 & 0 & 0 & 0 \end{bmatrix}$$

$$\{r\} = \begin{bmatrix} h_1 \\ v_1 \\ h_2 \\ v_2 \\ h_3 \\ v_3 \\ h_4 \\ v_4 \\ \lambda_a \\ M_1 \\ M_2 \\ M_3 \\ M_4 \end{bmatrix} \qquad \{q\} = \begin{bmatrix} 0 \\ f_{g1} \\ -f_{g1}\Delta x_{1,CM1} \\ 0 \\ f_{g2} \\ f_{g2}\Delta x_{2,CM2} \\ 0 \\ f_{g3} \\ -f_{g3}\Delta x_{3,CM3} \\ 0 \\ 0 \\ 0 \\ 0 \end{bmatrix} \tag{43}$$

3.3.4 Combined-Hinge Mechanisms

The combined-hinge mechanisms are the result of a double release of freedom at one mechanical joint in exchange for another mechanical joint in the system. This condition is the result of the of the simultaneous development of a hinge and the exceedance of static friction at a mechanical joint. This removes the requirement of the moment variable at the combined joint since the hinge is initiated. The removal of a mechanical joint results in either the loss of an element or the combination of two elements in the free-body diagram. This introduces a statically determinate system without the inclusion of the loading variable (for example the three-pinned arch). The loading variable is necessary however to create the kinematic condition beginning from a stable state. The inclusion of the friction angle defines the relationship between orthogonal reactions at the joint (Eqns. 22 and 23) and its inclusion in the free-body diagram must be paired with the loading variable to maintain the determinacy of the equations of equilibrium.

For the combined-hinge mechanisms, mechanisms Type XVII through Type XIX place the combination at the first joint, C_1, in exchange for hinge H_4, H_3, and H_2 respectively. Mechanisms Type XX through Type XXII assign C_2 in exchange for hinge H_4, H_3, and H_1 respectively. Mechanisms Type XXIII through Type XXV assign C_3 in exchange for hinge H_4, H_2, and H_1 respectively. Lastly, mechanisms Type XXVI through Type XXVIII assign C_4 in exchange for H_3, H_2, and H_1 respectively.

3.3.4.1 Type XVII – C_1 H_2 H_3 --

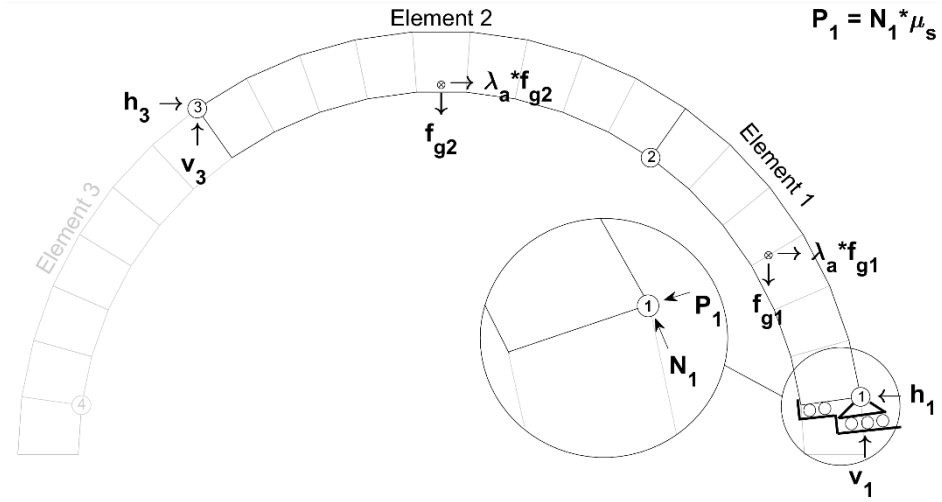

Figure 35. Free-body diagram for the Type XVII mechanism

The equations of equilibrium for the condition shown in Figure 35 is

$$[BC] = \begin{bmatrix} -1 & 0 & 1 & 0 & 0 & 0 & f_{g1} \\ 0 & 1 & 0 & -1 & 0 & 0 & 0 \\ 0 & 0 & -\Delta y_{2,1} & \Delta x_{1,2} & 0 & 0 & -f_{g1}\Delta y_{CM1,1} \\ 0 & 0 & -1 & 0 & 1 & 0 & f_{g2} \\ 0 & 0 & 0 & 1 & 0 & 1 & 0 \\ 0 & 0 & 0 & 0 & \Delta y_{3,2} & \Delta x_{2,3} & f_{g2}\Delta y_{2,CM2} \\ \tan(\alpha_1) & 1 & 0 & 0 & 0 & 0 & 0 \end{bmatrix}$$

$$\{r\} = \begin{bmatrix} h_1 \\ v_1 \\ h_2 \\ v_2 \\ h_3 \\ v_3 \\ \lambda_a \end{bmatrix} \qquad \{q\} = \begin{bmatrix} 0 \\ f_{g1} \\ -f_{g1}\Delta x_{1,CM1} \\ 0 \\ f_{g2} \\ f_{g2}\Delta x_{2,CM2} \\ 0 \end{bmatrix} \tag{44}$$

3.3.4.2 Type XVIII – C_1 H_2 -- H_4

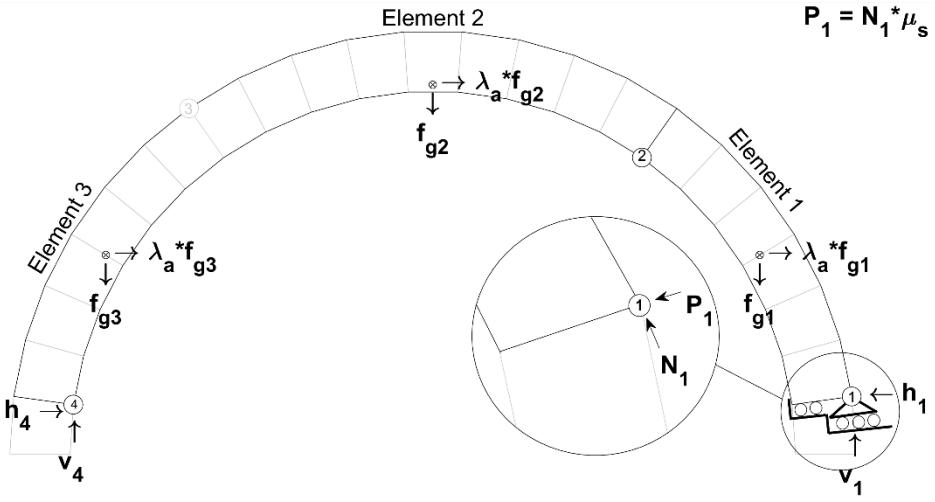

Figure 36. Free-body diagram for the Type XVIII mechanism

The equations of equilibrium for the condition shown in Figure 36 is

$$[BC] = \begin{bmatrix} -1 & 0 & 1 & 0 & 0 & 0 \\ 0 & 1 & 0 & -1 & 0 & 0 \\ 0 & 0 & -\Delta y_{2,1} & \Delta x_{1,2} & 0 & 0 \\ 0 & 0 & -1 & 0 & 1 & 0 \\ 0 & 0 & 0 & 1 & 0 & 1 \\ 0 & 0 & 0 & 0 & \Delta y_{2,4} & -\Delta x_{2,4} \\ \tan(\alpha_1) & 1 & 0 & 0 & 0 & 0 \end{bmatrix} \begin{bmatrix} f_{g1} \\ 0 \\ -f_{g1}\Delta y_{CM1,1} \\ f_{g2} + f_{g3} \\ 0 \\ f_{g2}\Delta y_{2,CM2} + f_{g3}\Delta y_{2,CM3} \\ 0 \end{bmatrix}$$

$$\{r\} = \begin{bmatrix} h_1 \\ v_1 \\ h_2 \\ v_2 \\ h_4 \\ v_4 \\ \lambda_a \end{bmatrix} \qquad \{q\} = \begin{bmatrix} 0 \\ f_{g1} \\ -f_{g1}\Delta x_{1,CM1} \\ 0 \\ f_{g2} + f_{g3} \\ -f_{g2}\Delta x_{2,CM2} - f_{g3}\Delta x_{2,CM3} \\ 0 \end{bmatrix} \tag{45}$$

3.3.4.3 Type XIX – C_1 -- H_3 H_4

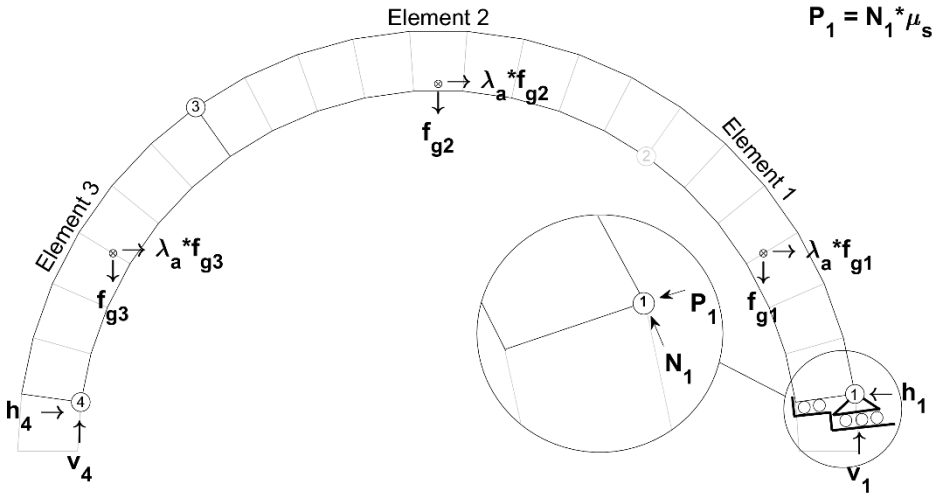

Figure 37. Free-body diagram for the Type XIX mechanism

The equations of equilibrium for the condition shown in Figure 37 is

$$[BC] = \begin{bmatrix} -1 & 0 & 1 & 0 & 0 & 0 \\ 0 & 1 & 0 & -1 & 0 & 0 \\ 0 & 0 & -\Delta y_{3,1} & -\Delta x_{1,3} & 0 & 0 \\ 0 & 0 & -1 & 0 & 1 & 0 \\ 0 & 0 & 0 & 1 & 0 & 1 \\ 0 & 0 & 0 & 0 & \Delta y_{3,4} & -\Delta x_{3,4} \\ \tan(\alpha_1) & 1 & 0 & 0 & 0 & 0 \end{bmatrix} \begin{bmatrix} f_{g1} + f_{g2} \\ 0 \\ -f_{g1}\Delta y_{CM1,1} - f_{g2}\Delta y_{CM2,1} \\ f_{g3} \\ 0 \\ f_{g3}\Delta y_{3,CM3} \\ 0 \end{bmatrix}$$

$$\{r\} = \begin{bmatrix} h_1 \\ v_1 \\ h_3 \\ v_3 \\ h_4 \\ v_4 \\ \lambda_a \end{bmatrix} \qquad \{q\} = \begin{bmatrix} 0 \\ f_{g1} + f_{g2} \\ -f_{g1}\Delta x_{1,CM1} - f_{g2}\Delta x_{1,CM2} \\ 0 \\ f_{g3} \\ -f_{g3}\Delta x_{3,CM3} \\ 0 \end{bmatrix} \tag{46}$$

3.3.4.4 Type XX – H_1 C_2 H_3 –

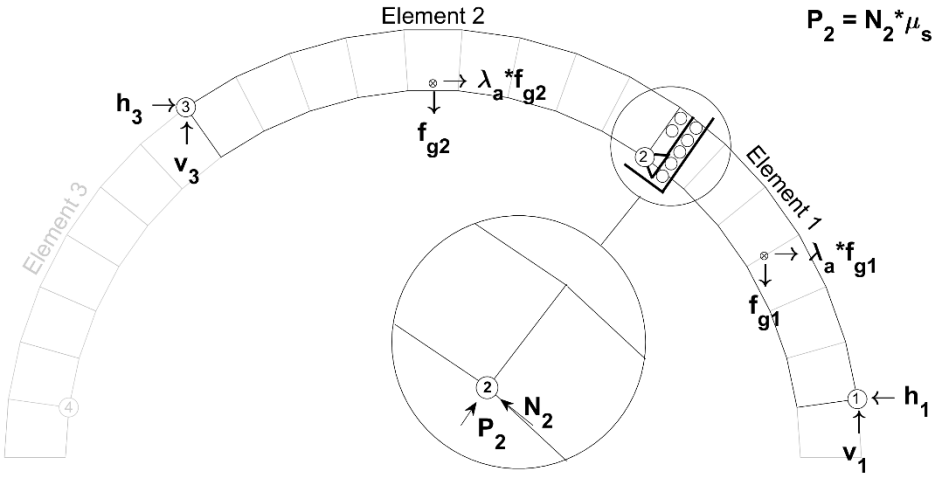

Figure 38. Free-body diagram for the Type XX mechanism

The equations of equilibrium for the condition shown in Figure 38 is

$$[BC] = \begin{bmatrix} -1 & 0 & 1 & 0 & 0 & 0 & f_{g1} \\ 0 & 1 & 0 & -1 & 0 & 0 & 0 \\ 0 & 0 & -\Delta y_{2,1} & \Delta x_{1,2} & 0 & 0 & -f_{g1}\Delta y_{CM1,1} \\ 0 & 0 & -1 & 0 & 1 & 0 & f_{g2} \\ 0 & 0 & 0 & 1 & 0 & 1 & 0 \\ 0 & 0 & 0 & 0 & \Delta y_{3,2} & \Delta x_{2,3} & f_{g2}\Delta y_{2,CM2} \\ 0 & 0 & \tan(\alpha_2) & 1 & 0 & 0 & 0 \end{bmatrix}$$

$$\{r\} = \begin{bmatrix} h_1 \\ v_1 \\ h_2 \\ v_2 \\ h_3 \\ v_3 \\ \lambda_a \end{bmatrix} \qquad \{q\} = \begin{bmatrix} 0 \\ f_{g1} \\ -f_{g1}\Delta x_{1,CM1} \\ 0 \\ f_{g2} \\ f_{g2}\Delta x_{2,CM2} \\ 0 \end{bmatrix} \tag{47}$$

3.3.4.5 Type XXI – H_1 C_2 -- H_4

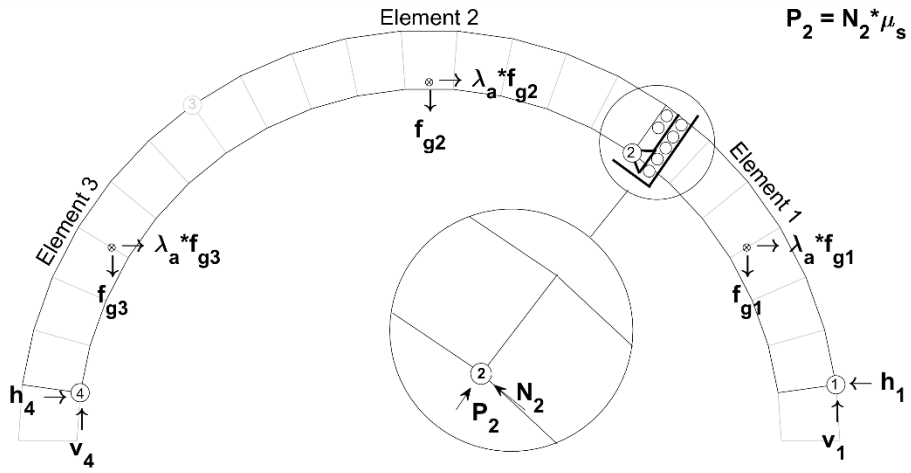

Figure 39. Free-body diagram for the Type XXI mechanism

The equations of equilibrium for the condition shown in Figure 39 is

$$[BC] = \begin{bmatrix} -1 & 0 & 1 & 0 & 0 & 0 & f_{g1} \\ 0 & 1 & 0 & -1 & 0 & 0 & 0 \\ 0 & 0 & -\Delta y_{2,1} & \Delta x_{1,2} & 0 & 0 & -f_{g1}\Delta y_{CM1,1} \\ 0 & 0 & -1 & 0 & 1 & 0 & f_{g2} + f_{g3} \\ 0 & 0 & 0 & 1 & 0 & 1 & 0 \\ 0 & 0 & 0 & 0 & \Delta y_{2,4} & \Delta x_{2,4} & f_{g2}\Delta y_{2,CM2} + f_{g3}\Delta y_{2,CM3} \\ 0 & 0 & \tan(\alpha_2) & 1 & 0 & 0 & 0 \end{bmatrix}$$

$$\{r\} = \begin{bmatrix} h_1 \\ v_1 \\ h_2 \\ v_2 \\ h_4 \\ v_4 \\ \lambda_a \end{bmatrix} \qquad \{q\} = \begin{bmatrix} 0 \\ f_{g1} \\ -f_{g1}\Delta x_{1,CM1} \\ 0 \\ f_{g2} + f_{g3} \\ f_{g2}\Delta x_{2,CM2} + f_{g3}\Delta x_{2,CM3} \\ 0 \end{bmatrix} \tag{48}$$

3.3.4.6 Type XXII – -- C_2 H_3 H_4

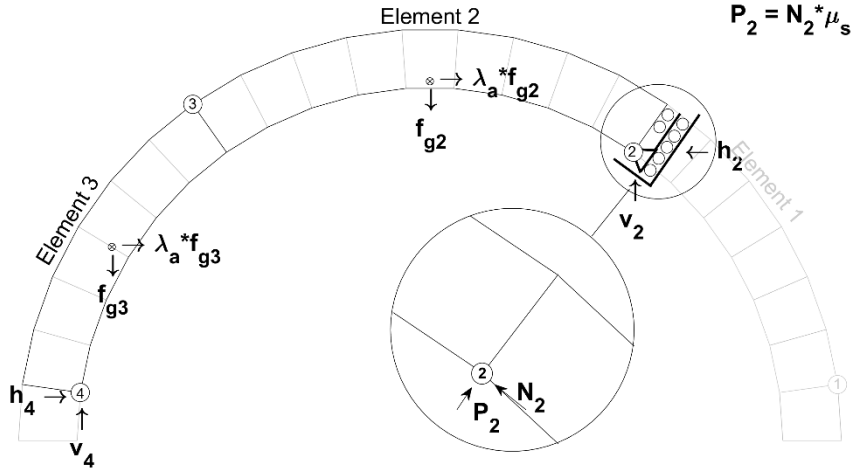

Figure 40. Free-body diagram for the Type XXII mechanism

The equations of equilibrium for the condition shown in Figure 40 is

$$[BC] = \begin{bmatrix} -1 & 0 & 1 & 0 & 0 & 0 & f_{g2} \\ 0 & 1 & 0 & -1 & 0 & 0 & 0 \\ 0 & 0 & -\Delta y_{3,2} & \Delta x_{2,3} & 0 & 0 & -f_{g2}\Delta y_{CM2,2} \\ 0 & 0 & -1 & 0 & 1 & 0 & f_{g3} \\ 0 & 0 & 0 & 1 & 0 & 1 & 0 \\ 0 & 0 & 0 & 0 & \Delta y_{3,2} & \Delta x_{2,3} & f_{g3}\Delta y_{3,CM3} \\ \tan(\alpha_2) & 1 & 0 & 0 & 0 & 0 & 0 \end{bmatrix}$$

$$\{r\} = \begin{bmatrix} h_2 \\ v_2 \\ h_3 \\ v_3 \\ h_4 \\ v_4 \\ \lambda_a \end{bmatrix} \qquad \{q\} = \begin{bmatrix} 0 \\ f_{g2} \\ -f_{g2}\Delta x_{2,CM2} \\ 0 \\ f_{g3} \\ f_{g3}\Delta x_{3,CM3} \\ 0 \end{bmatrix} \tag{49}$$

3.3.4.7 Type XXIII – $H_1\ H_2\ C_3$ –

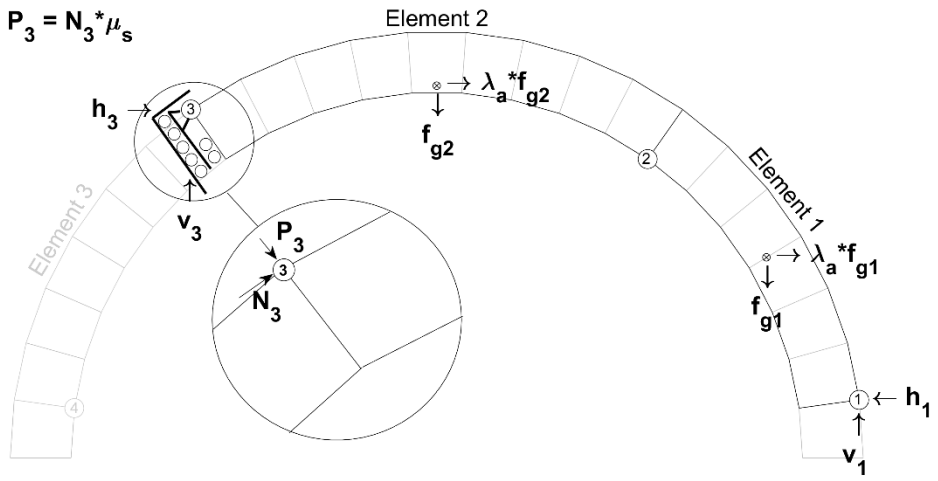

Figure 41. Free-body diagram for the Type XXIII mechanism

The equations of equilibrium for the condition shown in Figure 41 is

$$[BC] = \begin{bmatrix} -1 & 0 & 1 & 0 & 0 & 0 & f_{g1} \\ 0 & 1 & 0 & -1 & 0 & 0 & 0 \\ 0 & 0 & -\Delta y_{2,1} & \Delta x_{1,2} & 0 & 0 & -f_{g1}\Delta y_{CM1,1} \\ 0 & 0 & -1 & 0 & 1 & 0 & f_{g2} \\ 0 & 0 & 0 & 1 & 0 & 1 & 0 \\ 0 & 0 & 0 & 0 & \Delta y_{3,2} & \Delta x_{2,3} & f_{g2}\Delta y_{2,CM2} \\ 0 & 0 & 0 & 0 & \tan(\alpha_3) & 1 & 0 \end{bmatrix}$$

$$\{r\} = \begin{bmatrix} h_1 \\ v_1 \\ h_2 \\ v_2 \\ h_3 \\ v_3 \\ \lambda_a \end{bmatrix} \qquad \{q\} = \begin{bmatrix} 0 \\ f_{g1} \\ -f_{g1}\Delta x_{1,CM1} \\ 0 \\ f_{g2} \\ f_{g2}\Delta x_{2,CM2} \\ 0 \end{bmatrix} \tag{50}$$

3.3.4.8 Type XXIV – H_1 -- C_3 H_4

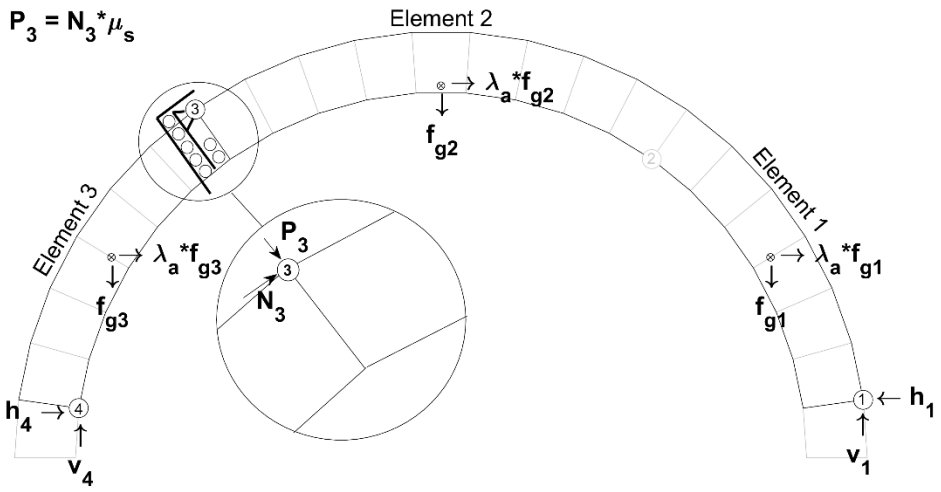

Figure 42. Free-body diagram for the Type XXIV mechanism

The equations of equilibrium for the condition shown in Figure 42 is

$$[BC] = \begin{bmatrix} -1 & 0 & 1 & 0 & 0 & 0 & f_{g1}+f_{g2} \\ 0 & 1 & 0 & -1 & 0 & 0 & 0 \\ 0 & 0 & -\Delta y_{3,1} & -\Delta x_{1,3} & 0 & 0 & -f_{g1}\Delta y_{CM1,1} - f_{g2}\Delta y_{CM2,1} \\ 0 & 0 & -1 & 0 & 1 & 0 & f_{g3} \\ 0 & 0 & 0 & 1 & 0 & 1 & 0 \\ 0 & 0 & 0 & 0 & \Delta y_{3,4} & -\Delta x_{3,4} & f_{g3}\Delta y_{3,CM3} \\ 0 & 0 & \tan(\alpha_3) & 1 & 0 & 0 & 0 \end{bmatrix}$$

$$\{r\} = \begin{bmatrix} h_1 \\ v_1 \\ h_3 \\ v_3 \\ h_4 \\ v_4 \\ \lambda_a \end{bmatrix} \qquad \{q\} = \begin{bmatrix} 0 \\ f_{g1}+f_{g2} \\ -f_{g1}\Delta x_{1,CM1} - f_{g2}\Delta x_{1,CM2} \\ 0 \\ f_{g3} \\ -f_{g3}\Delta x_{3,CM3} \\ 0 \end{bmatrix} \tag{51}$$

3.3.4.9 Type XXV – -- H_2 C_3 H_4

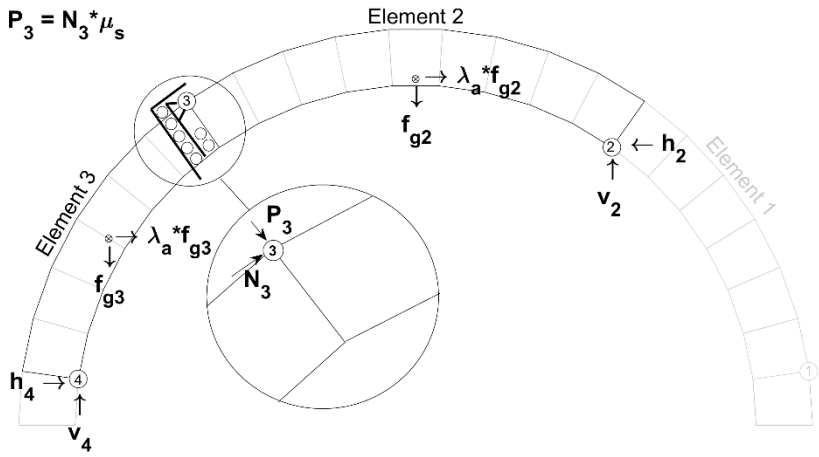

Figure 43. Free-body diagram for the Type XXV mechanism

The equations of equilibrium for the condition shown in Figure 43 is

$$[BC] = \begin{bmatrix} -1 & 0 & 1 & 0 & 0 & 0 & f_{g2} \\ 0 & 1 & 0 & -1 & 0 & 0 & 0 \\ 0 & 0 & -\Delta y_{3,2} & \Delta x_{2,3} & 0 & 0 & -f_{g2}\Delta y_{CM2,2} \\ 0 & 0 & -1 & 0 & 1 & 0 & f_{g3} \\ 0 & 0 & 0 & 1 & 0 & 1 & 0 \\ 0 & 0 & 0 & 0 & \Delta y_{3,2} & \Delta x_{2,3} & f_{g3}\Delta y_{3,CM3} \\ 0 & 0 & \tan(\alpha_3) & 1 & 0 & 0 & 0 \end{bmatrix}$$

$$\{r\} = \begin{bmatrix} h_2 \\ v_2 \\ h_3 \\ v_3 \\ h_4 \\ v_4 \\ \lambda_a \end{bmatrix} \qquad \{q\} = \begin{bmatrix} 0 \\ f_{g2} \\ -f_{g2}\Delta x_{2,CM2} \\ 0 \\ f_{g3} \\ f_{g3}\Delta x_{3,CM3} \\ 0 \end{bmatrix} \tag{52}$$

3.3.4.10 Type XXVI – H_1 H_2 -- C_4

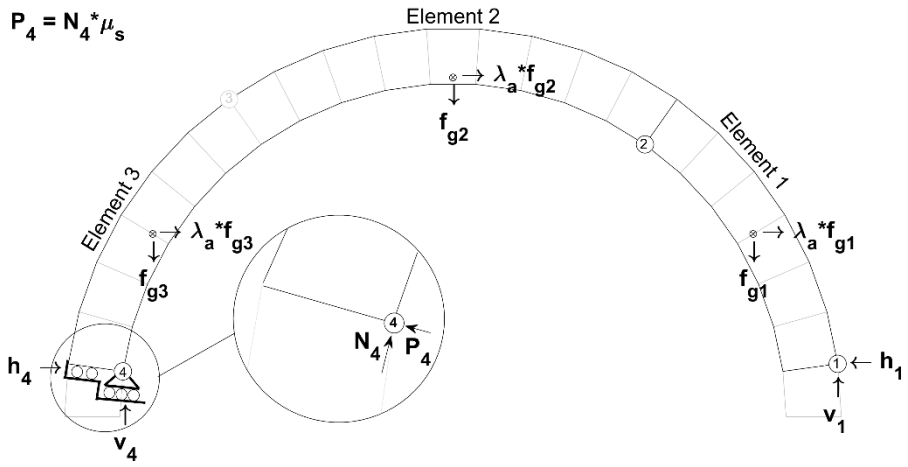

Figure 44. Free-body diagram for the Type XXVI mechanism

The equations of equilibrium for the condition shown in Figure 44 is

$$[BC] = \begin{bmatrix} -1 & 0 & 1 & 0 & 0 & 0 & f_{g1} \\ 0 & 1 & 0 & -1 & 0 & 0 & 0 \\ 0 & 0 & -\Delta y_{2,1} & \Delta x_{1,2} & 0 & 0 & -f_{g1}\Delta y_{CM1,1} \\ 0 & 0 & -1 & 0 & 1 & 0 & f_{g2} + f_{g3} \\ 0 & 0 & 0 & 1 & 0 & 1 & 0 \\ 0 & 0 & 0 & 0 & \Delta y_{2,4} & \Delta x_{2,4} & f_{g2}\Delta y_{2,CM2} + f_{g3}\Delta y_{2,CM3} \\ 0 & 0 & 0 & 0 & \tan(\alpha_4) & 1 & 0 \end{bmatrix}$$

$$\{r\} = \begin{bmatrix} h_1 \\ v_1 \\ h_2 \\ v_2 \\ h_4 \\ v_4 \\ \lambda_a \end{bmatrix} \qquad \{q\} = \begin{bmatrix} 0 \\ f_{g1} \\ -f_{g1}\Delta x_{1,CM1} \\ 0 \\ f_{g2} + f_{g3} \\ f_{g2}\Delta x_{2,CM2} + f_{g3}\Delta x_{2,CM3} \\ 0 \end{bmatrix} \tag{53}$$

3.3.4.11 Type XXVII – H_1 -- H_3 C_4

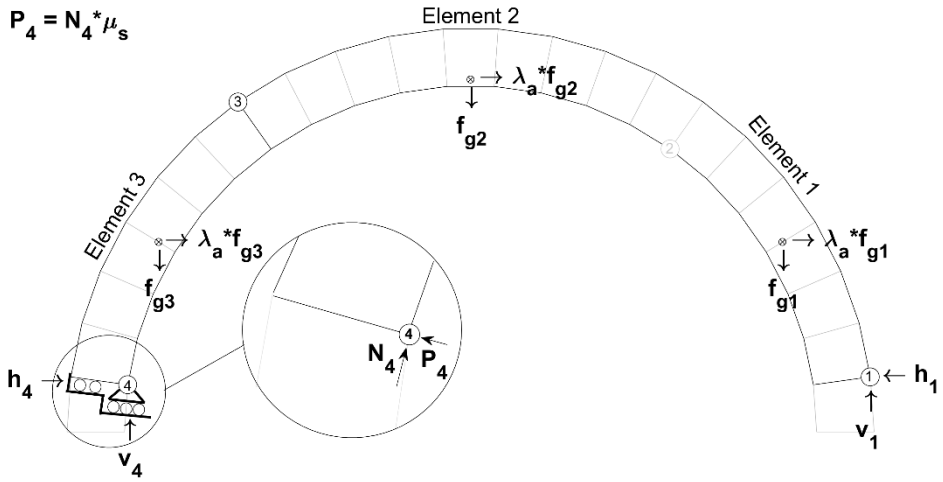

Figure 45. Free-body diagram for the Type XXVII mechanism

The equations of equilibrium for the condition shown in Figure 45 is

$$[BC] = \begin{bmatrix} -1 & 0 & 1 & 0 & 0 & 0 & f_{g1}+f_{g2} \\ 0 & 1 & 0 & -1 & 0 & 0 & 0 \\ 0 & 0 & -\Delta y_{3,1} & -\Delta x_{1,3} & 0 & 0 & -f_{g1}\Delta y_{CM1,1} - f_{g2}\Delta y_{CM2,1} \\ 0 & 0 & -1 & 0 & 1 & 0 & f_{g3} \\ 0 & 0 & 0 & 1 & 0 & 1 & 0 \\ 0 & 0 & 0 & 0 & \Delta y_{3,4} & -\Delta x_{3,4} & f_{g3}\Delta y_{3,CM3} \\ 0 & 0 & 0 & 0 & \tan(\alpha_4) & 1 & 0 \end{bmatrix}$$

$$\{r\} = \begin{bmatrix} h_1 \\ v_1 \\ h_3 \\ v_3 \\ h_4 \\ v_4 \\ \lambda_a \end{bmatrix} \qquad \{q\} = \begin{bmatrix} 0 \\ f_{g1}+f_{g2} \\ -f_{g1}\Delta x_{1,CM1} - f_{g2}\Delta x_{1,CM2} \\ 0 \\ f_{g3} \\ -f_{g3}\Delta x_{3,CM3} \\ 0 \end{bmatrix} \tag{54}$$

3.3.4.12 Type XXVIII – -- H_2 H_3 C_4

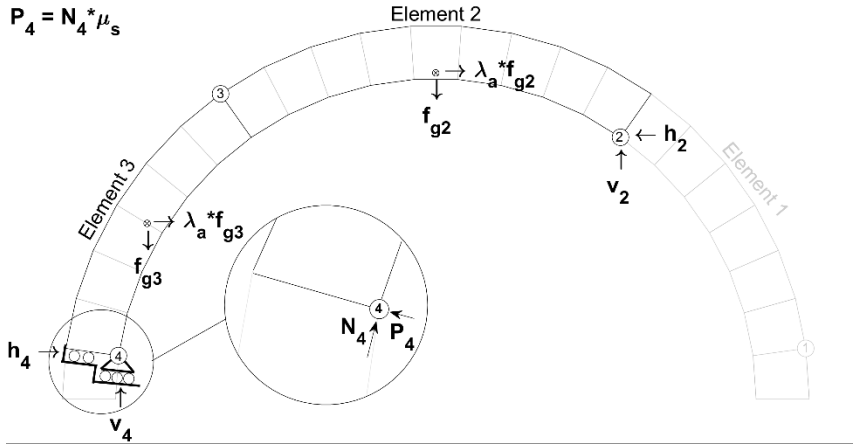

Figure 46. Free-body diagram for the Type XXVIII mechanism

The equations of equilibrium for the condition shown in Figure 46 is

$$[BC] = \begin{bmatrix} -1 & 0 & 1 & 0 & 0 & 0 & f_{g2} \\ 0 & 1 & 0 & -1 & 0 & 0 & 0 \\ 0 & 0 & -\Delta y_{3,2} & \Delta x_{2,3} & 0 & 0 & -f_{g2}\Delta y_{CM2,2} \\ 0 & 0 & -1 & 0 & 1 & 0 & f_{g3} \\ 0 & 0 & 0 & 1 & 0 & 1 & 0 \\ 0 & 0 & 0 & 0 & \Delta y_{3,2} & \Delta x_{2,3} & f_{g3}\Delta y_{3,CM3} \\ 0 & 0 & 0 & 0 & \tan(\alpha_4) & 1 & 0 \end{bmatrix}$$

$$\{r\} = \begin{bmatrix} h_2 \\ v_2 \\ h_3 \\ v_3 \\ h_4 \\ v_4 \\ \lambda_a \end{bmatrix} \qquad \{q\} = \begin{bmatrix} 0 \\ f_{g2} \\ -f_{g2}\Delta x_{2,CM2} \\ 0 \\ f_{g3} \\ f_{g3}\Delta x_{3,CM3} \\ 0 \end{bmatrix} \tag{55}$$

3.3.5 Combined-Hinge-Slip Mechanisms

The combined-hinge-slip mechanisms take the reduced structure of the combined-hinge mechanisms and add the hinge-slip transformation to one of the non-combined mechanical joints.

Mechanisms Type XXIX and Type XXX assign C_1 in exchange for hinge H_4 with slips S_3 and S_2 respectively. Mechanisms Type XXXI and Type XXXII assign C_1 in exchange for hinge H_3 with slips S_4 and S_2 respectively. Mechanisms Type XXXIII and Type XXXIV assign C_1 in exchange for hinge H_2 with slips S_4 and S_3 respectively.

Mechanisms Type XXXV and Type XXXVI assign C_2 in exchange for hinge H_4 with slips S_3 and S_1 respectively. Mechanisms Type XXXVII and Type XXXVIII assign C_2 in exchange for hinge H_3 with slips S_4 and S_1 respectively. Mechanisms Type XXXIX and Type XL assign C_2 in exchange for hinge H_1 with slips S_4 and S_3 respectively.

Mechanisms Type XLI and Type XLII assign C_3 in exchange for hinge H_4 with slips S_2 and S_1 respectively. Mechanisms Type XLIII and Type XLIV assign C_3 in exchange for hinge H_2 with slips S_4 and S_1 respectively. Mechanisms Type XLV and Type XLVI assign C_3 in exchange for hinge H_1 with slips S_4 and S_2 respectively.

Lastly, mechanisms Type XLVII and Type XLVIII assign C_4 in exchange for hinge H_3 with slips S_2 and S_1 respectively. Mechanisms Type XLIX and Type L assign C_4 in exchange for hinge H_2 with slips S_3 and S_1 respectively. Mechanisms Type LI and Type LII assign C_4 in exchange for hinge H_1 with slips S_3 and S_2 respectively.

3.3.5.1 Type XXIX – $C_1 H_2 S_3$ –

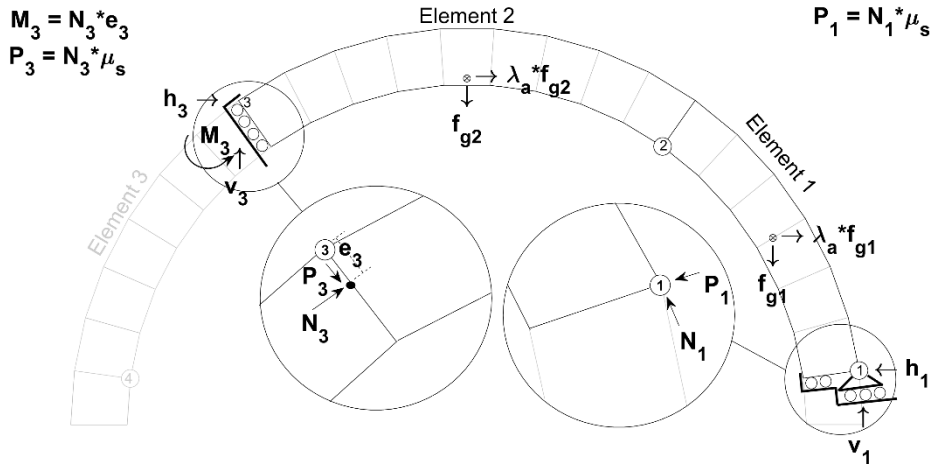

Figure 47. Free-body diagram for the Type XXIX mechanism

The equations of equilibrium for the condition shown in Figure 47 is

$$[BC] = \begin{bmatrix} -1 & 0 & 1 & 0 & 0 & 0 & f_{g1} & 0 \\ 0 & 1 & 0 & -1 & 0 & 0 & 0 & 0 \\ 0 & 0 & -\Delta y_{2,1} & \Delta x_{1,2} & 0 & 0 & -f_{g1}\Delta y_{CM1,1} & 0 \\ 0 & 0 & -1 & 0 & 1 & 0 & f_{g2} & 0 \\ 0 & 0 & 0 & 1 & 0 & 1 & 0 & 0 \\ 0 & 0 & 0 & 0 & \Delta y_{3,2} & \Delta x_{2,3} & f_{g2}\Delta y_{2,CM2} & 1 \\ \tan(\alpha_1) & 1 & 0 & 0 & 0 & 0 & 0 & 0 \\ 0 & 0 & 0 & 0 & \tan(\alpha_3) & -1 & 0 & 0 \end{bmatrix}$$

$$\{r\} = \begin{bmatrix} h_1 \\ v_1 \\ h_2 \\ v_2 \\ h_3 \\ v_3 \\ \lambda_a \\ M_3 \end{bmatrix} \qquad \{q\} = \begin{bmatrix} 0 \\ f_{g1} \\ -f_{g1}\Delta x_{1,CM1} \\ 0 \\ f_{g2} \\ f_{g2}\Delta x_{2,CM2} \\ 0 \\ 0 \end{bmatrix} \tag{56}$$

3.3.5.2 Type XXX – C_1 S_2 H_3 –

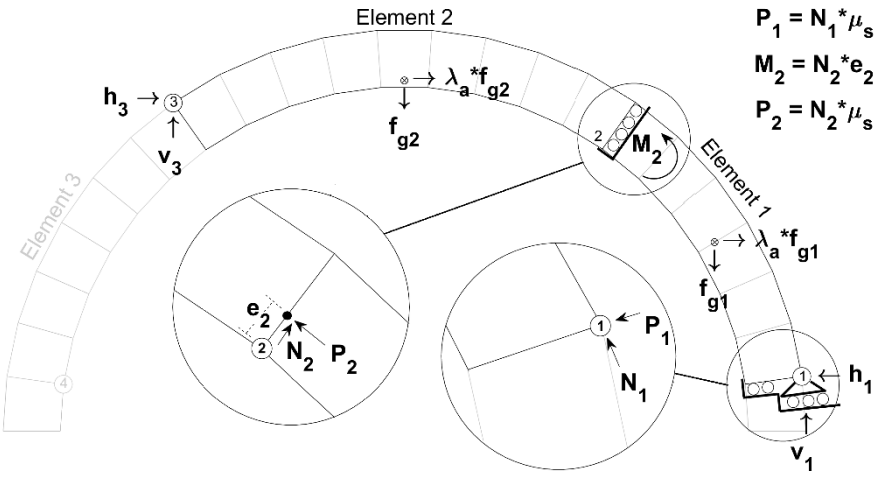

Figure 48. Free-body diagram for the Type XXX mechanism

The equations of equilibrium for the condition shown in Figure 48 is

$$[BC] = \begin{bmatrix} -1 & 0 & 1 & 0 & 0 & 0 & f_{g1} & 0 \\ 0 & 1 & 0 & -1 & 0 & 0 & 0 & 0 \\ 0 & 0 & -\Delta y_{2,1} & \Delta x_{1,2} & 0 & 0 & -f_{g1}\Delta y_{CM1,1} & -1 \\ 0 & 0 & -1 & 0 & 1 & 0 & f_{g2} & 0 \\ 0 & 0 & 0 & 1 & 0 & 1 & 0 & 0 \\ 0 & 0 & 0 & 0 & \Delta y_{3,2} & \Delta x_{2,3} & f_{g2}\Delta y_{2,CM2} & 1 \\ \tan(\alpha_1) & 1 & 0 & 0 & 0 & 0 & 0 & 0 \\ 0 & 0 & \tan(\alpha_2) & -1 & 0 & 0 & 0 & 0 \end{bmatrix}$$

$$\{r\} = \begin{bmatrix} h_1 \\ v_1 \\ h_2 \\ v_2 \\ h_3 \\ v_3 \\ \lambda_a \\ M_2 \end{bmatrix} \qquad \{q\} = \begin{bmatrix} 0 \\ f_{g1} \\ -f_{g1}\Delta x_{1,CM1} \\ 0 \\ f_{g2} \\ f_{g2}\Delta x_{2,CM2} \\ 0 \\ 0 \end{bmatrix} \tag{57}$$

3.3.5.3 Type XXXI – C_1 H_2 -- S_4

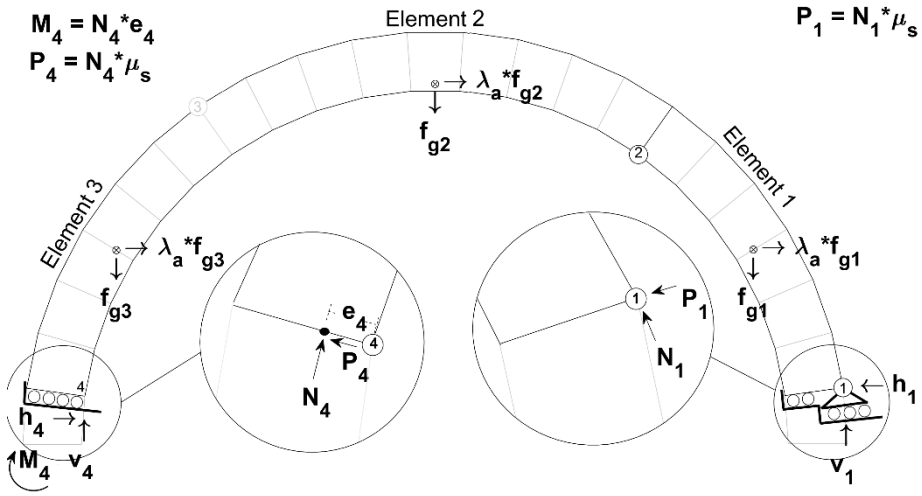

Figure 49. Free-body diagram for the Type XXXI mechanism

The equations of equilibrium for the condition shown in Figure 49 is

$$[BC] = \begin{bmatrix} -1 & 0 & 1 & 0 & 0 & 0 & f_{g1} & 0 \\ 0 & 1 & 0 & -1 & 0 & 0 & 0 & 0 \\ 0 & 0 & -\Delta y_{2,1} & -\Delta x_{1,2} & 0 & 0 & -f_{g1}\Delta y_{CM1,1} & 0 \\ 0 & 0 & -1 & 0 & 1 & 0 & f_{g2}+f_{g3} & 0 \\ 0 & 0 & 0 & 1 & 0 & 1 & 0 & 0 \\ 0 & 0 & 0 & 0 & \Delta y_{2,4} & -\Delta x_{2,4} & f_{g2}\Delta y_{CM2,2}+f_{g3}\Delta y_{2,CM3} & 1 \\ \tan(\alpha_1) & 1 & 0 & 0 & 0 & 0 & 0 & 0 \\ 0 & 0 & 0 & 0 & \tan(\alpha_4) & -1 & 0 & 0 \end{bmatrix}$$

$$\{r\} = \begin{bmatrix} h_1 \\ v_1 \\ h_2 \\ v_2 \\ h_4 \\ v_4 \\ \lambda_a \\ M_4 \end{bmatrix} \qquad \{q\} = \begin{bmatrix} 0 \\ f_{g1} \\ -f_{g1}\Delta x_{1,CM1} \\ 0 \\ f_{g2}+f_{g3} \\ -f_{g2}\Delta x_{1,CM2} - f_{g3}\Delta x_{3,CM3} \\ 0 \\ 0 \end{bmatrix} \tag{58}$$

3.3.5.4 Type XXXII – C_1 S_2 -- H_4

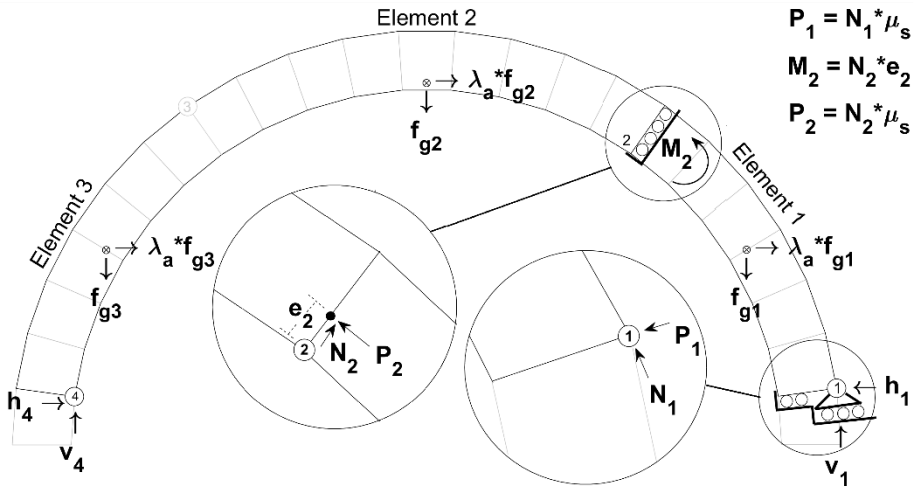

Figure 50. Free-body diagram for the Type XXXII mechanism

The equations of equilibrium for the condition shown in Figure 50 is

$$[BC] = \begin{bmatrix} -1 & 0 & 1 & 0 & 0 & 0 & f_{g1} & 0 \\ 0 & 1 & 0 & -1 & 0 & 0 & 0 & 0 \\ 0 & 0 & -\Delta y_{2,1} & -\Delta x_{1,2} & 0 & 0 & -f_{g1}\Delta y_{CM1,1} & -1 \\ 0 & 0 & -1 & 0 & 1 & 0 & f_{g2} + f_{g3} & 0 \\ 0 & 0 & 0 & 1 & 0 & 1 & 0 & 0 \\ 0 & 0 & 0 & 0 & \Delta y_{2,4} & -\Delta x_{2,4} & f_{g2}\Delta y_{CM2,2} + f_{g3}\Delta y_{2,CM3} & 1 \\ \tan(\alpha_1) & 1 & 0 & 0 & 0 & 0 & 0 & 0 \\ 0 & 0 & \tan(\alpha_2) & -1 & 0 & 0 & 0 & 0 \end{bmatrix}$$

$$\{r\} = \begin{bmatrix} h_1 \\ v_1 \\ h_2 \\ v_2 \\ h_4 \\ v_4 \\ \lambda_a \\ M_2 \end{bmatrix} \qquad \{q\} = \begin{bmatrix} 0 \\ f_{g1} \\ -f_{g1}\Delta x_{1,CM1} \\ 0 \\ f_{g2} + f_{g3} \\ -f_{g2}\Delta x_{2,CM2} - f_{g3}\Delta x_{2,CM3} \\ 0 \\ 0 \end{bmatrix} \tag{59}$$

3.3.5.5 Type XXXIII – C_1 -- H_3 S_4

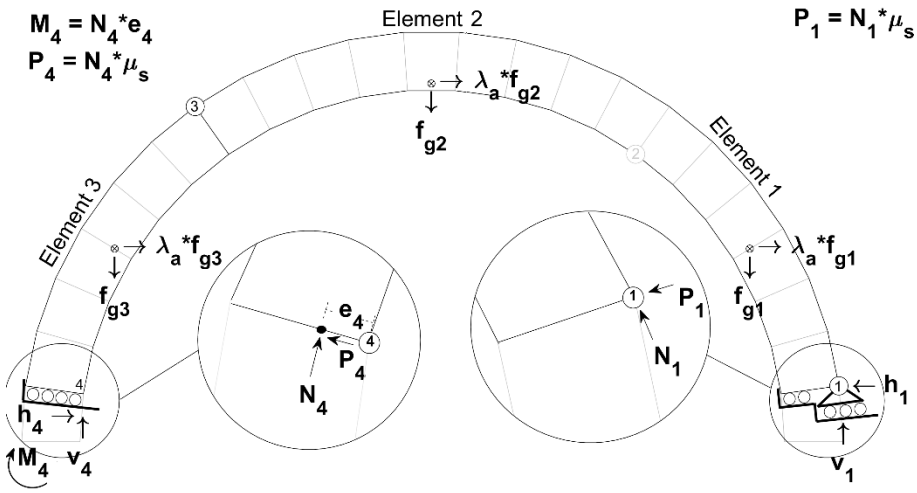

Figure 51. Free-body diagram for the Type XXXIII mechanism

The equations of equilibrium for the condition shown in Figure 51 is

$$[BC] = \begin{bmatrix} -1 & 0 & 1 & 0 & 0 & 0 & f_{g1}+f_{g2} & 0 \\ 0 & 1 & 0 & -1 & 0 & 0 & 0 & 0 \\ 0 & 0 & -\Delta y_{3,1} & -\Delta x_{1,3} & 0 & 0 & -f_{g1}\Delta y_{CM1,1} - f_{g2}\Delta y_{CM2,1} & 0 \\ 0 & 0 & -1 & 0 & 1 & 0 & f_{g3} & 0 \\ 0 & 0 & 0 & 1 & 0 & 1 & 0 & 0 \\ 0 & 0 & 0 & 0 & \Delta y_{3,4} & -\Delta x_{3,4} & f_{g3}\Delta y_{3,CM3} & 1 \\ \tan(\alpha_1) & 1 & 0 & 0 & 0 & 0 & 0 & 0 \\ 0 & 0 & 0 & 0 & \tan(\alpha_4) & -1 & 0 & 0 \end{bmatrix}$$

$$\{r\} = \begin{bmatrix} h_1 \\ v_1 \\ h_3 \\ v_3 \\ h_4 \\ v_4 \\ \lambda_a \\ M_4 \end{bmatrix} \qquad \{q\} = \begin{bmatrix} 0 \\ f_{g1}+f_{g2} \\ -f_{g1}\Delta x_{1,CM1} - f_{g2}\Delta x_{1,CM2} \\ 0 \\ f_{g3} \\ -f_{g3}\Delta x_{3,CM3} \\ 0 \\ 0 \end{bmatrix} \tag{60}$$

3.3.5.6 Type XXXIV – C_1 -- S_3 H_4

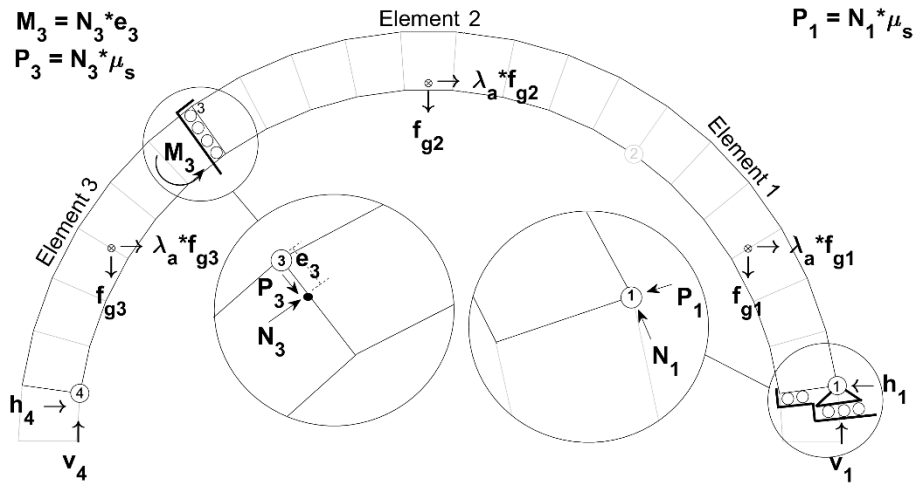

Figure 52. Free-body diagram for the Type XXXIV mechanism

The equations of equilibrium for the condition shown in Figure 52 is

$$[BC] = \begin{bmatrix} -1 & 0 & 1 & 0 & 0 & 0 & f_{g1}+f_{g2} & 0 \\ 0 & 1 & 0 & -1 & 0 & 0 & 0 & 0 \\ 0 & 0 & -\Delta y_{3,1} & -\Delta x_{1,3} & 0 & 0 & -f_{g1}\Delta y_{CM1,1} - f_{g2}\Delta y_{CM2,1} & -1 \\ 0 & 0 & -1 & 0 & 1 & 0 & f_{g3} & 0 \\ 0 & 0 & 0 & 1 & 0 & 1 & 0 & 0 \\ 0 & 0 & 0 & 0 & \Delta y_{3,4} & -\Delta x_{3,4} & f_{g3}\Delta y_{3,CM3} & 1 \\ \tan(\alpha_1) & 1 & 0 & 0 & 0 & 0 & 0 & 0 \\ 0 & 0 & \tan(\alpha_3) & -1 & 0 & 0 & 0 & 0 \end{bmatrix}$$

$$\{r\} = \begin{bmatrix} h_1 \\ v_1 \\ h_3 \\ v_3 \\ h_4 \\ v_4 \\ \lambda_a \\ M_2 \end{bmatrix} \qquad \{q\} = \begin{bmatrix} 0 \\ f_{g1}+f_{g2} \\ -f_{g1}\Delta x_{1,CM1} \\ 0 \\ f_{g3} \\ -f_{g2}\Delta x_{1,CM2} - f_{g3}\Delta x_{3,CM3} \\ 0 \\ 0 \end{bmatrix} \tag{61}$$

3.3.5.7 Type XXXV – $H_1\ C_2\ S_3$ –

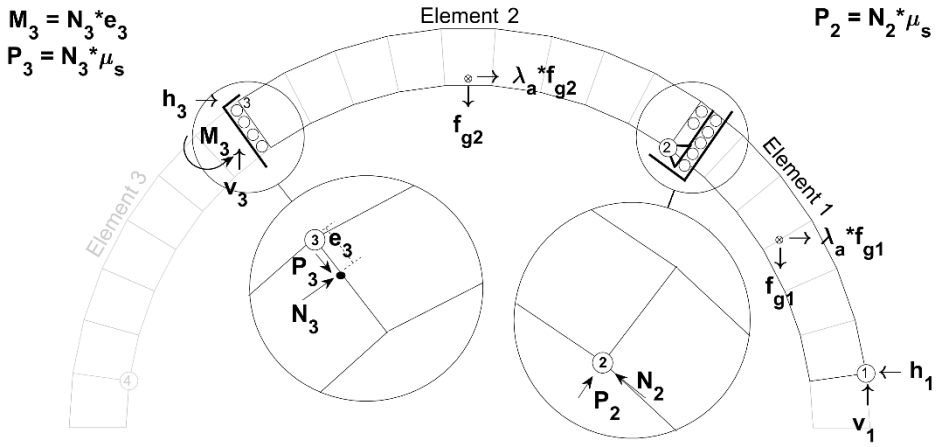

Figure 53. Free-body diagram for the Type XXXV mechanism

The equations of equilibrium for the condition shown in Figure 53 is

$$[BC] = \begin{bmatrix} -1 & 0 & 1 & 0 & 0 & 0 & f_{g1} & 0 \\ 0 & 1 & 0 & -1 & 0 & 0 & 0 & 0 \\ 0 & 0 & -\Delta y_{2,1} & \Delta x_{1,2} & 0 & 0 & -f_{g1}\Delta y_{CM1,1} & 0 \\ 0 & 0 & -1 & 0 & 1 & 0 & f_{g2} & 0 \\ 0 & 0 & 0 & 1 & 0 & 1 & 0 & 0 \\ 0 & 0 & 0 & 0 & \Delta y_{3,2} & \Delta x_{2,3} & f_{g2}\Delta y_{2,CM2} & 1 \\ 0 & 0 & \tan(\alpha_2) & 1 & 0 & 0 & 0 & 0 \\ 0 & 0 & 0 & 0 & \tan(\alpha_3) & -1 & 0 & 0 \end{bmatrix}$$

$$\{r\} = \begin{bmatrix} h_1 \\ v_1 \\ h_2 \\ v_2 \\ h_3 \\ v_3 \\ \lambda_a \\ M_3 \end{bmatrix} \qquad \{q\} = \begin{bmatrix} 0 \\ f_{g1} \\ -f_{g1}\Delta x_{1,CM1} \\ 0 \\ f_{g2} \\ f_{g2}\Delta x_{2,CM2} \\ 0 \\ 0 \end{bmatrix} \tag{62}$$

3.3.5.8 Type XXXVI – $S_1\,C_2\,H_3$ –

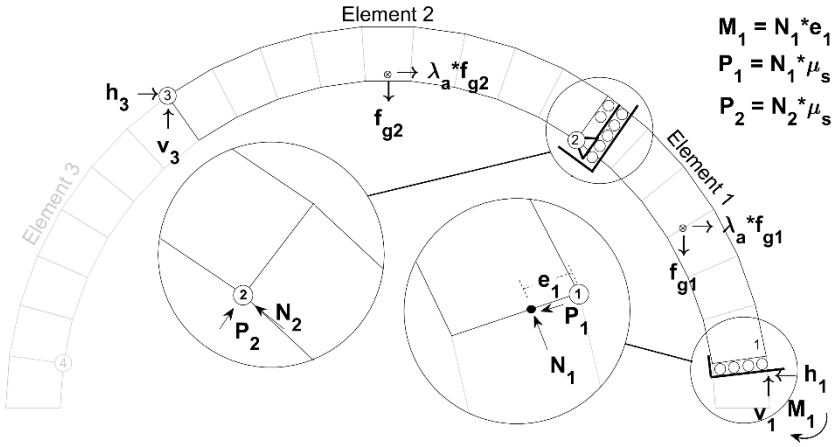

Figure 54. Free-body diagram for the Type XXXVI mechanism

The equations of equilibrium for the condition shown in Figure 54 is

$$[BC] = \begin{bmatrix} -1 & 0 & 1 & 0 & 0 & 0 & f_{g1} & 0 \\ 0 & 1 & 0 & -1 & 0 & 0 & 0 & 0 \\ 0 & 0 & -\Delta y_{2,1} & \Delta x_{1,2} & 0 & 0 & -f_{g1}\Delta y_{CM1,1} & -1 \\ 0 & 0 & -1 & 0 & 1 & 0 & f_{g2} & 0 \\ 0 & 0 & 0 & 1 & 0 & 1 & 0 & 0 \\ 0 & 0 & 0 & 0 & \Delta y_{3,2} & \Delta x_{2,3} & f_{g2}\Delta y_{2,CM2} & 0 \\ 0 & 0 & \tan(\alpha_2) & 1 & 0 & 0 & 0 & 0 \\ \tan(\alpha_1) & -1 & 0 & 0 & 0 & 0 & 0 & 0 \end{bmatrix}$$

$$\{r\} = \begin{bmatrix} h_1 \\ v_1 \\ h_2 \\ v_2 \\ h_3 \\ v_3 \\ \lambda_a \\ M_1 \end{bmatrix} \qquad \{q\} = \begin{bmatrix} 0 \\ f_{g1} \\ -f_{g1}\Delta x_{1,CM1} \\ 0 \\ f_{g2} \\ f_{g2}\Delta x_{2,CM2} \\ 0 \\ 0 \end{bmatrix} \tag{63}$$

3.3.5.9 Type XXXVII – H_1 C_2 -- S_4

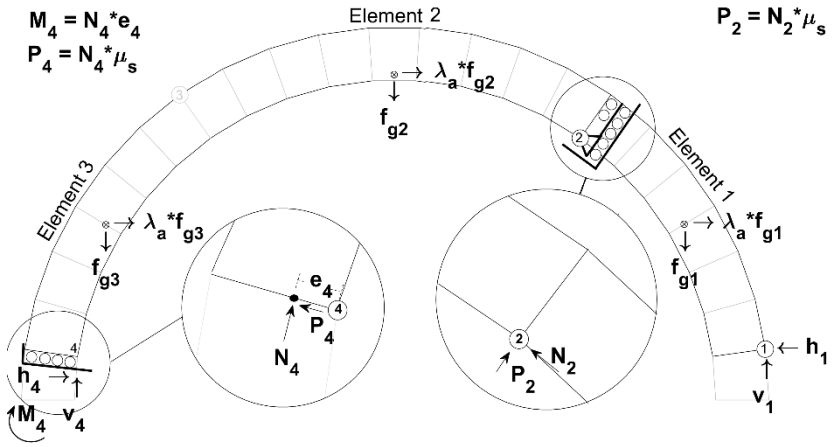

Figure 55. Free-body diagram for the Type XXXVII mechanism

The equations of equilibrium for the condition shown in Figure 55 is

$$[BC] = \begin{bmatrix} -1 & 0 & 1 & 0 & 0 & 0 & f_{g1} & 0 \\ 0 & 1 & 0 & -1 & 0 & 0 & 0 & 0 \\ 0 & 0 & -\Delta y_{2,1} & \Delta x_{1,2} & 0 & 0 & -f_{g1}\Delta y_{CM1,1} & 0 \\ 0 & 0 & -1 & 0 & 1 & 0 & f_{g2}+f_{g3} & 0 \\ 0 & 0 & 0 & 1 & 0 & 1 & 0 & 0 \\ 0 & 0 & 0 & 0 & \Delta y_{3,2} & \Delta x_{2,3} & f_{g2}\Delta y_{2,CM2}+f_{g3}\Delta y_{2,CM3} & 1 \\ 0 & 0 & \tan(\alpha_2) & 1 & 0 & 0 & 0 & 0 \\ 0 & 0 & 0 & 0 & \tan(\alpha_4) & -1 & 0 & 0 \end{bmatrix}$$

$$\{r\} = \begin{bmatrix} h_1 \\ v_1 \\ h_2 \\ v_2 \\ h_4 \\ v_4 \\ \lambda_a \\ M_4 \end{bmatrix} \qquad \{q\} = \begin{bmatrix} 0 \\ f_{g1} \\ -f_{g1}\Delta x_{1,CM1} \\ 0 \\ f_{g2}+f_{g3} \\ f_{g2}\Delta x_{2,CM2}+f_{g3}\Delta x_{2,CM3} \\ 0 \\ 0 \end{bmatrix} \tag{64}$$

3.3.5.10 Type XXXVIII – $S_1\ C_2$ -- H_4

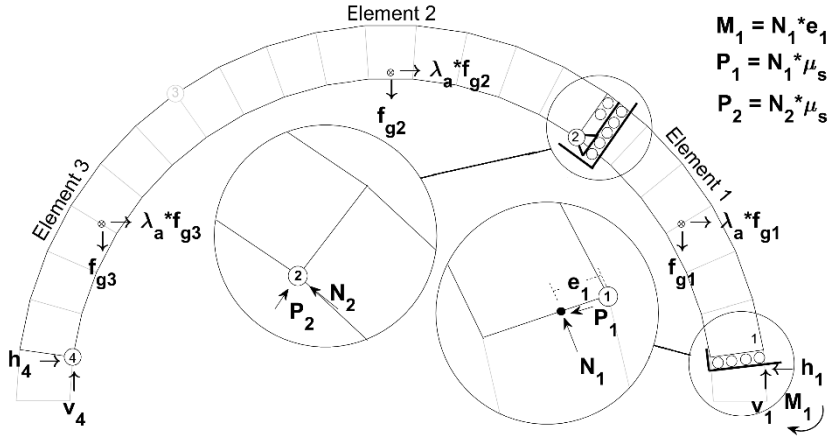

Figure 56. Free-body diagram for the Type XXXVIII mechanism

The equations of equilibrium for the condition shown in Figure 56 is

$$[BC] = \begin{bmatrix} -1 & 0 & 1 & 0 & 0 & 0 & f_{g1} & 0 \\ 0 & 1 & 0 & -1 & 0 & 0 & 0 & 0 \\ 0 & 0 & -\Delta y_{2,1} & \Delta x_{1,2} & 0 & 0 & -f_{g1}\Delta y_{CM1,1} & -1 \\ 0 & 0 & -1 & 0 & 1 & 0 & f_{g2} + f_{g3} & 0 \\ 0 & 0 & 0 & 1 & 0 & 1 & 0 & 0 \\ 0 & 0 & 0 & 0 & \Delta y_{4,2} & \Delta x_{2,4} & f_{g2}\Delta y_{2,CM2} + f_{g3}\Delta y_{2,CM3} & 0 \\ 0 & 0 & \tan(\alpha_2) & 1 & 0 & 0 & 0 & 0 \\ \tan(\alpha_1) & -1 & 0 & 0 & 0 & 0 & 0 & 0 \end{bmatrix}$$

$$\{r\} = \begin{bmatrix} h_1 \\ v_1 \\ h_2 \\ v_2 \\ h_4 \\ v_4 \\ \lambda_a \\ M_1 \end{bmatrix} \qquad \{q\} = \begin{bmatrix} 0 \\ f_{g1} \\ -f_{g1}\Delta x_{1,CM1} \\ 0 \\ f_{g2} + f_{g3} \\ f_{g2}\Delta x_{2,CM2} + f_{g3}\Delta x_{2,CM3} \\ 0 \\ 0 \end{bmatrix} \tag{65}$$

3.3.5.11 Type XXXIX – -- $C_2 H_3 S_4$

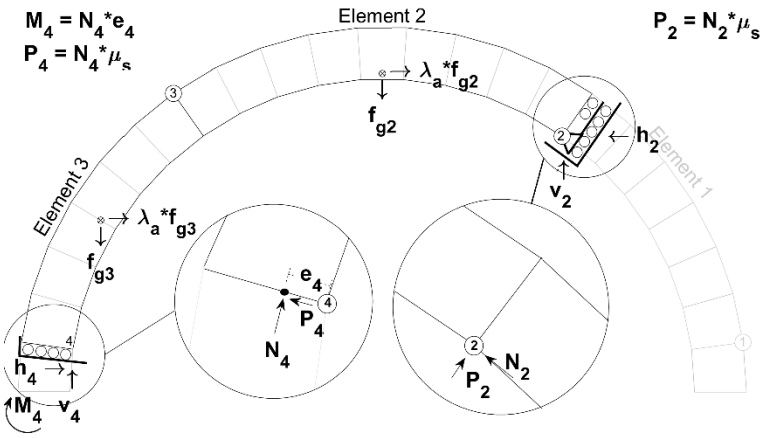

Figure 57. Free-body diagram for the Type XXXIX mechanism

The equations of equilibrium for the condition shown in Figure 57 is

$$[BC] = \begin{bmatrix} -1 & 0 & 1 & 0 & 0 & 0 & f_{g2} & 0 \\ 0 & 1 & 0 & -1 & 0 & 0 & 0 & 0 \\ 0 & 0 & \Delta y_{3,2} & \Delta x_{2,3} & 0 & 0 & -f_{g2}\Delta y_{CM2,2} & 0 \\ 0 & 0 & -1 & 0 & 1 & 0 & f_{g3} & 0 \\ 0 & 0 & 0 & 1 & 0 & 1 & 0 & 0 \\ 0 & 0 & 0 & 0 & \Delta y_{4,3} & \Delta x_{3,4} & f_{g3}\Delta y_{3,CM3} & 1 \\ \tan(\alpha_2) & 1 & 0 & 0 & 0 & 0 & 0 & 0 \\ 0 & 0 & 0 & 0 & \tan(\alpha_4) & -1 & 0 & 0 \end{bmatrix}$$

$$\{r\} = \begin{bmatrix} h_2 \\ v_2 \\ h_3 \\ v_3 \\ h_4 \\ v_4 \\ \lambda_a \\ M_4 \end{bmatrix} \qquad \{q\} = \begin{bmatrix} 0 \\ f_{g2} \\ -f_{g2}\Delta x_{2,CM2} \\ 0 \\ f_{g3} \\ f_{g3}\Delta x_{3,CM3} \\ 0 \\ 0 \end{bmatrix} \tag{66}$$

3.3.5.12 Type XL – -- C_2 S_3 H_4

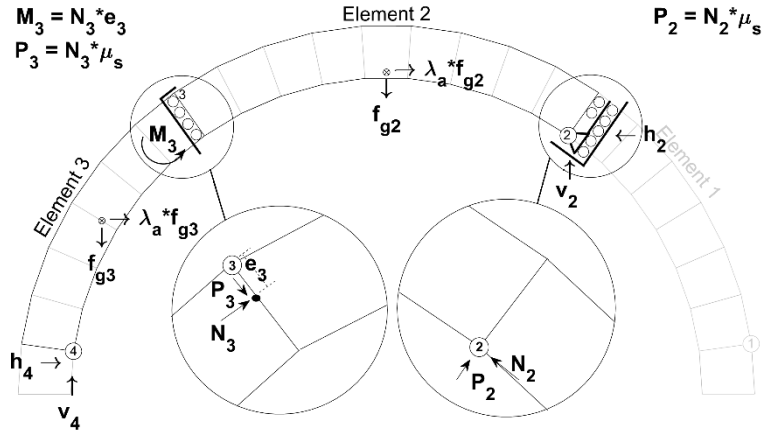

Figure 58. Free-body diagram for the Type XL mechanism

The equations of equilibrium for the condition shown in Figure 58 is

$$[BC] = \begin{bmatrix} -1 & 0 & 1 & 0 & 0 & 0 & f_{g2} & 0 \\ 0 & 1 & 0 & -1 & 0 & 0 & 0 & 0 \\ 0 & 0 & \Delta y_{3,2} & \Delta x_{2,3} & 0 & 0 & -f_{g2}\Delta y_{CM2,2} & -1 \\ 0 & 0 & -1 & 0 & 1 & 0 & f_{g3} & 0 \\ 0 & 0 & 0 & 1 & 0 & 1 & 0 & 0 \\ 0 & 0 & 0 & 0 & \Delta y_{4,3} & \Delta x_{3,4} & f_{g3}\Delta y_{3,CM3} & 1 \\ \tan(\alpha_2) & 1 & 0 & 0 & 0 & 0 & 0 & 0 \\ 0 & 0 & \tan(\alpha_3) & -1 & 0 & 0 & 0 & 0 \end{bmatrix}$$

$$\{r\} = \begin{bmatrix} h_2 \\ v_2 \\ h_2 \\ v_2 \\ h_4 \\ v_4 \\ \lambda_a \\ M_3 \end{bmatrix} \qquad \{q\} = \begin{bmatrix} 0 \\ f_{g2} \\ -f_{g2}\Delta x_{2,CM2} \\ 0 \\ f_{g3} \\ f_{g3}\Delta x_{3,CM3} \\ 0 \\ 0 \end{bmatrix} \tag{67}$$

3.3.5.13 Type XLI – $H_1\ S_2\ C_3$ –

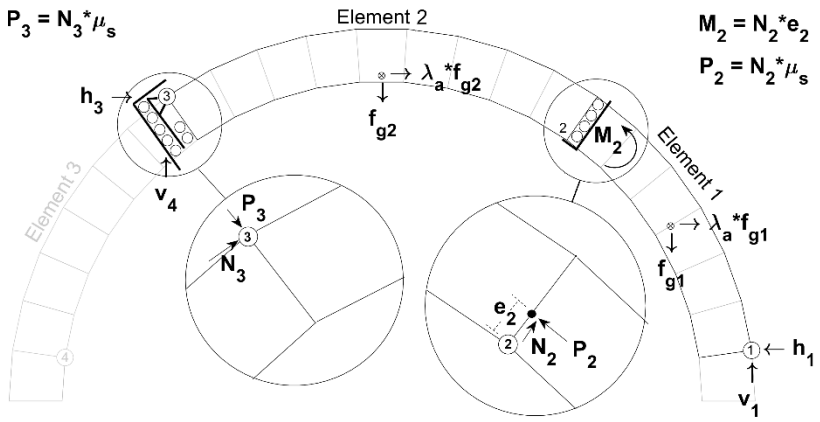

Figure 59. Free-body diagram for the Type XLI mechanism

The equations of equilibrium for the condition shown in Figure 59 is

$$[BC] = \begin{bmatrix} -1 & 0 & 1 & 0 & 0 & 0 & f_{g1} & 0 \\ 0 & 1 & 0 & -1 & 0 & 0 & 0 & 0 \\ 0 & 0 & -\Delta y_{2,1} & \Delta x_{1,2} & 0 & 0 & -f_{g1}\Delta y_{CM1,1} & -1 \\ 0 & 0 & -1 & 0 & 1 & 0 & f_{g2} & 0 \\ 0 & 0 & 0 & 1 & 0 & 1 & 0 & 0 \\ 0 & 0 & 0 & 0 & \Delta y_{3,2} & \Delta x_{2,3} & f_{g2}\Delta y_{2,CM2} & 1 \\ 0 & 0 & 0 & 0 & \tan(\alpha_3) & 1 & 0 & 0 \\ 0 & 0 & \tan(\alpha_2) & -1 & 0 & 0 & 0 & 0 \end{bmatrix}$$

$$\{r\} = \begin{bmatrix} h_1 \\ v_1 \\ h_2 \\ v_2 \\ h_3 \\ v_3 \\ \lambda_a \\ M_2 \end{bmatrix} \qquad \{q\} = \begin{bmatrix} 0 \\ f_{g1} \\ -f_{g1}\Delta x_{1,CM1} \\ 0 \\ f_{g2} \\ f_{g2}\Delta x_{2,CM2} \\ 0 \\ 0 \end{bmatrix} \tag{68}$$

3.3.5.14 Type XLII – S_1 H_2 C_3 –

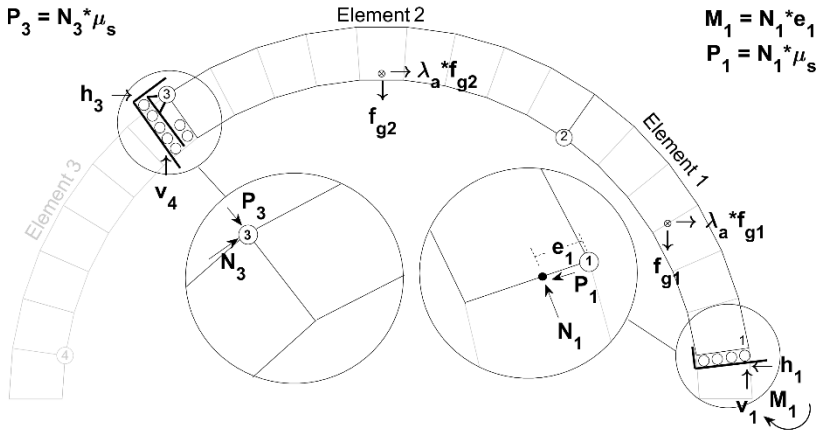

Figure 60. Free-body diagram for the Type XLI mechanism

The equations of equilibrium for the condition shown in Figure 60 is

$$[BC] = \begin{bmatrix} -1 & 0 & 1 & 0 & 0 & 0 & f_{g1} & 0 \\ 0 & 1 & 0 & -1 & 0 & 0 & 0 & 0 \\ 0 & 0 & -\Delta y_{2,1} & \Delta x_{1,2} & 0 & 0 & -f_{g1}\Delta y_{CM1,1} & -1 \\ 0 & 0 & -1 & 0 & 1 & 0 & f_{g2} & 0 \\ 0 & 0 & 0 & 1 & 0 & 1 & 0 & 0 \\ 0 & 0 & 0 & 0 & \Delta y_{3,2} & \Delta x_{2,3} & f_{g2}\Delta y_{2,CM2} & 0 \\ 0 & 0 & 0 & 0 & \tan(\alpha_3) & 1 & 0 & 0 \\ \tan(\alpha_1) & -1 & 0 & 0 & 0 & 0 & 0 & 0 \end{bmatrix}$$

$$\{r\} = \begin{bmatrix} h_1 \\ v_1 \\ h_2 \\ v_2 \\ h_3 \\ v_3 \\ \lambda_a \\ M_1 \end{bmatrix} \qquad \{q\} = \begin{bmatrix} 0 \\ f_{g1} \\ -f_{g1}\Delta x_{1,CM1} \\ 0 \\ f_{g2} \\ f_{g2}\Delta x_{2,CM2} \\ 0 \\ 0 \end{bmatrix} \tag{69}$$

3.3.5.15 Type XLIII – H_1 -- C_3 S_4

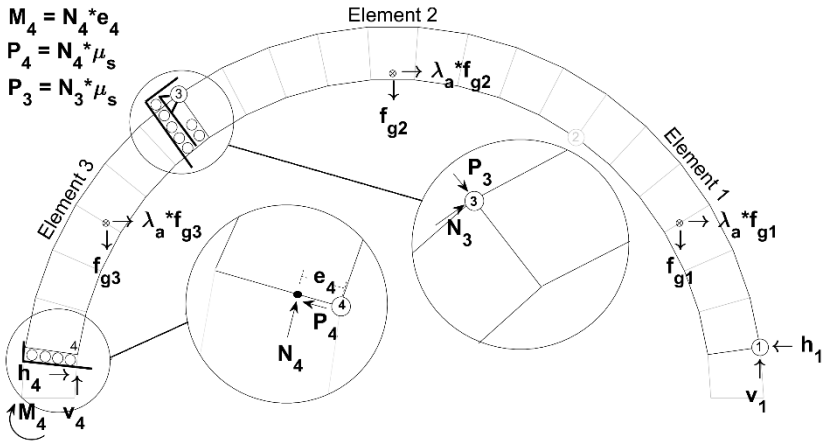

Figure 61. Free-body diagram for the Type XLIII mechanism

The equations of equilibrium for the condition shown in Figure 61 is

$$[BC] = \begin{bmatrix} -1 & 0 & 1 & 0 & 0 & 0 & f_{g1}+f_{g2} & 0 \\ 0 & 1 & 0 & -1 & 0 & 0 & 0 & 0 \\ 0 & 0 & -\Delta y_{3,1} & \Delta x_{1,3} & 0 & 0 & -f_{g1}\Delta y_{CM1,1} - f_{g2}\Delta y_{1,CM2} & 0 \\ 0 & 0 & -1 & 0 & 1 & 0 & f_{g3} & 0 \\ 0 & 0 & 0 & 1 & 0 & 1 & 0 & 0 \\ 0 & 0 & 0 & 0 & \Delta y_{3,2} & \Delta x_{2,3} & f_{g3}\Delta y_{2,CM3} & 1 \\ 0 & 0 & \tan(\alpha_3) & 1 & 0 & 0 & 0 & 0 \\ 0 & 0 & 0 & 0 & \tan(\alpha_4) & -1 & 0 & 0 \end{bmatrix}$$

$$\{r\} = \begin{bmatrix} h_1 \\ v_1 \\ h_3 \\ v_3 \\ h_4 \\ v_4 \\ \lambda_a \\ M_4 \end{bmatrix} \qquad \{q\} = \begin{bmatrix} 0 \\ f_{g1}+f_{g2} \\ -f_{g1}\Delta x_{1,CM1} - f_{g2}\Delta x_{1,CM2} \\ 0 \\ f_{g3} \\ f_{g3}\Delta x_{3,CM3} \\ 0 \\ 0 \end{bmatrix} \tag{70}$$

3.3.5.16 Type XLIV – S_1 -- C_3 H_4

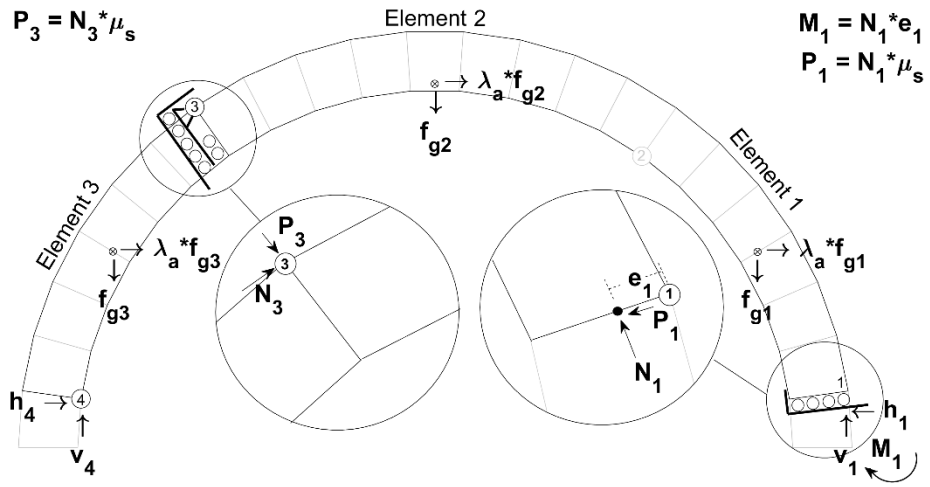

Figure 62. Free-body diagram for the Type XLIII mechanism

The equations of equilibrium for the condition shown in Figure 62 is

$$[BC] = \begin{bmatrix} -1 & 0 & 1 & 0 & 0 & 0 & f_{g1}+f_{g2} & 0 \\ 0 & 1 & 0 & -1 & 0 & 0 & 0 & 0 \\ 0 & 0 & -\Delta y_{3,1} & \Delta x_{1,3} & 0 & 0 & -f_{g1}\Delta y_{CM1,1} - f_{g2}\Delta y_{1,CM2} & -1 \\ 0 & 0 & -1 & 0 & 1 & 0 & f_{g3} & 0 \\ 0 & 0 & 0 & 1 & 0 & 1 & 0 & 0 \\ 0 & 0 & 0 & 0 & \Delta y_{3,2} & \Delta x_{2,3} & f_{g3}\Delta y_{2,CM3} & 0 \\ 0 & 0 & \tan(\alpha_3) & 1 & 0 & 0 & 0 & 0 \\ \tan(\alpha_1) & -1 & 0 & 0 & 0 & 0 & 0 & 0 \end{bmatrix}$$

$$\{r\} = \begin{bmatrix} h_1 \\ v_1 \\ h_3 \\ v_3 \\ h_4 \\ v_4 \\ \lambda_a \\ M_1 \end{bmatrix} \qquad \{q\} = \begin{bmatrix} 0 \\ f_{g1}+f_{g2} \\ -f_{g1}\Delta x_{1,CM1} - f_{g2}\Delta x_{1,CM2} \\ 0 \\ f_{g3} \\ f_{g3}\Delta x_{3,CM3} \\ 0 \\ 0 \end{bmatrix} \tag{71}$$

3.3.5.17 Type XLV – -- H_2 C_3 S_4

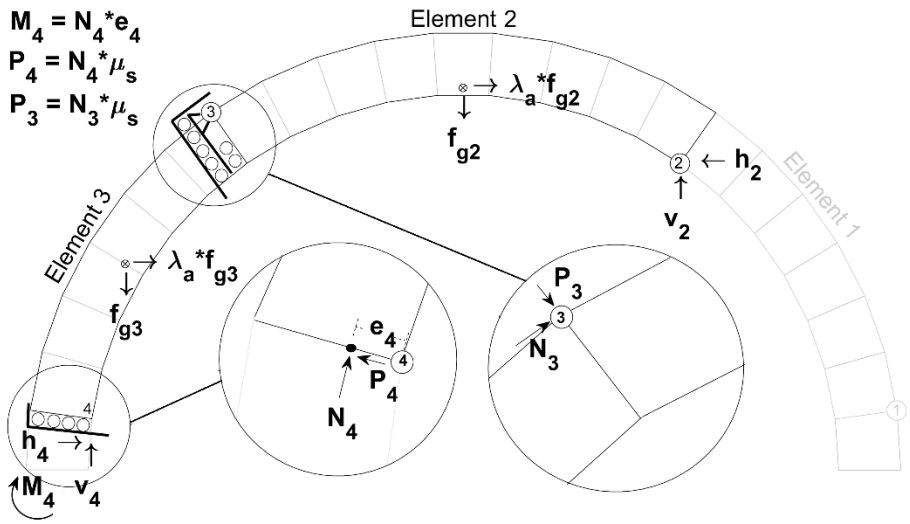

Figure 63. Free-body diagram for the Type XLV mechanism

The equations of equilibrium for the condition shown in Figure 63 is

$$[BC] = \begin{bmatrix} -1 & 0 & 1 & 0 & 0 & 0 & f_{g2} & 0 \\ 0 & 1 & 0 & -1 & 0 & 0 & 0 & 0 \\ 0 & 0 & \Delta y_{3,2} & \Delta x_{2,3} & 0 & 0 & -f_{g2}\Delta y_{CM2,2} & 0 \\ 0 & 0 & -1 & 0 & 1 & 0 & f_{g3} & 0 \\ 0 & 0 & 0 & 1 & 0 & 1 & 0 & 0 \\ 0 & 0 & 0 & 0 & \Delta y_{4,3} & \Delta x_{3,4} & f_{g3}\Delta y_{3,CM3} & 1 \\ 0 & 0 & \tan(\alpha_3) & -1 & 0 & 0 & 0 & 0 \\ 0 & 0 & 0 & 0 & \tan(\alpha_4) & -1 & 0 & 0 \end{bmatrix}$$

$$\{r\} = \begin{bmatrix} h_2 \\ v_2 \\ h_3 \\ v_3 \\ h_4 \\ v_4 \\ \lambda_a \\ M_4 \end{bmatrix} \qquad \{q\} = \begin{bmatrix} 0 \\ f_{g2} \\ -f_{g2}\Delta x_{2,CM2} \\ 0 \\ f_{g3} \\ f_{g3}\Delta x_{3,CM3} \\ 0 \\ 0 \end{bmatrix} \tag{72}$$

3.3.5.18 Type XLVI – -- $S_2\,C_3\,H_4$

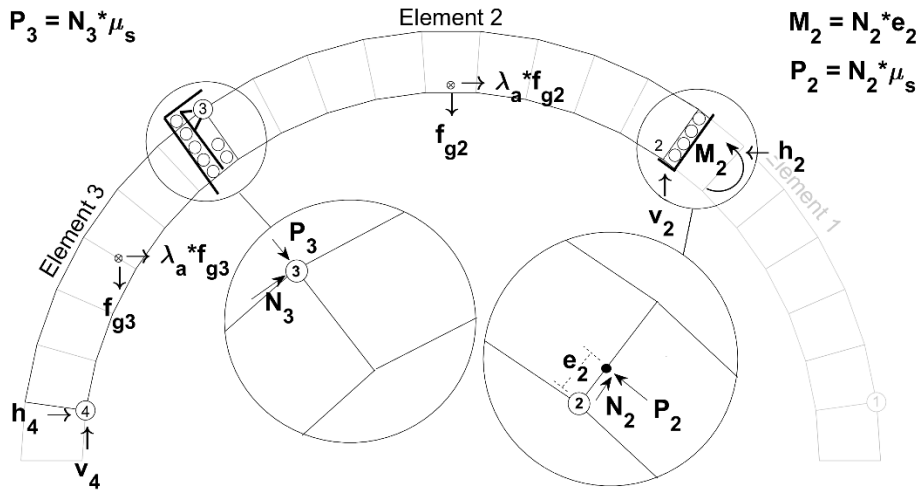

Figure 64. Free-body diagram for the Type XLVI mechanism

The equations of equilibrium for the condition shown in Figure 64 is

$$[BC] = \begin{bmatrix} -1 & 0 & 1 & 0 & 0 & 0 & f_{g2} & 0 \\ 0 & 1 & 0 & -1 & 0 & 0 & 0 & 0 \\ 0 & 0 & \Delta y_{3,2} & \Delta x_{2,3} & 0 & 0 & -f_{g2}\Delta y_{CM2,2} & -1 \\ 0 & 0 & -1 & 0 & 1 & 0 & f_{g3} & 0 \\ 0 & 0 & 0 & 1 & 0 & 1 & 0 & 0 \\ 0 & 0 & 0 & 0 & \Delta y_{4,3} & \Delta x_{3,4} & f_{g3}\Delta y_{3,CM3} & 0 \\ 0 & 0 & \tan(\alpha_3) & -1 & 0 & 0 & 0 & 0 \\ \tan(\alpha_2) & -1 & 0 & 0 & 0 & 0 & 0 & 0 \end{bmatrix}$$

$$\{r\} = \begin{bmatrix} h_2 \\ v_2 \\ h_3 \\ v_3 \\ h_4 \\ v_4 \\ \lambda_a \\ M_2 \end{bmatrix} \qquad \{q\} = \begin{bmatrix} 0 \\ f_{g2} \\ -f_{g2}\Delta x_{2,CM2} \\ 0 \\ f_{g3} \\ f_{g3}\Delta x_{3,CM3} \\ 0 \\ 0 \end{bmatrix} \tag{73}$$

3.3.5.19 Type XLVII – H_1 S_2 -- C_4

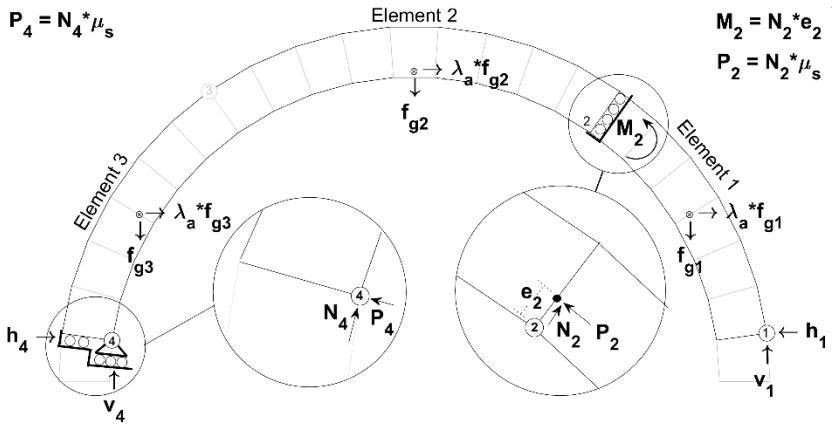

Figure 65. Free-body diagram for the Type XLVII mechanism

The equations of equilibrium for the condition shown in Figure 65 is

$$[BC] = \begin{bmatrix} -1 & 0 & 1 & 0 & 0 & 0 & f_{g1} & 0 \\ 0 & 1 & 0 & -1 & 0 & 0 & 0 & 0 \\ 0 & 0 & -\Delta y_{2,1} & \Delta x_{1,2} & 0 & 0 & -f_{g1}\Delta y_{CM1,1} & -1 \\ 0 & 0 & -1 & 0 & 1 & 0 & f_{g2}+f_{g3} & 0 \\ 0 & 0 & 0 & 1 & 0 & 1 & 0 & 0 \\ 0 & 0 & 0 & 0 & \Delta y_{4,2} & \Delta x_{2,4} & f_{g2}\Delta y_{2,CM2}+f_{g3}\Delta y_{2,CM3} & 1 \\ 0 & 0 & 0 & 0 & \tan(\alpha_4) & 1 & 0 & 0 \\ 0 & 0 & \tan(\alpha_2) & -1 & 0 & 0 & 0 & 0 \end{bmatrix}$$

$$\{r\} = \begin{bmatrix} h_1 \\ v_1 \\ h_2 \\ v_2 \\ h_4 \\ v_4 \\ \lambda_a \\ M_2 \end{bmatrix} \qquad \{q\} = \begin{bmatrix} 0 \\ f_{g1} \\ -f_{g1}\Delta x_{1,CM1} \\ 0 \\ f_{g2}+f_{g3} \\ f_{g2}\Delta x_{2,CM2}+f_{g3}\Delta x_{2,CM3} \\ 0 \\ 0 \end{bmatrix} \tag{74}$$

3.3.5.20 Type XLVIII – S_1 H_2 -- C_4

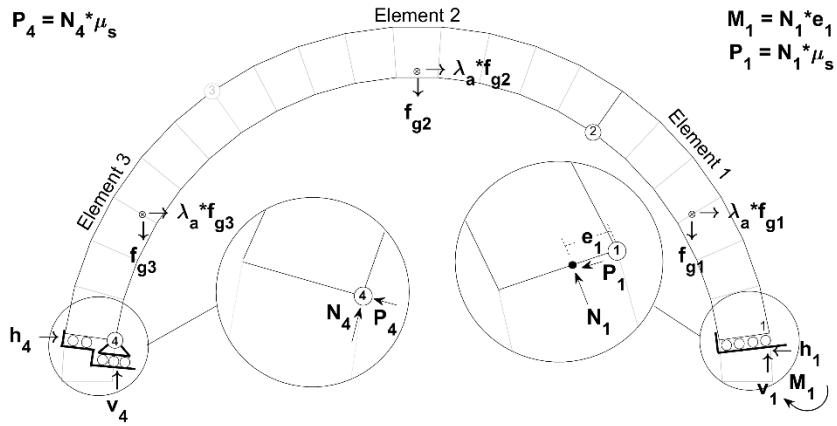

Figure 66. Free-body diagram for the Type XLVIII mechanism

The equations of equilibrium for the condition shown in Figure 66 is

$$[BC] = \begin{bmatrix} -1 & 0 & 1 & 0 & 0 & 0 & f_{g1} & 0 \\ 0 & 1 & 0 & -1 & 0 & 0 & 0 & 0 \\ 0 & 0 & -\Delta y_{2,1} & \Delta x_{1,2} & 0 & 0 & -f_{g1}\Delta y_{CM1,1} & -1 \\ 0 & 0 & -1 & 0 & 1 & 0 & f_{g2}+f_{g3} & 0 \\ 0 & 0 & 0 & 1 & 0 & 1 & 0 & 0 \\ 0 & 0 & 0 & 0 & \Delta y_{4,2} & \Delta x_{2,4} & f_{g2}\Delta y_{2,CM2}+f_{g3}\Delta y_{2,CM3} & 0 \\ 0 & 0 & 0 & 0 & \tan(\alpha_4) & 1 & 0 & 0 \\ \tan(\alpha_1) & -1 & 0 & 0 & 0 & 0 & 0 & 0 \end{bmatrix}$$

$$\{r\} = \begin{bmatrix} h_1 \\ v_1 \\ h_2 \\ v_2 \\ h_4 \\ v_4 \\ \lambda_a \\ M_1 \end{bmatrix} \qquad \{q\} = \begin{bmatrix} 0 \\ f_{g1} \\ -f_{g1}\Delta x_{1,CM1} \\ 0 \\ f_{g2}+f_{g3} \\ f_{g2}\Delta x_{2,CM2}+f_{g3}\Delta x_{2,CM3} \\ 0 \\ 0 \end{bmatrix} \tag{75}$$

3.3.5.21 Type XLIX – H_1 -- S_3 C_4

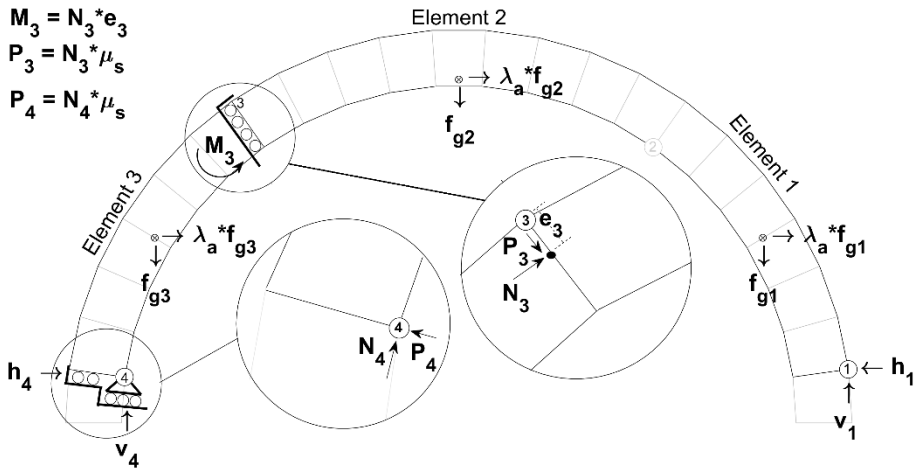

Figure 67. Free-body diagram for the Type XLIX mechanism

The equations of equilibrium for the condition shown in Figure 67 is

$$[BC] = \begin{bmatrix} -1 & 0 & 1 & 0 & 0 & 0 & f_{g1}+f_{g2} & 0 \\ 0 & 1 & 0 & -1 & 0 & 0 & 0 & 0 \\ 0 & 0 & -\Delta y_{3,1} & \Delta x_{1,3} & 0 & 0 & -f_{g1}\Delta y_{CM1,1} - f_{g2}\Delta y_{1,CM2} & 1 \\ 0 & 0 & -1 & 0 & 1 & 0 & f_{g3} & 0 \\ 0 & 0 & 0 & 1 & 0 & 1 & 0 & 0 \\ 0 & 0 & 0 & 0 & \Delta y_{3,2} & \Delta x_{2,3} & f_{g3}\Delta y_{2,CM3} & -1 \\ 0 & 0 & 0 & 0 & \tan(\alpha_4) & 1 & 0 & 0 \\ 0 & 0 & \tan(\alpha_3) & -1 & 0 & 0 & 0 & 0 \end{bmatrix}$$

$$\{r\} = \begin{bmatrix} h_1 \\ v_1 \\ h_3 \\ v_3 \\ h_4 \\ v_4 \\ \lambda_a \\ M_3 \end{bmatrix} \qquad \{q\} = \begin{bmatrix} 0 \\ f_{g1}+f_{g2} \\ -f_{g1}\Delta x_{1,CM1} - f_{g2}\Delta x_{1,CM2} \\ 0 \\ f_{g3} \\ f_{g3}\Delta x_{3,CM3} \\ 0 \\ 0 \end{bmatrix} \tag{76}$$

3.3.5.22 Type L – S_1 -- H_3 C_4

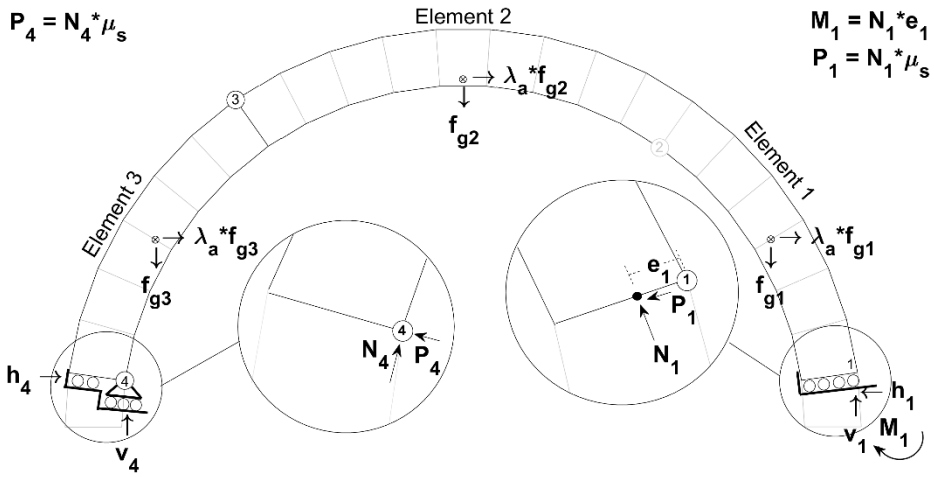

Figure 68. Free-body diagram for the Type L mechanism

The equations of equilibrium for the condition shown in Figure 68 is

$$[BC] = \begin{bmatrix} -1 & 0 & 1 & 0 & 0 & 0 & f_{g1}+f_{g2} & 0 \\ 0 & 1 & 0 & -1 & 0 & 0 & 0 & 0 \\ 0 & 0 & -\Delta y_{3,1} & \Delta x_{1,3} & 0 & 0 & -f_{g1}\Delta y_{CM1,1} - f_{g2}\Delta y_{1,CM2} & -1 \\ 0 & 0 & -1 & 0 & 1 & 0 & f_{g3} & 0 \\ 0 & 0 & 0 & 1 & 0 & 1 & 0 & 0 \\ 0 & 0 & 0 & 0 & \Delta y_{3,2} & \Delta x_{2,3} & f_{g3}\Delta y_{2,CM3} & 0 \\ 0 & 0 & 0 & 0 & \tan(\alpha_4) & 1 & 0 & 0 \\ \tan(\alpha_1) & -1 & 0 & 0 & 0 & 0 & 0 & 0 \end{bmatrix}$$

$$\{r\} = \begin{bmatrix} h_1 \\ v_1 \\ h_3 \\ v_3 \\ h_4 \\ v_4 \\ \lambda_a \\ M_1 \end{bmatrix} \qquad \{q\} = \begin{bmatrix} 0 \\ f_{g1}+f_{g2} \\ -f_{g1}\Delta x_{1,CM1} - f_{g2}\Delta x_{1,CM2} \\ 0 \\ f_{g3} \\ f_{g3}\Delta x_{3,CM3} \\ 0 \\ 0 \end{bmatrix} \tag{77}$$

3.3.5.23 Type LI – -- H_2 S_3 C_4

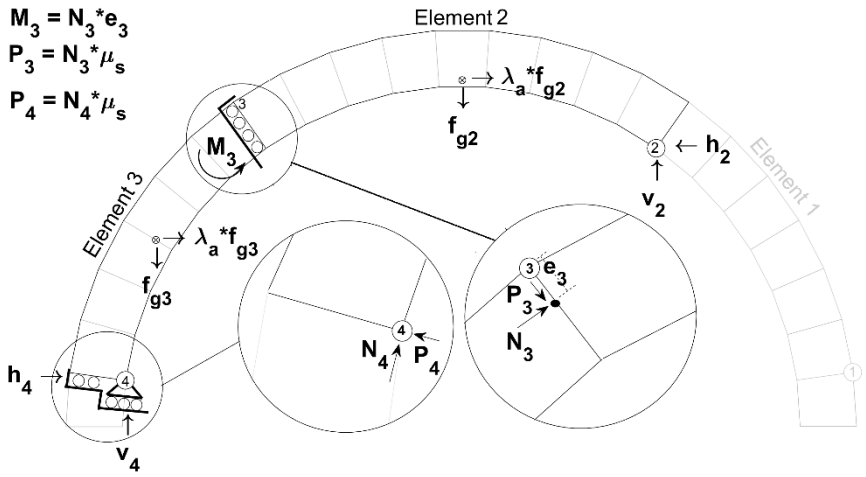

Figure 69. Free-body diagram for the Type LI mechanism

The equations of equilibrium for the condition shown in Figure 69 is

$$[BC] = \begin{bmatrix} -1 & 0 & 1 & 0 & 0 & 0 & f_{g2} & 0 \\ 0 & 1 & 0 & -1 & 0 & 0 & 0 & 0 \\ 0 & 0 & -\Delta y_{3,2} & \Delta x_{2,3} & 0 & 0 & -f_{g2}\Delta y_{1,CM2} & -1 \\ 0 & 0 & -1 & 0 & 1 & 0 & f_{g3} & 0 \\ 0 & 0 & 0 & 1 & 0 & 1 & 0 & 0 \\ 0 & 0 & 0 & 0 & \Delta y_{4,3} & \Delta x_{3,4} & f_{g3}\Delta y_{3,CM3} & 1 \\ 0 & 0 & 0 & 0 & \tan(\alpha_4) & 1 & 0 & 0 \\ 0 & 0 & \tan(\alpha_3) & -1 & 0 & 0 & 0 & 0 \end{bmatrix}$$

$$\{r\} = \begin{bmatrix} h_2 \\ v_2 \\ h_3 \\ v_3 \\ h_4 \\ v_4 \\ \lambda_a \\ M_3 \end{bmatrix} \qquad \{q\} = \begin{bmatrix} 0 \\ f_{g2} \\ -f_{g2}\Delta x_{2,CM2} \\ 0 \\ f_{g3} \\ f_{g3}\Delta x_{3,CM3} \\ 0 \\ 0 \end{bmatrix} \tag{78}$$

3.3.5.24 Type LII – -- S_2 H_3 C_4

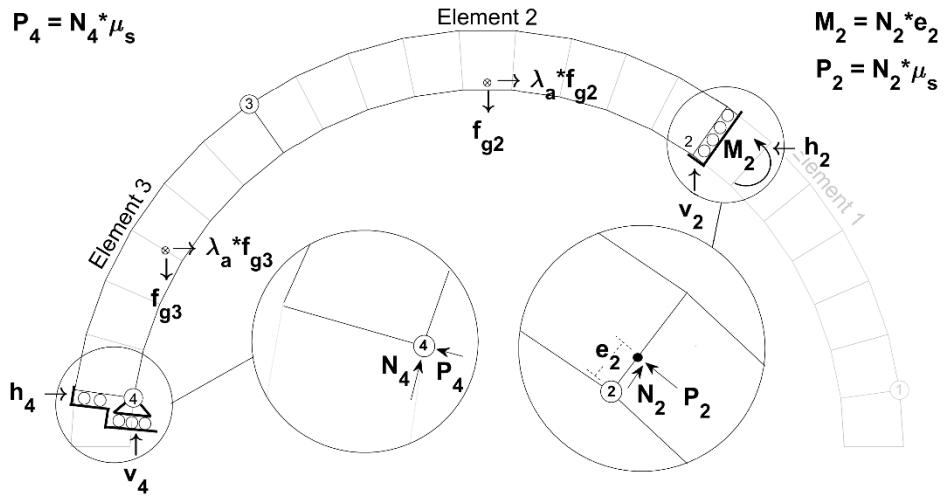

Figure 70. Free-body diagram for the Type LII mechanism

The equations of equilibrium for the condition shown in Figure 70 is

$$[BC] = \begin{bmatrix} -1 & 0 & 1 & 0 & 0 & 0 & f_{g2} & 0 \\ 0 & 1 & 0 & -1 & 0 & 0 & 0 & 0 \\ 0 & 0 & -\Delta y_{3,2} & \Delta x_{2,3} & 0 & 0 & -f_{g2}\Delta y_{1,CM2} & 1 \\ 0 & 0 & -1 & 0 & 1 & 0 & f_{g3} & 0 \\ 0 & 0 & 0 & 1 & 0 & 1 & 0 & 0 \\ 0 & 0 & 0 & 0 & \Delta y_{4,3} & \Delta x_{3,4} & f_{g3}\Delta y_{3,CM3} & 0 \\ 0 & 0 & 0 & 0 & \tan(\alpha_4) & 1 & 0 & 0 \\ \tan(\alpha_2) & -1 & 0 & 0 & 0 & 0 & 0 & 0 \end{bmatrix}$$

$$\{r\} = \begin{bmatrix} h_2 \\ v_2 \\ h_3 \\ v_3 \\ h_4 \\ v_4 \\ \lambda_a \\ M_2 \end{bmatrix} \qquad \{q\} = \begin{bmatrix} 0 \\ f_{g2} \\ -f_{g2}\Delta x_{2,CM2} \\ 0 \\ f_{g3} \\ f_{g3}\Delta x_{3,CM3} \\ 0 \\ 0 \end{bmatrix} \tag{79}$$

3.3.6 Combined-Slip Mechanisms

The combined-slip mechanisms take the reduced structure of the combined-hinge mechanisms and replaces both of the non-combined mechanical joints with slip translation.

Mechanisms Type LIII through LV assign C_1 in exchange of slip S_4, S_3 and S_2 respectively. Mechanisms Type LVI through LVIII assign C_2 in exchange of slip S_4, S_3 and S_1 respectively. Mechanisms Type LIX through LXI assign C_3 in exchange of slip S_4, S_2 and S_1 respectively. Lastly, mechanisms Type LXII through LXIV assign C_4 in exchange of slip S_3, S_2 and S_1 respectively.

3.3.6.1 Type LIII – C_1 S_2 S_3 –

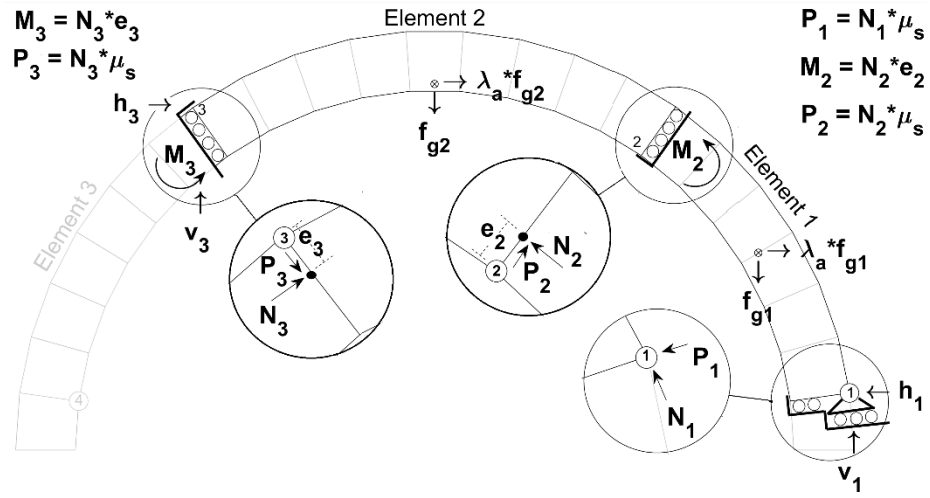

Figure 71. Free-body diagram for the Type LIII mechanism

The equations of equilibrium for the condition shown in Figure 71 is

$$[BC] = \begin{bmatrix} -1 & 0 & 1 & 0 & 0 & 0 & f_{g1} & 0 & 0 \\ 0 & 1 & 0 & -1 & 0 & 0 & 0 & 0 & 0 \\ 0 & 0 & -\Delta y_{2,1} & \Delta x_{1,2} & 0 & 0 & -f_{g1}\Delta y_{1,CM1} & -1 & 0 \\ 0 & 0 & -1 & 0 & 1 & 0 & f_{g2} & 0 & 0 \\ 0 & 0 & 0 & 1 & 0 & 1 & 0 & 0 & 0 \\ 0 & 0 & 0 & 0 & \Delta y_{3,2} & \Delta x_{2,3} & f_{g2}\Delta y_{2,CM2} & 1 & -1 \\ \tan(\alpha_1) & -1 & 0 & 0 & 0 & 0 & 0 & 0 & 0 \\ 0 & 0 & \tan(\alpha_2) & -1 & 0 & 0 & 0 & 0 & 0 \\ 0 & 0 & 0 & 0 & \tan(\alpha_3) & -1 & 0 & 0 & 0 \end{bmatrix}$$

$$\{r\} = \begin{bmatrix} h_1 \\ v_1 \\ h_2 \\ v_2 \\ h_3 \\ v_3 \\ \lambda_a \\ M_2 \\ M_3 \end{bmatrix} \qquad \{q\} = \begin{bmatrix} 0 \\ f_{g1} \\ -f_{g1}\Delta x_{1,CM1} \\ 0 \\ f_{g2} \\ f_{g2}\Delta x_{2,CM2} \\ 0 \\ 0 \\ 0 \end{bmatrix} \tag{80}$$

3.3.6.2 Type LIV – C_1 S_2 -- S_4

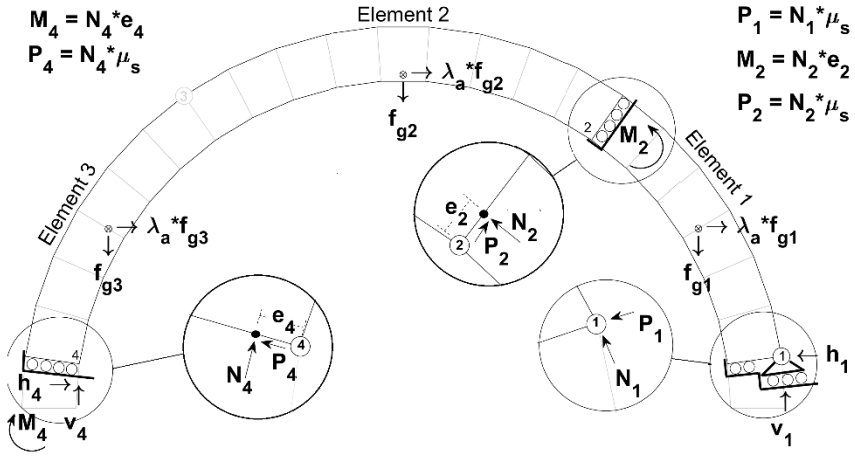

Figure 72. Free-body diagram for the Type LIV mechanism

The equations of equilibrium for the condition shown in Figure 72 is

$$[BC] = \begin{bmatrix} -1 & 0 & 1 & 0 & 0 & 0 & f_{g1} & 0 & 0 \\ 0 & 1 & 0 & -1 & 0 & 0 & 0 & 0 & 0 \\ 0 & 0 & -\Delta y_{2,1} & \Delta x_{1,2} & 0 & 0 & -f_{g1}\Delta y_{1,CM1} & -1 & 0 \\ 0 & 0 & -1 & 0 & 1 & 0 & f_{g2}+f_{g3} & 0 & 0 \\ 0 & 0 & 0 & 1 & 0 & 1 & 0 & 0 & 0 \\ 0 & 0 & 0 & 0 & \Delta y_{4,2} & \Delta x_{2,4} & f_{g2}\Delta y_{2,CM2}+f_{g3}\Delta y_{2,CM3} & 1 & -1 \\ \tan(\alpha_1) & -1 & 0 & 0 & 0 & 0 & 0 & 0 & 0 \\ 0 & 0 & \tan(\alpha_2) & -1 & 0 & 0 & 0 & 0 & 0 \\ 0 & 0 & 0 & 0 & \tan(\alpha_4) & -1 & 0 & 0 & 0 \end{bmatrix}$$

$$\{r\} = \begin{bmatrix} h_1 \\ v_1 \\ h_2 \\ v_2 \\ h_4 \\ v_4 \\ \lambda_a \\ M_2 \\ M_4 \end{bmatrix} \qquad \{q\} = \begin{bmatrix} 0 \\ f_{g1} \\ -f_{g1}\Delta x_{1,CM1} \\ 0 \\ f_{g2}+f_{g3} \\ f_{g2}\Delta x_{2,CM2}+f_{g3}\Delta x_{2,CM3} \\ 0 \\ 0 \\ 0 \end{bmatrix} \tag{81}$$

3.3.6.3 Type LV – C_1 -- S_3 S_4

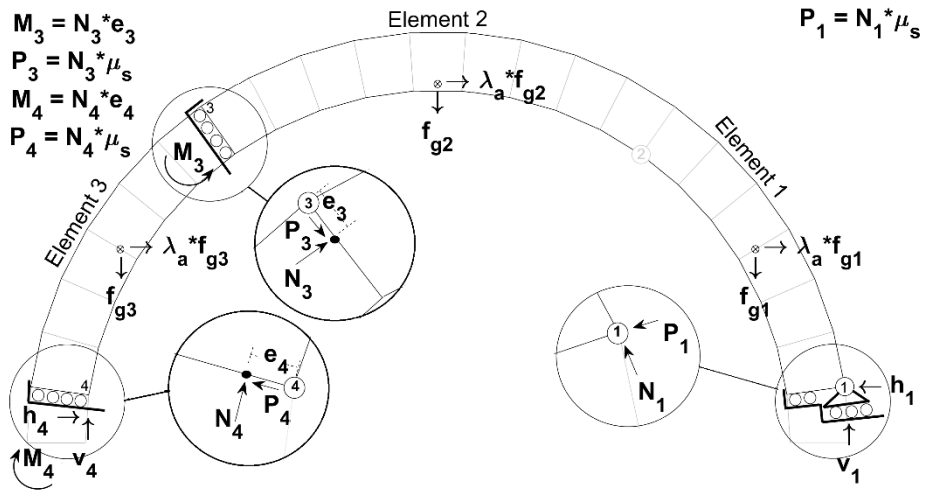

Figure 73. Free-body diagram for the Type LV mechanism

The equations of equilibrium for the condition shown in Figure 73 is

$$[BC] = \begin{bmatrix} -1 & 0 & 1 & 0 & 0 & 0 & f_{g1}+f_{g2} & 0 & 0 \\ 0 & 1 & 0 & -1 & 0 & 0 & 0 & 0 & 0 \\ 0 & 0 & -\Delta y_{3,1} & \Delta x_{1,3} & 0 & 0 & -f_{g1}\Delta y_{1,CM1} - f_{g2}\Delta y_{1,CM2} & -1 & 0 \\ 0 & 0 & -1 & 0 & 1 & 0 & f_{g3} & 0 & 0 \\ 0 & 0 & 0 & 1 & 0 & 1 & 0 & 0 & 0 \\ 0 & 0 & 0 & 0 & \Delta y_{4,3} & \Delta x_{3,4} & f_{g3}\Delta y_{3,CM3} & 1 & -1 \\ \tan(\alpha_1) & -1 & 0 & 0 & 0 & 0 & 0 & 0 & 0 \\ 0 & 0 & \tan(\alpha_3) & -1 & 0 & 0 & 0 & 0 & 0 \\ 0 & 0 & 0 & 0 & \tan(\alpha_4) & -1 & 0 & 0 & 0 \end{bmatrix}$$

$$\{r\} = \begin{bmatrix} h_1 \\ v_1 \\ h_3 \\ v_3 \\ h_4 \\ v_4 \\ \lambda_a \\ M_3 \\ M_4 \end{bmatrix} \qquad \{q\} = \begin{bmatrix} 0 \\ f_{g1}+f_{g2} \\ -f_{g1}\Delta x_{1,CM1} - f_{g2}\Delta x_{1,CM2} \\ 0 \\ f_{g2}+f_{g3} \\ f_{g3}\Delta x_{3,CM3} \\ 0 \\ 0 \\ 0 \end{bmatrix} \tag{82}$$

3.3.6.4 Type LVI – $S_1\ C_2\ S_3$ –

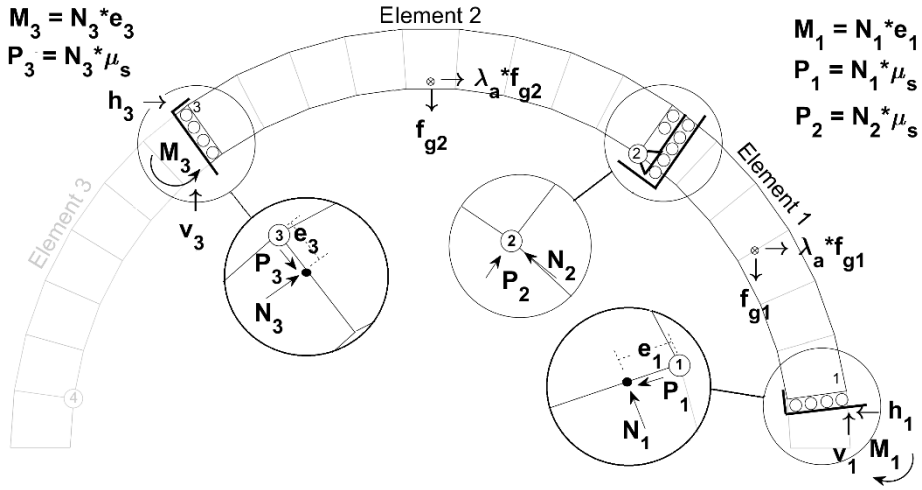

Figure 74. Free-body diagram for the Type LVI mechanism

The equations of equilibrium for the condition shown in Figure 74 is

$$[BC] = \begin{bmatrix} -1 & 0 & 1 & 0 & 0 & 0 & f_{g1} & 0 & 0 \\ 0 & 1 & 0 & -1 & 0 & 0 & 0 & 0 & 0 \\ 0 & 0 & -\Delta y_{2,1} & \Delta x_{1,2} & 0 & 0 & -f_{g1}\Delta y_{1,CM1} & -1 & 0 \\ 0 & 0 & -1 & 0 & 1 & 0 & f_{g2} & 0 & 0 \\ 0 & 0 & 0 & 1 & 0 & 1 & 0 & 0 & 0 \\ 0 & 0 & 0 & 0 & \Delta y_{3,2} & \Delta x_{2,3} & f_{g2}\Delta y_{2,CM2} & 0 & -1 \\ 0 & 0 & \tan(\alpha_2) & -1 & 0 & 0 & 0 & 0 & 0 \\ \tan(\alpha_1) & -1 & 0 & 0 & 0 & 0 & 0 & 0 & 0 \\ 0 & 0 & 0 & 0 & \tan(\alpha_3) & -1 & 0 & 0 & 0 \end{bmatrix}$$

$$\{r\} = \begin{bmatrix} h_1 \\ v_1 \\ h_2 \\ v_2 \\ h_3 \\ v_3 \\ \lambda_a \\ M_1 \\ M_3 \end{bmatrix} \qquad \{q\} = \begin{bmatrix} 0 \\ f_{g1} \\ -f_{g1}\Delta x_{1,CM1} \\ 0 \\ f_{g2} \\ f_{g2}\Delta x_{2,CM2} \\ 0 \\ 0 \\ 0 \end{bmatrix} \tag{83}$$

3.3.6.5 Type LVII – S_1 C_2 -- S_4

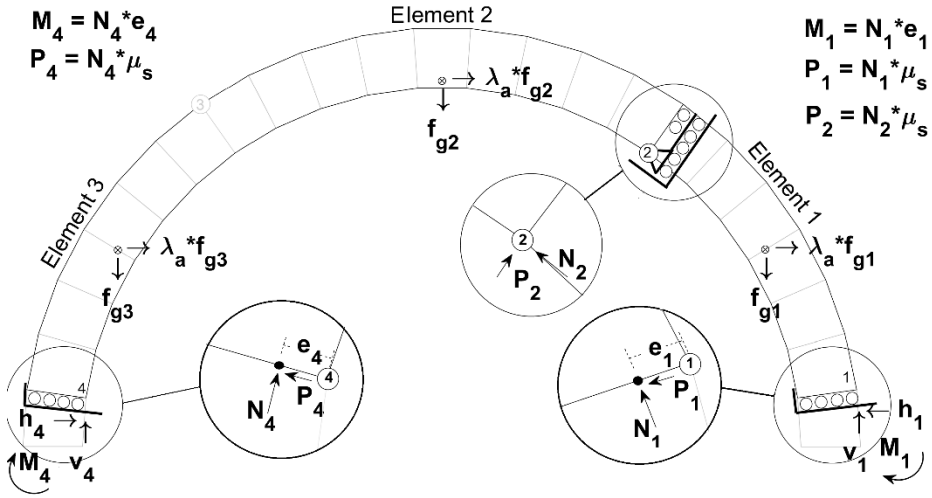

Figure 75. Free-body diagram for the Type LVII mechanism

The equations of equilibrium for the condition shown in Figure 75 is

$$[BC] = \begin{bmatrix} -1 & 0 & 1 & 0 & 0 & 0 & f_{g1} & 0 & 0 \\ 0 & 1 & 0 & -1 & 0 & 0 & 0 & 0 & 0 \\ 0 & 0 & -\Delta y_{2,1} & \Delta x_{1,2} & 0 & 0 & -f_{g1}\Delta y_{1,CM1} & -1 & 0 \\ 0 & 0 & -1 & 0 & 1 & 0 & f_{g2}+f_{g3} & 0 & 0 \\ 0 & 0 & 0 & 1 & 0 & 1 & 0 & 0 & 0 \\ 0 & 0 & 0 & 0 & \Delta y_{4,2} & \Delta x_{2,4} & f_{g2}\Delta y_{2,CM2}+f_{g3}\Delta y_{2,CM3} & 0 & -1 \\ 0 & 0 & \tan(\alpha_2) & -1 & 0 & 0 & 0 & 0 & 0 \\ \tan(\alpha_1) & -1 & 0 & 0 & 0 & 0 & 0 & 0 & 0 \\ 0 & 0 & 0 & 0 & \tan(\alpha_4) & -1 & 0 & 0 & 0 \end{bmatrix}$$

$$\{r\} = \begin{bmatrix} h_1 \\ v_1 \\ h_2 \\ v_2 \\ h_4 \\ v_4 \\ \lambda_a \\ M_1 \\ M_4 \end{bmatrix} \qquad \{q\} = \begin{bmatrix} 0 \\ f_{g1} \\ -f_{g1}\Delta x_{1,CM1} \\ 0 \\ f_{g2}+f_{g3} \\ f_{g2}\Delta x_{2,CM2}+f_{g3}\Delta x_{2,CM3} \\ 0 \\ 0 \\ 0 \end{bmatrix} \tag{84}$$

3.3.6.6 Type LVIII – -- C_2 S_3 S_4

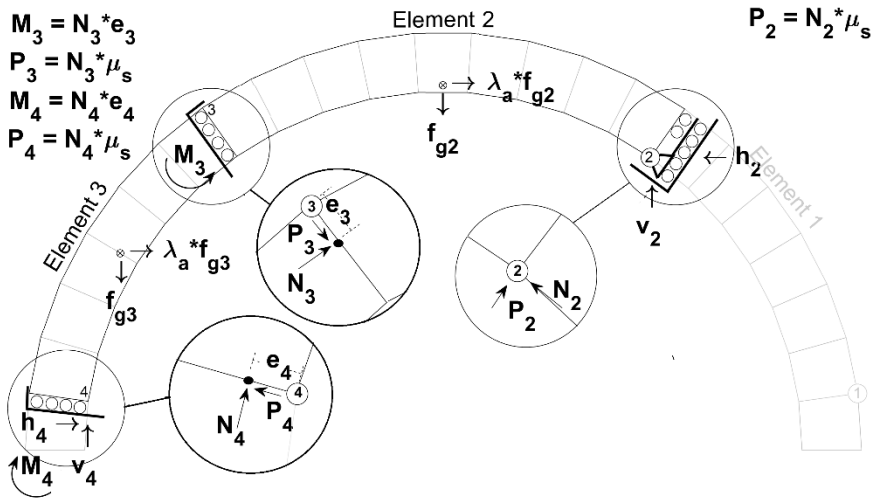

Figure 76. Free-body diagram for the Type LVIII mechanism

The equations of equilibrium for the condition shown in Figure 76 is

$$[BC] = \begin{bmatrix} -1 & 0 & 1 & 0 & 0 & 0 & f_{g2} & 0 & 0 \\ 0 & 1 & 0 & -1 & 0 & 0 & 0 & 0 & 0 \\ 0 & 0 & \Delta y_{3,2} & \Delta x_{2,3} & 0 & 0 & f_{g2}\Delta y_{2,CM2} & -1 & 0 \\ 0 & 0 & -1 & 0 & 1 & 0 & f_{g3} & 0 & 0 \\ 0 & 0 & 0 & 1 & 0 & 1 & 0 & 0 & 0 \\ 0 & 0 & 0 & 0 & \Delta y_{4,3} & \Delta x_{3,4} & f_{g3}\Delta y_{3,CM3} & 1 & -1 \\ \tan(\alpha_2) & -1 & 0 & 0 & 0 & 0 & 0 & 0 & 0 \\ 0 & 0 & \tan(\alpha_3) & -1 & 0 & 0 & 0 & 0 & 0 \\ 0 & 0 & 0 & 0 & \tan(\alpha_4) & -1 & 0 & 0 & 0 \end{bmatrix}$$

$$\{r\} = \begin{bmatrix} h_2 \\ v_2 \\ h_3 \\ v_3 \\ h_4 \\ v_4 \\ \lambda_a \\ M_3 \\ M_4 \end{bmatrix} \qquad \{q\} = \begin{bmatrix} 0 \\ f_{g2} \\ -f_{g2}\Delta x_{2,CM2} \\ 0 \\ f_{g3} \\ f_{g3}\Delta x_{3,CM3} \\ 0 \\ 0 \\ 0 \end{bmatrix} \tag{85}$$

3.3.6.7 Type LIX – $S_1\ S_2\ C_3$ –

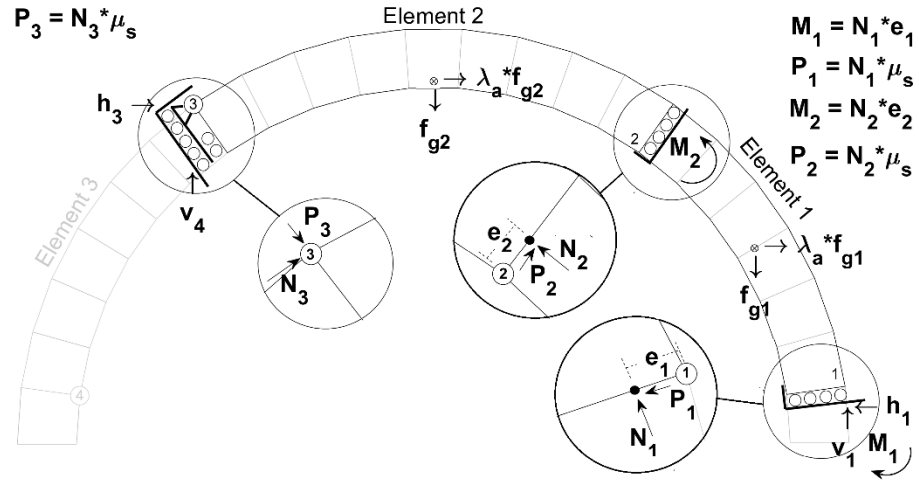

Figure 77. Free-body diagram for the Type LIX mechanism

The equations of equilibrium for the condition shown in Figure 77 is

$$[BC] = \begin{bmatrix} -1 & 0 & 1 & 0 & 0 & 0 & f_{g1} & 0 & 0 \\ 0 & 1 & 0 & -1 & 0 & 0 & 0 & 0 & 0 \\ 0 & 0 & -\Delta y_{2,1} & \Delta x_{1,2} & 0 & 0 & -f_{g1}\Delta y_{1,CM1} & -1 & 1 \\ 0 & 0 & -1 & 0 & 1 & 0 & f_{g2} & 0 & 0 \\ 0 & 0 & 0 & 1 & 0 & 1 & 0 & 0 & 0 \\ 0 & 0 & 0 & 0 & \Delta y_{3,2} & \Delta x_{2,3} & f_{g2}\Delta y_{2,CM2} & 0 & -1 \\ 0 & 0 & 0 & -1 & \tan(\alpha_3) & -1 & 0 & 0 & 0 \\ \tan(\alpha_1) & -1 & 0 & 0 & 0 & 0 & 0 & 0 & 0 \\ 0 & 0 & \tan(\alpha_2) & -1 & 0 & 0 & 0 & 0 & 0 \end{bmatrix}$$

$$\{r\} = \begin{bmatrix} h_1 \\ v_1 \\ h_2 \\ v_2 \\ h_3 \\ v_3 \\ \lambda_a \\ M_1 \\ M_2 \end{bmatrix} \qquad \{q\} = \begin{bmatrix} 0 \\ f_{g1} \\ -f_{g1}\Delta x_{1,CM1} \\ 0 \\ f_{g2} \\ f_{g2}\Delta x_{2,CM2} \\ 0 \\ 0 \\ 0 \end{bmatrix} \tag{86}$$

3.3.6.8 Type LX – S_1 -- C_3 S_4

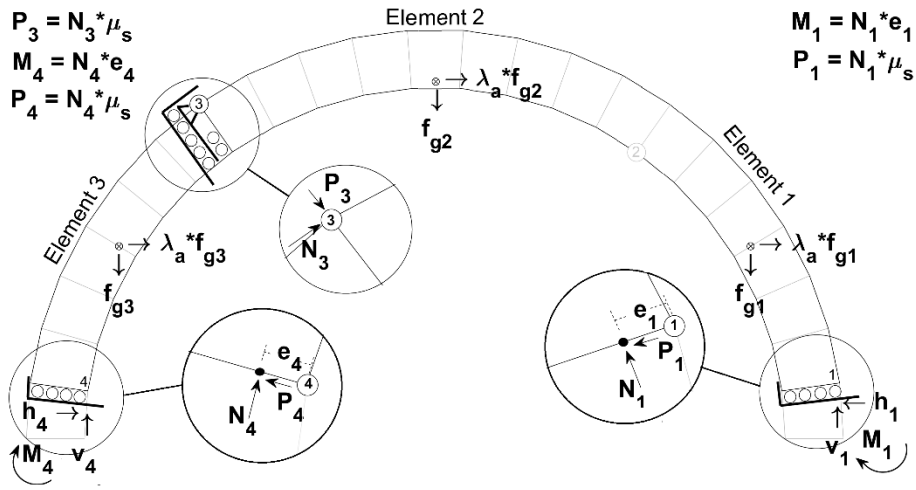

Figure 78. Free-body diagram for the Type LX mechanism

The equations of equilibrium for the condition shown in Figure 78 is

$$[BC] = \begin{bmatrix} -1 & 0 & 1 & 0 & 0 & 0 & f_{g1}+f_{g2} & 0 & 0 \\ 0 & 1 & 0 & -1 & 0 & 0 & 0 & 0 & 0 \\ 0 & 0 & -\Delta y_{3,1} & \Delta x_{1,3} & 0 & 0 & -f_{g1}\Delta y_{1,CM1} - f_{g2}\Delta y_{1,CM2} & -1 & 0 \\ 0 & 0 & -1 & 0 & 1 & 0 & f_{g3} & 0 & 0 \\ 0 & 0 & 0 & 1 & 0 & 1 & 0 & 0 & 0 \\ 0 & 0 & 0 & 0 & \Delta y_{4,3} & \Delta x_{3,4} & f_{g3}\Delta y_{3,CM3} & 0 & -1 \\ 0 & 0 & \tan(\alpha_3) & -1 & 0 & 0 & 0 & 0 & 0 \\ \tan(\alpha_1) & -1 & 0 & 0 & 0 & 0 & 0 & 0 & 0 \\ 0 & 0 & 0 & 0 & \tan(\alpha_4) & -1 & 0 & 0 & 0 \end{bmatrix}$$

$$\{r\} = \begin{bmatrix} h_1 \\ v_1 \\ h_3 \\ v_3 \\ h_4 \\ v_4 \\ \lambda_a \\ M_1 \\ M_4 \end{bmatrix} \qquad \{q\} = \begin{bmatrix} 0 \\ f_{g1}+f_{g2} \\ -f_{g1}\Delta x_{1,CM1} - f_{g2}\Delta x_{1,CM2} \\ 0 \\ f_{g2}+f_{g3} \\ f_{g3}\Delta x_{3,CM3} \\ 0 \\ 0 \\ 0 \end{bmatrix} \tag{87}$$

3.3.6.9 Type LXI – -- S_2 C_3 S_4

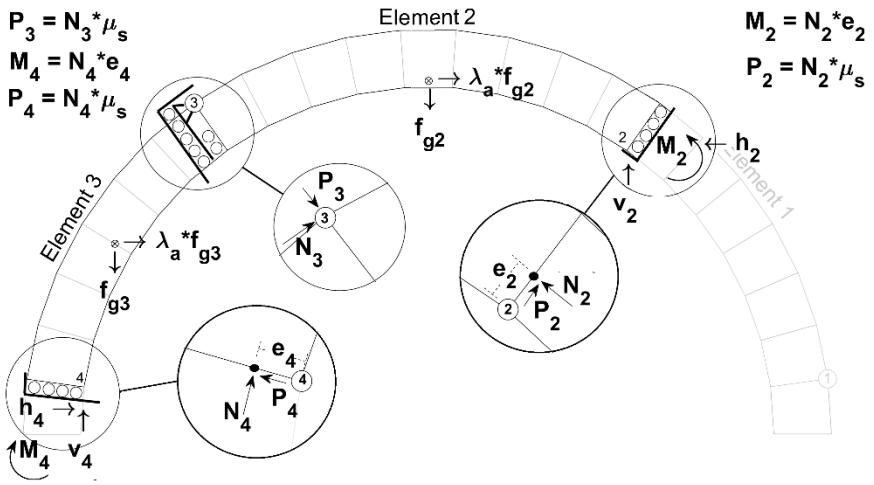

Figure 79. Free-body diagram for the Type LXI mechanism

The equations of equilibrium for the condition shown in Figure 79 is

$$[BC] = \begin{bmatrix} -1 & 0 & 1 & 0 & 0 & 0 & f_{g2} & 0 & 0 \\ 0 & 1 & 0 & -1 & 0 & 0 & 0 & 0 & 0 \\ 0 & 0 & \Delta y_{3,2} & \Delta x_{2,3} & 0 & 0 & f_{g2}\Delta y_{2,CM2} & -1 & 0 \\ 0 & 0 & -1 & 0 & 1 & 0 & f_{g3} & 0 & 0 \\ 0 & 0 & 0 & 1 & 0 & 1 & 0 & 0 & 0 \\ 0 & 0 & 0 & 0 & \Delta y_{4,3} & \Delta x_{3,4} & f_{g3}\Delta y_{3,CM3} & 0 & -1 \\ 0 & 0 & \tan(\alpha_3) & -1 & 0 & 0 & 0 & 0 & 0 \\ \tan(\alpha_2) & -1 & 0 & 0 & 0 & 0 & 0 & 0 & 0 \\ 0 & 0 & 0 & 0 & \tan(\alpha_4) & -1 & 0 & 0 & 0 \end{bmatrix}$$

$$\{r\} = \begin{bmatrix} h_2 \\ v_2 \\ h_3 \\ v_3 \\ h_4 \\ v_4 \\ \lambda_a \\ M_2 \\ M_4 \end{bmatrix} \qquad \{q\} = \begin{bmatrix} 0 \\ f_{g2} \\ -f_{g2}\Delta x_{2,CM2} \\ 0 \\ f_{g3} \\ f_{g3}\Delta x_{3,CM3} \\ 0 \\ 0 \\ 0 \end{bmatrix} \tag{88}$$

3.3.6.10 Type LXII – S_1 S_2 -- C_4

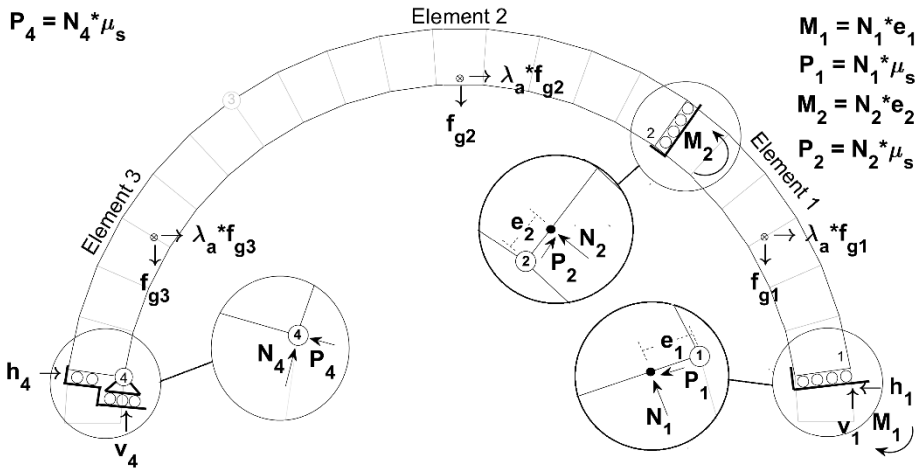

Figure 80. Free-body diagram for the Type LVII mechanism

The equations of equilibrium for the condition shown in Figure 80 is

$$[BC] = \begin{bmatrix} -1 & 0 & 1 & 0 & 0 & 0 & f_{g1} & 0 & 0 \\ 0 & 1 & 0 & -1 & 0 & 0 & 0 & 0 & 0 \\ 0 & 0 & -\Delta y_{2,1} & \Delta x_{1,2} & 0 & 0 & -f_{g1}\Delta y_{1,CM1} & -1 & 1 \\ 0 & 0 & -1 & 0 & 1 & 0 & f_{g2}+f_{g3} & 0 & 0 \\ 0 & 0 & 0 & 1 & 0 & 1 & 0 & 0 & 0 \\ 0 & 0 & 0 & 0 & \Delta y_{4,2} & \Delta x_{2,4} & f_{g2}\Delta y_{2,CM2}+f_{g3}\Delta y_{2,CM3} & 0 & -1 \\ 0 & 0 & 0 & 0 & \tan(\alpha_4) & -1 & 0 & 0 & 0 \\ \tan(\alpha_1) & -1 & 0 & 0 & 0 & 0 & 0 & 0 & 0 \\ 0 & 0 & \tan(\alpha_2) & -1 & 0 & 0 & 0 & 0 & 0 \end{bmatrix}$$

$$\{r\} = \begin{bmatrix} h_1 \\ v_1 \\ h_2 \\ v_2 \\ h_4 \\ v_4 \\ \lambda_a \\ M_1 \\ M_2 \end{bmatrix} \qquad \{q\} = \begin{bmatrix} 0 \\ f_{g1} \\ -f_{g1}\Delta x_{1,CM1} \\ 0 \\ f_{g2}+f_{g3} \\ f_{g2}\Delta x_{2,CM2}+f_{g3}\Delta x_{2,CM3} \\ 0 \\ 0 \\ 0 \end{bmatrix} \tag{89}$$

3.3.6.11 Type LXIII – S_1 -- S_3 C_4

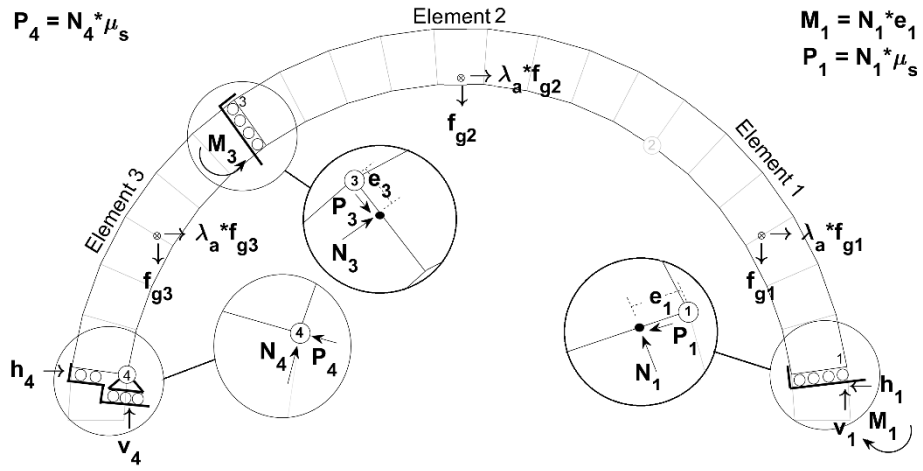

Figure 81. Free-body diagram for the Type LXIII mechanism

The equations of equilibrium for the condition shown in Figure 81 is

$$[BC] = \begin{bmatrix} -1 & 0 & 1 & 0 & 0 & 0 & f_{g1}+f_{g2} & 0 & 0 \\ 0 & 1 & 0 & -1 & 0 & 0 & 0 & 0 & 0 \\ 0 & 0 & -\Delta y_{3,1} & \Delta x_{1,3} & 0 & 0 & -f_{g1}\Delta y_{1,CM1} - f_{g2}\Delta y_{1,CM2} & -1 & 1 \\ 0 & 0 & -1 & 0 & 1 & 0 & f_{g3} & 0 & 0 \\ 0 & 0 & 0 & 1 & 0 & 1 & 0 & 0 & 0 \\ 0 & 0 & 0 & 0 & \Delta y_{4,3} & \Delta x_{3,4} & f_{g3}\Delta y_{3,CM3} & 0 & -1 \\ 0 & 0 & 0 & 0 & \tan(\alpha_4) & -1 & 0 & 0 & 0 \\ \tan(\alpha_1) & -1 & 0 & 0 & 0 & 0 & 0 & 0 & 0 \\ 0 & 0 & \tan(\alpha_3) & -1 & 0 & 0 & 0 & 0 & 0 \end{bmatrix}$$

$$\{r\} = \begin{bmatrix} h_1 \\ v_1 \\ h_3 \\ v_3 \\ h_4 \\ v_4 \\ \lambda_a \\ M_1 \\ M_3 \end{bmatrix} \qquad \{q\} = \begin{bmatrix} 0 \\ f_{g1}+f_{g2} \\ -f_{g1}\Delta x_{1,CM1} - f_{g2}\Delta x_{1,CM2} \\ 0 \\ f_{g2}+f_{g3} \\ f_{g3}\Delta x_{3,CM3} \\ 0 \\ 0 \\ 0 \end{bmatrix} \tag{90}$$

3.3.6.12 Type LXIV – -- S_2 S_3 C_4

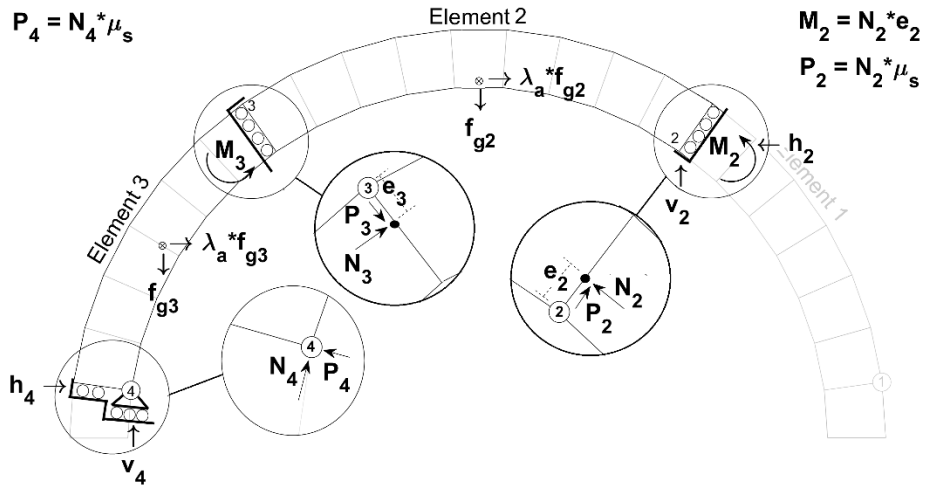

Figure 82. Free-body diagram for the Type LXIV mechanism

The equations of equilibrium for the condition shown in Figure 82 is

$$[BC] = \begin{bmatrix} -1 & 0 & 1 & 0 & 0 & 0 & f_{g2} & 0 & 0 \\ 0 & 1 & 0 & -1 & 0 & 0 & 0 & 0 & 0 \\ 0 & 0 & \Delta y_{3,2} & \Delta x_{2,3} & 0 & 0 & f_{g2}\Delta y_{2,CM2} & -1 & 1 \\ 0 & 0 & -1 & 0 & 1 & 0 & f_{g3} & 0 & 0 \\ 0 & 0 & 0 & 1 & 0 & 1 & 0 & 0 & 0 \\ 0 & 0 & 0 & 0 & \Delta y_{4,3} & \Delta x_{3,4} & f_{g3}\Delta y_{3,CM3} & 0 & -1 \\ 0 & 0 & 0 & 0 & \tan(\alpha_4) & -1 & 0 & 0 & 0 \\ \tan(\alpha_2) & -1 & 0 & 0 & 0 & 0 & 0 & 0 & 0 \\ 0 & 0 & \tan(\alpha_3) & -1 & 0 & 0 & 0 & 0 & 0 \end{bmatrix}$$

$$\{r\} = \begin{bmatrix} h_2 \\ v_2 \\ h_3 \\ v_3 \\ h_4 \\ v_4 \\ \lambda_a \\ M_2 \\ M_3 \end{bmatrix} \qquad \{q\} = \begin{bmatrix} 0 \\ f_{g2} \\ -f_{g2}\Delta x_{2,CM2} \\ 0 \\ f_{g3} \\ f_{g3}\Delta x_{3,CM3} \\ 0 \\ 0 \\ 0 \end{bmatrix} \tag{91}$$

3.3.7 Combined Mechanisms

The combined mechanisms assign two slip-hinge combination joints in exchange for the other two mechanical joints. This condition produces a single element with two mechanical joints.

Mechanisms Type LXV through Type LXVII assign C_1 with C_4, C_3, and C_2 respectively. Mechanisms Type LXVIII and Type LXIX assign C_2 with C_4 and C_3 respectively. The final mechanism, Type LXX, assigns C_3 and C_4.

3.3.7.1 Type LXV – C_1 -- -- C_4

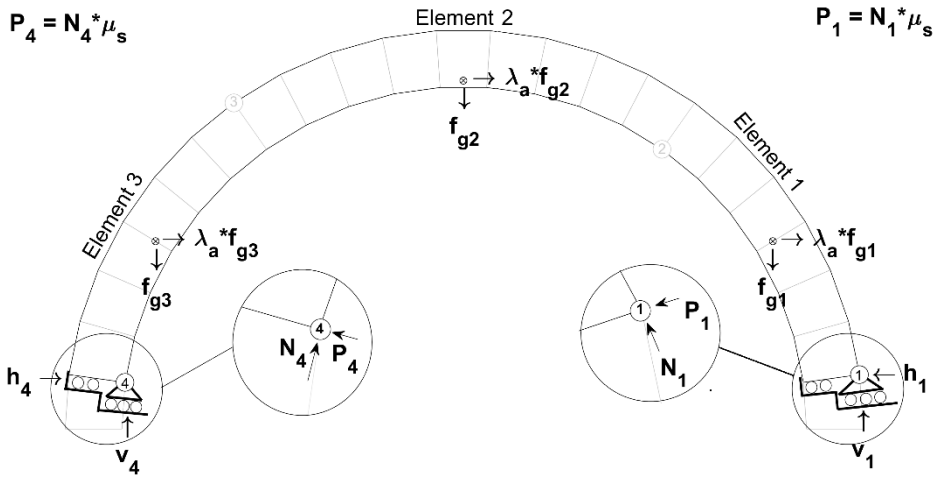

Figure 83. Free-body diagram for the Type LXV mechanism

The equations of equilibrium for the condition shown in Figure 83 is

$$[BC] = \begin{bmatrix} -1 & 0 & 1 & 0 & f_{g1}+f_{g2}+f_{g3} \\ 0 & 1 & 0 & -1 & 0 \\ 0 & 0 & -\Delta y_{4,1} & -\Delta x_{1,4} & -f_{g1}\Delta y_{CM1,1} - f_{g2}\Delta y_{CM2,1} - f_{g3}\Delta y_{CM3,1} \\ \tan(\alpha_1) & -1 & 0 & 0 & 0 \\ 0 & 0 & \tan(\alpha_4) & -1 & 0 \end{bmatrix}$$

$$\{r\} = \begin{bmatrix} h_1 \\ v_1 \\ h_4 \\ v_4 \\ \lambda_a \end{bmatrix} \qquad \{q\} = \begin{bmatrix} 0 \\ f_{g1}+f_{g2}+f_{g3} \\ -f_{g1}\Delta x_{1,CM1} - f_{g2}\Delta x_{1,CM2} - f_{g3}\Delta x_{1,CM3} \\ 0 \\ 0 \end{bmatrix} \tag{92}$$

3.3.7.2 Type LXVI – C_1 -- C_3 –

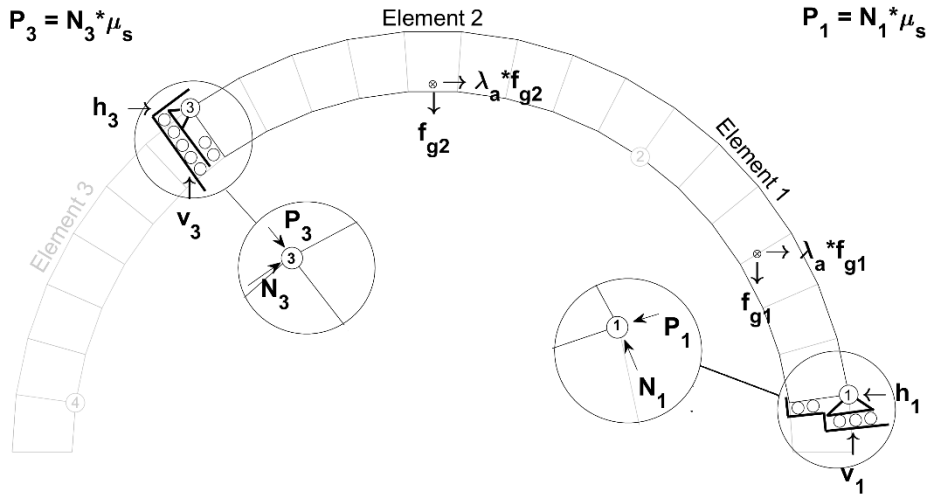

Figure 84. Free-body diagram for the Type LXVI mechanism

The equations of equilibrium for the condition shown in Figure 84 is

$$[BC] = \begin{bmatrix} -1 & 0 & 1 & 0 & f_{g1} + f_{g2} \\ 0 & 1 & 0 & -1 & 0 \\ 0 & 0 & -\Delta y_{3,1} & -\Delta x_{1,3} & -f_{g1}\Delta y_{CM1,1} - f_{g2}\Delta y_{CM2,1} \\ \tan(\alpha_1) & -1 & 0 & 0 & 0 \\ 0 & 0 & \tan(\alpha_3) & -1 & 0 \end{bmatrix}$$

$$\{r\} = \begin{bmatrix} h_1 \\ v_1 \\ h_3 \\ v_3 \\ \lambda_a \end{bmatrix} \qquad \{q\} = \begin{bmatrix} 0 \\ f_{g1} + f_{g2} \\ -f_{g1}\Delta x_{1,CM1} - f_{g2}\Delta x_{1,CM2} \\ 0 \\ 0 \end{bmatrix} \tag{93}$$

3.3.7.3 Type LXVII – C_1 C_2 -- --

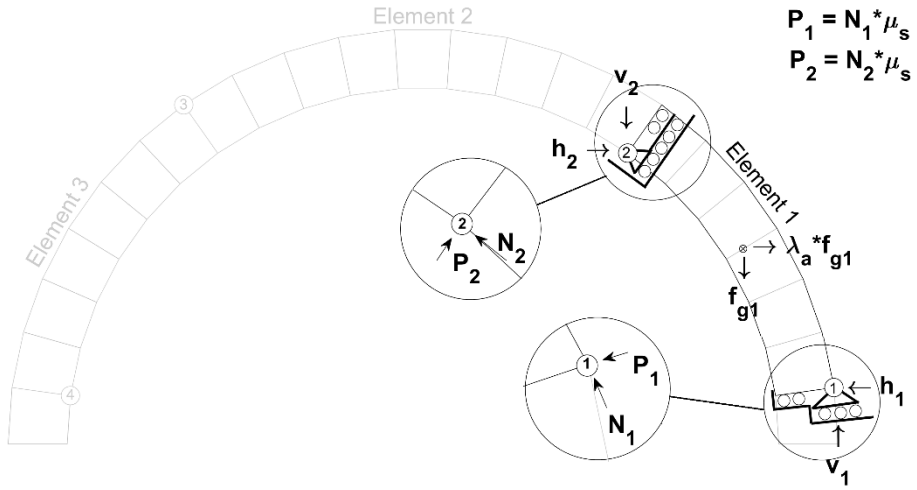

Figure 85. Free-body diagram for the Type LXVII mechanism

The equations of equilibrium for the condition shown in Figure 85 is

$$[BC] = \begin{bmatrix} -1 & 0 & 1 & 0 & f_{g1} \\ 0 & 1 & 0 & -1 & 0 \\ 0 & 0 & -\Delta y_{2,1} & -\Delta x_{1,2} & -f_{g1}\Delta y_{CM1,1} \\ \tan(\alpha_1) & -1 & 0 & 0 & 0 \\ 0 & 0 & \tan(\alpha_2) & -1 & 0 \end{bmatrix}$$

$$\{r\} = \begin{bmatrix} h_1 \\ v_1 \\ h_2 \\ v_2 \\ \lambda_a \end{bmatrix} \qquad \{q\} = \begin{bmatrix} 0 \\ f_{g1} \\ -f_{g1}\Delta x_{1,CM1} \\ 0 \\ 0 \end{bmatrix} \tag{94}$$

3.3.7.4 Type LXVIII – -- C_2 – C_4

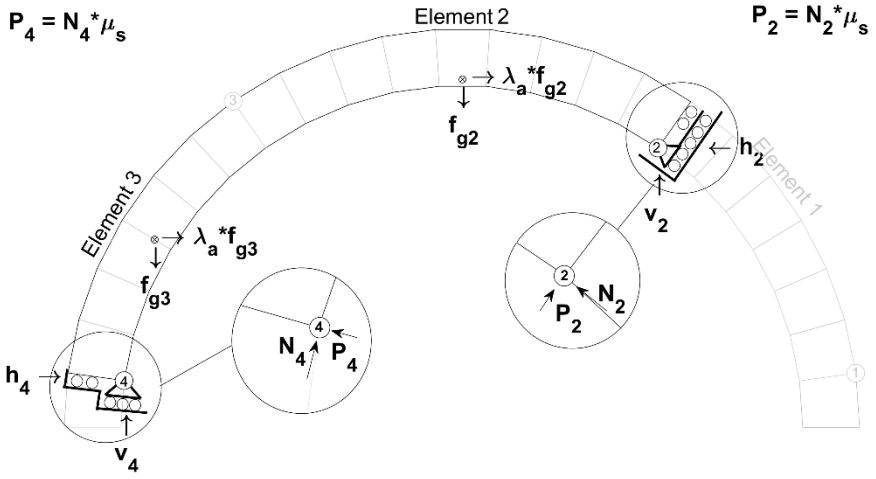

Figure 86. Free-body diagram for the Type LXVIII mechanism

The equations of equilibrium for the condition shown in Figure 86 is

$$[BC] = \begin{bmatrix} -1 & 0 & 1 & 0 & f_{g2} + f_{g3} \\ 0 & 1 & 0 & -1 & 0 \\ 0 & 0 & -\Delta y_{4,2} & -\Delta x_{2,4} & f_{g2}\Delta y_{CM2,2} - f_{g3}\Delta y_{CM3,2} \\ \tan(\alpha_2) & -1 & 0 & 0 & 0 \\ 0 & 0 & \tan(\alpha_4) & -1 & 0 \end{bmatrix}$$

$$\{r\} = \begin{bmatrix} h_2 \\ v_2 \\ h_4 \\ v_4 \\ \lambda_a \end{bmatrix} \qquad \{q\} = \begin{bmatrix} 0 \\ f_{g2} + f_{g3} \\ -f_{g2}\Delta x_{2,CM2} - f_{g3}\Delta x_{2,CM3} \\ 0 \\ 0 \end{bmatrix} \tag{95}$$

3.3.7.5 Type LXIX – -- C_2 C_3 –

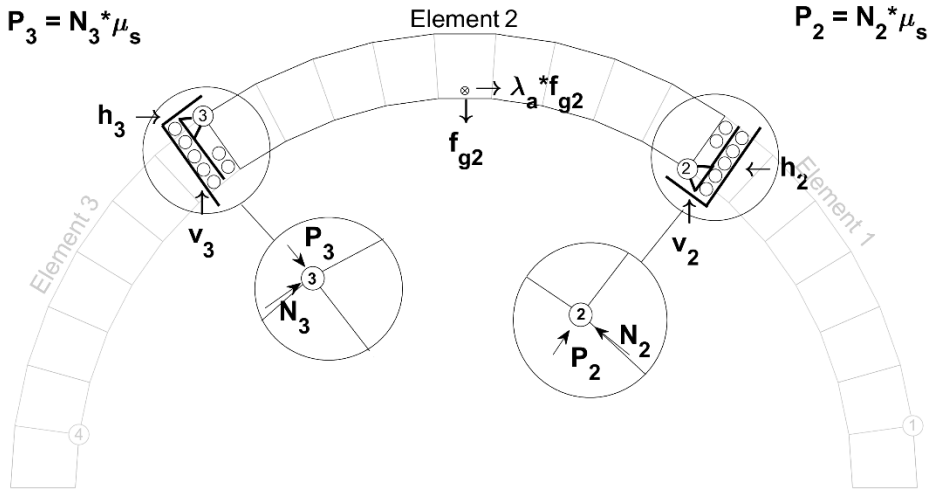

Figure 87. Free-body diagram for the Type LXIX mechanism

The equations of equilibrium for the condition shown in Figure 87 is

$$[BC] = \begin{bmatrix} -1 & 0 & 1 & 0 & f_{g2} \\ 0 & 1 & 0 & -1 & 0 \\ 0 & 0 & -\Delta y_{3,2} & -\Delta x_{2,3} & f_{g2}\Delta y_{CM2,2} \\ \tan(\alpha_2) & -1 & 0 & 0 & 0 \\ 0 & 0 & \tan(\alpha_3) & -1 & 0 \end{bmatrix}$$

$$\{r\} = \begin{bmatrix} h_2 \\ v_2 \\ h_3 \\ v_3 \\ \lambda_a \end{bmatrix} \qquad \{q\} = \begin{bmatrix} 0 \\ f_{g2} \\ -f_{g2}\Delta x_{2,CM2} \\ 0 \\ 0 \end{bmatrix} \tag{96}$$

3.3.7.6 Type LXX – -- -- C_3 C_4

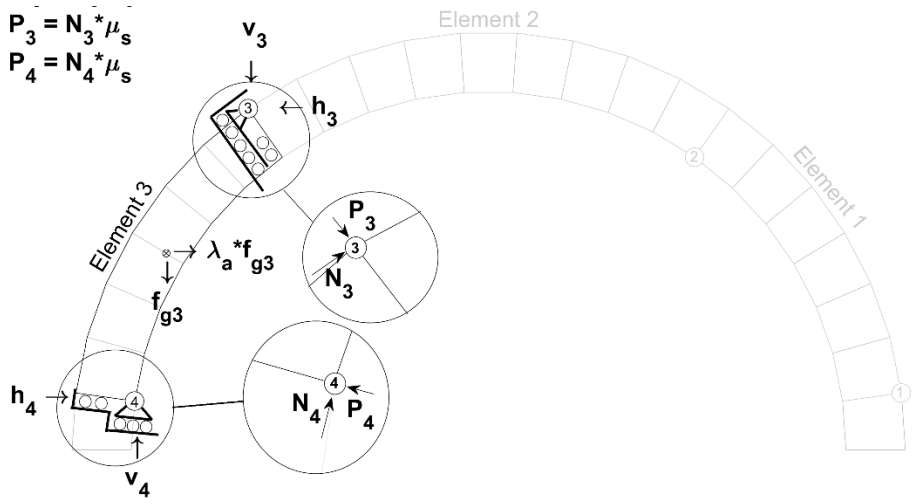

Figure 88. Free-body diagram for the Type LXX mechanism

The equations of equilibrium for the condition shown in Figure 88 is

$$[BC] = \begin{bmatrix} -1 & 0 & 1 & 0 & f_{g3} \\ 0 & 1 & 0 & -1 & 0 \\ 0 & 0 & -\Delta y_{4,3} & -\Delta x_{3,4} & -f_{g3}\Delta y_{CM3,3} \\ \tan(\alpha_2) & -1 & 0 & 0 & 0 \\ 0 & 0 & \tan(\alpha_4) & -1 & 0 \end{bmatrix}$$

$$\{r\} = \begin{bmatrix} h_3 \\ v_3 \\ h_4 \\ v_4 \\ \lambda_a \end{bmatrix} \qquad \{q\} = \begin{bmatrix} 0 \\ f_{g3} \\ -f_{g3}\Delta x_{3,CM3} \\ 0 \\ 0 \end{bmatrix} \tag{97}$$

3.4 Equilibrium Matrix Construction Strategies

Section 3.2 presented the kinematic equilibrium diagrams and the corresponding equations of equilibrium for various loading conditions applied to the standard mechanism. The loading conditions included constant accelerations, point loads and distributed loads. Section 3.3 presented all the potential mechanisms for constant horizontal acceleration loading and the inclusion of a slip potential at the mechanical joints. From these sections a more generalized image of the equilibrium matrix construction can be visualized.

Examining the different load cases highlighted a single column in the balance condition that contained the information associated with the collapse multiplier variable (see Figure 15). The inclusion of static friction at the mechanical joints introduces the potential slip and slip-hinge mechanical conditions. The slip

condition results in the release of the pin connection and introduces an additional variable (i.e. moment) into the evaluation. This added moment is then balanced through the inclusion of the friction angle and its relationship with the parallel and normal reactions at the mechanical joint. The slip-hinge condition maintains the pin connection at the slip-joint which results in the removal of another pin connection in the system. In terms of the equilibrium evaluation this reduces the matrix by three equations through combining two elements while adding the friction condition relationship.

Both the different loads and slip conditions have distinct and somewhat isolated effects on the equations of equilibrium. Figure 89 presents the general layout of the equations of equilibrium. Under this structure it can be noted that the inclusion of a slip joint adds friction rows and moment columns to the set. If a combined slip-hinge joint exists, then the added row(s) for the inclusion of friction are coupled with a reduction in the reaction variables and columns. Lastly, the effects of the applied loads accumulate in the constants vector less the loading variable under investigation. This generalized format for the development of equations of equilibrium in turn allows for the piecewise construction of additional conditions for evaluation.

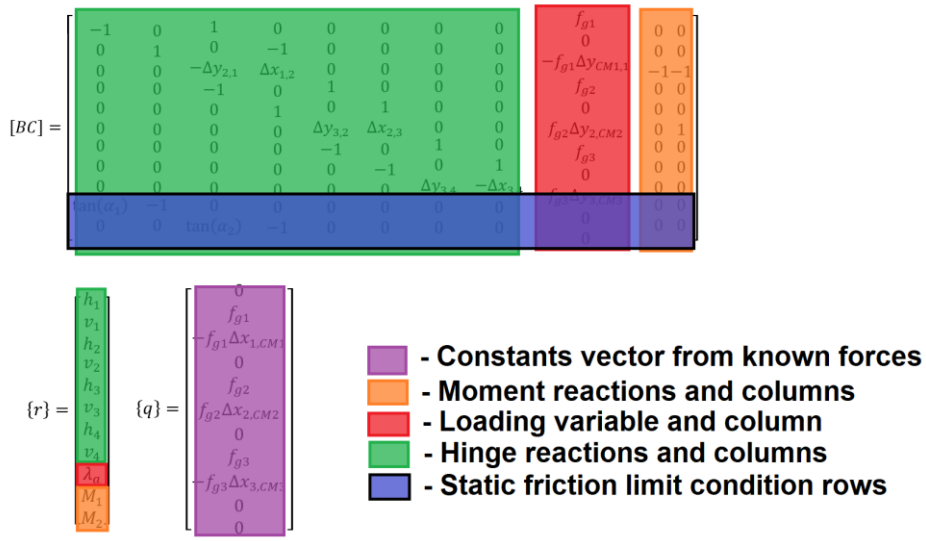

Figure 89. Breakdown of the equations of equilibrium structure

3.5 Concluding Remarks

In the context of determinacy and stability, the four-pinned arch is considered an unstable structure and modern structural analysis textbooks end the discussion of the unstable system with a recommendation of avoiding them. Since the failure of the arch is the transformation into an unstable system, kinematic equilibrium has been previously overlooked. Kinematic equilibrium therefore establishes the divergence point of masonry arch analysis, and it is the

foundation for all analysis tools and structures developed in the remaining chapters of this dissertation.

CHAPTER 4

BLACK BOX ANALYSIS

List of Abbreviations and Symbols

A_i — Polynomial fit constants for cartesian deformation path of the CM

ACSE — American Society of Civil Engineers

α_i — Rotation angle of the i^{th} mechanical joint

B_i — Polynomial fit constants for Element lever arm rotations versus horizontal CM position

BVP — Boundary value problem

$\hat{B}_0$ — y-intercept for joint line equations used in thrust point calculations

$\hat{B}_1$ — Slope constant for joint line equations used in thrust point calculations

CA — Center of area

CM — Center of mass

$\widehat{CM}$ — Center of mass identifier for arch segments used in the thrust point calculations

$\Delta\gamma_{23}$ — Polar angle change between the 2nd and 3rd mechanical joint after a deformation

e_i — Thrust line eccentricity from the i^{th} hinge position along the joint line

F_d — Net force of a distributed load

F_n — Normal reaction force at the selected joint in the KCLC

F_p — Parallel reaction force at the selected joint in the KCLC

$\hat{F}_d$ — Net force of a partial distributed load

$\hat{f}_g$	—	Gravitational body force for arch segment used in thrust point calculations
GUI	—	Graphical user interface
H_acc	—	Horizontal acceleration load selection parameter for the original KCLC
H_i	—	Identifier for the i^{th} hinge
h_P	—	Horizontal reaction force for determining the thrust point position along a joint line
KCLC	—	Kinematic collapse load calculator
l_{ij}	—	Rigid length between the i^{th} and j^{th} mechanical joints
λ_a	—	Collapse multiplier for uniform acceleration
λ_P	—	Collapse multiplier for an applied point load
M_n	—	Moment required to shift the thrust line to the material boundary for a selected joint
N	—	Number of Blocks input parameter for the original KCLC
PL	—	Point load selection parameter for the original KCLC
R	—	Intrados radius input parameter for original KCLC
RSBD	—	Reinforced stability-based design
$\boldsymbol{r}$	—	Reaction vector of the equations of equilibrium
SDOF	—	Single degree of freedom
S_i	—	Identifier for the i^{th} slip joint
T_i	—	Tension compensation force required at the i^{th} joint for defining rigid elements
T_n	—	Normal tension force required to shift the thrust line to the material boundary for a selected joint
t_i	—	Thickness of the i^{th} joint
T_R	—	Thickness to radius ratio input parameter for the original KCLC
θ_{Ej}	—	Rotation angle of the j^{th} element's lever arm connection to CM of the full arch
θ_{ij}	—	Polar angle between the undeformed position of the i^{th} and j^{th} mechanical joints
θ'_{ij}	—	Polar angle between the deformed position of the i^{th} and j^{th} mechanical joints

v_P	—	Vertical reaction force for determining the thrust point position along a joint line
(x_b, y_b)	—	Cartesian coordinates of a joint line boundary point
(x_{cm}, y_{cm})	—	Cartesian coordinates of the CM
(x_{d1}, y_{d1})	—	Cartesian boundary point limits of a distributed load
(x_{d2}, y_{d2})	—	Cartesian boundary point limits of a distributed load
(x_d, y_d)	—	Centroid point of a distributed load applied to a surface
$(\hat{x}_d, \hat{y}_d)$	—	Centroid point of a partial distributed load applied to a surface
(x_P, y_P)	—	Cartesian coordinates of a point load
$(\hat{x}, \hat{y})$	—	Cartesian coordinates for a joint line equation used in thrust point calculations

The failure of a stable dry-stack masonry arch is a BVP who's capacity is defined by the onset of a mechanism. This mechanism creation is a physical phenomenon that arises from the destruction of the stable state and presents a singularity into a system that otherwise has infinite solutions. This singularity thus creates a black box condition to the input (loading condition) and output (mechanism) of the arch.

In Chapter 3 the concept of kinematic equilibrium was derived for the masonry arch directly from the equations of equilibrium and the inclusion of an external loading variable. The free-body diagrams were defined, and the resulting equations of equilibrium were developed for various loading conditions and for the complete set of potential mechanisms that can exist with the removal of the traditional no-slip assumption. Every developed equations of equilibrium is a determinant system and its application into Eqn. 4 generates a singularity condition for the defined state. These solution sets however have no constraints on their own and do not consider the laws governing the system from which they were derived. They provide a link between the input and output of the arch's failure, but the link itself must be evaluated to consider if it can physically exist.

As a compression only system with fixed boundary conditions defined by the material's geometry, the potential singularity must abide by the rules of motion and the laws governing forces. For instance, consider the point load condition applied to the hinge H_3 side of Element 2 in the traditional mechanism structure (see Figure 10). If the solution to this condition resulted in a negative collapse load multiplier, λ_p, then any motion would require an overlap of the block boundaries which physically cannot occur. Therefore, the admissibility of the singularity must be evaluated to determine whether or not it can exist.

The black box analysis of masonry arches is a direct reference to the evaluation of admissibility. Every determinant system has a solution, but in the context of

the mechanization of the masonry arch there are a distinct set of conditions that must exist. These conditions are physical and do not require the application of engineering judgement. Therefore, they can be housed under a black box structure.

The objective of Chapter 4 is to introduce the kinematic admissibility requirements of the arch and combine them into an analysis structure that allows the comprehensive and efficient analysis of the kinematic condition. First, kinematic admissibility requirements are developed and then followed by the introduction of the KCLC software. The KCLC is an adaptable Graphical User Interface (GUI), developed in Matlab® and specifically designed to execute the black box analysis of dry-stack masonry arches through control of the input parameters required to create a determinant condition. Lastly, some consequences of kinematic equilibrium and admissibility are discussed. These consequences are the capacity compensation requirements for the existence of non-stable, kinematically admissible mechanisms and of mechanically deformed conditions with admissible solutions.

4.1 Kinematic Admissibility

The admissibility of a given loading-mechanism condition of a dry-stack masonry arch can be subdivided into a two-stage evaluation process. The first stage is a direct assessment of the solutions obtained for the reaction vector ***r***. For the traditional four-hinged mechanism under vertical point load or uniform acceleration these requirements are that the collapse multiplier is positive and the reactions at the hinges are compressive. For more generalized loading conditions, the collapse multiplier must generate a force that meets the kinematic boundary conditions. The inclusion of the slip-hinge replacement at a mechanical joint adds the condition that the moment is positive as well.

The second stage of the analysis process is an evaluation of the resulting thrust line geometry that is established from the calculated reactions of the singularity conditions. The thrust line is a theoretical line that represents the flow of concentrated compressive forces through the arch. For the arch to be stable, the line of thrust must exist within the material of the arch. In terms of admissibility of the solution to the kinematic equilibrium of a loading-mechanism condition however, the limits of the thrust line are only held at the mechanical joints. A hinge forms when this line reaches an arch boundary. Therefore, the admissibility of the traditional mechanism requires that the thrust line pass through each hinge. The same is true for the combined joint condition as well.

For the slip condition, the trust line must cross the joint boundary in such a way that the nature of the mechanism under evaluation is maintained. Additionally, a negative eccentricity in Eqn. 5 would indicate that the thrust line lies outside the mechanical joint boundary. This limits the eccentricity between the hinge edge and half the joint thickness

$$0 \leq e_i \leq \frac{1}{2} t_i \tag{98}$$

4.1.1 Thrust Line

Since the hinge locations or eccentricity of the slip condition are known from the solution to the reaction vector, the thrust line can be established at each section along the arch by evaluating the free-body diagram at each section against hinge H_1 or slip S_1. The flow of compressive forces can also be considered as the line of zero moment. Therefore, the thrust point at each joint in the arch can be determined by locating the point along the joint line where the vertical, v_P, and horizontal, h_P, point reactions maintain a zero moment at hinge H_1 or slip S_1.

Figure 90 shows an example of the free-body diagram used to calculate the thrust point for the constant horizontal acceleration and hinge H_1 condition. Through the intrados and extrados boundary points of the joint, the slope, $\hat{B}_1$, and intercept, $\hat{B}_0$, of the linear joint line equation

$$\hat{y} = \hat{B}_1\hat{x} + \hat{B}_o \tag{99}$$

can be established. Calculating the sum of the moments about hinge H_1 with a clockwise positive definition generates

$$\sum M_1 = v_P(\hat{x} - x_1) - h_P(\hat{y} - y_1) + \hat{f}_g[(x_{\widehat{CM}} - x_1) - \lambda_a(y_{\widehat{CM}} - y_1)] = 0 \tag{100}$$

Combining Eqns. 99 and 100 and rearranging the terms produces the horizontal position of the thrust point

$$\hat{x} = \frac{\left(h_1 - \lambda_a\hat{\bar{f}}_g\right)(y_1 - \hat{B}_0) + \left(v_1 - \hat{\bar{f}}_g\right)x_1 + \hat{\bar{f}}_g\left(\lambda_a\Delta y_{\widehat{CM},1} - \Delta x_{\widehat{CM},1}\right)}{v_1 + h_1\hat{B}_0} \tag{101}$$

Applying the solution from Eqn. 101 to Eqn. 99 establishes the cartesian coordinates of the thrust point $(\hat{x}, \hat{y})$ along the joint line. Repeating this process for each joint line of the arche and connecting the calculated points generates the thrust line.

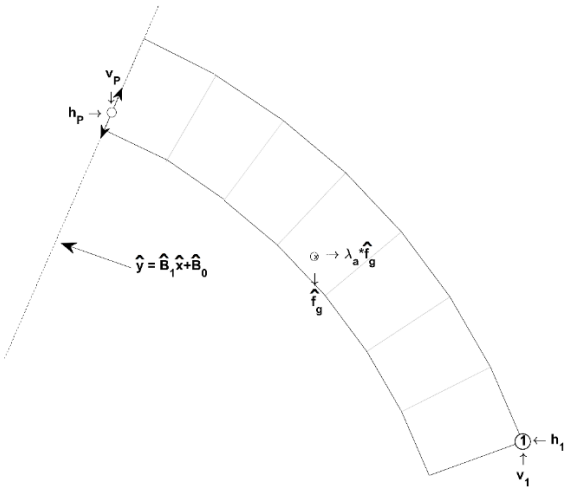

Figure 90. Free-body diagram for calculating the thrust point position along line $\hat{y} = \hat{B}_1\hat{x} + \hat{B}_0$ for horizontal acceleration condition

The calculation of the thrust points requires the evaluation of imposed moments between hinge H_1 and the joint under evaluation. Consequently, changes in loading conditions across an arch will result in changes to the moment calculation and thus the calculation of the thrust point. Therefore, the joint line based thrust point equations must be established for each loading condition.

Once the thrust line is established from the calculated thrust points based upon the position of hinge H_1 or slip S_1, it can be evaluated against the remaining mechanical joints to determine admissibility of the kinematic condition.

4.1.1.1 Thrust Point Position Equations

As stated, the thrust point at each joint of the arch can be established by determining the location along the joint line (Eqn. 99) that maintains a zero moment at either H_1 or S_1 depending on the mechanism being evaluated, and a position equation must be constructed for each loading change along the span of the arch. Following the same methodology used for the horizontal acceleration condition (see Figure 90 and Eqns. 99-101), this section presents the cartesian $\hat{x}$ coordinate thrust point equations to combine with Eqn. 99 for each of the loading conditions presented in Section 3.2. Note that in the construction of the thrust point position equations, establishing equivalent forces is done from the loads within the boundaries of evaluation.

4.1.1.1.1 Horizontal Acceleration

Constant horizontal accelerations generate a uniform loading condition across the arch. This results in Eqn. 101 that was derived to from condition shown in Figure 90 in the explanation of obtaining the thrust line.

4.1.1.1.2 2D Acceleration

Constant 2D accelerations maintain the uniformity of the horizontal condition, and thus a single equation

$$\hat{x} = \frac{(h_1 - \lambda_a \hat{f}_g \cos(\theta_a))(y_1 - \hat{B}_0) + \left(v_1 - \hat{f}_g(1 - \lambda_a \sin(\theta_a))\right)x_1 + \hat{f}_g\left(\lambda_a \cos(\theta_a)\Delta y_{\bar{CM},1} - (1 - \lambda_a \sin(\theta_a))\Delta x_{\bar{CM},1}\right)}{v_1 + h_1 \hat{B}_0} \quad (102)$$

is structured from the condition shown in Figure 91.

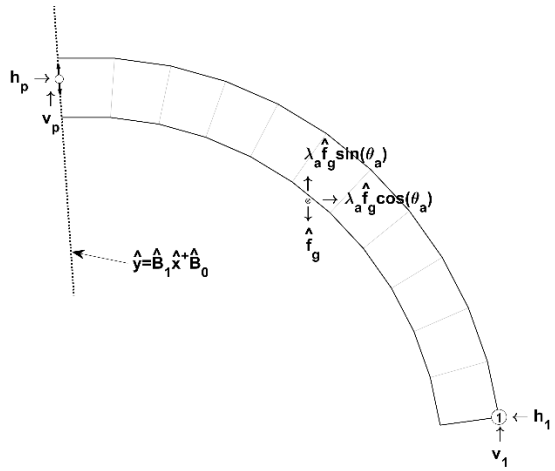

Figure 91. Free-body diagram for 2D acceleration thrust point calculation

4.1.1.1.3 Point Load

The thrust point calculation for the point load condition requires two equations to account for the discrete positioning (x_P, y_P) of the point load

$$\hat{x} = \begin{cases} \frac{(h_1)(y_1-\hat{B}_0)+(v_1-\hat{f}_g)x_1+\hat{f}_g\Delta x_{\widehat{CM},1}}{v_1+h_1\hat{B}_0}; \hat{x} > x_P \\ \frac{(h_1-\lambda_P\cos(\theta_P))(y_1-\hat{B}_0)+(v_1-\hat{f}_g-\lambda_P\sin(\theta_P))x_1+\hat{f}_g\Delta x_{\widehat{CM},1}+\lambda_P(\sin(\theta_P)\Delta x_{P,1}-\cos(\theta_P)\Delta y_{P,1})}{v_1+h_1\hat{B}_0}; \hat{x} \le x_P \end{cases} \quad (103)$$

Figure 92 shows the two conditions evaluated for the thrust point calculation. Note that unlike the free-body diagrams (see Section 3.2.2), the arch segment evaluated is constructed from the results of the reaction vector. The free body diagram that generates the thrust point relies on the definition of a single point (i.e. Hinge H_1 or slip S_1) and the loading geometries. Equation 103 thus holds for all three point load free-body diagrams formulated in Section 3.2.2.

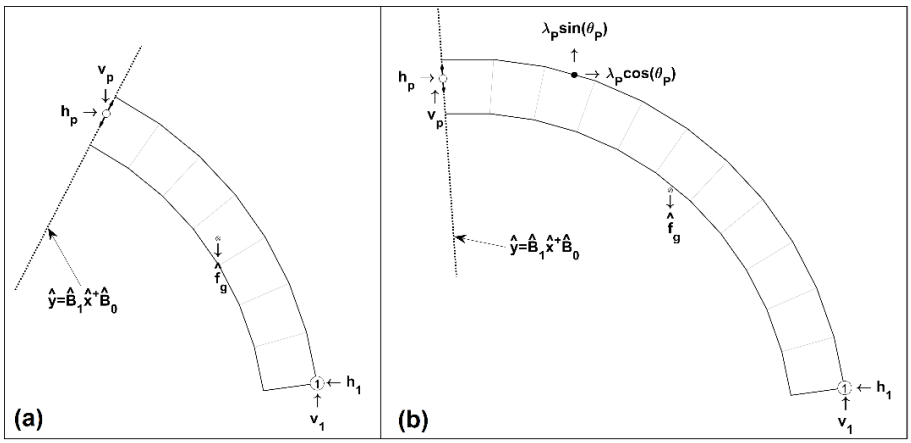

Figure 92. Free-body diagram (a) before and (b) after crossing the point load for the thrust point calculations.

4.1.1.1.4 Distributed Load

Both the horizontal and vertical distributed load conditions discussed in Section 3.2.3 apply external loading to a section of the extrados. This generates a potential of three distinct free-body diagrams. The first condition is the arch section between hinge H_1 and the boundary (x_{d2}, y_{d2}) of the distributed load. Figure 92a shows the free-body diagram used to calculate the thrust point. The second condition exists for thrust point evaluations within the boundary of the distributed load. This results in a floating magnitude, $\hat{F}_d$, and position, $(\hat{x}_d, \hat{y}_d)$ of the equivalent force for thrust point calculations between the boundaries (x_{d2}, y_{d2}) and (x_{d1}, y_{d1}). After passing through the distributed load, the full equivalent force, F_d, is fixed at position (x_d, y_d) for the remaining thrust point calculations. Figure 93 shows the latter two free-body diagrams for the case of a vertical distributed load, and the thrust point position equation can be established as

$$\hat{x} = \begin{cases} \frac{(h_1)(y_1-\hat{B}_0)+(v_1-\hat{f}_g)x_1+\hat{f}_g\Delta x_{\bar{CM},1}}{v_1+h_1\hat{B}_0}; \hat{x} > x_2 \\ \frac{(h_1-\lambda_d\hat{F}_d\cos(\theta_d))(y_1-\hat{B}_0)+(v_1-\hat{f}_g-\lambda_d\hat{F}_d\sin(\theta_d))x_1+\hat{f}_g\Delta x_{\bar{CM},1}+\lambda_d\hat{F}_d\left(\sin(\theta_d)\Delta x_{\bar{d},1}-\cos(\theta_d)\Delta y_{\bar{d},1}\right)}{v_1+h_1\hat{B}_0}; x_1 < \hat{x} \leq x_2 \\ \frac{(h_1-\lambda_d F_d\cos(\theta_d))(y_1-\hat{B}_0)+(v_1-\hat{f}_g-\lambda_d F_d\sin(\theta_d))x_1+\hat{f}_g\Delta x_{\bar{CM},1}+\lambda_d F_d\left(\sin(\theta_d)\Delta x_{d,1}-\cos(\theta_d)\Delta y_{d,1}\right)}{v_1+h_1\hat{B}_0}; \hat{x} \leq x_1 \end{cases} \quad (104)$$

for a given distributed load.

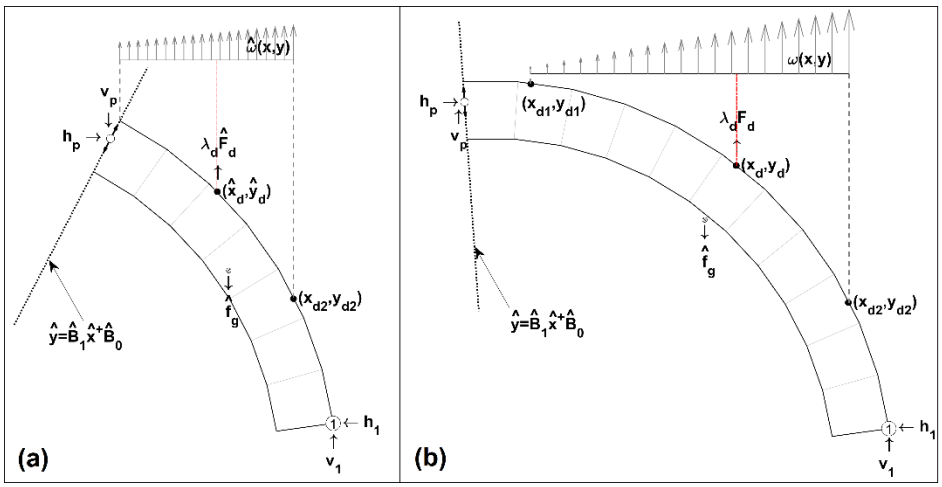

Figure 93. Free-body diagram (a) within and (b) past the boundaries of a distributed load for the thrust point calculations

4.1.1.1.5 Combining Loads

From the free-body diagrams for the thrust point position calculations it can be seen that the key condition to establishing the thrust line is changes to the free-body diagram. Each change that is crossed along the arch path requires a change to the position equation. Therefore, combining loads requires a geometric discretization of the loads on the arch and corresponding thrust point position equations for each.

4.2 Kinematic Collapse Load Calculator

Both the kinematic equations of equilibrium and the formation of the thrust line are highly dependent on the geometry of the arch and its block joints. Additionally, the solution to the reaction vector requires the inverse matrix calculation of the balance condition. These conditions are too labor intensive to regularly perform by hand. With the aid of modern computing power and drafting software these conditions become trivial and require almost no computation time to solve. Therefore, the Kinematic Collapse Load Calculator (KCLC) was developed.

The KCLC is the software tool developed to perform the black box analysis of masonry arches. Its purpose is to provide an interactive platform to simplify and aid in the understanding of the mechanized failure of masonry arches, and to provide a platform for a robust and efficient structural analysis tool for masonry arches [126]. The original KCLC utilizes the kinematic equations of equilibrium and kinematic admissibility conditions to provide an interactive analysis of user defined circular arches through adjusting the locations of the hinges.

4.2.1 KCLC Software Description

The original KCLC is a stand-alone open source interactive GUI developed in MATLAB® for the limit analysis of semi-circular masonry arches with the standard Type I mechanism subjected to two of the most common loading conditions: asymmetric point load and constant horizontal acceleration. The KCLC takes the user-specified geometric parameters of a circular arch and constructs an interactive analysis through a combination of displayed output data and the ability to change the kinematic mechanism through adjusting the hinge locations. Figure 94 shows the original KCLC user interface.

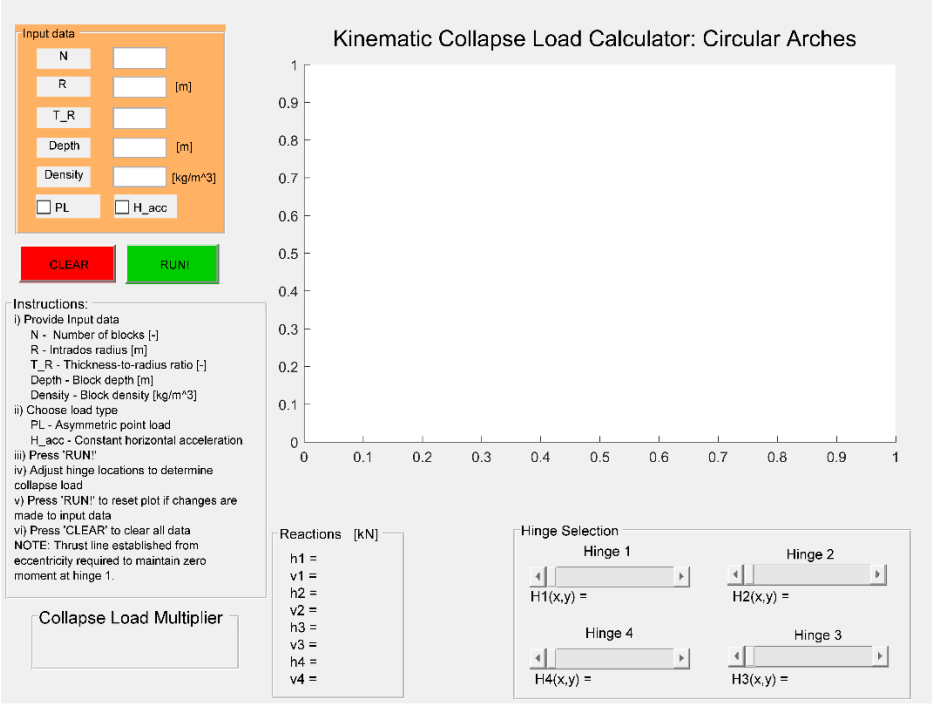

Figure 94. The original KCLC upon execution of the MATLAB® script [126]**.**

As stated in the instructions, the input data include the arch input parameters and load type selection. The arch data required are the number of blocks, intrados radius, thickness-to-radius ratio, depth, and density. The load type is chosen by selecting the appropriate check box.

When the “RUN!” button is pressed, the input data is checked against the allowed parameters of the program. If the input data does not meet these requirements an error message is displayed indicating the error.

If there are no errors in the input data, then after pushing the “RUN!” button the block boundary points are established; the initial value and limits of the hinges are defined; the arch, hinges and loading condition are drawn in the plot window; and the resulting conditions are passed to the developed evaluation function (“Eval”) in the MATLAB® script. The “Eval” function performs the analysis on the set condition, displays the output data, and plots thrust line. The hinge sliders are then activated, and the hinge locations can be adjusted by the user. For each change in the hinge position, the reaction vector and the thrust line are recalculated and displayed. The minimum stable collapse load can then be determined by finding the minimum collapse load that contains the thrust line within the material boundaries. Figure 95 and Figure 96 show the steps involved with determining the minimum configuration of two semi-circular arches subjected to a constant horizontal acceleration and a point load at hinge H_3 respectively.

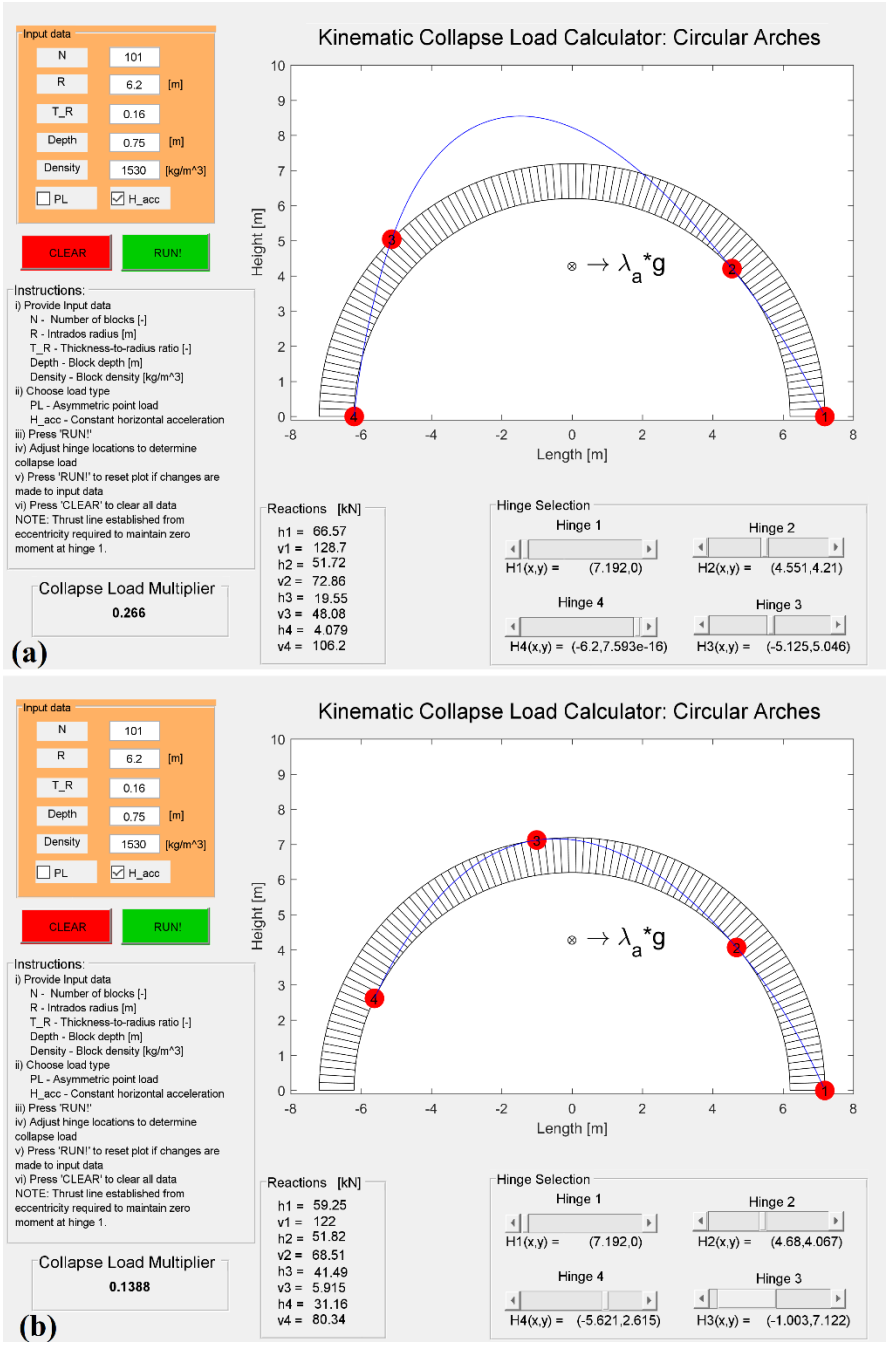

Figure 95. The KCLC (a) initialization and (b) minimum collapse condition

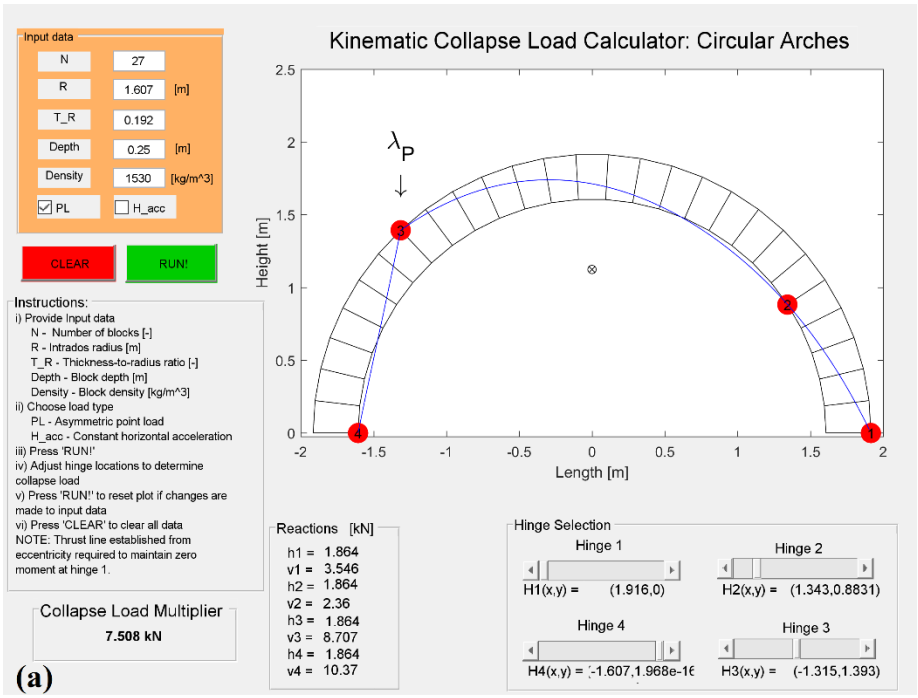
Input data
N 27
R 1.607 [m]
T_R 0.192
Depth 0.25 [m]
Density 1530 [kg/m^3]
PL
H_acc
CLEAR
RUN!
Instructions:
i) Provide Input data
N - Number of blocks [-]
R - Intrados radius [m]
T_R - Thickness-to-radius ratio [-]
Depth - Block depth [m]
Density - Block density [kg/m^3]
ii) Choose load type
PL - Asymmetric point load
H_acc - Constant horizontal acceleration
iii) Press 'RUN!'
iv) Adjust hinge locations to determine collapse load
v) Press 'RUN!' to reset plot if changes are made to input data
vi) Press 'CLEAR' to clear all data
NOTE: Thrust line established from eccentricity required to maintain zero moment at hinge 1.
Collapse Load Multiplier
7.508 kN
Kinematic Collapse Load Calculator: Circular Arches
λP
Height [m]
Length [m]
Reactions [kN]
h1 = 1.864
v1 = 3.546
h2 = 1.864
v2 = 2.36
h3 = 1.864
v3 = 8.707
h4 = 1.864
v4 = 10.37
Hinge Selection
Hinge 1
H1(x,y) = (1.916,0)
Hinge 2
H2(x,y) = (1.343,0.8831)
Hinge 4
H4(x,y) = (-1.607,1.968e-16
Hinge 3
H3(x,y) = (-1.315,1.393)

(a)

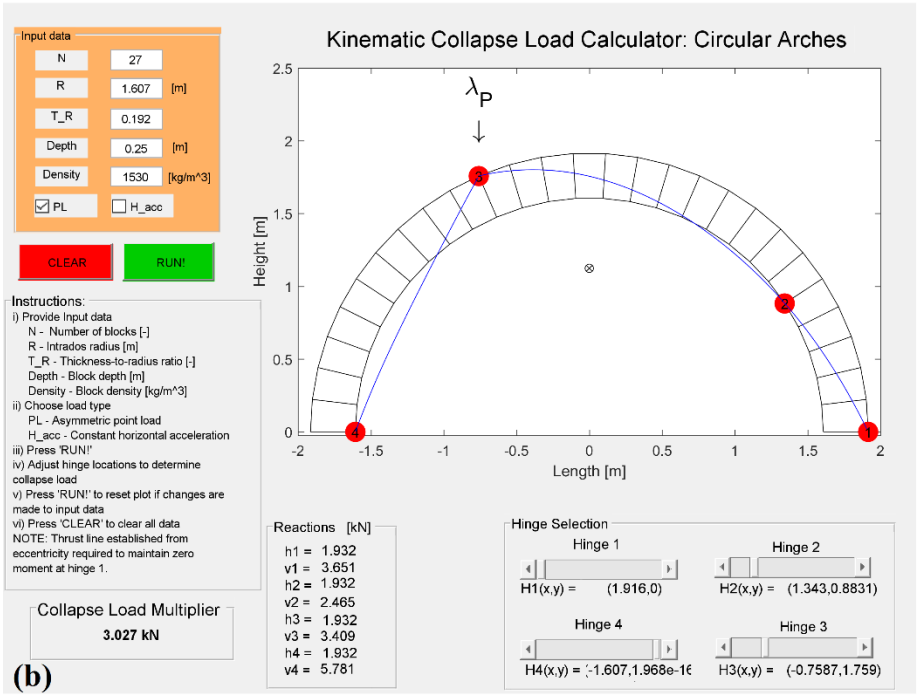
Input data
N 27
R 1.607 [m]
T_R 0.192
Depth 0.25 [m]
Density 1530 [kg/m^3]
PL
H_acc
CLEAR
RUN!
Instructions:
i) Provide Input data
N - Number of blocks [-]
R - Intrados radius [m]
T_R - Thickness-to-radius ratio [-]
Depth - Block depth [m]
Density - Block density [kg/m^3]
ii) Choose load type
PL - Asymmetric point load
H_acc - Constant horizontal acceleration
iii) Press 'RUN!'
iv) Adjust hinge locations to determine collapse load
v) Press 'RUN!' to reset plot if changes are made to input data
vi) Press 'CLEAR' to clear all data
NOTE: Thrust line established from eccentricity required to maintain zero moment at hinge 1.
Collapse Load Multiplier
3.027 kN
Kinematic Collapse Load Calculator: Circular Arches
λP
Height [m]
Length [m]
Reactions [kN]
h1 = 1.932
v1 = 3.651
h2 = 1.932
v2 = 2.465
h3 = 1.932
v3 = 3.409
h4 = 1.932
v4 = 5.781
Hinge Selection
Hinge 1
H1(x,y) = (1.916,0)
Hinge 2
H2(x,y) = (1.343,0.8831)
Hinge 4
H4(x,y) = (-1.607,1.968e-16
Hinge 3
H3(x,y) = (-0.7587,1.759)

(b)

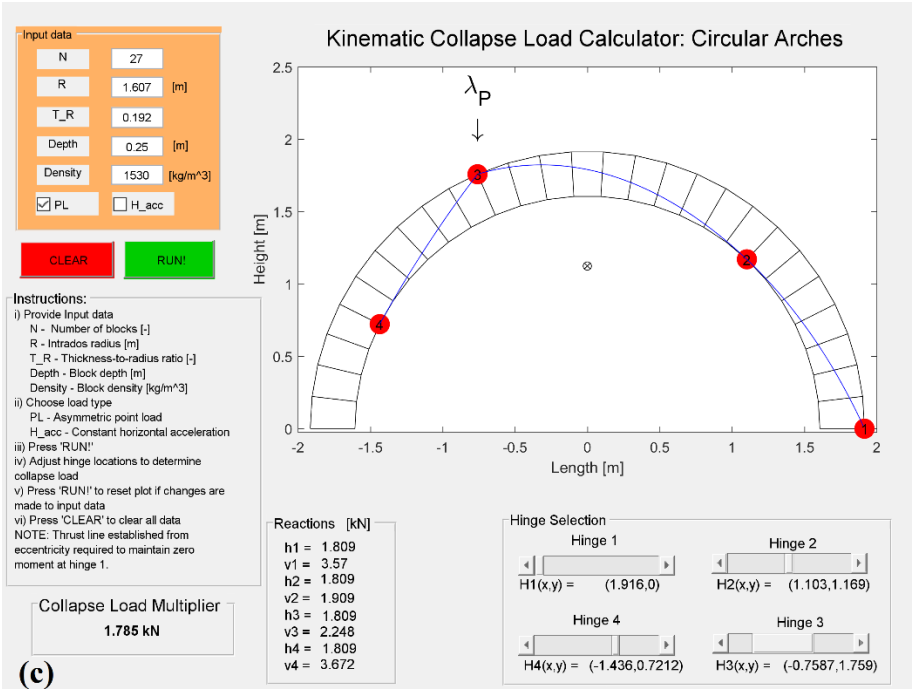

Figure 96. The KCLC (a) initialization, (b) point load placement and (c) minimum collapse configuration

The original KCLC provides a stand-alone analysis tool for the upper bound limit analysis of semi-circular masonry arches. It requires no understanding of the analysis techniques used (hence the black box designation), which enables it to become an effective educational tool for teaching the concepts of the kinematic theorem as well as the thrust line and stability. The ability to control the arch input parameters allows the effects these parameters have on the analysis to be studied. Finally, the ability to control the hinge positions provides the opportunity to gain an insight into the relationships between stability, kinematically admissible mechanisms and the overall strength of the system.

4.2.2 KCLC and Multi-Mechanism Analysis

In its original form, the KCLC only represents semi-circular arches with ideal conditions and the traditional Type I mechanism. This limits its usefulness to an educational application, but the structure of the software was designed to act as the foundation for a robust, efficient and effective structural analysis platform. In order for the software to be a useful structural analysis tool that can support the design of arches for new construction, it must adapt and expand to cover the full range of potential mechanisms.

The first adaptations to the KCLC have been successfully implemented. Focusing on seismic capacity, and thus the horizontal acceleration condition as the starting point, six additional mechanism types have been incorporated into

the software [124]. The added mechanisms were Type II, Type VII, Type VIII, Type XVII, Type XVIII and Type XIX. These mechanisms were chosen as the most plausible options from the observed failure of the first experimental campaign focusing on hinge control (see Section 5.2) [125]. A friction angle input parameter was included into the KCLC along with “MIN” and “MAX” buttons that determine the minimum and maximum friction angle, if any, that produce an admissible mechanism. Figure 97 through Figure 102 show each of the six added mechanism types, each with two different friction angles that produce admissible mechanisms for the given mechanical joint configurations. While these added mechanism types are only a fraction of the full set discussed in Chapter 3, they highlight the efficiency, and potential of the KCLC structure.

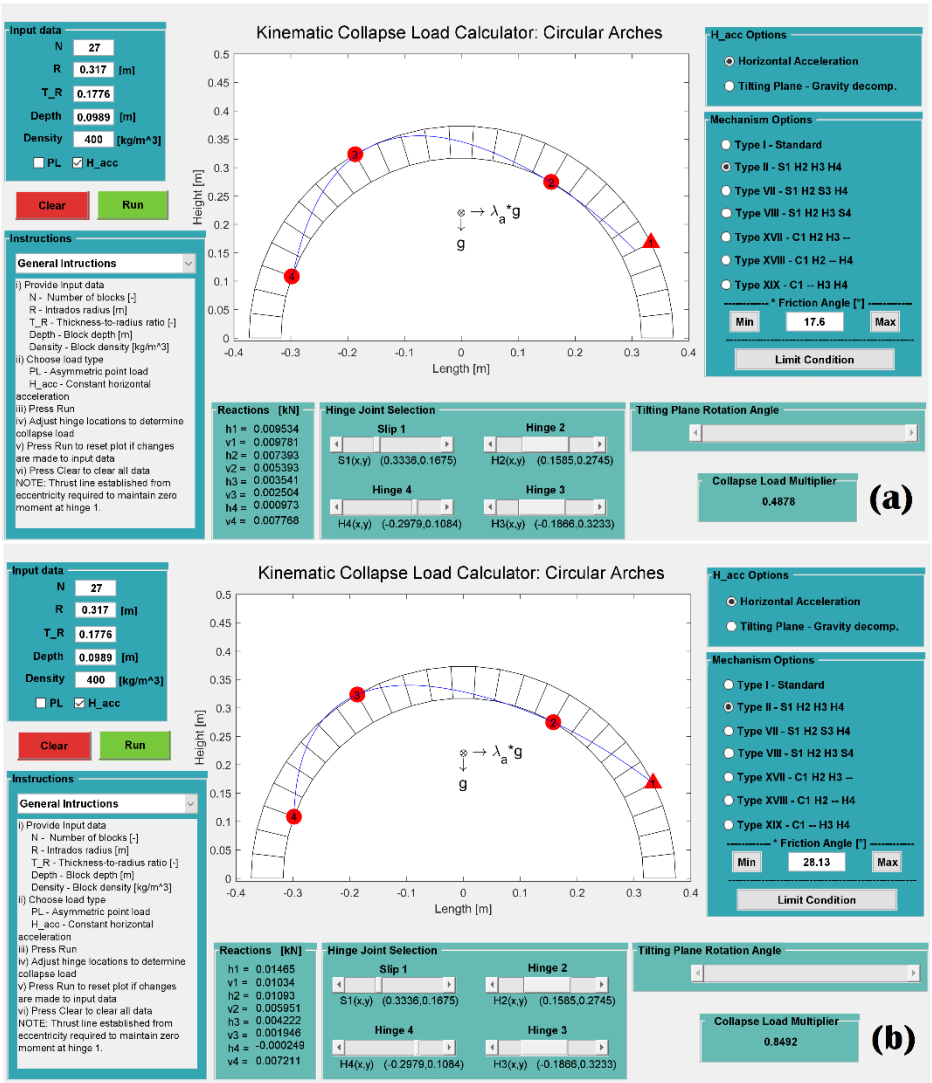

Figure 97. Admissible Type II mechanism under constant horizontal acceleration with friction angles of (a) 17.6° and (b) 28.13°

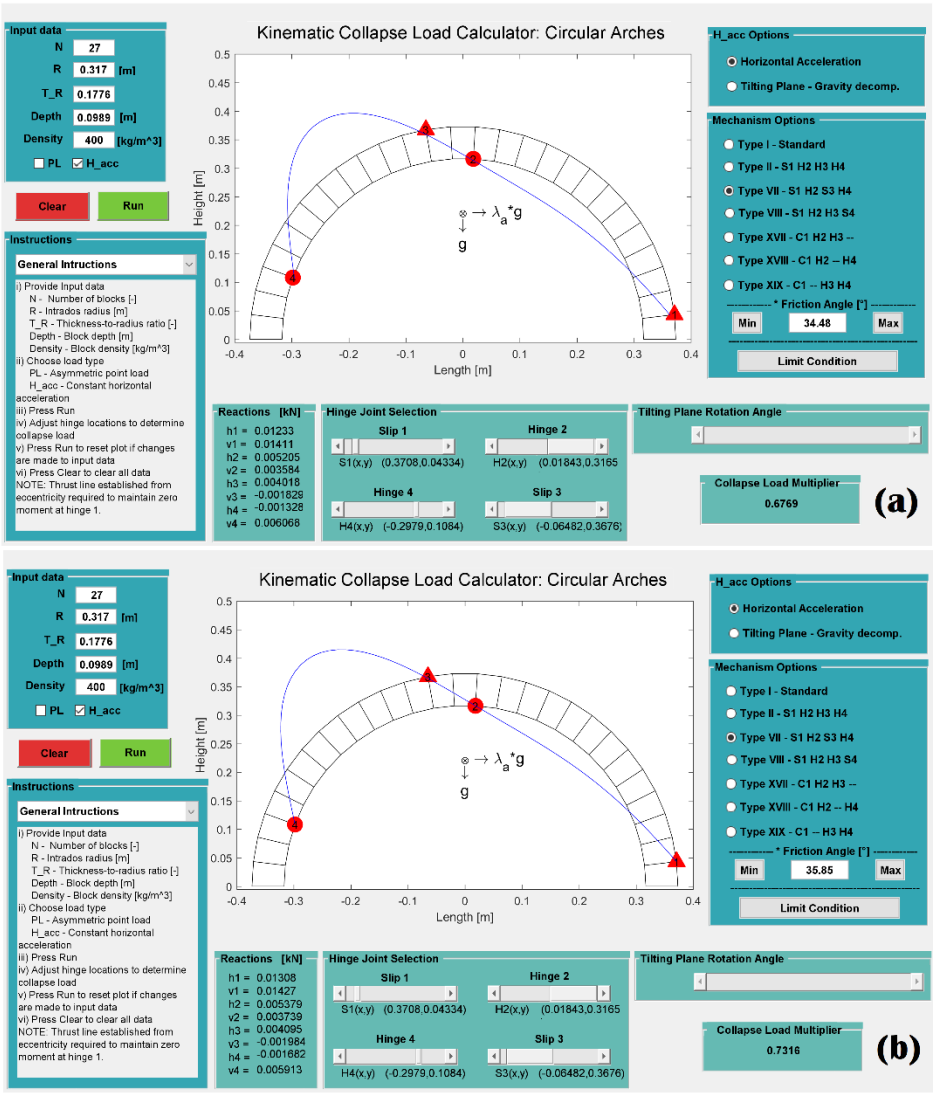

Figure 98. Admissible Type VII mechanism under constant horizontal acceleration with friction angles of (a) 34.48° and (b) 35.85°

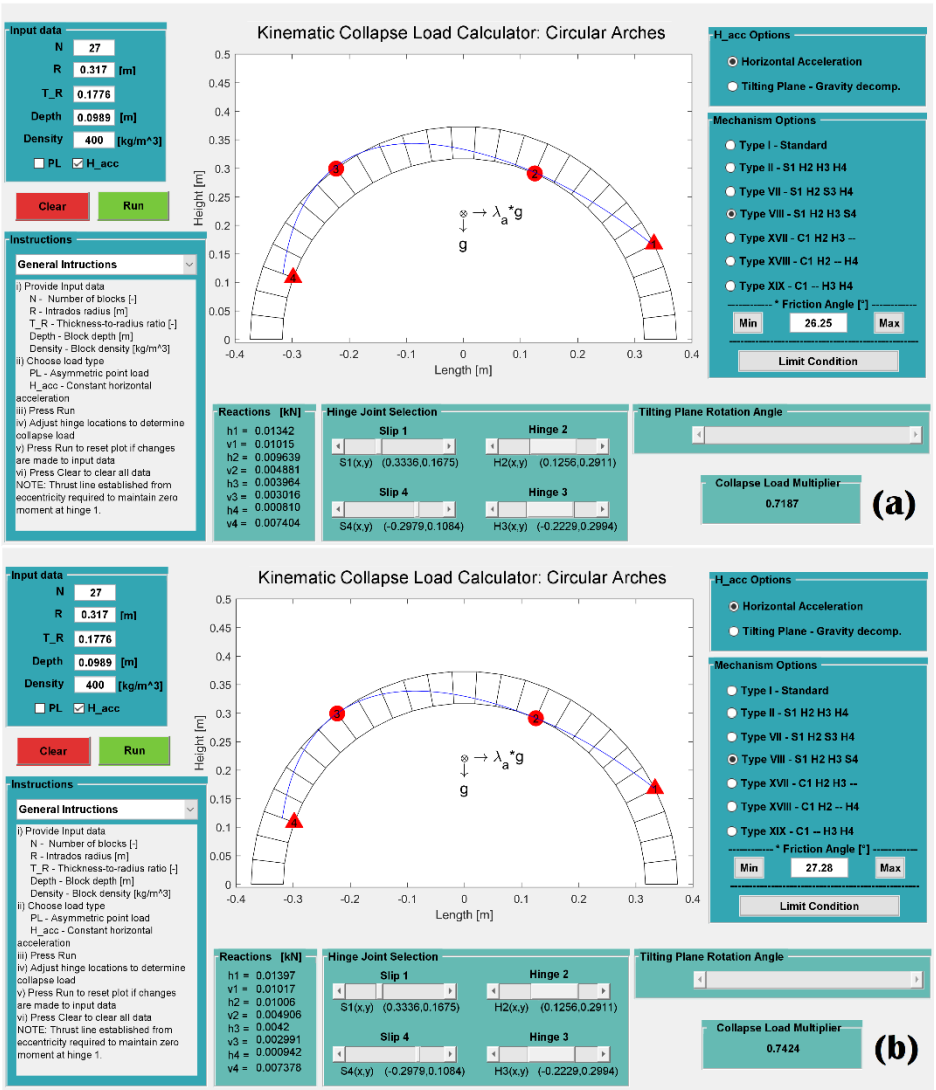

Figure 99. Admissible Type VIII mechanism under constant horizontal acceleration with friction angles of (a) 26.25° and (b) 27.28°

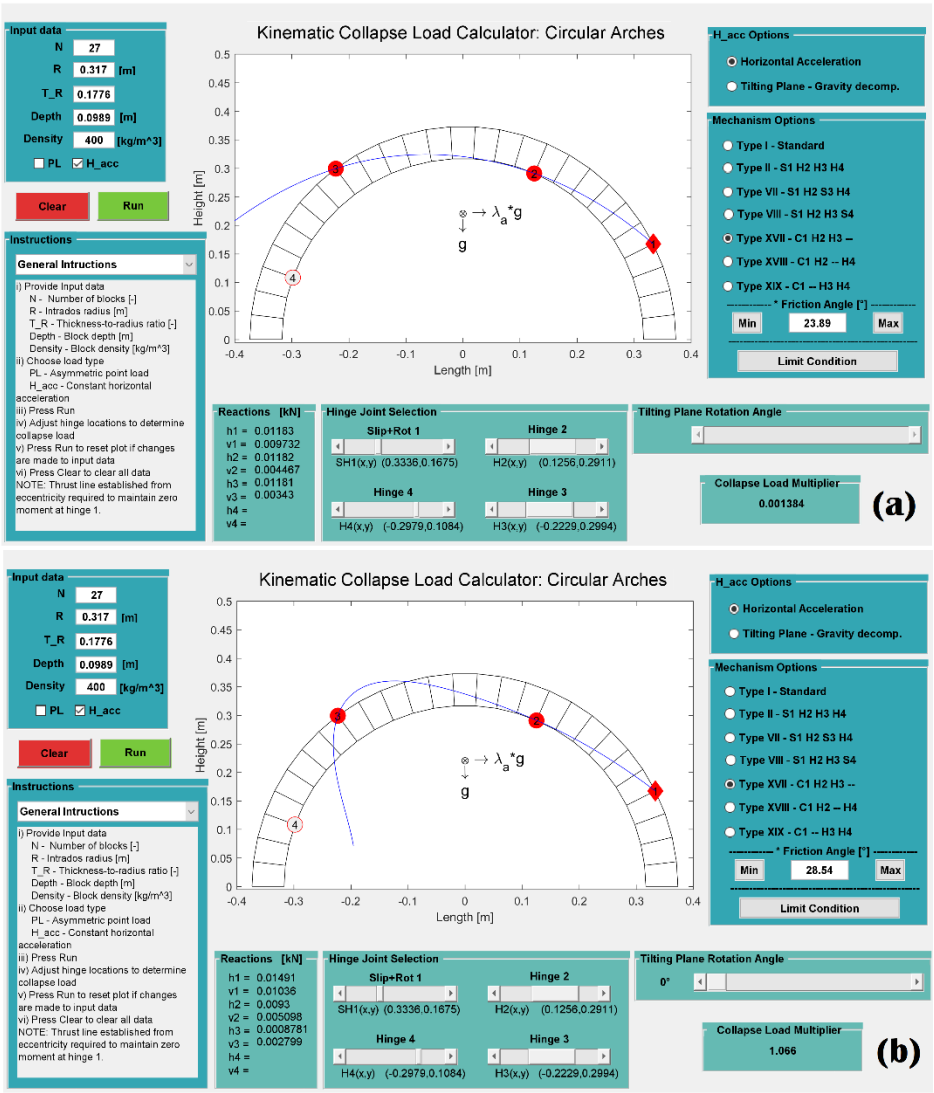

Figure 100. Admissible Type XVII mechanism under constant horizontal acceleration with friction angles of (a) 23.89° and (b) 28.54°

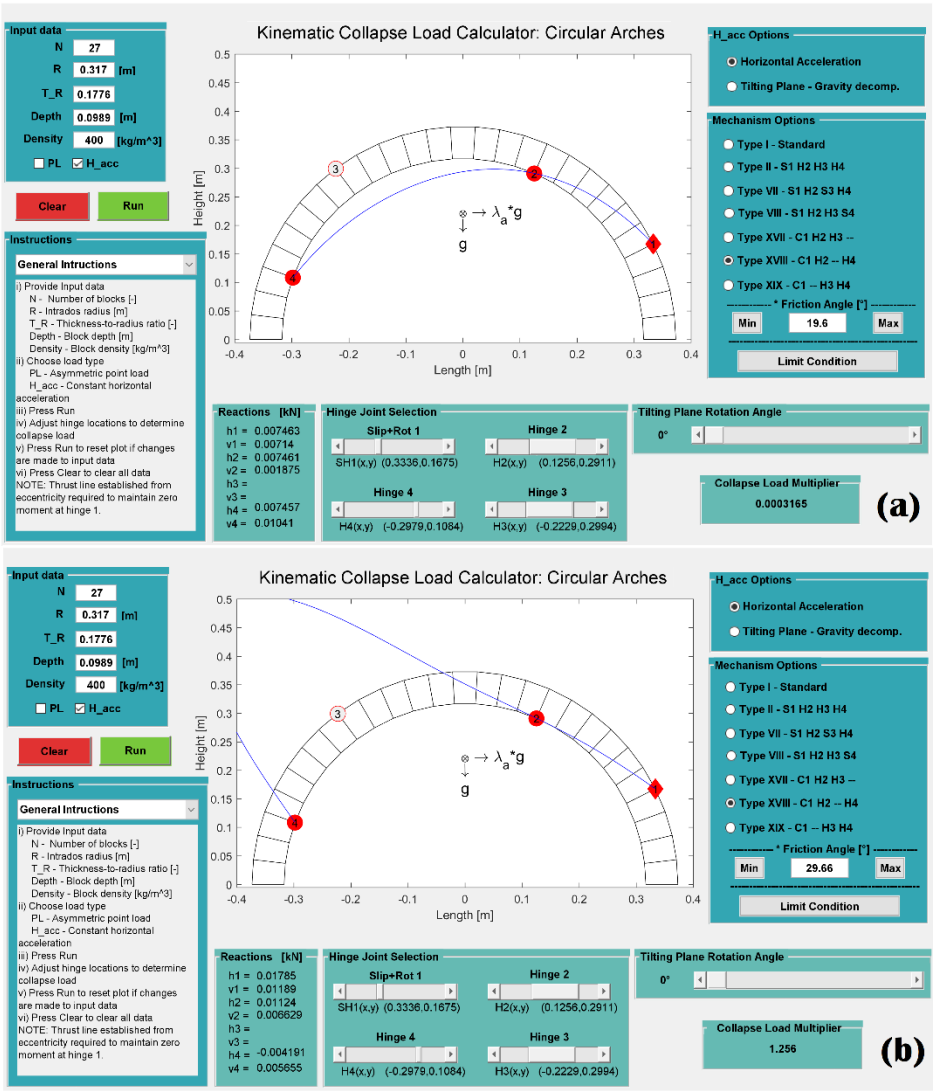

Figure 101. Admissible Type XVIII mechanism under constant horizontal acceleration with friction angles of (a) 19.6° and (b) 29.66°

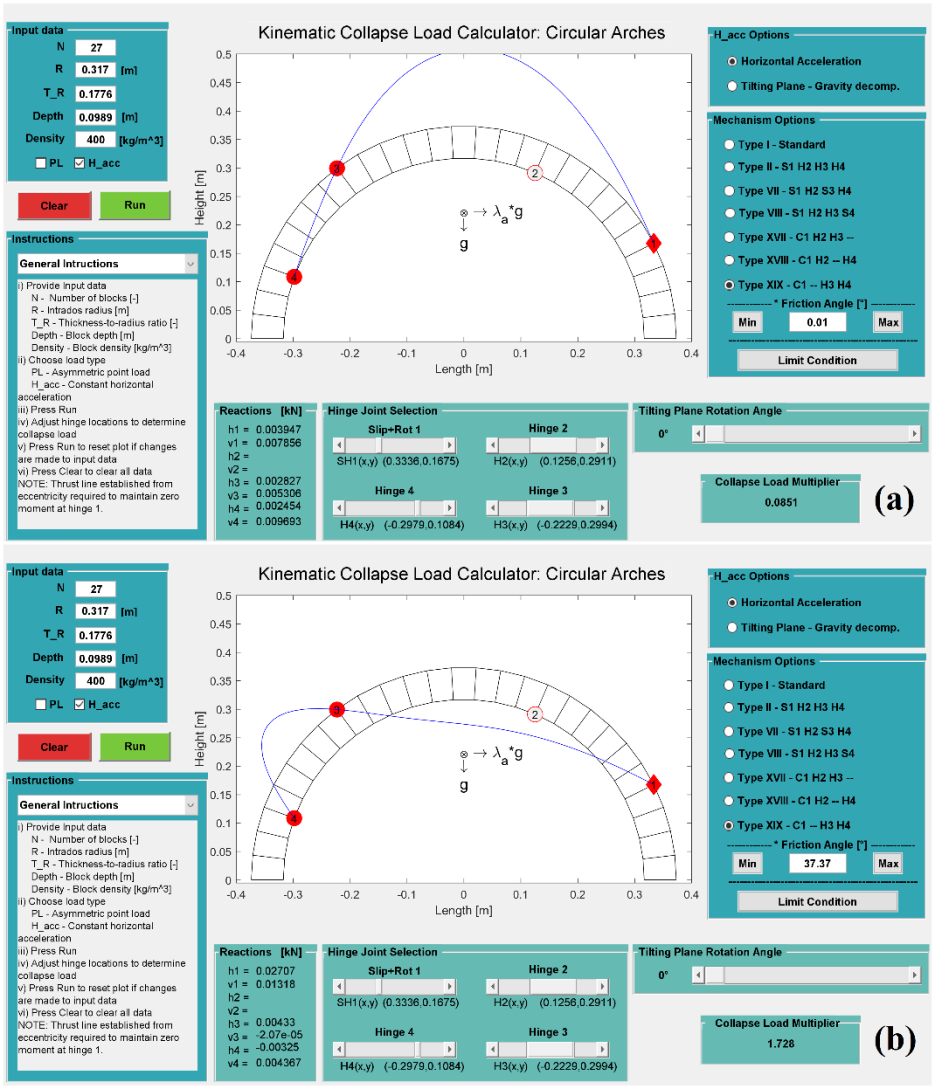

Figure 102. Admissible Type XIX mechanism under constant horizontal acceleration with friction angles of (a) 0.01° and (b) 37.37°

4.2.3 KCLC and the Limiting Condition

From the previous section it becomes clear that the KCLC can adapt and expand to incorporate additional mechanism types required to remove the ideal assumption of no slippage between blocks. With the inclusion of additional mechanism options and associated friction angle introduces an additional evaluation: the limiting mechanism condition.

The limiting mechanism condition evaluation considers all the selected mechanism types and identifies the condition with the minimum collapse

multiplier. Deselecting the minimum condition then switches the KCLC to the next minimum and so on. In this way, all of the admissible mechanisms can be considered for a given arch-mechanical joint set in ascending order. This process is highlighted in Figure 103 and Figure 104 and further reinforces the simplicity, robustness and adaptability of the analysis approach.

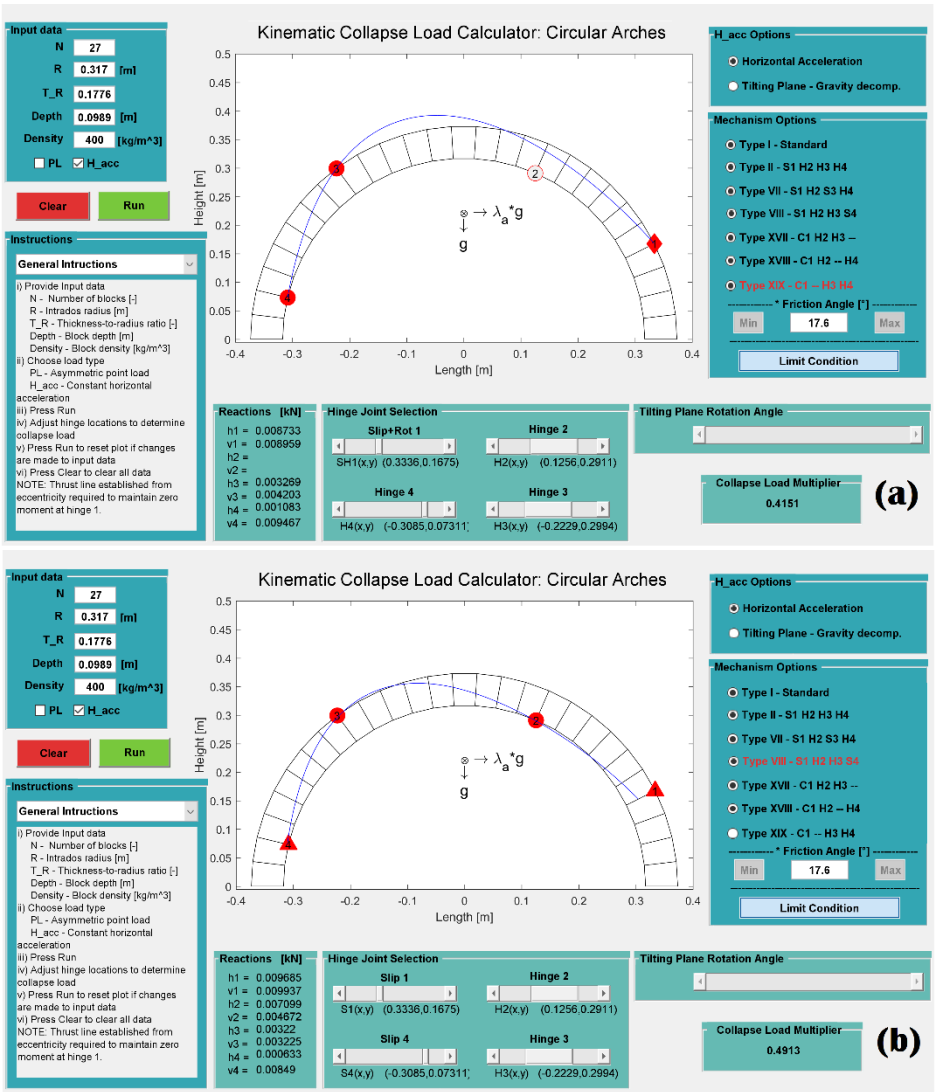

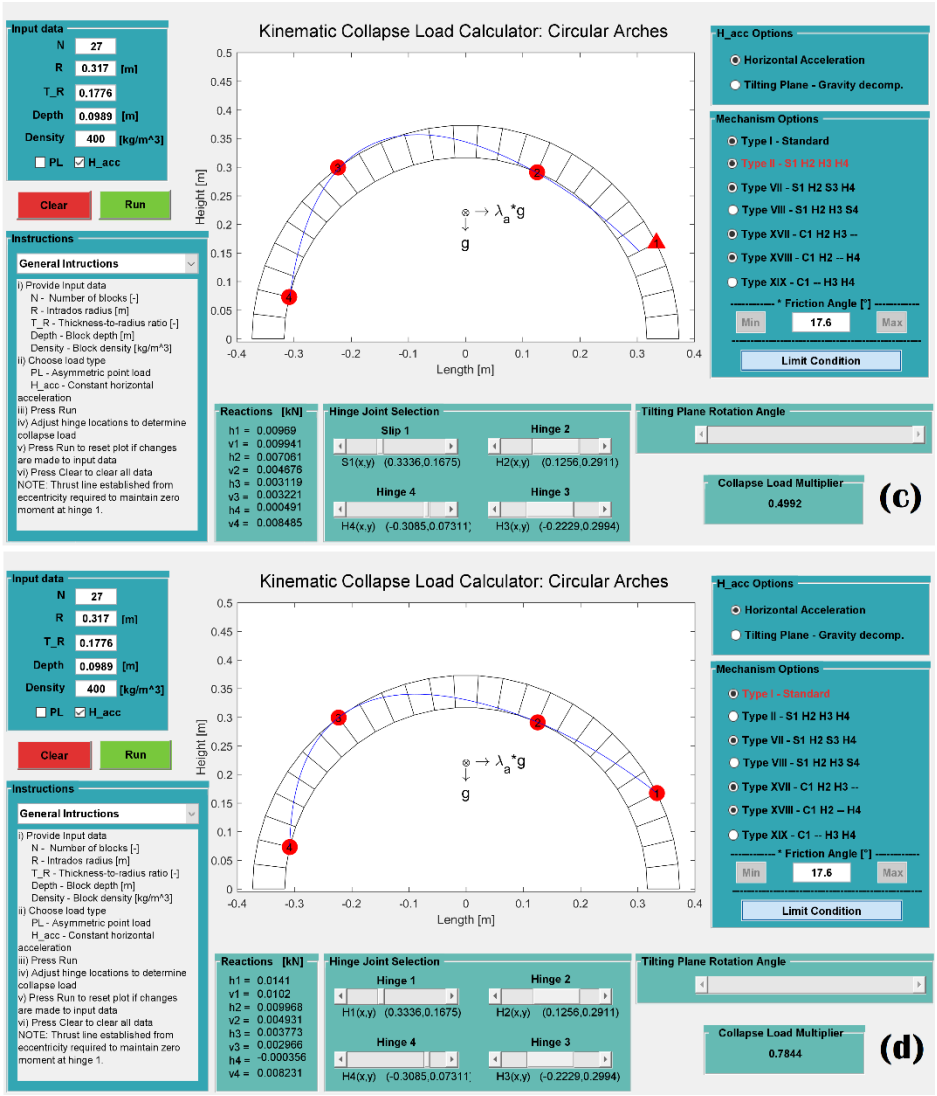

Figure 103. Limiting condition evaluation with (a) Type XIX controlling, followed by (b) Type VII, (c) Type II and lastly (d) Type I

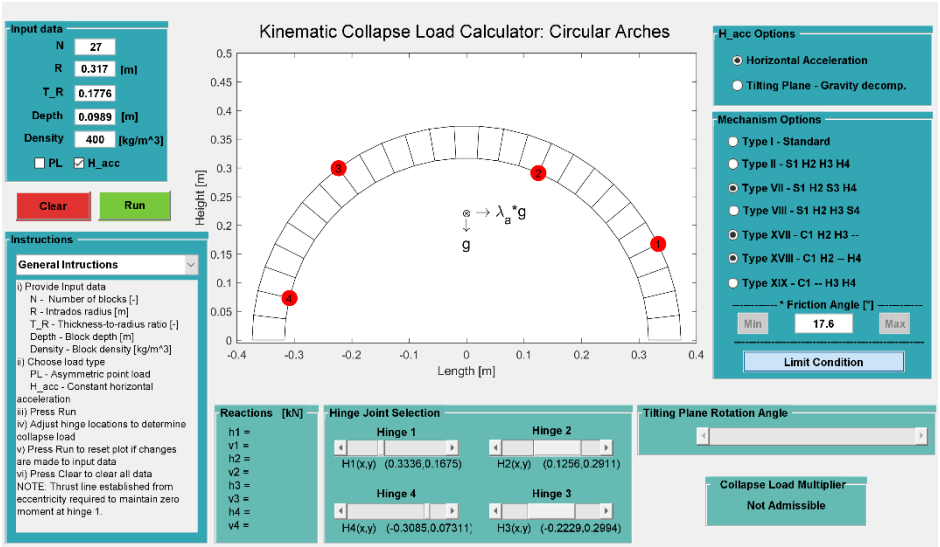

Figure 104. Non-admissible system at the end of the limiting condition sequence shown in Figure 103

4.2.4 KCLC and Generic Arches

Based upon the equations of equilibrium in Chapter 3, it can be seen that the information required to calculate capacity and admissibility through the black box analysis approach is the load geometry, arch block geometry, mechanical joint locations, and the centroid and magnitude of each blocks mass. Adding the assumptions of uniform depth and density as well means that the centroid of each elements center of mass can be determined through calculating the centroid of its area. AutoCAD® thus provides the ideal tool to establish these geometric parameters, but the simplicity of the equations of equilibrium does not transpose into simplified general reaction and collapse load equations, nor is AutoCAD® the ideal platform for matrix manipulations. The KCLC has already shown that MATLAB® provides an ideal space for matrix manipulations and the creation of simple analysis tools, but it lacks the ease and efficiency of drafting. In order to utilize the strengths of both programs, an AutoLISP® script was created to extract the arch geometry information and compile it into a text file that can be read in MATLAB® [127]. The script connects the selected boundary points into blocks with lines and executes the *massprop* function on each block [128]. The boundary points, centroid and area for each block are then compiled. The blocks and centroids are also drawn on the AutoCAD® file to check their accuracy before saving the text file. Figure 105 through Figure 108 show the geometric data extraction sequence applied to a tapered arch, a drop arch, a lancet arch with the trinity detail, and a rough arch respectively. Note that a simplified KCLC was employed with the minimum stable mechanism shown to highlight the data extraction and incorporation sequence.

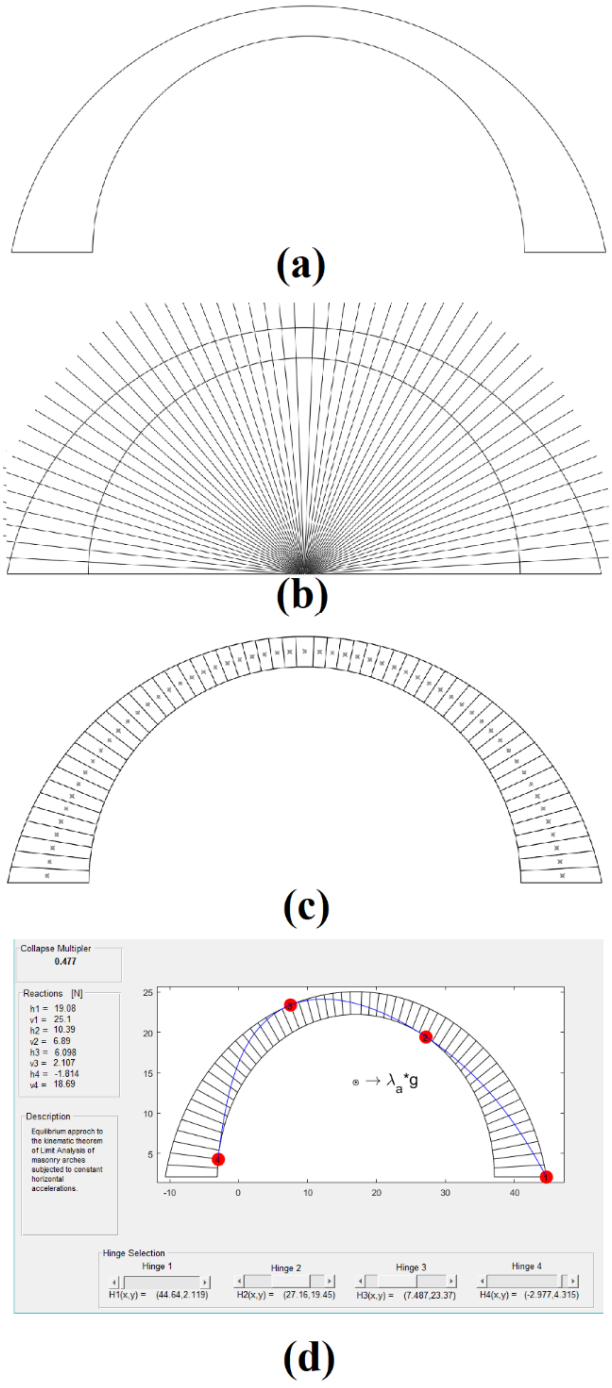

Figure 105. A (a) drawn tapered arch with (b) defined block boundaries and the (c) resulting arch data and (d) its incorporation into a custom KCLC

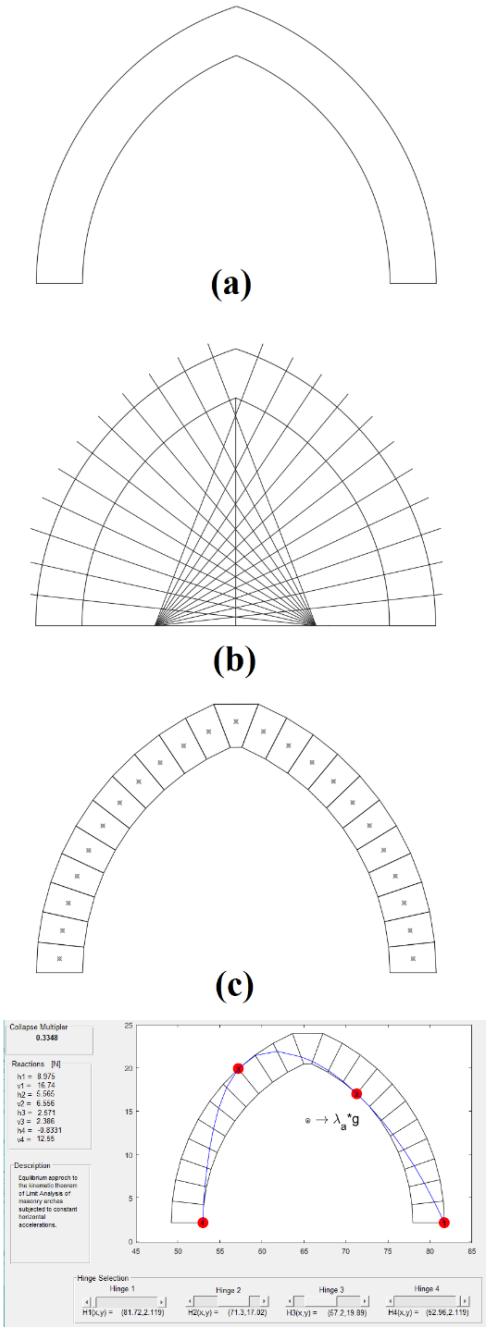

Figure 106. A (a) drawn drop arch with (b) defined block boundaries and the (c) resulting arch data and (d) its incorporation into a custom KCLC

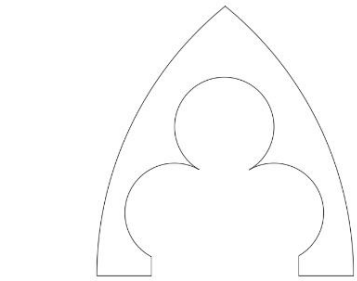

(a)

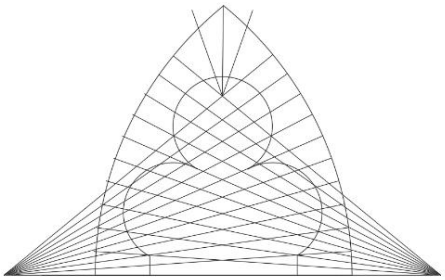

(b)

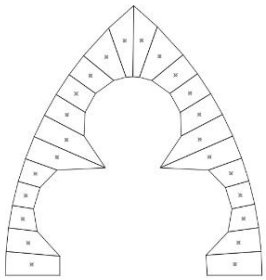

(c)

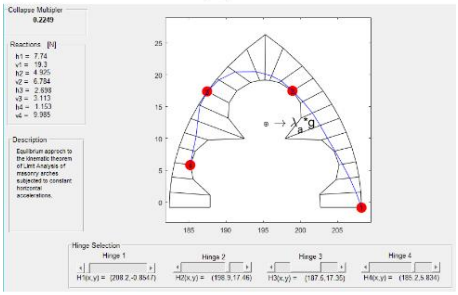

(d)

Figure 107. A (a) drawn lancet arch with (b) defined block boundaries and the (c) resulting arch data and (d) its incorporation into a custom KCLC

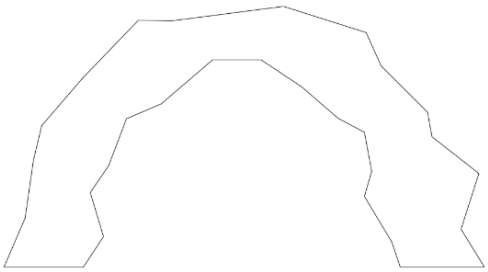

(a)

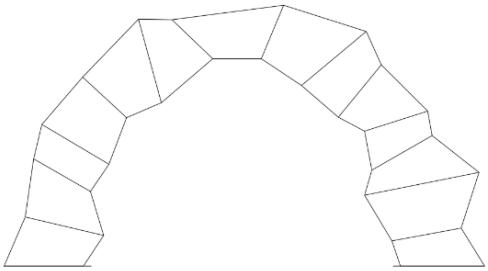

(b)

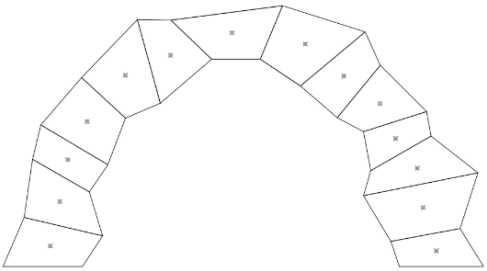

(c)

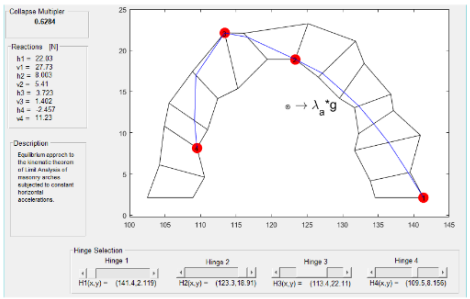

(d)

Figure 108. A (a) drawn rough arch with (b) defined block boundaries and the (c) resulting arch data and (d) its incorporation into a custom KCLC

4.2.4.1 Generic Arches and the Limiting Condition

The generic arches derived from the data extraction technique can also be incorporated into the KCLC with the limiting condition sequence for horizontal accelerations. Figure 109 shows the limiting condition applied to the drawn tapered arch after the minimum friction angle was determined for the Type II mechanism and the given mechanical joint set.

Figure 110 shows another example with the limiting condition sequence applied to the lancet arch. Again, the minimum friction angle was determined for the Type II mechanism and the given mechanical joint set. This limiting sequence is notable in the small variances in all the admissible mechanism and that Type I and Type XIX have equivalent capacities. Between the various arches considered, both the versatility of the approach and the importance of extending the evaluation beyond the standard four-hinge mechanism is observed. Also note the non-admissible ending of the sequence is not shown.

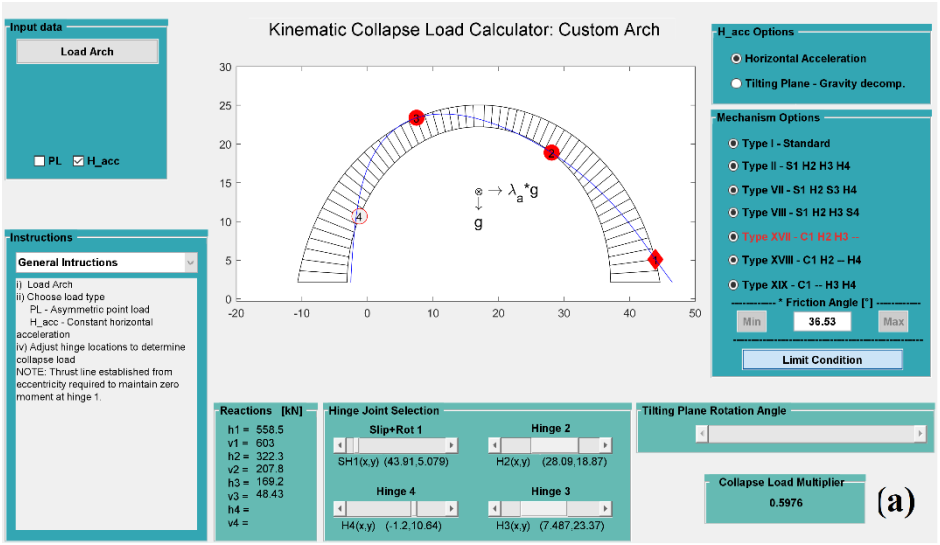
Input data
Load Arch
PL
H_acc
Kinematic Collapse Load Calculator: Custom Arch
H_acc Options
Horizontal Acceleration
Tilting Plane - Gravity decomp.
Mechanism Options
Type I - Standard
Type II - S1 H2 H3 H4
Type VII - S1 H2 S3 H4
Type VIII - S1 H2 H3 S4
Type XVII - C1 H2 H3 --
Type XVIII - C1 H2 -- H4
Type XIX - C1 -- H3 H4
* Friction Angle [°]
Min
36.53
Max
Limit Condition
Instructions
General Intructions
i) Load Arch
ii) Choose load type
PL - Asymmetric point load
H_acc - Constant horizontal acceleration
iv) Adjust hinge locations to determine collapse load
NOTE: Thrust line established from eccentricity required to maintain zero moment at hinge 1.
Reactions [kN]
h1 = 558.5
v1 = 603
h2 = 322.3
v2 = 207.8
h3 = 169.2
v3 = 48.43
h4 =
v4 =
Hinge Joint Selection
Slip+Rot 1
SH1(x,y) (43.91,5.079)
Hinge 2
H2(x,y) (28.09,18.87)
Hinge 4
H4(x,y) (-1.2,10.64)
Hinge 3
H3(x,y) (7.487,23.37)
Tilting Plane Rotation Angle
Collapse Load Multiplier
0.5976
(a)

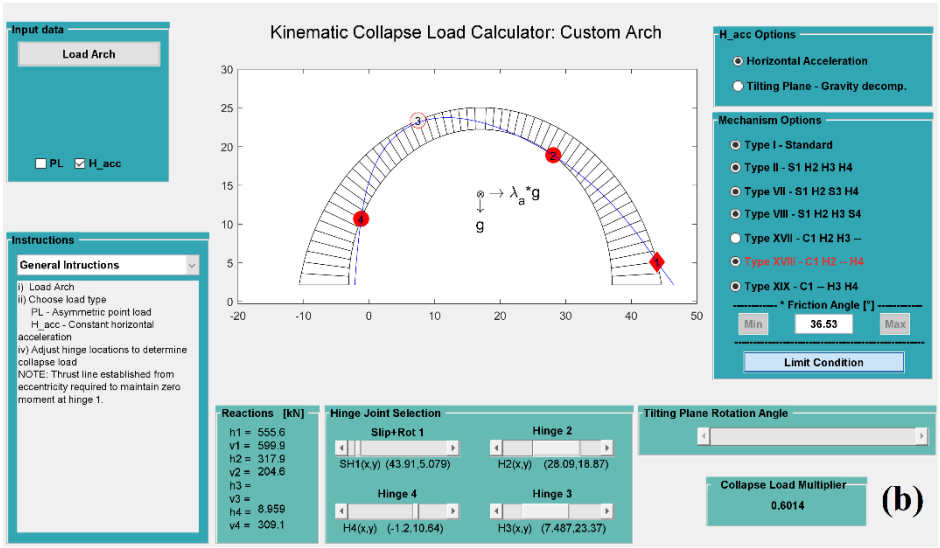
Input data
Load Arch
PL
H_acc
Kinematic Collapse Load Calculator: Custom Arch
H_acc Options
Horizontal Acceleration
Tilting Plane - Gravity decomp.
Mechanism Options
Type I - Standard
Type II - S1 H2 H3 H4
Type VII - S1 H2 S3 H4
Type VIII - S1 H2 H3 S4
Type XVII - C1 H2 H3 --
Type XVIII - C1 H2 -- H4
Type XIX - C1 -- H3 H4
* Friction Angle [°]
Min
36.53
Max
Limit Condition
Instructions
General Intructions
i) Load Arch
ii) Choose load type
PL - Asymmetric point load
H_acc - Constant horizontal acceleration
iv) Adjust hinge locations to determine collapse load
NOTE: Thrust line established from eccentricity required to maintain zero moment at hinge 1.
Reactions [kN]
h1 = 555.6
v1 = 599.9
h2 = 317.9
v2 = 204.6
h3 =
v3 =
h4 = 8.959
v4 = 309.1
Hinge Joint Selection
Slip+Rot 1
SH1(x,y) (43.91,5.079)
Hinge 2
H2(x,y) (28.09,18.87)
Hinge 4
H4(x,y) (-1.2,10.64)
Hinge 3
H3(x,y) (7.487,23.37)
Tilting Plane Rotation Angle
Collapse Load Multiplier
0.6014
(b)

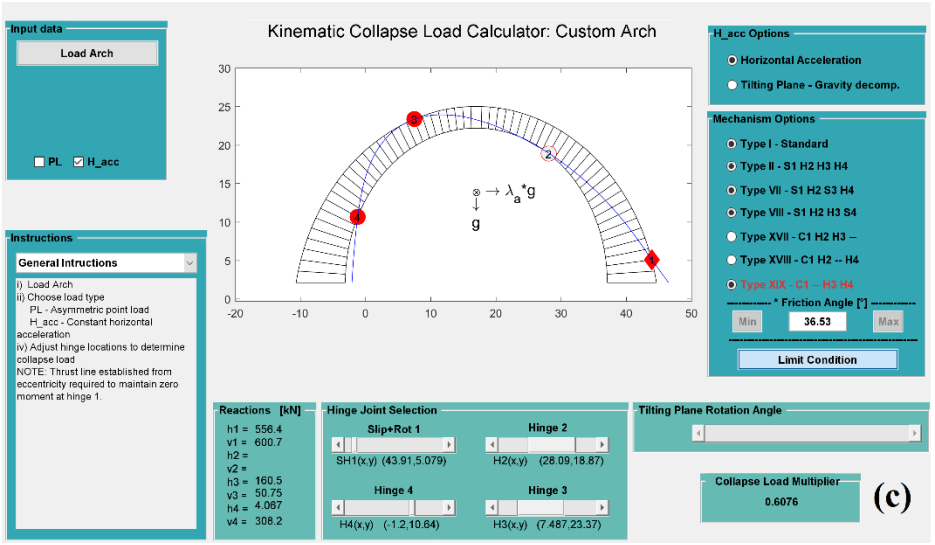
Input data
Load Arch
PL
H_acc
Kinematic Collapse Load Calculator: Custom Arch
H_acc Options
Horizontal Acceleration
Tilting Plane - Gravity decomp.
Mechanism Options
Type I - Standard
Type II - S1 H2 H3 H4
Type VII - S1 H2 S3 H4
Type VIII - S1 H2 H3 S4
Type XVII - C1 H2 H3 --
Type XVIII - C1 H2 -- H4
Type XIX - C1 -- H3 H4
* Friction Angle [°]
Min
36.53
Max
Limit Condition
Instructions
General Intructions
i) Load Arch
ii) Choose load type
PL - Asymmetric point load
H_acc - Constant horizontal acceleration
iv) Adjust hinge locations to determine collapse load
NOTE: Thrust line established from eccentricity required to maintain zero moment at hinge 1.
Reactions [kN]
h1 = 556.4
v1 = 600.7
h2 =
v2 =
h3 = 160.5
v3 = 50.75
h4 = 4.087
v4 = 308.2
Hinge Joint Selection
Slip+Rot 1
SH1(x,y) (43.91,5.079)
Hinge 2
H2(x,y) (28.09,18.87)
Hinge 4
H4(x,y) (-1.2,10.64)
Hinge 3
H3(x,y) (7.487,23.37)
Tilting Plane Rotation Angle
Collapse Load Multiplier
0.6076
(c)

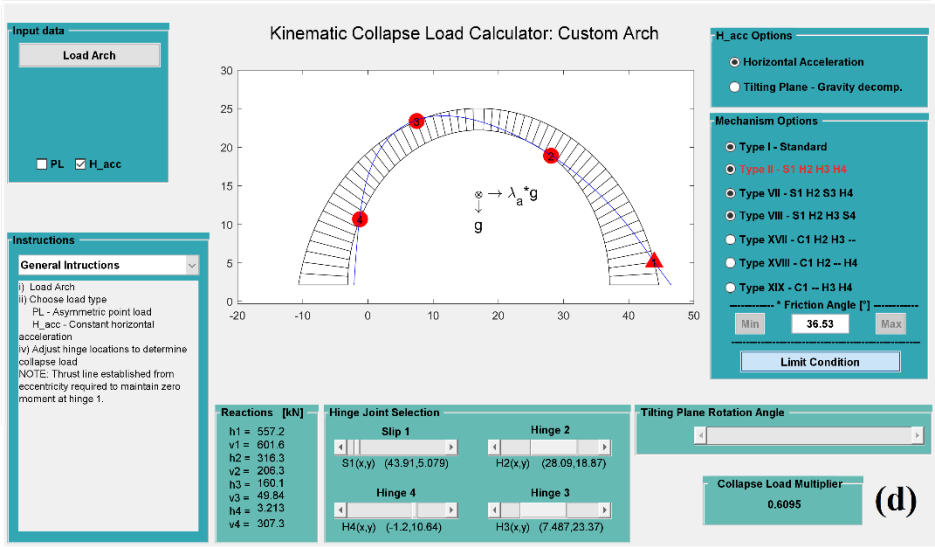
Input data
Load Arch
PL
H_acc
Kinematic Collapse Load Calculator: Custom Arch
H_acc Options
Horizontal Acceleration
Tilting Plane - Gravity decomp.
Mechanism Options
Type I - Standard
Type II - S1 H2 H3 H4
Type VII - S1 H2 S3 H4
Type VIII - S1 H2 H3 S4
Type XVII - C1 H2 H3 --
Type XVIII - C1 H2 -- H4
Type XIX - C1 -- H3 H4
* Friction Angle [°]
Min
36.53
Max
Limit Condition
Instructions
General Intructions
i) Load Arch
ii) Choose load type
PL - Asymmetric point load
H_acc - Constant horizontal acceleration
iv) Adjust hinge locations to determine collapse load
NOTE: Thrust line established from eccentricity required to maintain zero moment at hinge 1.
Reactions [kN]
h1 = 557.2
v1 = 601.6
h2 = 316.3
v2 = 206.3
h3 = 160.1
v3 = 49.84
h4 = 3.213
v4 = 307.3
Hinge Joint Selection
Slip 1
S1(x,y) (43.91,5.079)
Hinge 2
H2(x,y) (28.09,18.87)
Hinge 4
H4(x,y) (-1.2,10.64)
Hinge 3
H3(x,y) (7.487,23.37)
Tilting Plane Rotation Angle
Collapse Load Multiplier
0.6095
(d)

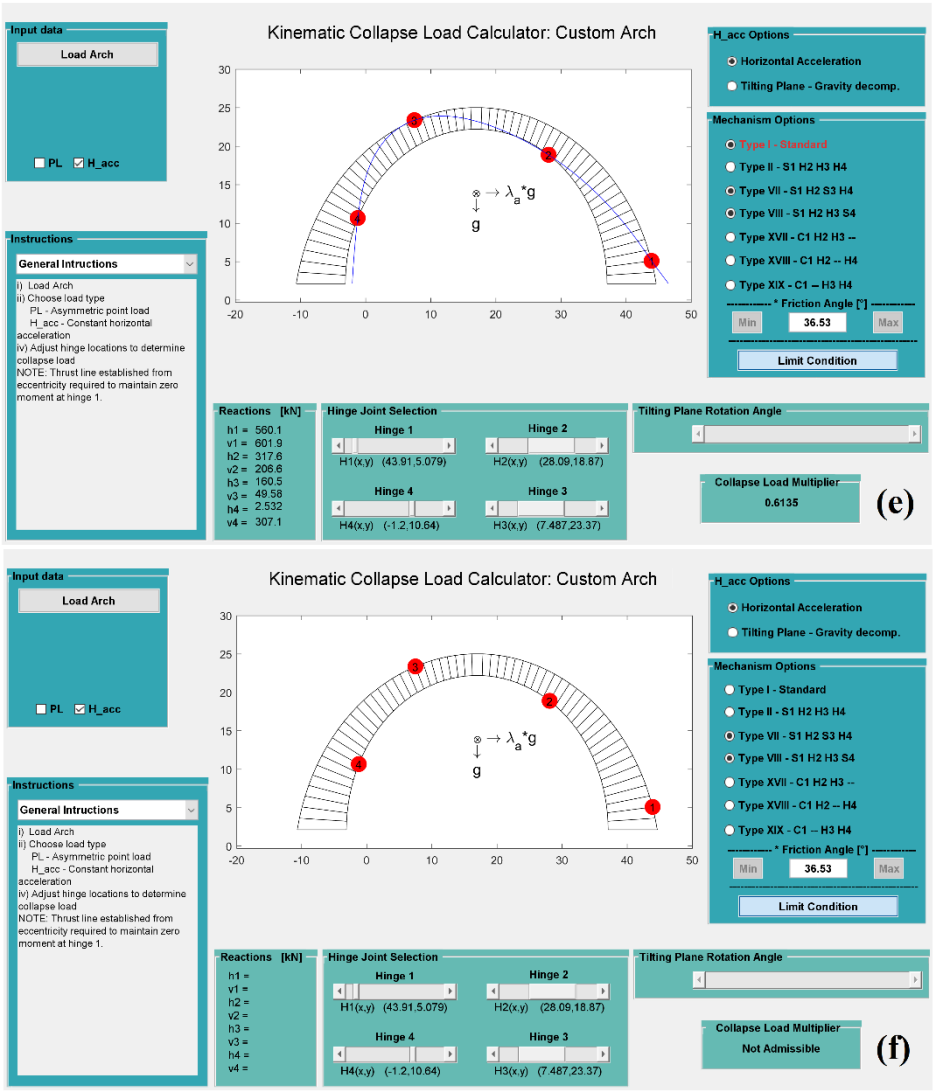

Figure 109. Limiting condition sequence of the tapered arch

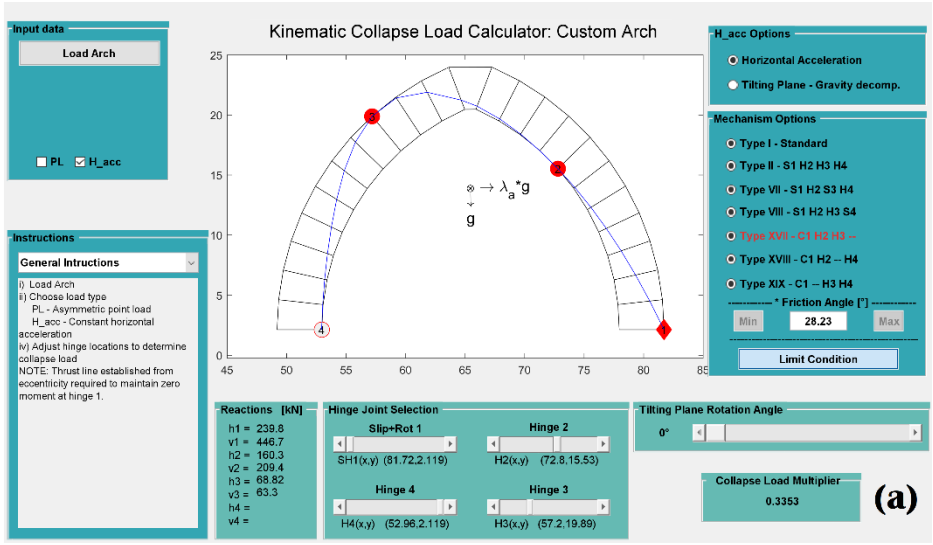
Input data
Load Arch
PL
H_acc
Kinematic Collapse Load Calculator: Custom Arch
H_acc Options
Horizontal Acceleration
Tilting Plane - Gravity decomp.
Mechanism Options
Type I - Standard
Type II - S1 H2 H3 H4
Type VII - S1 H2 S3 H4
Type VIII - S1 H2 H3 S4
Type XVII - C1 H2 H3 --
Type XVIII - C1 H2 -- H4
Type XIX - C1 -- H3 H4
* Friction Angle [°] *
Min
28.23
Max
Limit Condition
Instructions
General Intructions
i) Load Arch
ii) Choose load type
PL - Asymmetric point load
H_acc - Constant horizontal acceleration
iv) Adjust hinge locations to determine collapse load
NOTE: Thrust line established from eccentricity required to maintain zero moment at hinge 1.
Reactions [kN]
h1 = 239.8
v1 = 446.7
h2 = 160.3
v2 = 209.4
h3 = 68.82
v3 = 63.3
h4 =
v4 =
Hinge Joint Selection
Slip+Rot 1
SH1(x,y) (81.72,2.119)
Hinge 2
H2(x,y) (72.8,15.53)
Hinge 4
H4(x,y) (52.96,2.119)
Hinge 3
H3(x,y) (57.2,19.89)
Tilting Plane Rotation Angle
0°
Collapse Load Multiplier
0.3353
(a)

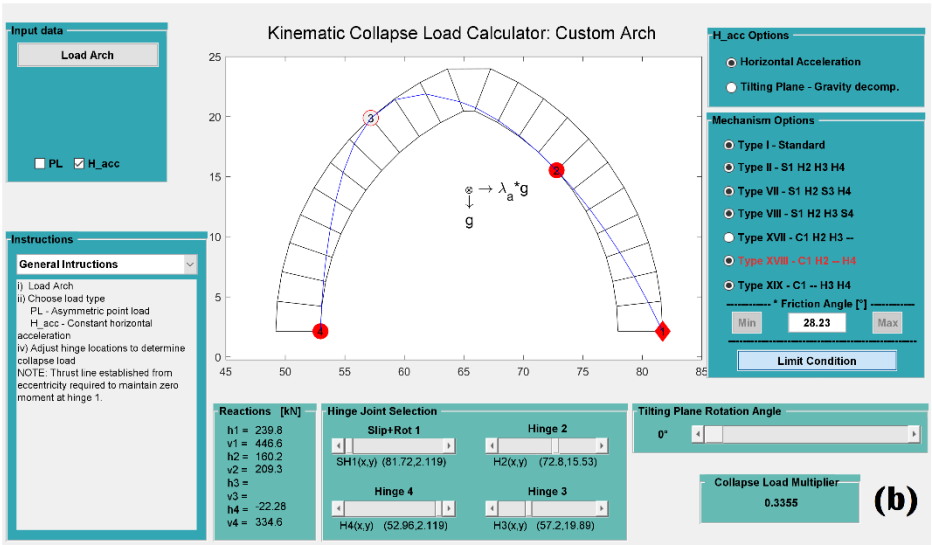
Input data
Load Arch
PL
H_acc
Kinematic Collapse Load Calculator: Custom Arch
H_acc Options
Horizontal Acceleration
Tilting Plane - Gravity decomp.
Mechanism Options
Type I - Standard
Type II - S1 H2 H3 H4
Type VII - S1 H2 S3 H4
Type VIII - S1 H2 H3 S4
Type XVII - C1 H2 H3 --
Type XVIII - C1 H2 -- H4
Type XIX - C1 -- H3 H4
* Friction Angle [°] *
Min
28.23
Max
Limit Condition
Instructions
General Intructions
i) Load Arch
ii) Choose load type
PL - Asymmetric point load
H_acc - Constant horizontal acceleration
iv) Adjust hinge locations to determine collapse load
NOTE: Thrust line established from eccentricity required to maintain zero moment at hinge 1.
Reactions [kN]
h1 = 239.8
v1 = 446.6
h2 = 160.2
v2 = 209.3
h3 =
v3 =
h4 = -22.28
v4 = 334.6
Hinge Joint Selection
Slip+Rot 1
SH1(x,y) (81.72,2.119)
Hinge 2
H2(x,y) (72.8,15.53)
Hinge 4
H4(x,y) (52.96,2.119)
Hinge 3
H3(x,y) (57.2,19.89)
Tilting Plane Rotation Angle
0°
Collapse Load Multiplier
0.3355
(b)

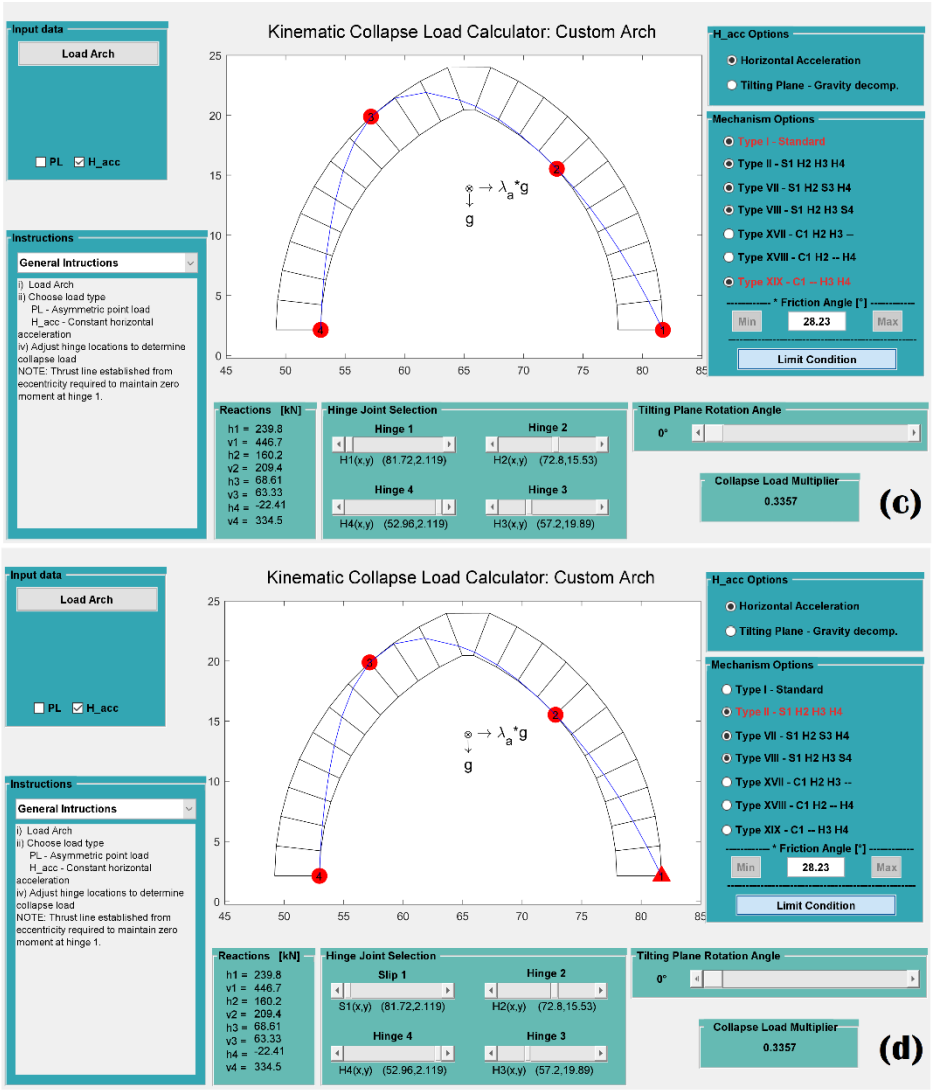

Figure 110. Limiting condition sequence applied to the drop arch

4.3 Capacity Compensation for Non-Stable Mechanisms

An arch is considered stable if a line of thrust is found to lie entirely within the material boundary. This traditional consideration of the thrust line is not a requirement of kinematic admissibility, which considers the condition of motion. In establishing the condition of motion through kinematic equilibrium and the subsequent evaluation of its admissibility, the only constraints applied are at the mechanical joints. This allows the thrust line in its traditional consideration to

exist outside the material boundaries of the arch. The thrust line however is a physical phenomenon as observed through the hanging chain and its existence outside the material of the arch violates the laws governing forces. Consequently, the existence of a kinematically admissible non-stable configuration requires an adjustment to the thrust line such that it once again lies entirely within the material boundary.

The thrust line can be adjusted by imposing an eccentric shift at each block joint where the thrust line lies outside the material boundary and balancing it with a required moment. Utilizing the free-body diagrams for thrust point calculations (Section 4.1) in combination with the calculated thrust point position, $(\hat{x}, \hat{y})$ allows the eccentricity to be determined by

$$e_i = \sqrt{(\hat{x} - x_b)^2 + (\hat{y} - y_b)^2} \tag{105}$$

where (x_b, y_b) are the nearest joint boundary coordinates to the thrust point position. The normal reaction force to the joint line can be determined by through the geometric relationships (see Figure 19) derived for the slip joint evaluations in Section 3.3 with the friction angle replacing α as the variable in Eqns. 25-28.

With the normal force and eccentricity determined, the required moment to maintain the thrust line within the joint boundary can be obtained through Eqn. 21. Therefore, by adjusting the thrust line through an eccentricity shift, a local joint-based moment capacity requirement is introduced to the system. This capacity requirement is necessary to maintain the rigid element assumption and obtain traditionally non-stable kinematically admissible failure states.

This joint based moment requirement can be achieved through the application of a flexural hinge reinforcement technique such as the application of FRPs or TRM. If a tensile reinforcement is applied to the external surface of the arch, then the required tensile capacity, *T*, of the reinforcement can be determined by;

$$T_i = M_i \cdot t_i \tag{106}$$

for the i^{th} joint with thickness *t*. Thus, the minimum reinforcement configuration and capacity can be established for the non-stable kinematically admissible condition.

Figure 111 and Figure 112 show the implementation of the capacity compensation into the KCLC structure for the moment and tension evaluations applied to the drop arch. First a Thrust Line Point Selection slider was added in conjunction with a blue dot on the thrust line plot indicating the location of the thrust point under evaluation. A Thrust Force panel displaying the normal, F_n and parallel, F_p, components of the thrust force at the selected thrust point was added to the display in order to directly obtain the forces at the joint. A Capacity Compensation panel was also added with a checkbox for the moment representation, M_n, and the tensile representation, T_n, of any capacity compensation requirements. Lastly, in the plot window, a small dot was added to the joints that require a capacity compensation in the center for the evaluation of moments (Figure 111) and at the boundary where the tensile resistance is required under the tension evaluation (Figure 112). When the selected thrust

point lies within the joint boundary the capacity compensation values are zero (see Figure 111b and Figure 112a). For joints requiring the capacity compensation, the required moment (Figure 111a) or tension (Figure 112b) is displayed. Also note that the capacity compensation requirements are an additive condition to the equilibrium solution and therefore the tension requirements must be balanced with additional compressive normal forces to maintain equilibrium. The additional compressive forces are directly added to the displayed thrust normal force (see Figure 112b).

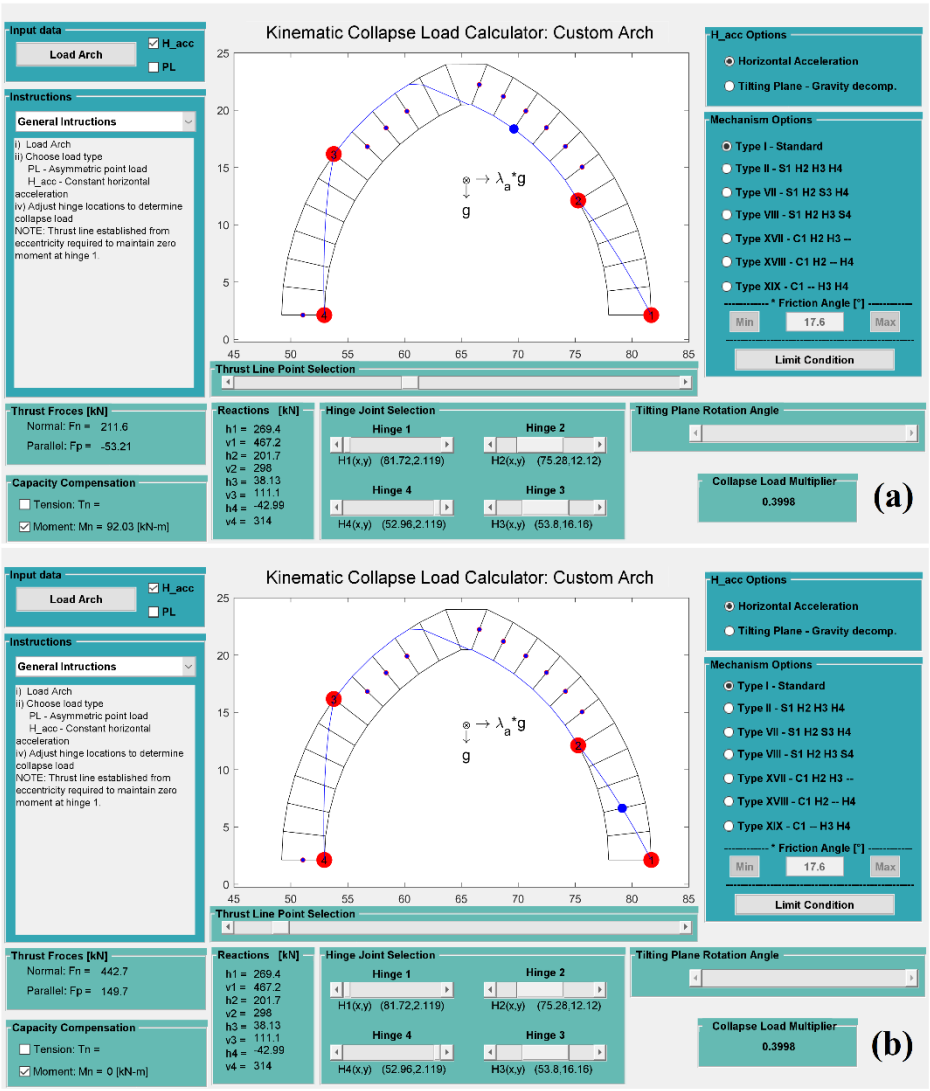

Figure 111. Moment capacity compensation for the drop arch and defined hinge configuration with a (a) non-stable joint and a(b) stable joint selected as indicated by the blue dot on the thrust line plot

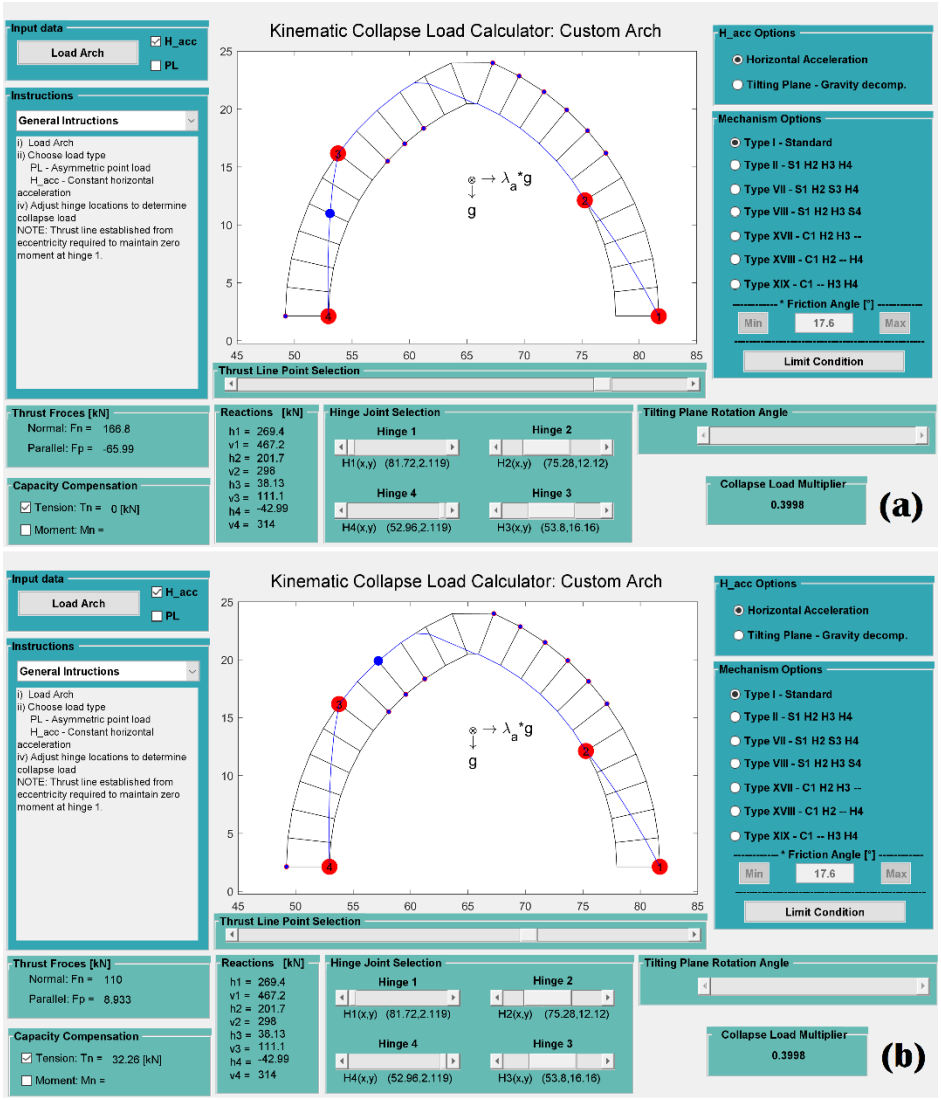

Figure 112. Tensile capacity compensation for the drop arch and defined hinge configuration with a (a) stable joint and a (b) non-stable joint selected as indicated by the blue dot on the thrust line plot

Combining the capacity compensation with limiting condition evaluation reveals the potential to reduce an arches capacity from reinforcing. Figure 113 shows the comparison of the Type XIX and Type I mechanisms for the tapered arch with the tension force selected for the capacity compensation display. From this figure it can be seen that the Type XIX mechanism requires the continuous reinforcement of over half the joints of the arch, but the resulting capacity is dramatically reduced when compared against the traditional Type I mechanism.

This highlights the importance of a reinforcing strategy and a clear definition of the desired mechanism to prevent unwanted collapse mechanisms.

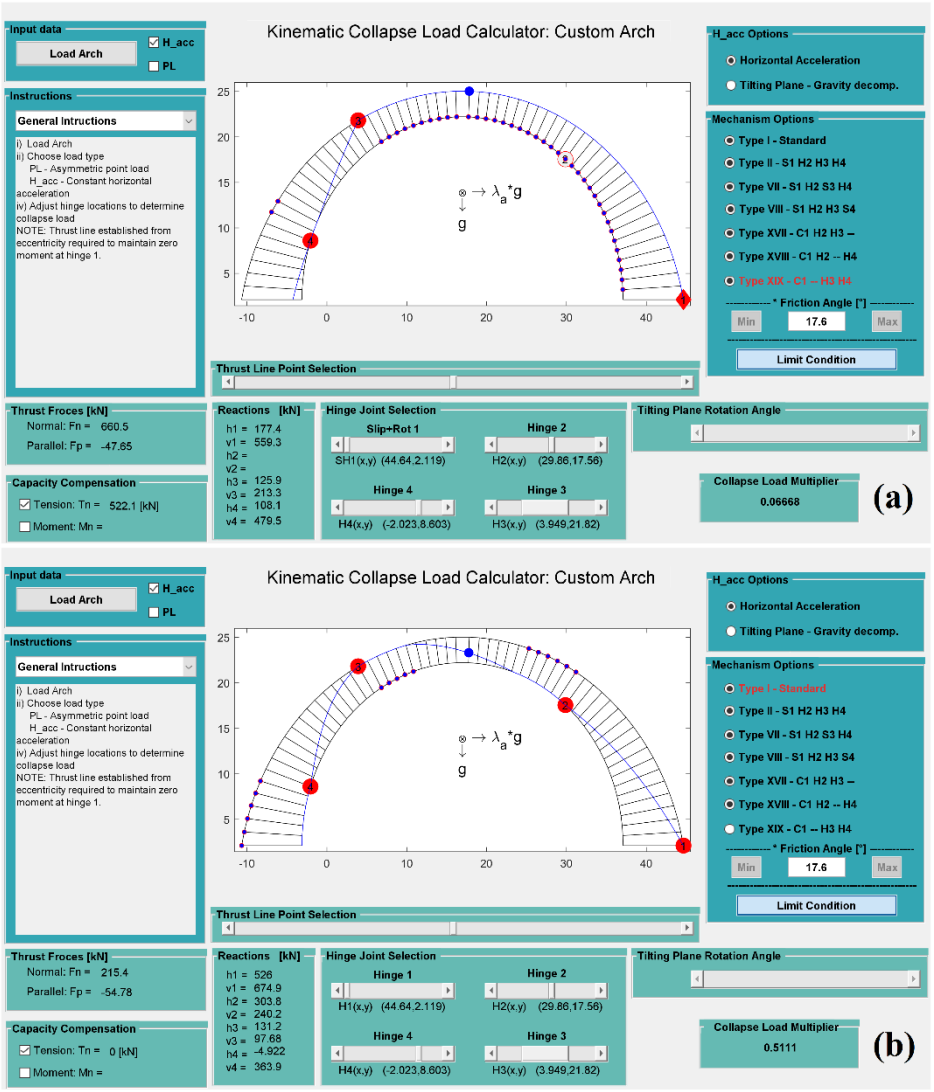

Figure 113. Comparison of the capacity compensation for the (a) Type XIX and (b) Type I mechanisms for the tapered arch and given hinge configuration

4.4 Mechanical Deformations

The final consideration in the black box analysis of dry-stack masonry arches is the direct incorporation of the mechanical deformations from the defined kinematic condition and the effects they can have on the system. It is widely accepted that an arch can be in a mechanically deformed condition while

maintaining a static state. These deformed conditions can arise from foundation settlements, finite reinforcement stiffness and loading conditions the initiate the mechanical failure but do not provide the additional force required to reach collapse. These mechanically deformed static states result in changes to the boundary conditions, but they must abide by the same kinematic equilibrium and admissibility conditions as their undeformed counterparts under static evaluations. Therefore, the ability to impose these deformations in the analysis structure is necessary.

In terms of motion, the kinematic condition of a dry-stack masonry arch is a Single Degree of Freedom (SDOF) problem. For finite hinge stiffness and overloading, this SDOF is confined to the mechanical joints. This section examines this SDOF structure applied to the black box analysis for the traditional motion.

Note that the subsequent discussions and developments in the analysis structure are limited to the standard Type I mechanism. The reason for this is that the primary motivation and subsequent focus is the reintroduction of structural masonry and RSBD as a modern building and design method. In this context, the mechanism is engineered as a Type I through reinforcing against non-ideal mechanisms and any capacity compensation requirements.

4.4.1 Mechanism Motion

To examine the mechanism based SDOF motion, a simplified KCLC was constructed for the dry-stack arch of the first experimental campaign were these static deformations were directly observed (see Section 5.2) [124], [125]. Figure 114 shows the simplified KCLC developed to address the mechanized motion. The SDOF motion is applied through a Hinge Motion slider that imposes the rotation of hinge H_1 and calculates the rotations of the remaining hinges. Also note that the collapse multiplier is the tilting plane rotation angle and the direction of the horizontal acceleration is reversed from previous discussions. These conditions were implemented to directly match the experimental conditions. Refer to Section 5.2 for a detailed description of this experimental campaign.

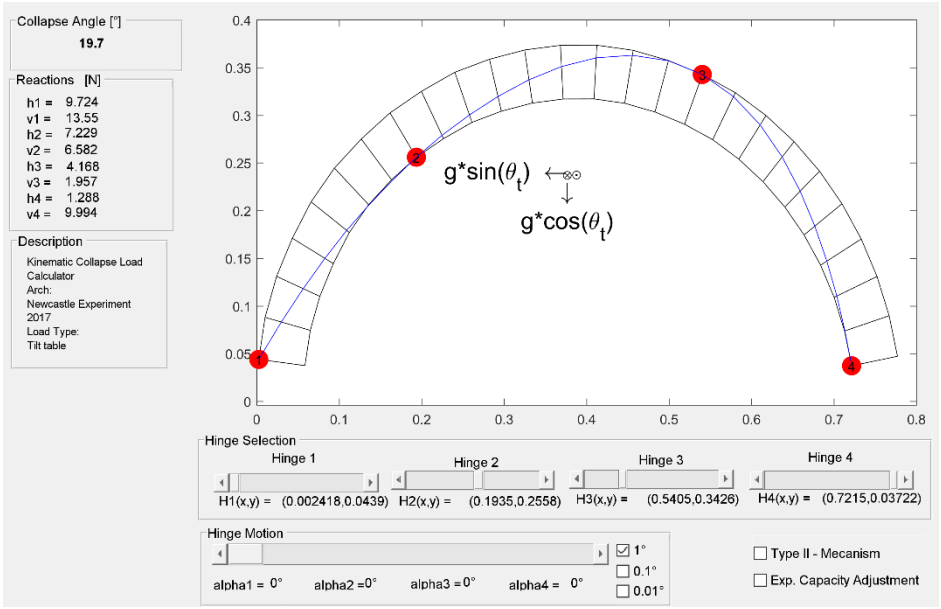

Figure 114. KCLC for the tilting plane and mechanical deformation assessment

SDOF motion requires the definition of one degree of motion to express the total deformation of the system. In the context of a dry-stack arch with defined mechanical hinge joints, the arch-hinge configuration in Figure 114 can be represented by three fixed lengths connected by four pins as seen in Figure 115. The SDOF that bounds the motion is the horizontal displacements of hinges H_2 and H_3. Hinges H_1 and H_4 are translationally fixed to their respective bases and thus are limited to rotations. For a given rotation, $\Delta\alpha_1$, at hinge H_1 the rotation of hinge H_4 can be expressed as

$$\Delta\alpha_4 = \cos^{-1}\left(\frac{l_{12}}{l_{34}}[\cos(\theta_{12}+\Delta\alpha_1)-\cos(\theta_{12})]+\cos(\theta_{43})\right)-\theta_{43} \tag{107}$$

where the lengths and angles are identified in Figure 115. The resulting translations of hinges H_2 and H_3 can then be used to determine the polar change, $\Delta\gamma_{23}$, of the H_2-H_3 connection

$$\Delta\gamma_{23} = \theta'_{23} - \theta_{23} \tag{108}$$

The rotations of hinges H_2 and H_3 are thus

$$\Delta\alpha_2 = \Delta\alpha_1 + \Delta\gamma_{23} \tag{109}$$

and

$$\Delta\alpha_3 = \Delta\alpha_4 + \Delta\gamma_{23} \tag{110}$$

respectively. Therefore, the SDOF motion can be defined solely by the rotation of hinge H_1.

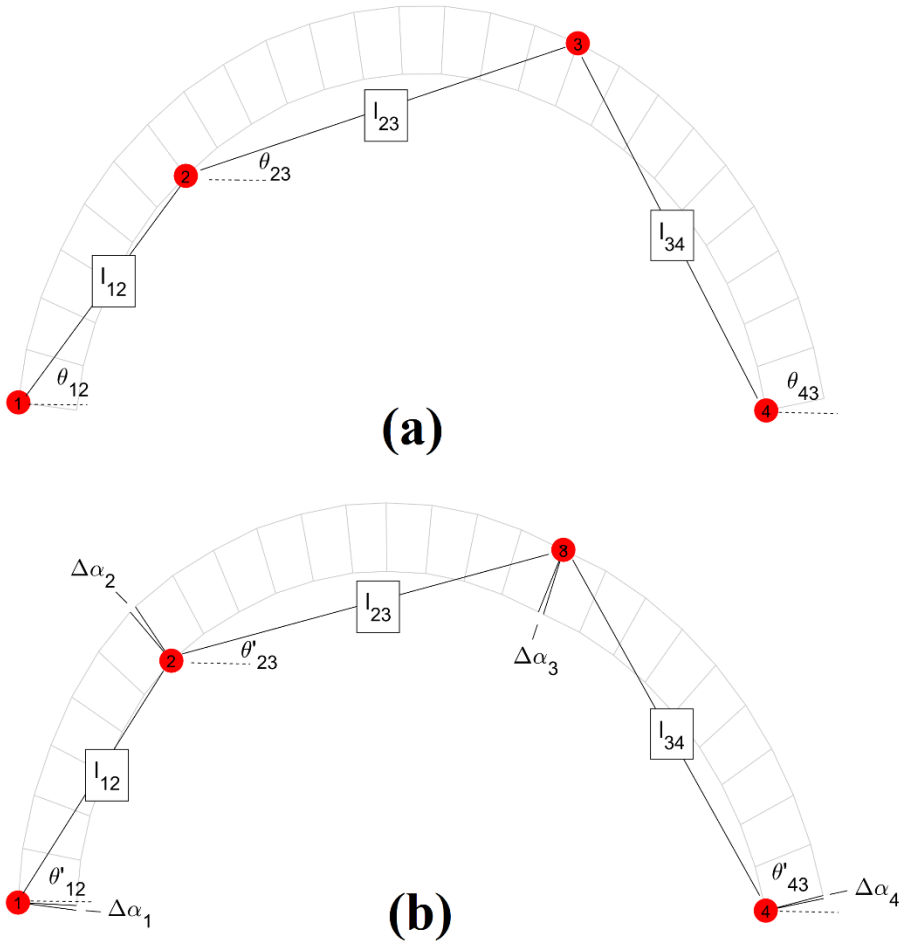

Figure 115. Pin-connected length representation of the standard Type I mechanism in its (a) initial state, and (b) after a deformation

Equations 107-110 are incorporated into the custom KCLC for the experimental arch through the inclusion of a slider that imposes the $\Delta\alpha_1$ rotations to hinge H_1. For a defined rotation, the rigid body rotations are first applied about the points H_1 and H_4 for the block elements associated with lengths l_{12} and l_{34} respectively. Next, the blocks associated with l_{23} are translated to the updated hinge H_2 position and followed by the prescribed rigid body rotations about H_2. After the deformation is applied, the updated boundary points and block centroids are used in the standard kinematic equations of equilibrium and admissibility evaluation. Figure 116 shows the arch-hinge configuration of Figure 114 with an applied deformation of 2° at hinge H_1. The existence of a solution to the applied rotation in Figure 116 indicates that the deformed state of the arch is in an admissible kinematic condition.

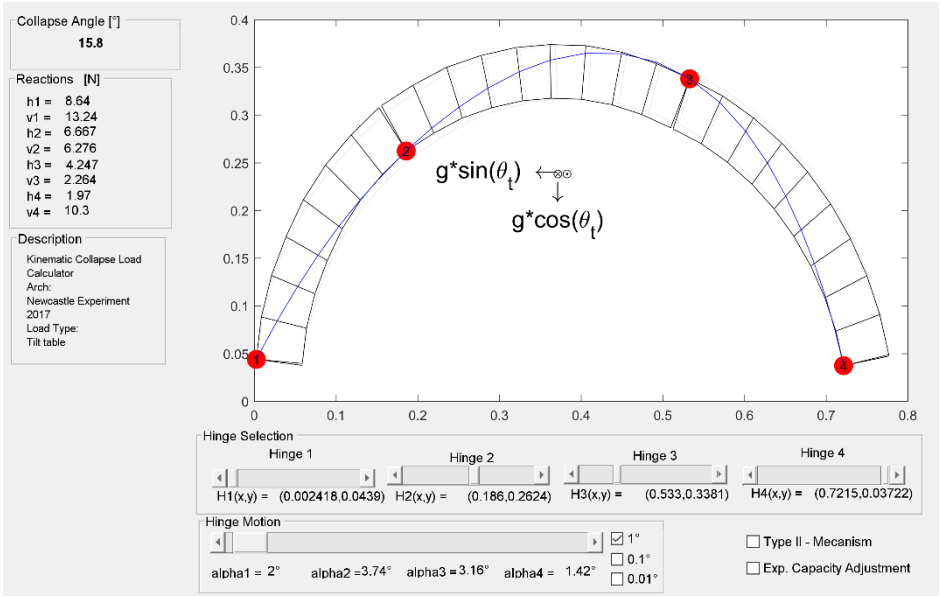

Figure 116. Custom KCLC with 2° rotation at hinge H_1

4.4.2 Kinematic Equilibrium of Static Deformations

Figure 117 shows another custom and simplified KCLC constructed for the evaluation of static deformations under the standard horizontal acceleration condition. In addition to the hinge motion panel, the centroid position information of the mechanical arch is displayed with both the center of mass, CM, and the center of area, CA, provided. This is to account for non-uniform block masses. Each block is assumed to have a uniform density, but that assumption is not held for all the blocks of the arch.

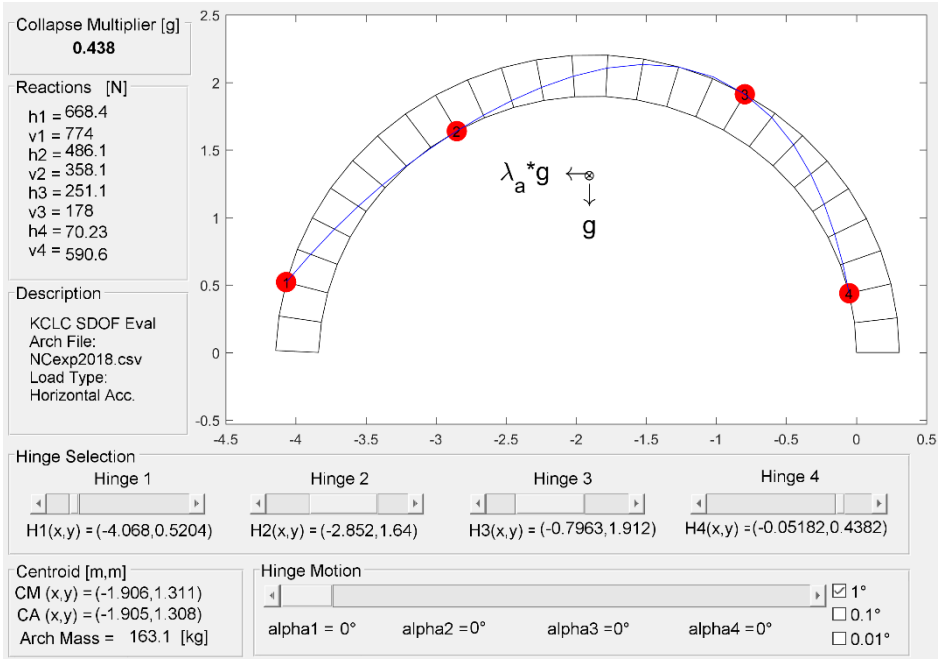

Figure 117. Custom KCLC with hinge rotation and centroid data display.

Figure 118 shows the KCLC and arch-hinge condition of Figure 117 with imposed hinge H_1 rotations of 4°, 8° and 12°. From the deformation sequence, an admissible kinematic free-body diagram is carried through 11° of rotation at H_1. Also note the deformation path of the centroid of the full arch. These conditions provide a clear and quantifiable deformation limit, the ability to evaluate the minimum required work necessary for collapse (see Section 6.1.1), and the establishment of equivalent deformation systems through parametric plotting.

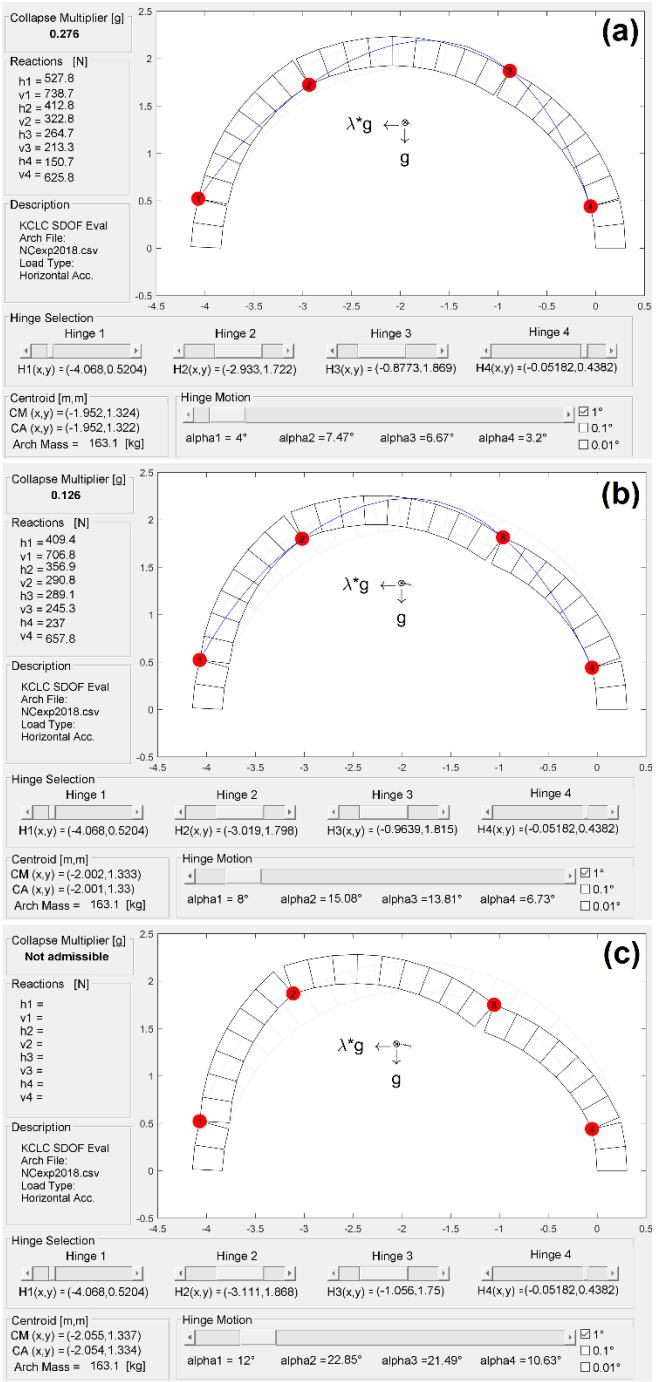

Figure 118. Custom KCLC with (a) 4°, (b) 8° and (c) 12° hinge H_1 rotations applied to the arch-hinge condition

4.4.3 Equivalent Systems

The process of applying a deformation to the mechanical arch-hinge system has been defined for the Type I mechanism through the rigid body rotations of three rigid pin-connected elements. This hinge rotation deformation was applied through the defined hinge H_1 rotation. From the defined rotation, all of the block boundaries and centroids of the deformed system can be obtained and independently evaluated for kinematic equilibrium. This relationship allows the establishment of equivalent systems through parametric plotting.

4.4.3.1 Translations

The record of the full arch centroid position for imposed hinge H_1 rotations generates the position (x,y) and increment (dx,dy) link between the arch element deformations and a single point system. Imposing the total mass at the centroid point and defining energy conservation generates equivalent systems bound by α_1. Figure 119 shows the centroid deformation path for the same arch-hinge configuration as Figure 117 and Figure 118 for α_1 between 0° and 12° with constant $\Delta\alpha_1$ of 0.1°. A polynomial fit of the deformation path reveals a reasonable representation of

$$y = A_1 x^2 + A_2 x + A_3 \tag{111}$$

and for the slope equation

$$\frac{dy}{dx} = \frac{1}{2} A_1 x + A_2 \tag{112}$$

where the constants A_i are shown in the Figure 119.

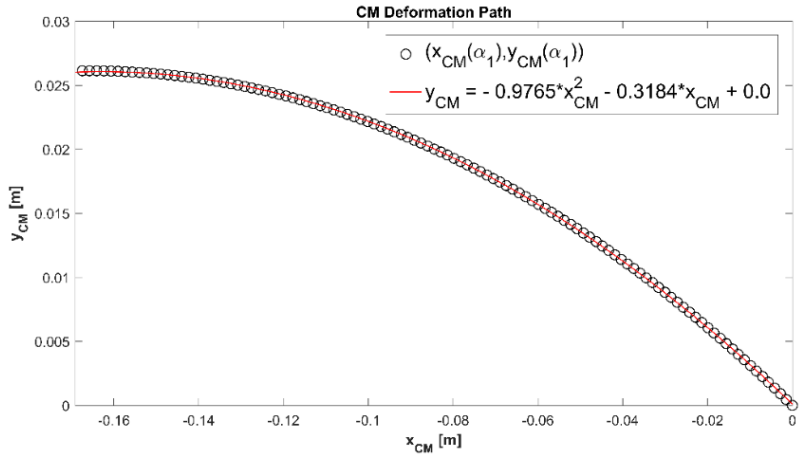

Figure 119. Parametric plot of the CM deformation path and the polynomial fit

4.4.3.2 Rotations

The deformation of the arch involves both the translation and rotation of the three pin-connected elements. The simplification of the structure into a single point system must also carry the consequences of these rotations. Therefore, zero

mass lever arms are defined between the centroid of the full arch and the centroid of each element. Maintaining the conservation of mass in the deformation process requires these lever arm lengths to remain fixed within the bound motion of the Type I mechanism, and this results in rotational changes.

Figure 120 shows the lever arm rotation angles, θ_{Ei}, versus horizontal CM displacement for each element of the arch-hinge configuration in Figure 117 and Figure 118 for α_1 between 0° and 12° with a constant $\Delta\alpha_1$ of 0.1°. A polynomial fit of the lever arm rotation paths reveals that each are reasonably represented by

$$\theta = B_1 x^2 + B_2 x + B_3 \tag{113}$$

and the slope equation by

$$\frac{d\theta}{dx} = \frac{1}{2} B_1 x + B_2 \tag{114}$$

where the constants B_i are shown in the Figure 120.

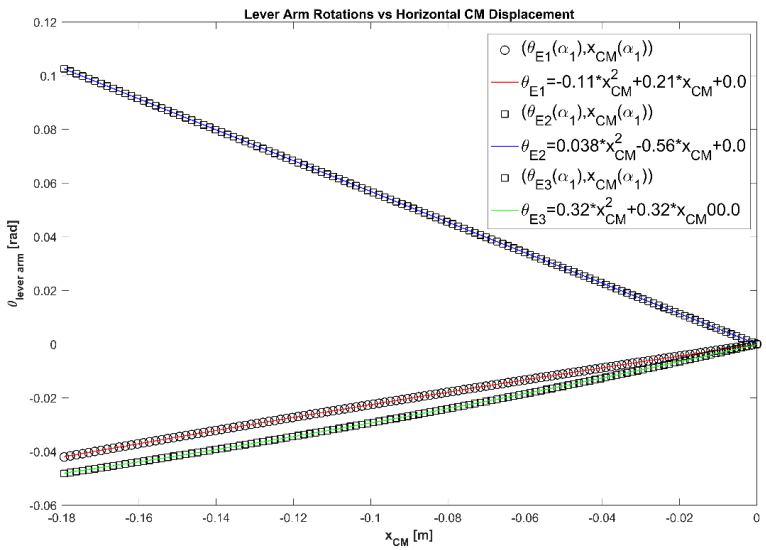

Figure 120. Parametric plots of lever arm rotation angles versus horizontal CM displacements and their polynomial fits

The establishment of the equivalent systems for the CM point translation and lever arm rotation representation of the SDOF deformation sequence allows the simplified establishment of the work equations for a given arch-hinge set condition (see Section 6.1.1).

4.4.4 Finite hinge stiffness

In the event of a finite hinge stiffness, the deformation structure applied to the KCLC allows the hinge positions to be modified after implementing a deformation as can be seen by the transition of hinge H_1 that was imposed after an applied deformation in Figure 121. Thus, the deformation and defined hinge

configuration can be decoupled in the evaluation of an arch. Also note in Figure 121b that a deformed stable configuration is identified between the hinges. This phenomena was directly observed during experimentation and is further discussed in Section 5.2 [124], [125]

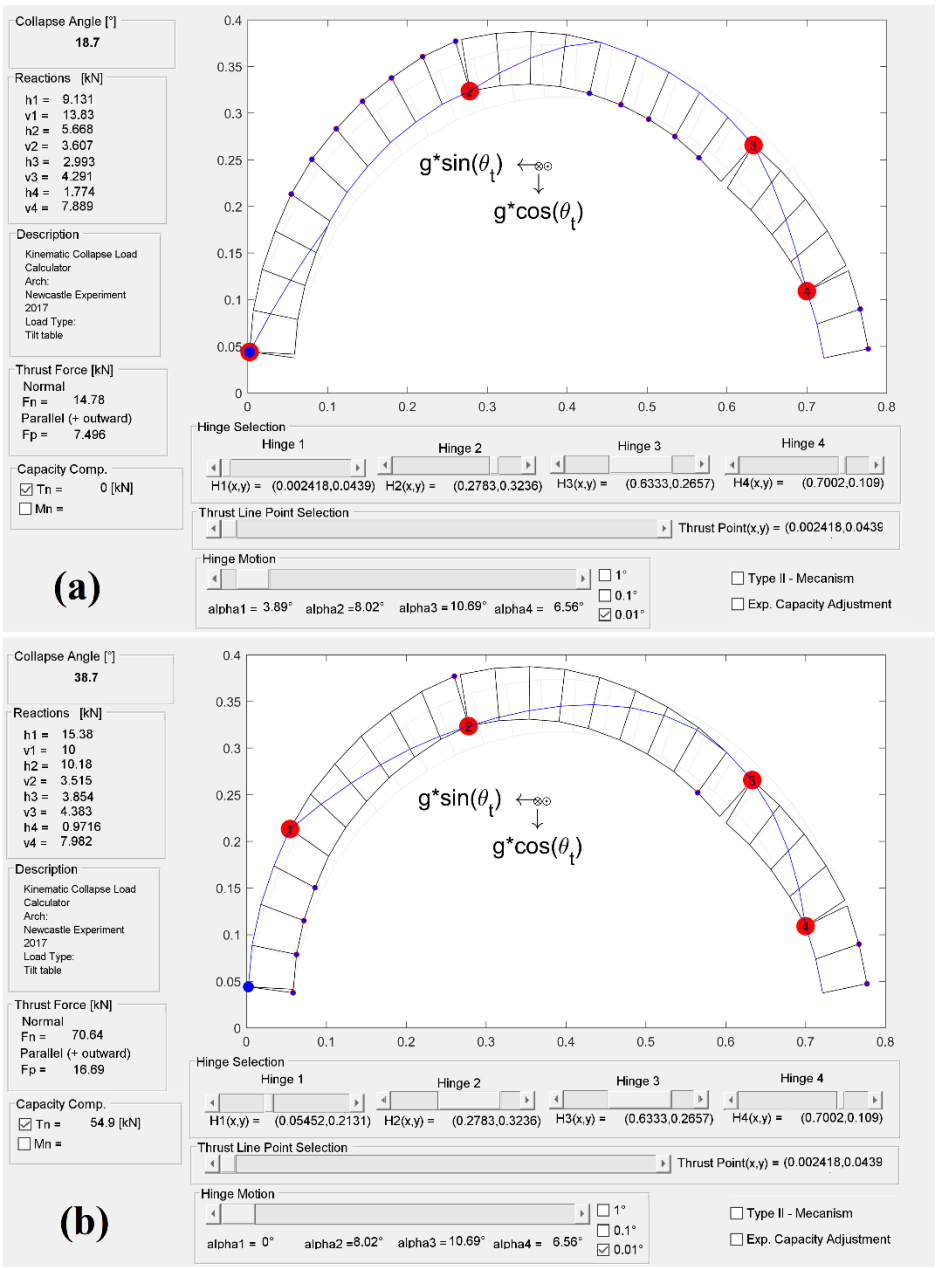

Figure 121. A (a) deformed arch condition and (b) hinge adjustment for evaluation

4.5 Concluding Remarks

Chapter 4 added the condition of kinematic admissibility through the independent calculation of the thrust line from the solutions to the equations of equilibrium and introduced the KCLC as a software structured to carry out the analysis in a black box format. The KCLC software was presented in an evolutionary format to highlight the versatility and adaptability of the software as well as the comprehensive analyses that can be performed under the kinematic equilibrium approach. The incorporation of non-ideal mechanisms revealed limiting condition evaluations amongst mechanisms. The inclusion of generic arch geometries connects the analysis to the most widely used computer aided drafting software and removes the complexity of defining the arch geometry.

Under the context of design and control, the minimum mechanism is not a reasonable evaluation condition as it will change with the various loading conditions required by design standards such as the American Society of Civil Engineer's (ASCE) **MINIMUM DESIGN LOADS AND ASSOCIATED CRITERIA FOR BUILDINGS AND OTHER STRUCTURES**, (also known as ASCE 7) [129]. This issue is corrected however with the capacity compensation requirements required to create the rigid elements between mechanical joints. It is important to note that the material properties have not been considered, and this includes the capacity compensation. The discussion of the reinforcement itself and the details of how it would be applied is outside the scope of this thesis which aims at establishing the extension to the structural analysis of free-body diagrams and equations of equilibrium.

Lastly in Chapter 4, the application of static deformations of the kinematic state was also incorporated into the analysis structure. This allows the analysis of statically deformed conditions, such as those experimentally observed, and introduces the ability to simplify the description of motion through parametric plotting. Again, the additional analysis features are housed under the same black box structure and undergo the same kinematic equilibrium evaluation.

CHAPTER 5

CHARACTERIZATION OF DRY-STACK MASONRY ARCHES

List of Abbreviations and Symbols

α_i — Angle relationship between the reaction vector, the i^{th} joint line, and the friction angle

C_{DEM} — Capacity adjustment equation between experimental and DEM analysis results

C_{LA} — Capacity adjustment equation between experimental and limit analysis results

CLD — Collapse load diagram

CM — Center of mass

DEM — Discrete element modelling

FRP — Fiber reinforced polymer

g — Gravitational acceleration constant

H_i — Identifier for the i^{th} hinge

J_k — Joint identification nomenclature

K_α — Hinge rotation stifness

KCLC — Kinematic collapse load multiplier

L_i — Fixed measurement length along tilting platform from rotation point

l_i — Height measurements of rotated platform lengths L_i

λ_a — Collapse multiplier for uniform acceleration

N_k — Block identification nomenclature

OSB — Oriented standard board

$\boldsymbol{q}$ — Constants vector of the equations of equilibrium

SDOF	—	Single degree of freedom
TRM	—	Textile reinforced mortar
θ_t	—	Tilting plane rotation capacity

The kinematic equilibrium equations (Chapter 3) and their application to the structural analysis of dry dry-stack masonry arches through the condition of admissibility and the black box analysis approach (Chapter 4) have demonstrated a simple analysis methodology. With the aid of the KCLC any defined condition of dry-stack masonry arches becomes accessible to the practicing engineer. A foundation is established for efficient, detailed and comprehensive static analyses of any arch. What is lacking is the characterization of the element itself. Given an arch how does it behave when subjected to hinge control; how can arch geometry and reinforcement be optimized; and how is experimentation linked with the theoretical analyses? Therefore, the behavior of the arch must be examined.

Chapter 5 focuses on the behavior and characterization of the dry-stack masonry arch subjected to hinge control. First, collapse load diagrams (CLD) are developed. These diagrams provide a first-order assessment strategy that can be utilized in the early stages of a project's design. The diagrams also introduce the novel consideration of a family of mechanisms for an arch and lay the framework for experimental testing. Two experimental campaigns are then discussed, one for an in-scale arch and the second for a full-scale arch, both subjected to tilting plane tests for a family of mechanisms defined from the formation of a CLD. It is the objective of the experimental test descriptions to highlight the development and application of the characterization strategy and its repeatability. Additionally, the tilting plane test was chosen because it provides a representation to seismic loading, it is relatively simple to perform with minimal equipment (i.e. the test is accessible to almost anybody), and the uniform distribution of acceleration renders the material density irrelevant.

5.1 Collapse Load Diagrams

First-order strategies of assessment typically exist for modern structural systems. These first-order assessments provide the platform for a project's planning, development, scope, cost estimates and allocation of funds. As such, they are a critical component to the success of any structural system. For civil projects, first-order assessments for structural systems can be carried beyond the 60% design stage. For existing systems, first-order assessment strategies streamline the inspection and intervention process. The speed of the assessments also becomes critical in post disaster situations.

Collapse Load Diagrams (CLD) are a first-order assessment strategy formulated by combining a set of capacity results with a single parameter [130]. These diagrams present the set of minimum collapse loads for all admissible combinations of the base hinges, H_1 and H_4, of the defined arch and plots them against the negative tangent of polar angle between the base hinges. The

construction of the diagrams is achieved by fixing the base hinges and determining the minimum positive collapse load multiplier for the admissible variations on the intermediate hinges, H_2 and H_3. The minimum multiplier and the associated hinge positions are recorded. Next, one base hinge position is changed, and the new minimum is determined for the variations in the intermittent hinges. This procedure is repeated until a minimum collapse load multiplier of all admissible configurations of the base hinges have been obtained. These values are plotted, and lines are drawn connecting the multipliers associated with one of the two base hinges remaining fixed. Figure 122 shows the schematic of the procedure for developing a CLD. Figure 123 and Figure 124 show the CLD and arch geometry for a 27-block semi-circular arch subjected to constant horizontal accelerations (Eqn. 6) and a vertical point load at H_3 (Eqn. 9) loading conditions respectively. In both loading cases, the collapse load diagram is accompanied by a subplot of the arch-load condition which also identifies the limits of admissible base hinge positions. This provides not only the capacity values, but a quick visualization of where the base hinges can be defined in the development of a hinge-controlled arch system.

From Figure 123 and Figure 124 it becomes clear that the CLDs provide a simple technique to present and examine a family of kinematically admissible conditions. Additionally, as mentioned the full hinge set is recorded for each determined minimum positive collapse multiplier presented in the CLD. Therefore, the intermediate hinges can be identified through the base hinge pair associated with a collapse multiplier. This identification can be programmatically or manually achieved though developing tables.

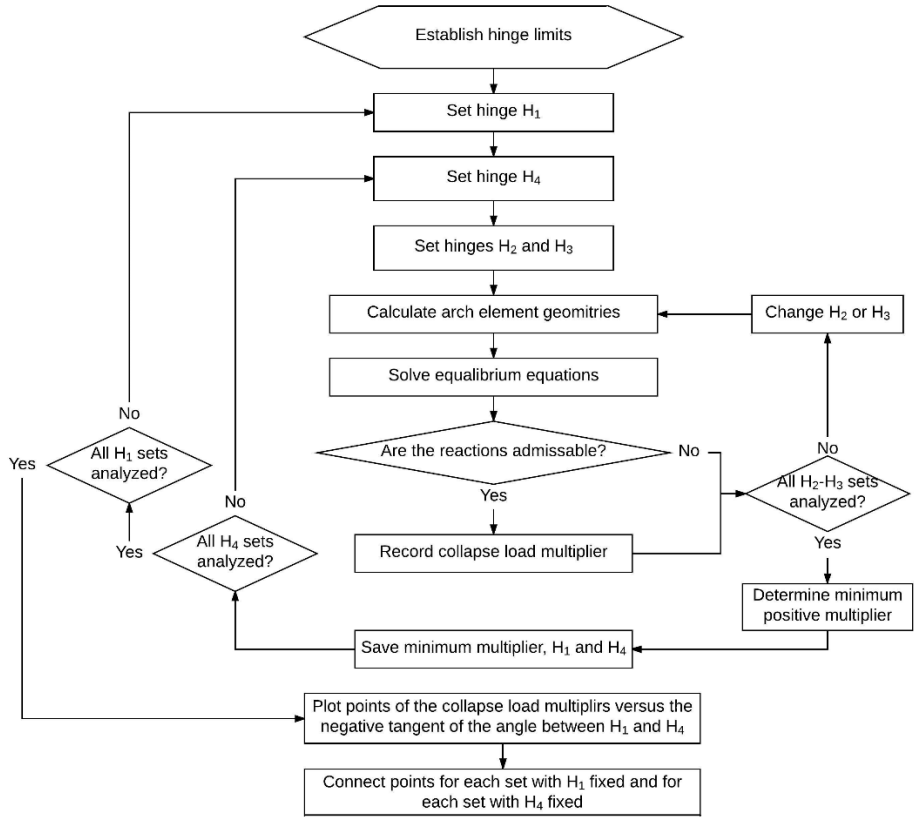

Figure 122. CLD development procedure [130]

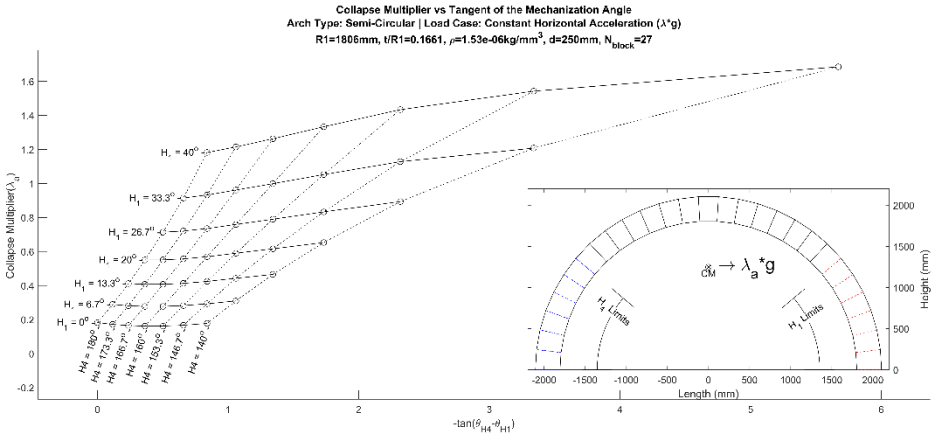

Figure 123. CLD for circular arch subjected to constant horizontal acceleration

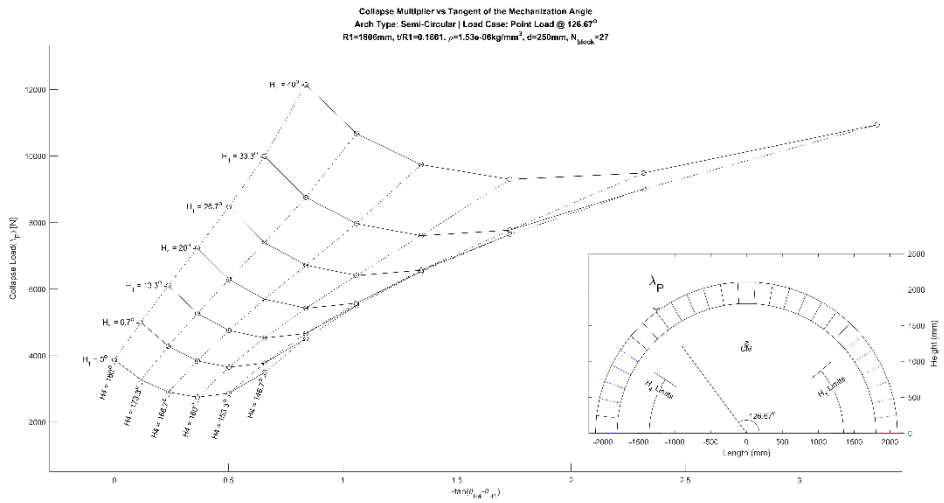

Figure 124. CLD for circular arch subjected to a vertical point load at H_3

The CLDs are developed from the same kinematic equilibrium analysis structure used in the KCLC, and thus also allow the incorporation of any drawn arch geometry through the AutoCAD® data extraction technique as can be seen in the following example [127].

5.1.1 CLD Application Example: Capacity Comparison

Consider two double-curvature arches drawn in AutoCAD® and subjected to a constant horizontal acceleration. Figure 125 shows the two drawn arches. The two arches have the same global dimensions including a clear span of 7.5 m, a crown height of 3.0 m, and a general block structure of a 0.6 m thickness and a 0.3 m intrados length. The differences in the arches is in the applied shifts to the rotation points of the two curves. The first double curvature arch is developed through diagonal shifts in the rotation point of both curves, whereas the second arch only applies a horizontal shift to the smaller radial arcs (see Figure 125). Figure 126 shows the assigned nomenclature for the blocks, N_k, and joints, J_k, of the two arches.

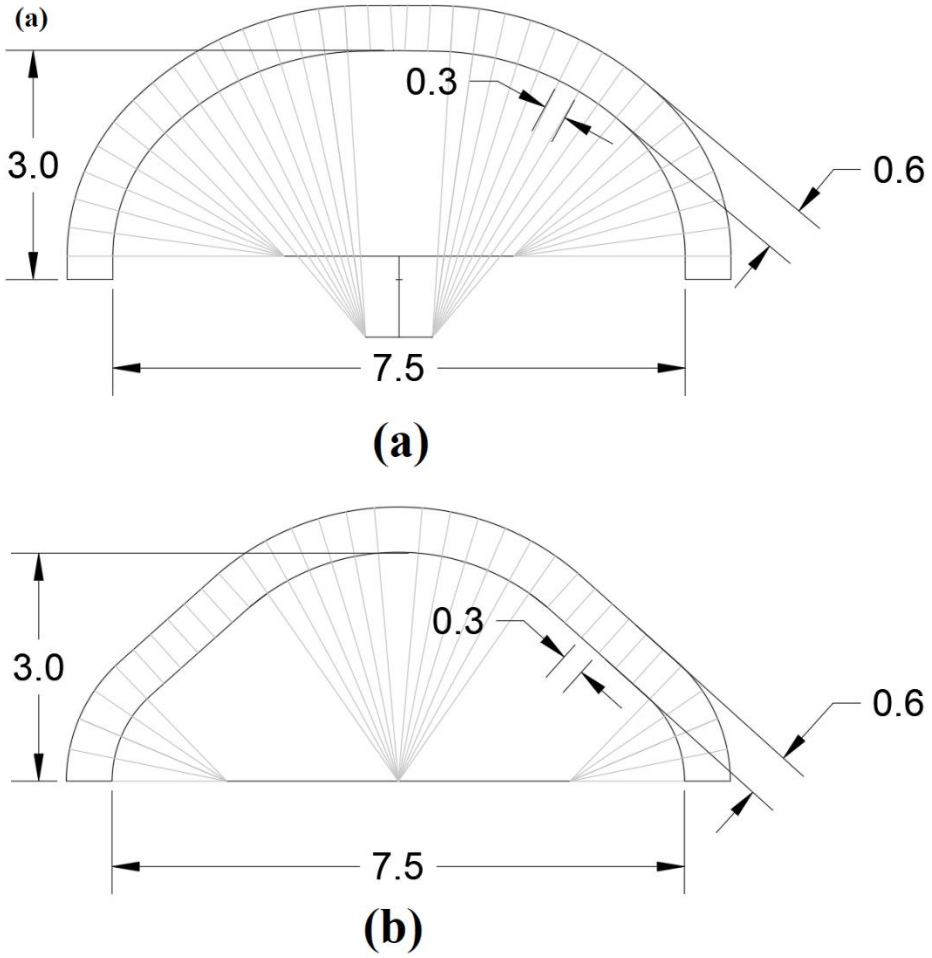

Figure 125. Design dimensions for two double curvature arches

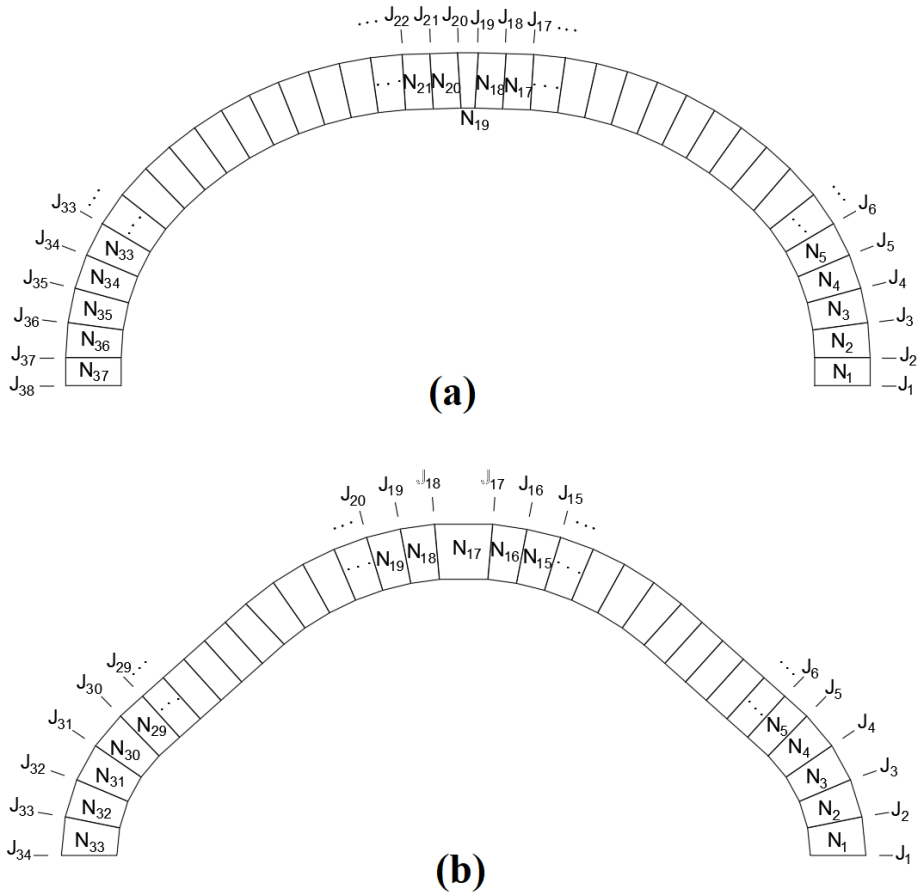

Figure 126. Block and joint nomenclature for the two double curvature arches

The geometric data from the AutoCAD® drawings of the two arches is used to construct the CLDs shown in Figure 127. From Figure 127 it can be seen that the diagonal shifted arch has a minimum λ_a of 8.83% with hinges H_1 and H_4 at joints J_1 and J_{32} respectively, and that the horizontal shifted arch has a minimum λ_a of 38.75% with hinges H_1 and H_4 at joints J_1 and J_{32} respectively. Also note that the rotation point for the negative tangent calculation is defined from the intersection of the base line and centroid of the full arch.

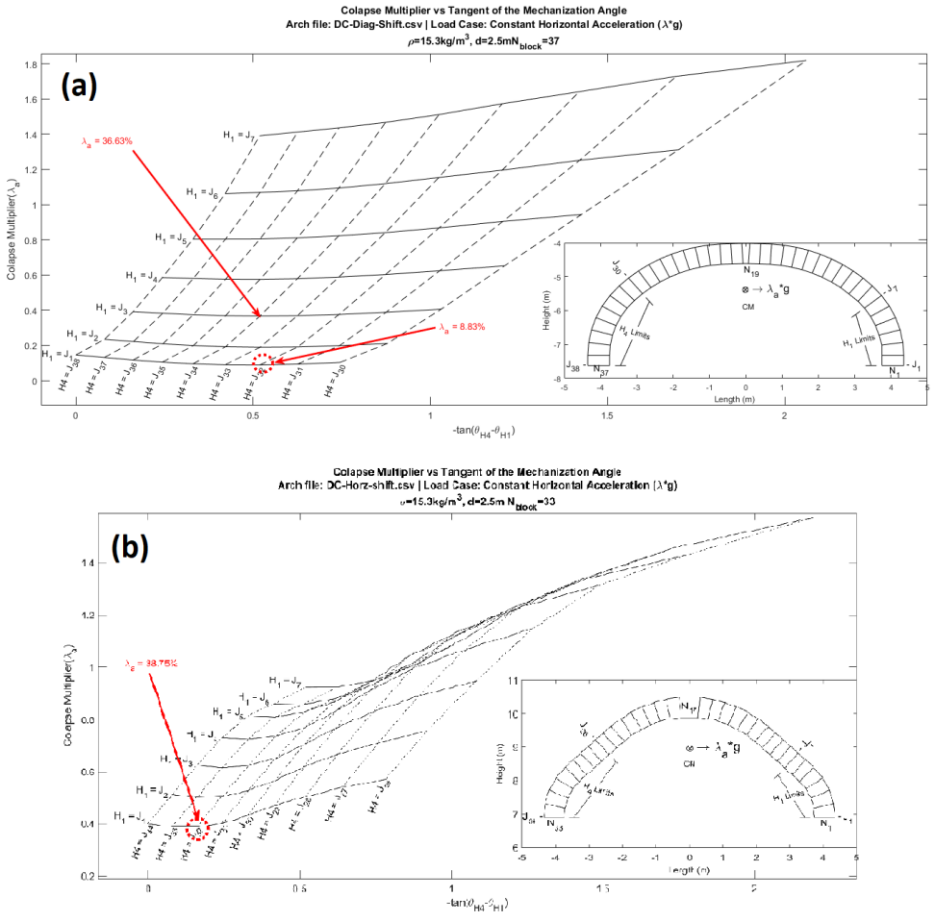

Figure 127. CLDs for the two double curvature arches

In addition to quickly obtaining the minimum, comparing the two diagrams allows the equivalent capacities between the arches to be determined. For the diagonally shifted arch, reinforcing the first two joints against extrados hinge rotations creates this capacity equivalence of 36.63%. Also note that H_4 shifts to joint J_{34} when H_1 is defined at J_3. The intermediate hinges are identified from the recorded hinge sets and the H_1-H_4 pair. Figure 128 shows these equivalent capacity arches and their minimum hinge configurations. Therefore, these two arches can be efficiently compared, and if for example they are also being evaluated for flow volume then the cost increase of reinforcing can be considered against the increase in flow capacity. Thus, the collapse load diagrams not only allow for a quick first-order capacity assessment, but they also provide the ability to efficiently compare arches, incorporate the effects of geometry and establish reinforcement strategies in the initial stages of planning and project scope development.

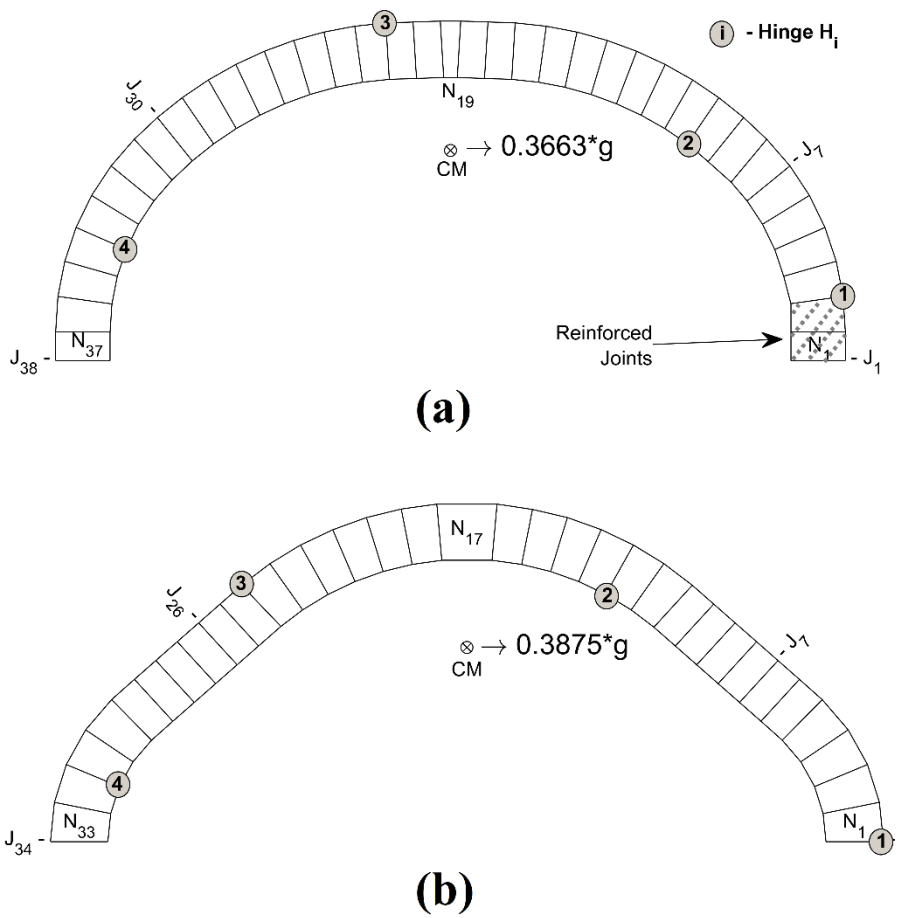

Figure 128. Equivalent capacity conditions for the two double curvature arches

From the capacity comparison example, it is clear that the CLDs provide an efficient and effective strategy for the first-order analysis of dry-stack arches for design and comparison. Additionally, these diagrams introduce insights into the behavior of an arch that is subjected to hinge control.

5.1.2 Hinge 1, Capacity, and Characterization

A notable characteristic observed with the CLDs is the hinge H_1 dominance on capacity. The effects of hinge H_4 while distinct are bound around the positioning of hinge H_1. This unique relationship allows the capacity behavior to be formulated into a single variable approximation (i.e. hinge H_1's position). This key variable in combination with experimental capacity measurements of a family of mechanisms generates a simplified link between a physical arch and its theoretical model. In other words, the arch can be characterized.

In the remaining sections of this chapter the process of characterizing an arch and linking the theoretical model to the experimental results is presented for two arches subjected to a tilting plane. The two experiments focus on a single loading condition to highlight the repeatability of the characterization approach.

5.2 Tilt Test Characterization of an In-Scale Arch

The first experimental campaign focusing on the capacity of a dry-stack masonry arch subjected to hinge control was carried out on an in-scale 27 block masonry arch undergoing quasi-static tilting plane loading [125]. This experimental campaign was carried out in the structure lab of the School of Engineering at Newcastle University, UK. A 27-block semi-circular arch was chosen for the campaign to ensure 25 distinct combinations of the base hinges exist so that a clear CLD can be established, and to formulate the characterization strategy.

5.2.1 Arch Construction

Timber was chosen as the material for the arch blocks. The reason timber was chosen was to ensure the blocks could endure a minimum of 75 collapses to measure the 25 mechanisms a minimum of three times each. The blocks were constructed from three 47mm x 75mm Canadian Lumber Standard timber boards. First, both 75mm sides of one board and one 75mm side on the other boards were planed. The planed sides were glued together. The resulting combined board had each surface planed to produce clean faces with sharp edges. The reason for combining the three boards was to increase the depth and create a more stable out-of-plane behavior. Finally, a trapezoid template was constructed with a short span of 38mm and tapered sides of 3.33° from square. This template was used to mark and cut each block from the combined board.

After cutting the blocks, the contact faces that make the arch boundary joints were scarified to increase roughness. The blocks were then assembled and adjusted to establish the most stable configuration (see Figure 129). Next, they were numbered and oriented, and the exposed faces were painted white. Finally, a four by four grid of fixed distance points was established across each joint with the template which is also shown in Figure 129. The mass, dimensions and point grid lengths of each block were measured and recorded.

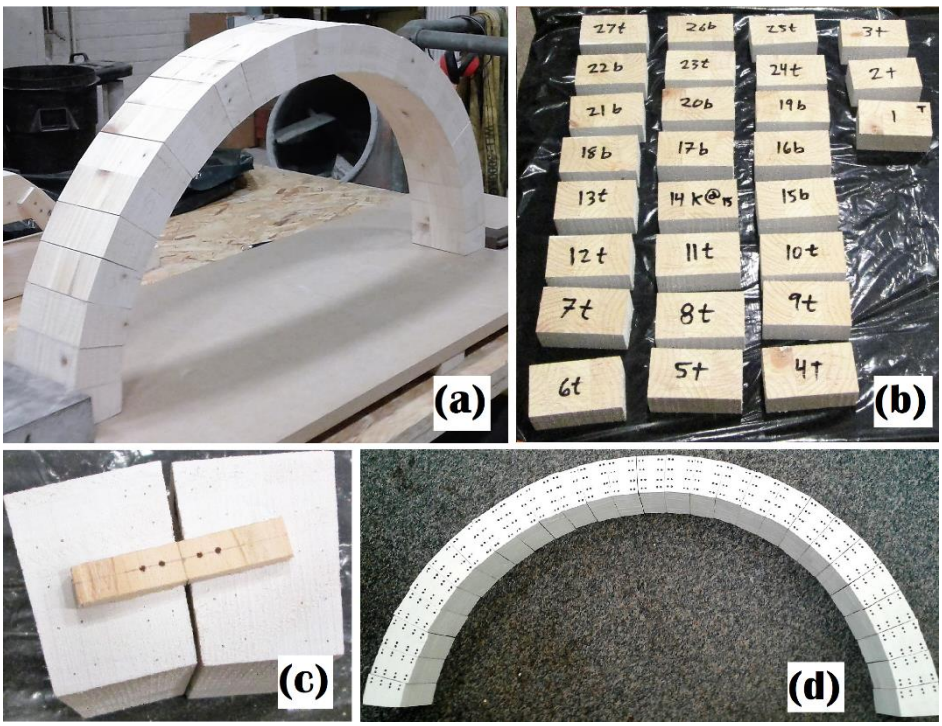

Figure 129. Photographs of the (a) best fit configuration; the (b) block numbering; the (c) parallel point grid template; and (d) the completed arch

After finishing construction and assembly, the arch was fitted to the platform via the base blocks. First, the left base block was anchored to the platform by screws driven from underneath the platform. The arch was assembled, and shims were added to the extrados of the right base block to provide the most stable configuration. Then the right base block was anchored to the platform with screws as well. The final assembled arch had a clear span of 0.6695±0.0005 m and a rise of 0.3170±0.0005 m. The platform was made from a dense composite board with risers to allow the use of the negative space for anchoring. The riser on the left edge was placed with a straight edge running the width of the platform and perpendicular to the arch to ensure in-plane rotations. A threaded steel bar was attached parallel to the rotation edge on the opposite side of the platform and a lifting chain was attached to the bar at centerline with the arch plane. Nuts and washers were added to the threaded bar to maintain the position of the lifting bar and remove potential out of plane motions. Figure 130 shows this described setup.

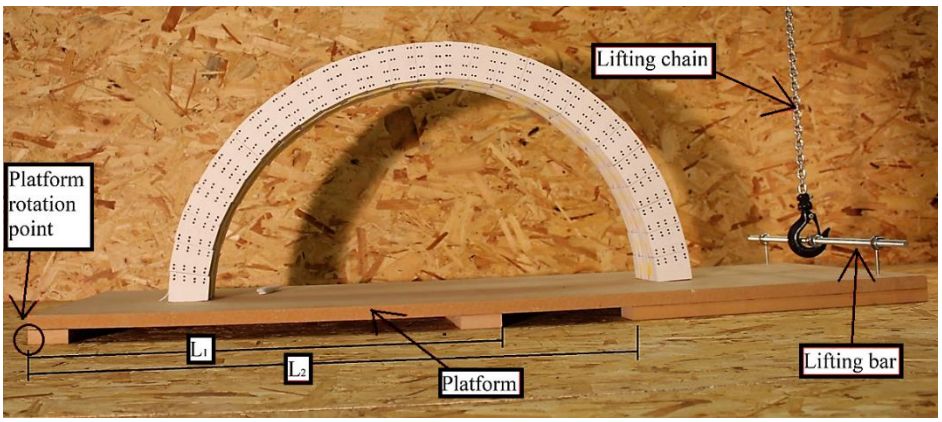

Figure 130. Image and annotation of the experimental arch-platform setup with measured lengths L_1 and L_2 identified

5.2.1.1 Hinge Control

The hinge control system for the experimental arch was constructed with Velcro®. The light weight of the blocks allows the use of the shear strength of Velcro® for flexural reinforcement while its own light weight creates a negligible effect to the stable system. Two circular hook-sided tabs were adhered on both the intrados and extrados of each block symmetrically about the centerline. Hinge control was achieved by applying loop-sided straps across all the block joints minus those selected for mechanization. Figure 131 highlights a defined mechanical joint.

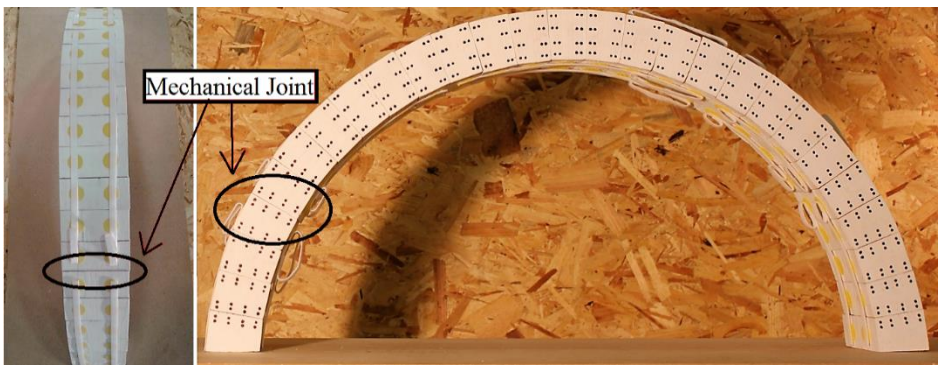

Figure 131. Velcro® defined mechanical joint

5.2.2 Arch Analysis Model

AutoCAD® was utilized to construct the arch analysis model from a statistical adjustment application to the averaged block model. The justification for the statistical approach was the high sensitivity that is associated with the block angles at the scale of the constructed arch. For example, the difference between a 27-block and 23-block arch under the dimensions of the constructed system is

a 0.5 mm (the thickness of a standard bandsaw blade) change in either the intrados or extrados length. The dimensions of the blocks were therefore averaged for the development of the analysis model. The averaged block dimensions and their standard deviations are shown in Figure 132.

To construct the model, the averaged block was drawn in AutoCAD® and the arch was constructed in the same manner as the physical system, left to right. Next, the extrados and intrados of random blocks were altered within the precision of the averaged block until the arch fit the rise, clear span, and slight rotation observed in the right base block. To validate the development of this statistical arch model, a lidar scan of the arch face was also taken. The 2D face of the drawn arch was compared against the point cloud from the scan. As can be seen in Figure 132, the two results are in strong agreement. Finally, the arch model data was extracted from AutoCAD® and passed to the black box analysis structure. Figure 133 shows the final drawn arch and defines its nomenclature for all further discussions.

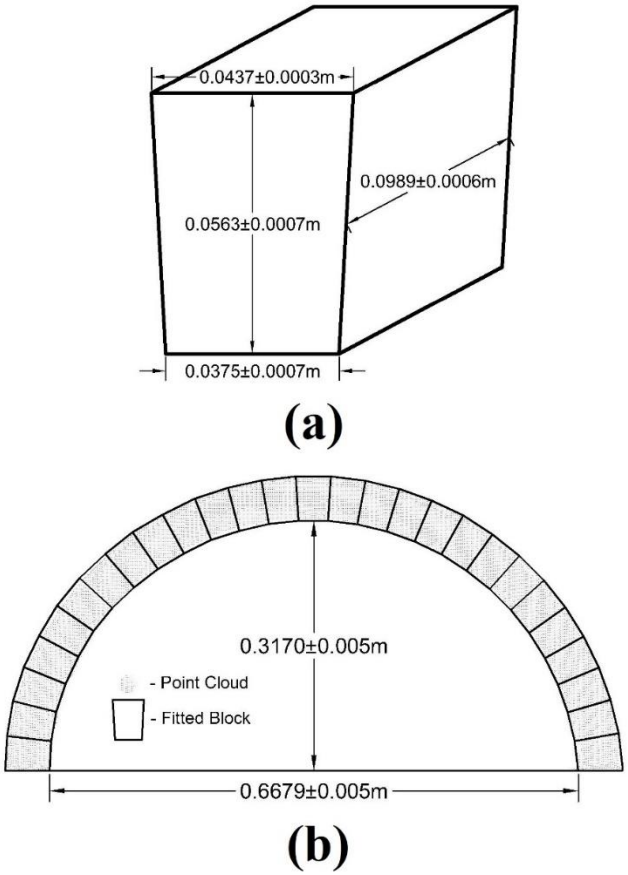

Figure 132. The (a) averaged block and the (b) developed analysis model and the point cloud verification

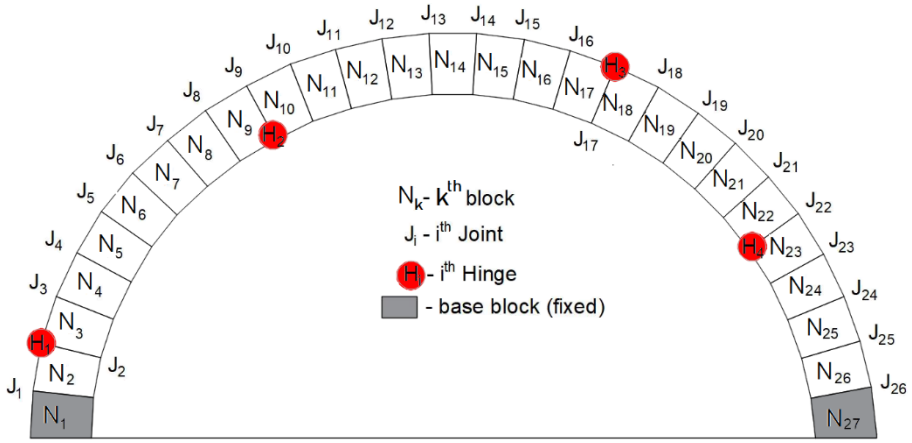

Figure 133. Assigned nomenclature for the arch in the first experimental campaign

5.2.3 Tilting Platform

The tilting plane was constructed from a dense composite board with a rotation edge and lifting chain (see Figure 130). Gravity's constant direction and magnitude result in the rotation of acceleration being equal to the tilting plane's rotation. Thus, a rotation of the tilting plane of θ_t, is equivalent to applying a horizontal acceleration of magnitude $\lambda_a \cdot g$ with

$$\lambda_a = \tan(\theta_t) \tag{115}$$

and

$$\theta_t = \sin^{-1}\frac{l}{L} \tag{116}$$

where *l* is the measured height after rotation of a known distance *L* along the plane of the board (see Figure 130).

The tilting plane was used because of the simplicity and repeatability of its application. Additionally, the distribution of forces throughout the body of the arch render the material properties irrelevant in the analysis, and the tests are a direct evaluation of the free-body diagram and associated equations of equilibrium. If the theory holds for the tilting test, then it holds for the other free-body diagrams as well. Lastly, the primary concern in the assessment of existing systems is their ability to withstand seismic events. This generates a direct value to the analysis for existing researches at the same time as validating the theory of kinematic equilibrium and developing the necessary characterization strategies for linking experimentation with the developed analysis model.

5.2.4 Procedure

The procedure for this experimental program consisted of:

- Assembling the arch
- Applying the Velcro® loop straps to define the mechanical joints
- Applying quasi statically tilting through a lifting chain until collapse
- Measuring the resulting heights l_1 and l_2 corresponding to known lengths L_1 and L_2 respectively (see Figure 134).
- Video recording each collapse for post-processing the collapse progression.

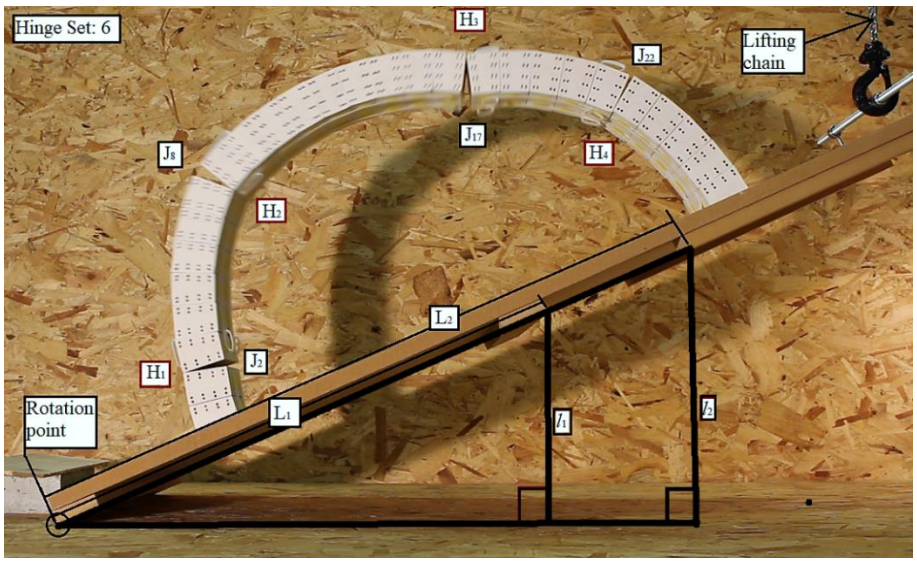

Figure 134. Mechanical collapse of the in-scale arch with the measured lengths l_1 and l_2 identified

As previously mentioned, the tilting plane testing procedure was repeated three times for every defined hinge set tested. Twenty-five distinct hinge sets were evaluated which generated a minimum total of 75 collapses. The defined procedure was systematically prescribed to each test.

5.2.4.1 Hinge Selection

The hinge selection for the experimental procedure was obtained from the development of a CLD from the ideal conditions of the constructed arch. The CLD and experimental limits are shown in Figure 135. The resulting mechanical joint sets are identified in Table 1.

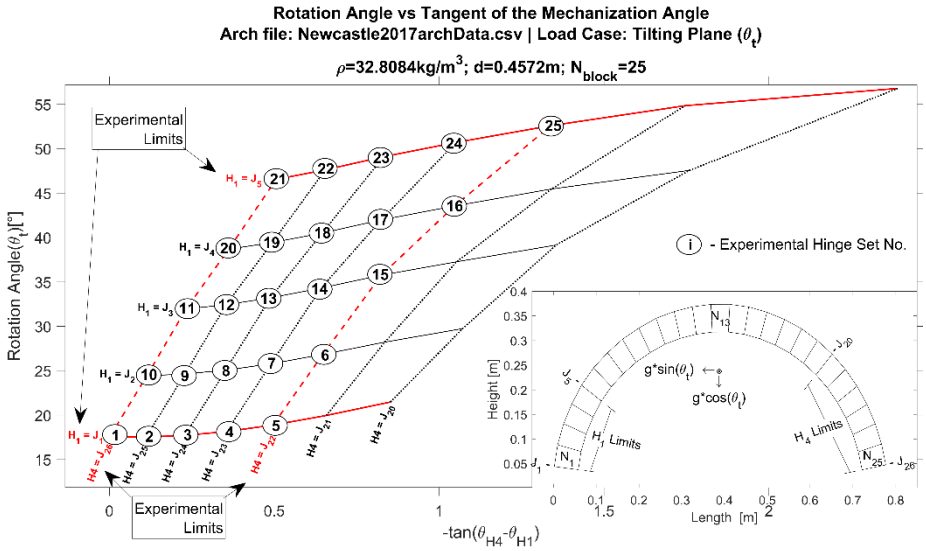

Figure 135. CLD for in-scale experimental arch

Table 1. Hinge joint configurations for each tested hinge set

Hinge Set	H_1	H_2	H_3	H_4	Hinge Set	H_1	H_2	H_3	H_4
1	J_1	J_8	J_{17}	J_{26}	**16**	J_4	J_{10}	J_{18}	J_{22}
2	J_1	J_8	J_{17}	J_{25}	**17**	J_4	J_{10}	J_{19}	J_{23}
3	J_1	J_8	J_{16}	J_{24}	**18**	J_4	J_{10}	J_{19}	J_{24}
4	J_1	J_8	J_{16}	J_{23}	**19**	J_4	J_{11}	J_{19}	J_{25}
5	J_1	J_8	J_{16}	J_{22}	**20**	J_4	J_{11}	J_{19}	J_{26}
6	J_2	J_8	J_{17}	J_{22}	**21**	J_5	J_{12}	J_{20}	J_{26}
7	J_2	J_9	J_{17}	J_{23}	**22**	J_5	J_{11}	J_{20}	J_{25}
8	J_2	J_9	J_{17}	J_{24}	**23**	J_5	J_{11}	J_{20}	J_{24}
9	J_2	J_9	J_{17}	J_{25}	**24**	J_5	J_{11}	J_{19}	J_{23}
10	J_2	J_9	J_{18}	J_{26}	**25**	J_5	J_{11}	J_{19}	J_{22}
11	J_3	J_{10}	J_{18}	J_{26}	Note: Refer to Figure 126 for identifying joint location.				
12	J_3	J_{10}	J_{18}	J_{25}					
13	J_3	J_{10}	J_{17}	J_{24}					
14	J_3	J_9	J_{17}	J_{23}					
15	J_3	J_9	J_{18}	J_{22}					

5.2.4.2 Collapse and Measurement

Each collapse was performed through the manual rotation of the platform by a lifting chain with a reverse locking hand crank (see Figure 134). The chain was raised until the arch collapsed and at a quasi-static rate. At the point of collapse the crank was locked and the heights l_1 and l_2 were recorded. The platform was

then lowered, and the system was reassembled. Each collapse was also recorded with a Cannon DSLR camera.

5.2.5 Data

The platform lengths L_1 and L_2 are 0.6110±0.0005 m and 0.7880±0.0005 m respectively. For each collapse, the heights and observed failure methods were recorded. The recorded values and observations are presented in Table 2.

Table 2. Recorded experimental data for the in-scale arch subjected to a tilting plane

Platform Measurements		precision		* M - MACHANISM
L1 [mm]	L2 [mm]	+/-	0.5 mm	S - SLIP
611	788			R - ROTATION

COLLAPSE DATA

Run	Hinge Set	l1 [mm]	l2 [mm]	Failure type *	notes:
1	1	172	222	M	
2	1	190	247.5	M	
3	1	187	245	MS	SMALL S AT H1
4	1	188	245.5	M	
11	1	187	245	M	
5	2	187	245	M	
6	2	194	248	M	
7	2	174	227	MS	SMALL S AT H1
8	2	195	254	M	
9	2	174.5	227	M	
10	2	189	246	MS	MODERATE S AT H1
12	3	190	247	MS	MODERATE S AT H1
13	3	191	248	MS	MODERATE S AT H1
14	3	184	239.5	M	
15	3	183	238	M	
16	4	178.5	232.5	M	
17	4	203	295	MS	SMALL S AT H1
18	4	174	227	MSM	MECH-SLIP-MECH
19	4	181	235.5	M	
20	5	187	244	MS	VERY SMALL S AT H1
21	5	177	230	M	
22	5	182	238.5	MSM	MECH-SLIP-MECH
23	6	230	298.5	M	
24	6	246	320	MR	SMALL OUT OF PLANE ROTATION
25	6	243	313.5	M	GOOD M
26	7	228	295	M	
27	7	243	313.5	M	
28	7	237	307.5	M	
29	8	233	302	M	
30	8	243.5	312	M	
31	8	228	295	M	
32	9	238.5	309.5	M	
33	9	237.5	309	M	
34	9	235	305.5	M	
35	10	222.5	289	M	
36	10	228	296	M	
37	10	225.5	293	SM	
38	11	248	322	M	
39	11	271	351	MRS	
40	11	233	303	MS	
41	12	256	334	MS	
42	12	259	336	M	
43	12	275	355.5	M	
44	13	264	341.5	MS	VERY SMALL S AT H1
45	13	275	356	MS	VERY SMALL S AT H1
46	13	275	356	SM	SMALL S AT H1 THEN M
47	14	281	364	SM	SMALL S AT H1 THEN M
48	14	281	364	SM	SMALL S AT H1 THEN M
49	14	285.5	369	SM	SMALL S AT H1 THEN M
50	15	292	377.5	SM	SMALL S AT H1 THEN M
51	15	283	366.5	SM	SMALL S AT H1 THEN M
52	15	279	362	SM	SMALL S AT H1 THEN M
53	16	346	447	MS	VERY SMALL S AT H1
54	16	337	436.5	MS	VERY SMALL S AT H1
55	16	337	435	MS	VERY SMALL S AT H1
56	17	315.5	409	SM	SMALL S AT H1 THEN M
57	17	315	407.5	SM	SMALL S AT H1 THEN M
58	17	307	398	SM	S AT H1 M BEGINS AT 1/2 BLOCK THICKNESS
59	18	301	392	SM	SMALL S AT H1 THEN M
60	18	314	416	SM	S AT H1 M BEGINS AT 1/2 BLOCK THICKNESS
61	18	275	355	SM	S AT H1 M BEGINS AT 1/2 BLOCK THICKNESS
62	19	296	383.5	SM	S AT H1 M BEGINS AT 1/2 BLOCK THICKNESS
63	19	300	388.5	SM	S AT H1 M BEGINS AT 1/2 BLOCK THICKNESS
64	19	273	355	SM	S AT H1 M BEGINS AT 1/2 BLOCK THICKNESS
65	20	280	363.5	SM	S AT H1 M BEGINS AT 1/2 BLOCK THICKNESS
66	20	279	363	SM	S AT H1 M BEGINS AT 1/2 BLOCK THICKNESS
67	20	282	365.5	SM	S AT H1 M BEGINS AT 1/2 BLOCK THICKNESS
68	21	321.5	417	M	SOME ROTATIONS AT J=1 RESTRAINED
69	21	322	418	M	SOME ROTATIONS AT J=1 RESTRAINED
70	21	323	419	M	SOME ROTATIONS AT J=1 RESTRAINED
71	22	339.5	439	M	LESS ROT AT J=1
72	22	314	406	M	LESS ROT AT J=1
73	22	313	404	M	LESS ROT AT J=2
74	23	324.5	423	M	LESS ROT AT J=2
75	23	351	454	M	LESS ROT AT J=2
76	23	343.5	442	M	LESS ROT AT J=2
77	24	336.5	435.5	M	LESS ROT AT J=1
78	24	326.5	422.5	M	SOME ROTATIONS AT J=1 RESTRAINED
79	24	339	439	M	SOME ROTATIONS AT J=1 RESTRAINED
80	25	364	469	MSR	H4 SLIDE-ROTATE, H1 SLIDE-ROTATE SOME TWIST
81	25	343	445	MSR	H4 SLIDE-ROTATE, H1 SLIDE-ROTATE SOME TWIST
82	25	363	468.5	MSR	H4 SLIDE-ROTATE, H1 SLIDE-ROTATE SOME TWIST

5.2.6 Results

The calculated rotation angles and subsequent multipliers were obtained by averaging the ratio of the height to platform length measurements for each run of a hinge set, then applying the result to Eqn. 116. The average and standard deviations were calculated for each hinge set. The measurement error was also manually propagated. The propagated measurement error and deviation of the

averaged collapse multipliers were compared to define precision and identify its source. Table 3 shows the resulting collapse load multipliers, precision and the source of the controlling error. The evaluation revealed that the variance in the rotation angles controlled for all cases except hinge sets 20 and 21. A minimum of two-digits of precision was obtained for all evaluated sets regardless of the controlling error.

Table 3. Calculated collapse multipliers, error and error source for the in-scale arch subjected to a tilting plane

Hinge Set	λ_a	±	source	Hinge Set	λ_a	±	source
1	0.32	0.02	stdv	**16**	0.67	0.01	stdv
2	0.32	0.02	stdv	**17**	0.60	0.01	stdv
3	0.323	0.008	stdv	**18**	0.56	0.05	stdv
4	0.32	0.04	stdv	**19**	0.54	0.03	stdv
5	0.31	0.01	stdv	**20**	0.519	0.003	meas
6	0.43	0.02	stdv	**21**	0.623	0.004	meas
7	0.42	0.02	stdv	**22**	0.62	0.04	stdv
8	0.42	0.02	stdv	**23**	0.67	0.04	stdv
9	0.423	0.004	stdv	**24**	0.65	0.02	stdv
10	0.398	0.006	stdv	**25**	0.72	0.03	stdv
11	0.45	0.04	stdv	* meas – measurement error stdv – standard deviation Note: Refer to Table 1 for hinge set details.			
12	0.48	0.02	stdv				
13	0.50	0.01	stdv				
14	0.523	0.006	stdv				
15	0.53	0.02	stdv				

The collapse rotation angles from the experimentation and from the black box analysis approach are presented in Figure 136. The hinge sets are represented in a decision tree format with H_1 at the base. Also note the inclusion of results form a discrete element modelling (DEM) analysis. The DEM analysis was performed to establish a validation trifecta with the developed analysis and executed experimentation. The details of the DEM analysis are presented in Appendix A and can also be found in the literature [124].

From Figure 136 it can be seen that the capacity of the experimental arch increased from the minimum mechanism's 16.7° rotation capacity to a maximum measured capacity of 30.3°. Note that the dominating factor controlling the capacity of the arch is the position of H_1 as observed with the CLDs. From these results it is clear that the arch behavior was captured but the numerical models overestimate capacity.

Also note in Figure 136 the strong precision of the experimental tests results. This indicates a repeatability potential in the designed capacity and that the difference in capacities between experimental and numerical are systematic in nature. A portion of the systematic difference is due to geometric differences between the physical arch and the model, but there is a general divergence in

the net capacities as hinge H_1 moves towards the crown. This indicates that additional factors are affecting the system and further analysis is required.

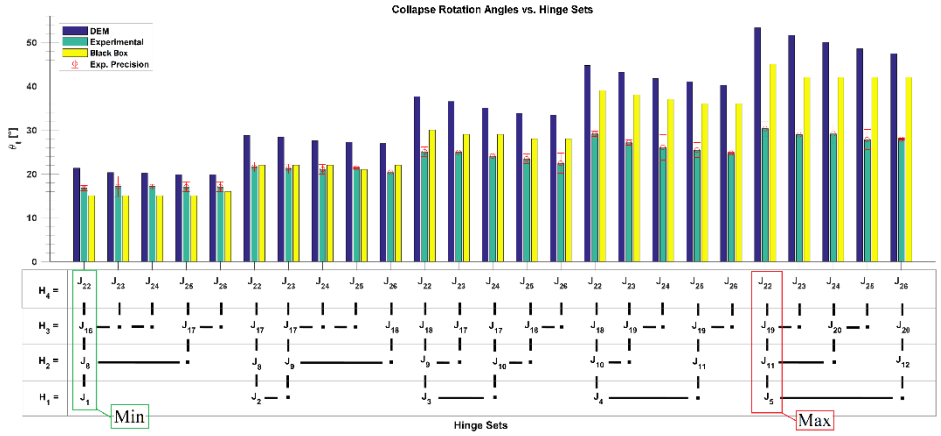

Figure 136. Numerical and experimental results for the in-scale arch subjected to a tilting plane.

5.2.6.1 Experimental Observations

In addition to the length measurements taken for each collapse, a video recording was made. These recordings revealed two non-ideal conditions in the experimentation. First, the Type II mechanism was clearly identified for all collapses with hinge H_1 set at joint J_4 (see Figure 137). Slip at the hinge H_1 joint did occur in other collapses (as noted in Table 2), but it was attributed to the non-perfect geometry and the 2D simplification because of its inconsistency. The second non-ideal condition was base deformations developed through reinforced hinge rotations. These static deformations were observable at joint J_1 when hinge H_1 was higher than J_3 as can also be seen in Figure 137.

The observed slip and static deformations are clearly contributing to the systematic error of the experimental results. These conditions must be further considered in the post-processing of the data, but also note the hinge H_1 position dominance over capacity. This provides a strong potential to directly link the theoretical model the experimental arch through the H_1 variable.

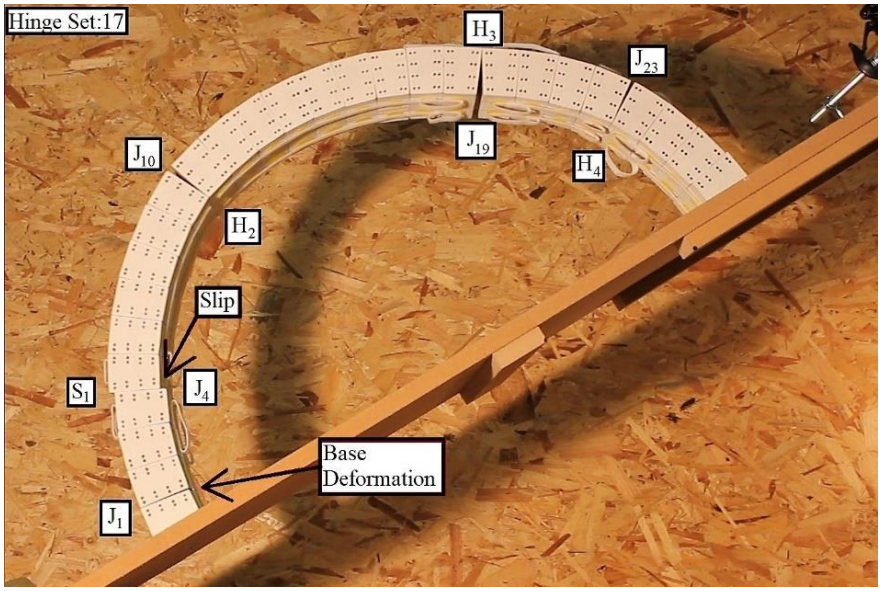

Figure 137. Image of Type II mechanism and base deformation

5.2.7 Post-Processing

The experimental results clearly highlight the need for capacity adjustments to more accurately match the models to the experimentation. Additionally, the Type II mechanism and base deformation must be directly assessed to justify observations, demonstrate the versatility of the kinematic equilibrium and black-box analysis approach, and highlight the simplification of the capacity adjustment equation that arises from the evaluation of a family of mechanisms.

5.2.7.1 Capacity Adjustment Equation

In the experimental results (Figure 136) the dominance of hinge H_1 on the capacity of the system is observed. Therefore, the ratio between experimental and modelled results for each hinge set were calculated. These ratios were then averaged for fixed hinge H_1 positions. Figure 138 shows the plot of these averaged ratios against the H_1 position for both the kinematic equilibrium and DEM models (see Appendix A for DEM model details). From Figure 138 a strong linearity between capacity ratios and hinge H_1's location is observed. This linearity establishes a simple equation to adjust capacity. The capacity adjustment equation for the kinematic equilibrium model is

$$C_{LA} = -0.0603 \cdot H_1 + 0.871 \quad (117)$$

and the capacity adjustment equation for the DEM analysis is

$$C_{DEM} = -0.0989 \cdot H_1 + 1.142 \quad (118)$$

Note that H_1 equal to J_1 is not included in Figure 138 because no reinforced base joints exist for this condition.

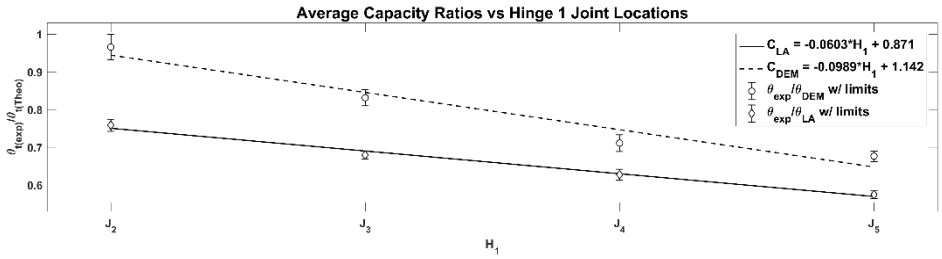

Figure 138. Linear fits to the averaged capacity ratios against H_1 position for the in-scale arch subjected to a tilting plane

The strong linearity in Figure 138, the two observed non-ideal conditions (i.e. Slip at H_1 and base deformation) and the fact that the slip condition was not present for all collapses, drives the postulation that the strength reduction relationship is driven by a non-infinite hinge stiffness of the Velcro® reinforcement at the left base. The linear fits thus produce capacity adjustment equations that are justified and can be applied to the models. Figure 139 shows the updated results with the capacity adjustment equations applied.

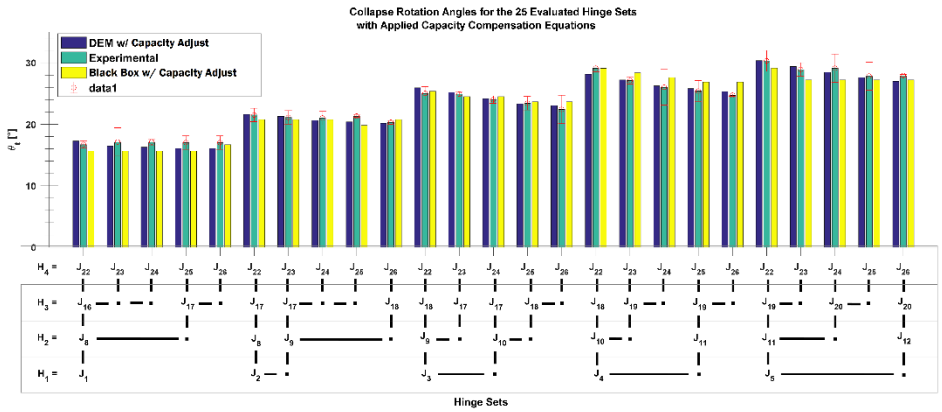

Figure 139. Experimental results of the in-scale arch subjected to a tilting plane with the applied capacity adjustment equations (Eqns. 117 and 118)

Figure 138 and Figure 139 highlight the observed base deformations as the dominate error in the capacity reduction of the system, but by evaluating a family of mechanisms that exist for the arch, the required compensation can be simply achieved through the evaluation of mechanical sets with the same H_1 locations. Additionally, the identification of the error and the validation of the results indicate that an improved hinge reinforcement system, such as FRPs or TRMs, has the potential to increase the capacity of the arch up to a factor of 3.2 times its minimum with the reinforcement applied as shown in Figure 140.

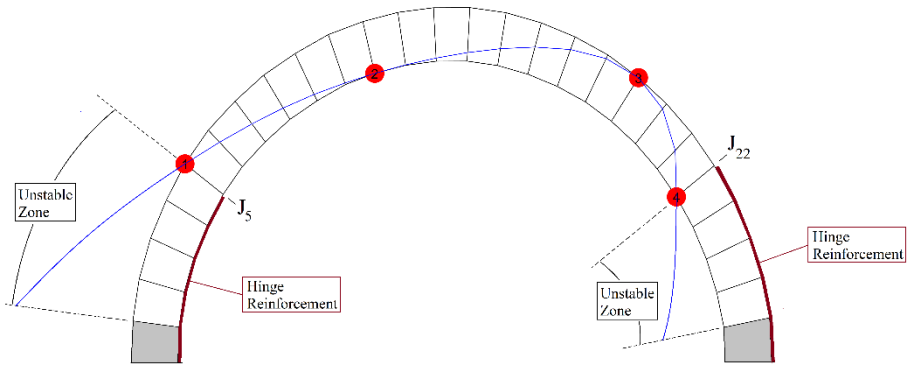

Figure 140. Reinforcement layout for maximum capacity of the in-scale arch subjected to a tilting plane

5.2.7.2 Finite Hinge Stiffness of the Base Joint

In the discussion of mechanical deformations and finite hinge stiffness in Section 4.4, the potential to have a stable deformation exists at a cost to capacity. Comparing the capacities of Figure 114 and Figure 116 reveal that the deformed arch resulting from a 2° rotation at H_1 decreases the tilting capacity from 19.7° to 15.8°. Expanding on this observed reduction, the rotation capacities versus rotation angle α_1 (see Section 4.4) were recorded for hinge sets 1 through 5 (see Table 1) where H_1 was located at the base (see Figure 141). From Figure 141 it can be seen that the capacity of the arch is reduced up to an angle between 7° and 10° before arriving at a non-admissible configuration. This range of admissibility thus reveals the limits for statically stable SDOF deformations.

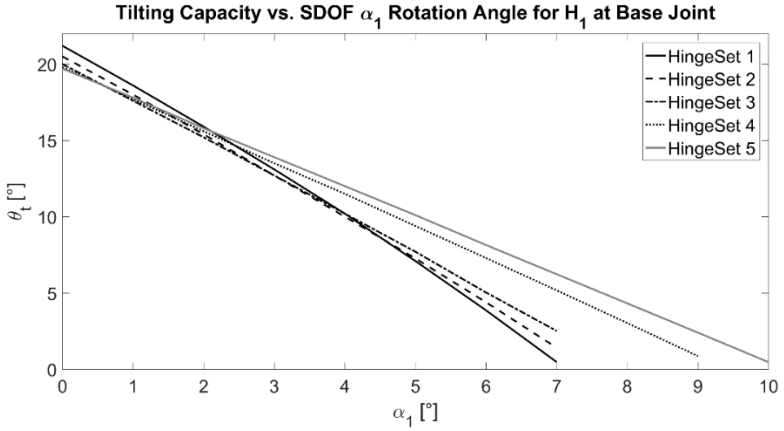

Figure 141. Tilting capacity versus α_1 rotation angle for hinge sets 1 through 5 from Table 1 for the in-scale arch

Figure 142 shows the pre and post-collapse condition of the experimental arch for hinge set 23 (refer to Table 1 for hinge set identification). In order to theoretically capture this collapse state with the KCLC for hinge sets 6 through

25, SDOF deformations were applied at 1° intervals to the KCLC with H_1 at J_1. Then H_1 was shifted to the assigned hinge set position and the capacity was recorded. This procedure was repeated until a non-admissible state was obtained. Figure 121 in Section 4.4 highlights this defined procedure.

A geometric reduction factor, obtained from the averaged experimental-theoretical capacities for hinge sets 1 through 5 where H_1 was at J_1, was applied to the recorded deformed capacities with H_1 greater than J_1. Capacity versus α_1 at J_1 plots similar to Figure 141 were created and used to determine a J_1 rotation (α_1) that produced the experimental capacity. The determined rotation angles were averaged for fixed H_1 hinge sets and plotted against hinge H_1's position (see Figure 143). The results show a strong linearity between the position of H_1 and α_1 at J_1 and provides a strong argument towards the classification and quantification of this systematic error observed in the experimental campaign.

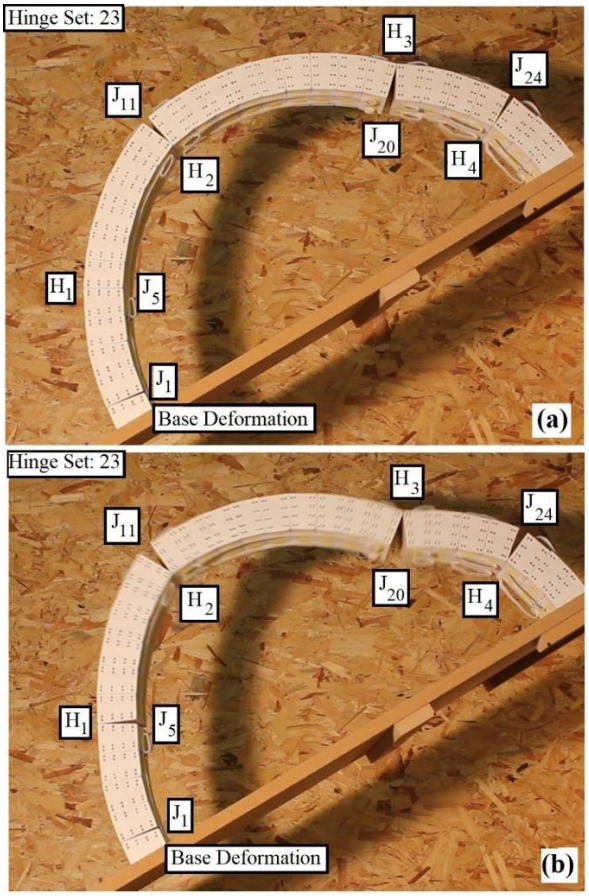

Figure 142. (a) Deformed stable state and (b) failure mechanism for hinge set 23 of the in-scale arch

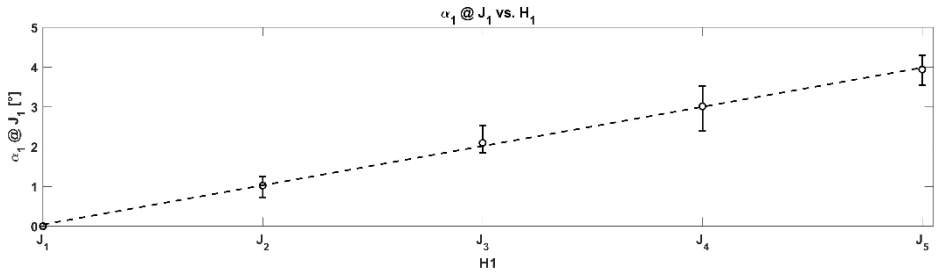

Figure 143. Averaged α_1 at J_1 angles versus H_1 position

5.2.7.2.1 Joint J_1 Stiffness

In order to determine a joint stiffness for J_1, a force must be established to evaluate against the deformed condition. To achieve this the capacity compensation for non-stable admissible mechanisms was incorporated into the custom KCLC (see Figure 121). The calculation of the tensile force was then obtained by applying the calculated deformation angle to J_1, adjusting H_1 to the defined position, and recording the tensile value at J_1. Again, Figure 121 shows the procedure applied to hinge set 23. Finally, a joint J_1 rotation stiffness was calculated by

$$K_\alpha = \frac{T_n}{\alpha_1} \tag{119}$$

for each hinge set with H_1 greater than J_1 and then averaged to produce a rotation stiffness of $K_\alpha = 0.19 \pm 0.05$ [kN/°].

The obtained two-digit precision of the calculated stiffness further reinforces the dominance the base deformation has in the capacity reduction of the experimental arch. It is important to note however that the calculation of this stiffness and the examination of SDOF deformations was unnecessary. For the practical purposes of design, the capacity adjustment equation (Eqn. 117) was sufficient in transferring the measured capacity of the arch into the analysis platform.

5.2.7.3 Type II Mechanism and the Friction Angle

Although the base deformations dominated capacity and the discrepancy between the models and experimental results, the observation of the Type II mechanism must be addressed as well. The inclusion of slip at H_1 means that the static friction at the joint was exceeded. Therefore, a friction value must be obtained and compared against the theoretical wood-wood friction values. To obtain a friction value, the standard equations of equilibrium was adjusted such that a moment at H_1 replaced the collapse multiplier in the reaction vector ***r*** and the collapse multiplier was incorporated into the constants vector ***q***. Applying this modified equations of equilibrium to the hinge sets and collapse values associated with H_1 at J_4 and utilizing Eqns. 21-23 produce a resulting friction angle associated with the collapse condition. Averaging these calculated friction angles produced a value of 17.6° ± 3°. The accepted friction angles for wood-

wood contact are between 11° and 27° and thus the calculated value falls within the accepted range.

The capacity compensation equation and Type II mechanism check was incorporated into the custom KCLC designed for the experiment. Evaluation of the hinge sets revealed that with the inclusion of the Type II mechanism and the calculated friction angle of 17.6° produced only admissible cases for H_1 greater than J_3. Additionally, the difference between the Type II mechanism and the Type I with the applied capacity adjustment equation is 0.3°. In fact, for all five hinge sets with a H_1 equal to J_4 the maximum difference between the two collapse angles is 1°. Consequently, the equivalent capacities of the Type II and capacity compensation for H_1 equal to J_4 coupled with the calculated friction angle within the range accepted for wood-wood interaction provides a sound validation of the experiment and analysis structure.

In the context of design, the potential for the slip joint must be removed with positive reinforcement, but the ability to theoretically capture this behavior with the developed analysis model shows a great potential for the analysis structure to expand beyond the simplifications necessary for efficient design.

5.2.8 Additional Remarks

The final remark on the in-scale arch testing is in regards the application of the limiting condition analysis described in Section 4.2.3. Note that Figure 103, which reflects the limiting condition evaluation of the generalized conditions of the in-scale experimental arch, the Type VII mechanism is controlling, but this was not observed in the experimental results. This discrepancy is the result of the static deformations from the finite stiffness of the base joint. The base joint deformation defines hinge H_4 and the intermediate hinges, H_2 and H_3, before the capacity of either the Type XIX or Type VII mechanisms is reached. Thus, they become non-admissible conditions through the imperfections of the reinforcement. The consequence of this further highlights the potential for the application of reinforcement to produce a weaker arch.

5.3 Tilt Test Characterization of a Full-Scale Arch

The second experimental campaign also focused on the characterization of a dry-stack arch subjected to hinge control and a tilting plane but with three key differences. These differences were that a full-scale arch was constructed, the arch blocks were engineered from a combination of materials and the friction angle was significantly increased to remove the admissibility of the Type II mechanism within the family of mechanisms evaluated. This experimental campaign was carried out as an independent research project in California.

The objective of repeating the same loading condition (i.e. the tilt test) as for the in-scale arch is to highlight the repeatability of the characterization strategy.

5.3.1 Arch Construction

A 27-block arch was constructed from engineered blocks.

5.3.1.1 Block Construction

The blocks of the full-scale arch were constructed from a combination of Oriented Standard Board (OSB) and galvanized steel pipe (see Figure 144). Arcs were cut from the OSB and clamped in sets of two to cut the joint faces. Holes were drilled in the clamped OSB block sets to maintain alignment and the galvanized steel pipe risers were anchored into the front block. The back block was attached to the risers and adjusted with locknuts to the defined block depth. A floor flange was also attached at the centroid of the front block and a removable centroid bar was added. Lastly, 36 grit sandpaper was applied to the joint faces to increase the friction angle and reduce the potential of a slip mechanism that was observed in the in-scale arch tests.

Figure 144. Constructed block for the full-scale arch

After the construction of the 27 blocks, the dimensions and masses were recorded. The averaged block details and variance are shown in Figure 145.

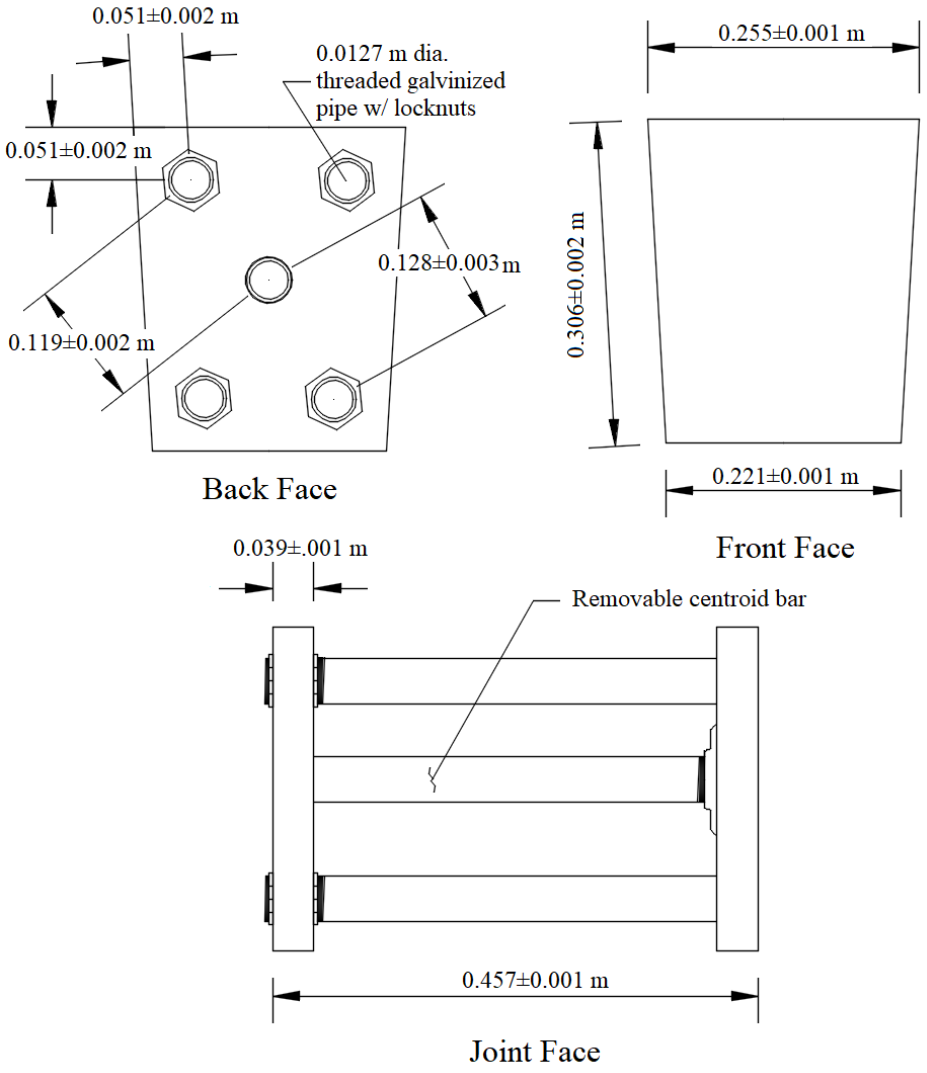

Figure 145. Block details for the full-scale arch

5.3.1.2 Arch Assembly

The arch was assembled block-by-block from right to left. Each block was placed and double-sided Velcro® straps were wrapped around the risers to reinforce the interface. After the first assembly of the arch, the forward faces were painted white. The arch was disassembled, and each block was weighed again to account for the added mass of the paint. Then the arch was reassembled and a 4x4 point grid was applied at each joint using a template, compass and markers. Figure 146 shows the details of the point grid and its application to the arch. The

final constructed arch is shown in Figure 147 and the measured dimensions in Figure 148.

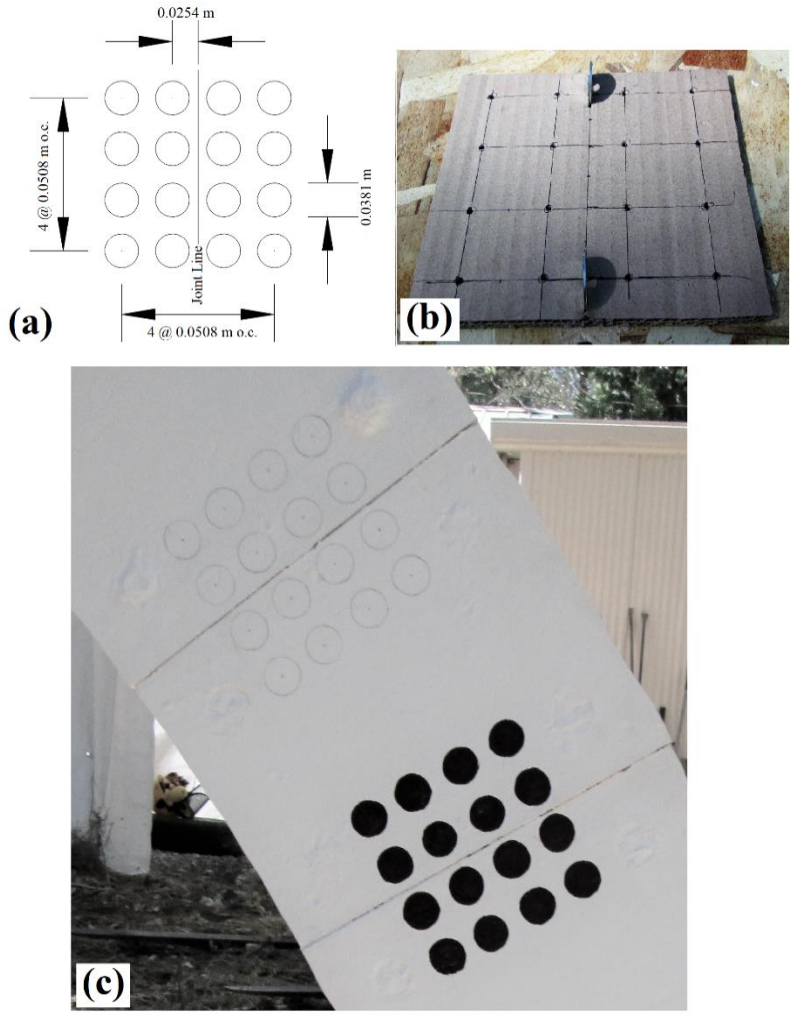

Figure 146. Point grid (a) dimensions, (b) template and (c) application to the full-scale arch

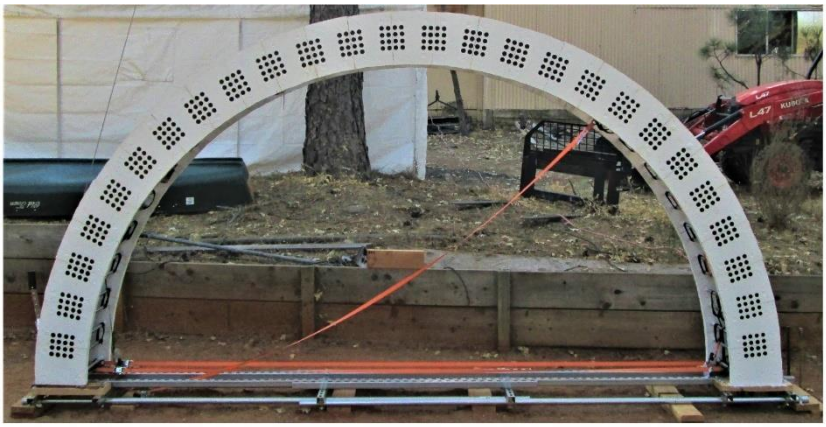

Front Face

Side View

Back Face

Figure 147. Constructed full-scale arch for the tilting plane tests

5.3.1.3 Hinge Reinforcement and Element Stiffening

For each measured collapse, all joints were reinforced minus the four defined joints of the mechanized arch. These mechanical joints had the Velcro® straps removed. Then cam straps were applied to the reinforced block groups to create three rigid elements connected by four dry joints. A defined mechanical joint can be seen in Figure 149. Also note that additional cam straps were applied as secondary safety systems to prevent the full collapse of the arch during experimentation.

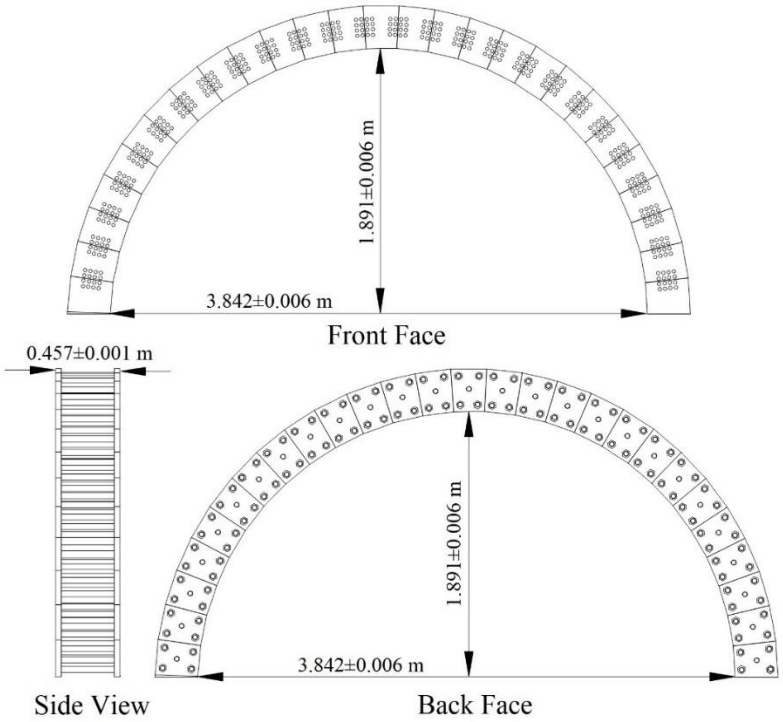

Figure 148. Final Dimensions of the constructed full-scale arch

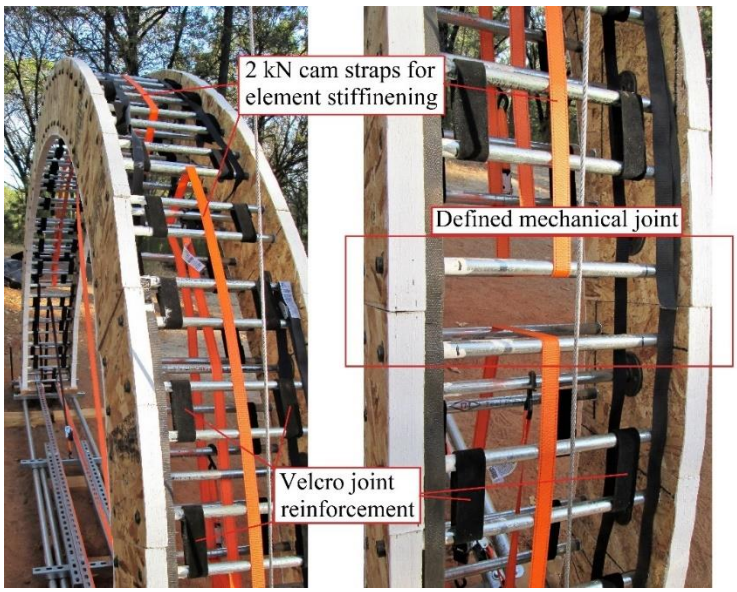

Figure 149. Velcro® Reinforcement, cam strap element stiffening and a defined mechanical joint for the full-scale arch

5.3.2 Arch Analysis Model

The arch model was constructed in AutoCAD® from the averaged block method used to develop the in-scale arch analysis model in Section 5.2.2. The averaged block geometry of Figure 145 was drawn and the arch model was constructed in the same manner as the physical system. This time from right to left to reflect the switch in the rotation line of the tilting platform. Next, the extrados and intrados of random blocks were altered within the precision of the averaged block until the arch fit the rise, clear span, and slight rotation observed in the left base block. Figure 150 shows the drawn arch model with supporting nomenclature.

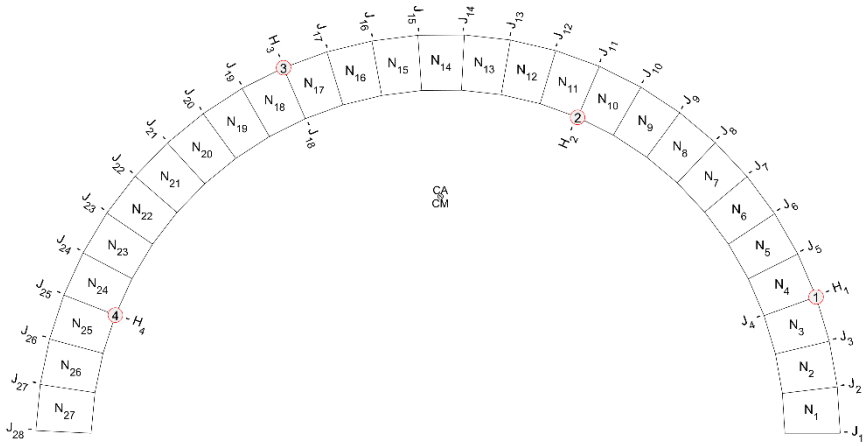

Figure 150. Drawn arch model and nomenclature for the full-scale arch subjected to a tilting plane

5.3.3 Tilting Platform

The tilting platform was constructed from a combination of steel conduit pipe and slotted standard Unistrut® galvanized channels. One end of the pipes was anchored to the rotation point created from standard hinges and wooden boards. The other end of the pipes was anchored to wooden boards with an eye bolt placed along the centerline. Wooden platforms were then attached to the pipe via cross struts and adjusted to the clear span of the arch. Additional longitudinal channel struts were then applied to stiffen the frame against moments that develop from platform suspensions during the tilting process. The frame was rotated using a Teckton 5547 4-Ton Dual Gear Power Puller. Figure 151 shows the tilting frame.

Four lengths were marked along the platform from the rotation point. These fixed lengths, L_i, were used to measure the collapse rotation angle and are identified in Figure 152. The collapse rotation angle is again determined by Eqn. 116.

Translation Base

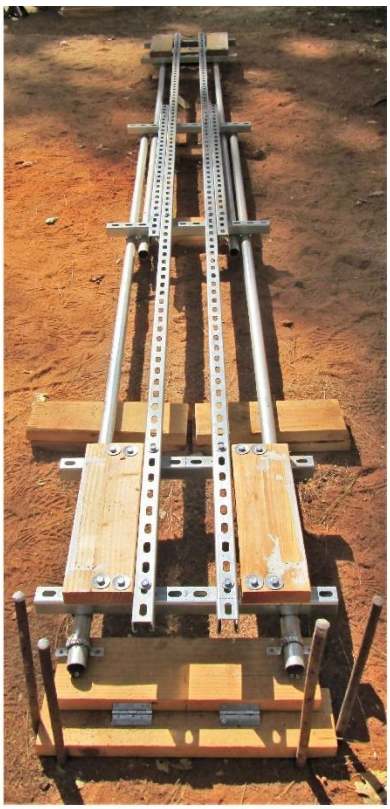

Rotation Base

Rotation Plane

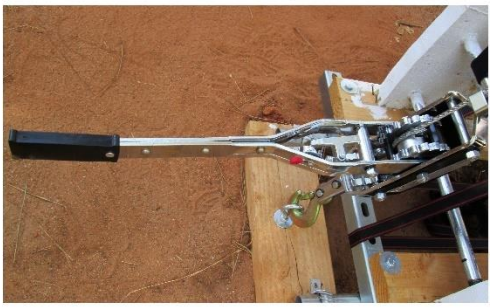

Tekton 5547 4-Ton
Dual Gear Power Puller

Figure 151. Tilting platform for full-scale arch tilt tests

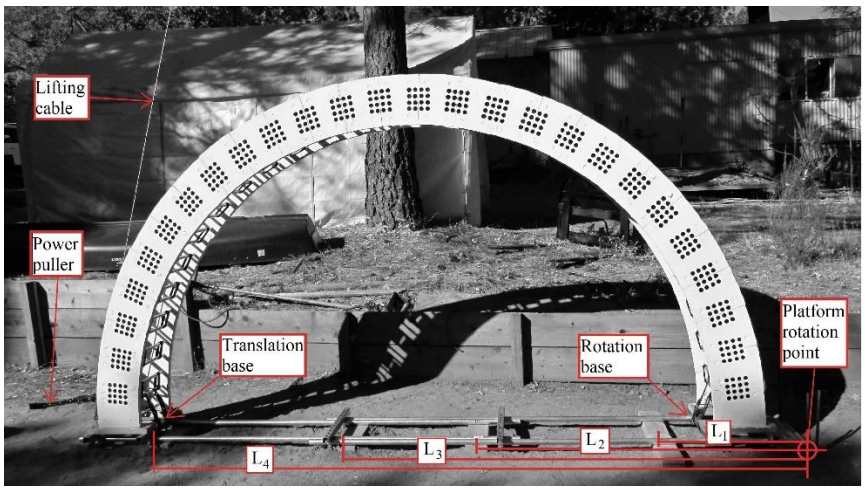

Figure 152. Tilting plane layout for full-scale arch

5.3.4 Procedure

The procedure for this experimental program consisted of:

- Assembling the arch
- Removing Velcro® straps to define the mechanical joints
- Applying cam straps to stiffen block groups into elements
- Applying secondary cam straps to prevent complete collapse
- Applying quasi statically tilting through the power puller until initiation of collapse mechanism
- Measuring the resulting heights l_1 through l_4 corresponding to known lengths L_1 through L_4 respectively (see Figure 153).
- Video recording each collapse for post-processing.

Three collapses were performed for each hinge set. As with the in-scale tests, 25 distinct hinge sets were tested which generated a total of 75 tilt tests performed. Note that after each test the platform was lowered to level and each joint was examined to ensure no deformations developed. Additionally, the element stiffening was fully released and then reapplied when the defined hinge set was changed to ensure the arch began in the same stable state.

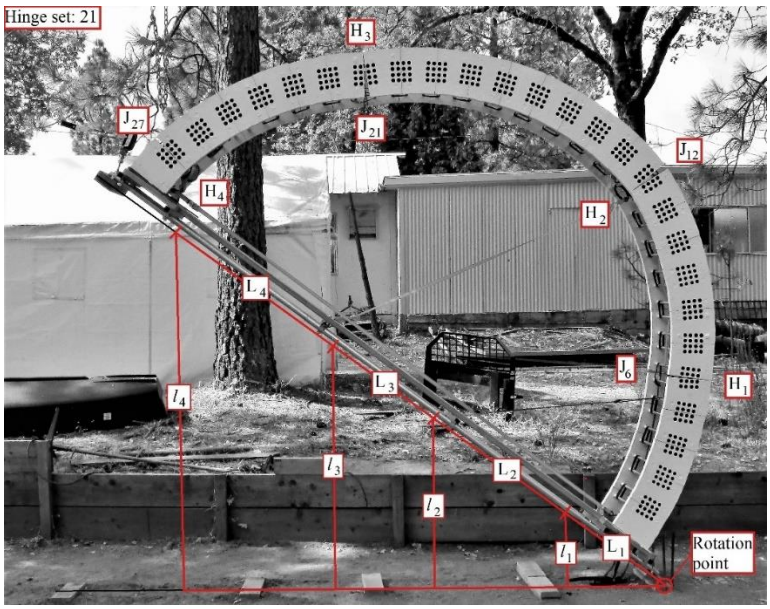

Figure 153. Mechanical collapse and the associated measurement lengths for hinge set 21 of the full-scale arch tests.

5.3.4.1 Hinge Selection

The hinge sets were selected through the development of a CLD. Figure 154 shows the constructed CLD and highlights the 25 capacities being evaluated. Note that blocks N_1 and N_{27} are fixed for the experimentation and thus the lower joint limits are J_2 and J_{27}. Also note that a theoretical capacity increase factor of 3.3 exists within the group of mechanical sets. Lastly Table 4 lists the 25 corresponding hinge set configurations.

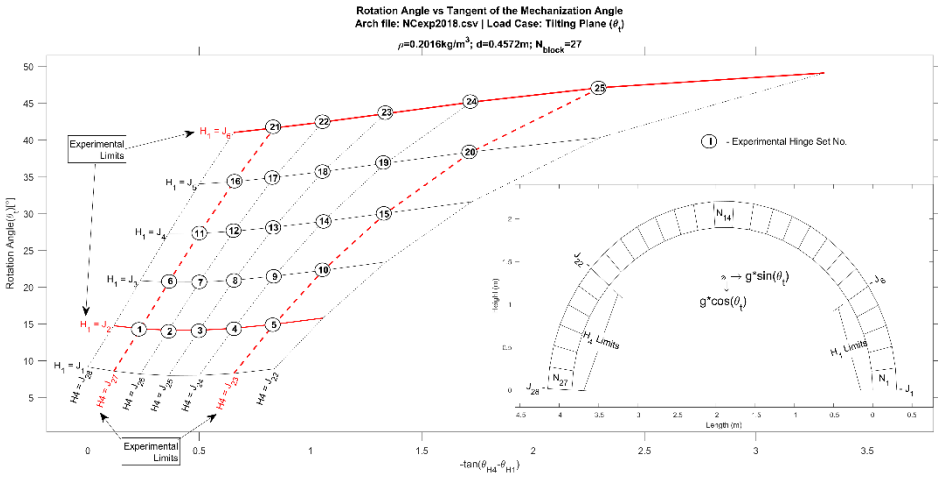

Figure 154. CLD for the full-scale arch subjected to a tilting plane

Table 4. The 25 hinge sets used for the full-scale arch capacity tests

Hinge Set	H_1	H_2	H_3	H_4	Hinge Set	H_1	H_2	H_3	H_4
1	J_2	J_8	J_{17}	J_{26}	**16**	J_5	J_{11}	J_{20}	J_{26}
2	J_2	J_8	J_{17}	J_{25}	**17**	J_5	J_{11}	J_{20}	J_{25}
3	J_2	J_8	J_{17}	J_{24}	**18**	J_5	J_{11}	J_{19}	J_{24}
4	J_2	J_8	J_{17}	J_{23}	**19**	J_5	J_{11}	J_{19}	J_{23}
5	J_2	J_8	J_{17}	J_{22}	**20**	J_5	J_{11}	J_{19}	J_{22}
6	J_3	J_9	J_{18}	J_{26}	**21**	J_6	J_{12}	J_{21}	J_{26}
7	J_3	J_9	J_{18}	J_{25}	**22**	J_6	J_{12}	J_{20}	J_{25}
8	J_3	J_9	J_{18}	J_{24}	**23**	J_6	J_{12}	J_{20}	J_{24}
9	J_3	J_9	J_{18}	J_{23}	**24**	J_6	J_{12}	J_{20}	J_{23}
10	J_3	J_9	J_{17}	J_{22}	**25**	J_6	J_{12}	J_{19}	J_{22}
11	J_4	J_{10}	J_{19}	J_{26}	Note: Refer to Figure 150 for identifying joint location.				
12	J_4	J_{10}	J_{19}	J_{25}					
13	J_4	J_{10}	J_{19}	J_{24}					
14	J_4	J_{10}	J_{18}	J_{23}					
15	J_4	J_{10}	J_{18}	J_{22}					

5.3.4.2 Collapse and Measurement

For each hinge set, three collapses were executed. Each collapse was performed through the manual rotation of the platform by the reverse locking power puller (see Figure 153). The platform was rotated until the arch initiated the collapse mechanism and at a quasi-static rate. At the point of collapse the crank was locked and the heights l_1 through l_2 were recorded. The platform was then lowered, and the system was checked for deformations. Each collapse was also recorded.

5.3.5 Data

The platform lengths were 0.864 m, 2.032 m, 2.896 m, and 4.166 m for L_1 through L_4 respectively. Table 5 lists the recorded data for full-sale arch tests.

Table 5. Recorded collapse data for the full-scale arch tests

Platform Measurements				precision	* M - MACHANISM
L1 [in]	L2 [in]	L3 [in]	L4 [in]	+/- 0.25 in	S - SLIP
34	80	114	164		R - ROTATION

COLLAPSE DATA						COLLAPSE DATA					
Run	Hinge Set	l1 [in]	l2 [in]	l3 [in]	l4 [in]	Run	Hinge Set	l1 [in]	l2 [in]	l3 [in]	l4 [in]
1	1	4.5	11.5625	17	25	40	14	12.1875	28.875	41.625	60.625
2	1	4	9.625	14.75	21.25	41	14	12.125	28.6875	41.1875	60.125
3	1	4.4375	10.6875	15.75	23.25	42	14	11.9375	28.125	39.5625	59.0625
4	2	4.3125	10.4375	15.25	22.625	43	15	12.6875	29.625	42.6875	62.1875
5	2	4.125	9.875	14.75	21.5	44	15	12.5	29.4375	42.3125	61.8125
6	2	4.25	10.3125	15	22.25	45	15	12.125	28.875	41.625	54.5625
7	3	4.0625	9.875	14.375	21.375	46	20	15.875	37.5625	54	78.3125
8	3	3.875	9.5	13.875	20.75	47	20	16.0625	37.8125	54.5625	79.3125
9	3	4.125	10	14.375	21.25	48	20	15.9375	37.4375	54	78.75
10	4	3.125	9.375	13.75	20.8125	49	19	15.8125	36.8125	53	77.6875
11	4	4.0625	9.75	14.25	21.375	50	19	15.875	36.8125	53.4375	77.3125
12	4	3.9375	9.5625	14	20.9375	51	19	15.75	36.8125	53.3125	77.25
13	5	4.0625	9.875	14.5	21.5	52	18	15.25	36.25	52.25	75.9375
14	5	3.9375	9.5	13.9375	20.5	53	18	15.4375	36.1875	52.6875	75.8125
15	5	4	9.625	14.0625	20.875	54	18	15.25	36.125	52.125	75.8125
16	10	8.9375	21.0625	30.5625	44.8125	55	17	15.8125	36.8125	53	77.25
17	10	8.875	21	30.5	44.625	56	17	15.8125	36.8125	53	77.1375
18	10	8.875	21	30.4375	44.4375	57	17	15.8125	36.75	52.9375	77.0625
19	9	8.4375	20	28.9375	42.3125	58	16	17	40.3125	56.875	83.9375
20	9	8.4375	20	28.9375	42.375	59	16	16.1875	38.3125	55	79.9375
21	9	8.4375	20.0625	28.6875	42.3125	60	16	16.1875	38	54.625	79.4375
22	8	8.5625	19.6875	29.0625	42.4375	61	21	20	47.8125	67.9375	97.9375
23	8	8.3125	19.4375	28.5625	41.75	62	21	20	47.0625	67.5625	97.1875
24	8	8.375	19.1525	29	42.4375	63	21	19.5625	46.1875	66.6875	96.5625
25	7	8.1875	19.1525	28.125	41.3125	64	22	20.0625	48.125	68.0625	98.8125
26	7	7.9375	19.0625	27.3125	40.5625	65	22	19.8125	46.25	66.4375	96.5625
27	7	8.1875	19.3125	28.0625	41.1875	66	22	19.8125	46.25	66.4375	96
28	6	8.3125	19.9375	28.9375	42.3125	67	23	19.6875	46.1875	67.4375	97.625
29	6	8.25	19.625	28.6875	41.9375	68	23	20.125	46.625	67.3125	97.0625
30	6	8.1875	19.3125	27.8125	41.0625	69	23	19.8125	46.125	66.4375	96
31	11	12.8125	29.6875	42.6875	62.3125	70	24	20.8125	47.875	67.875	97.25
32	11	12.4375	29.4375	42.3125	61.625	71	24	20.8125	47.9375	68	97.3125
33	11	12.375	29.3125	42.25	61.375	72	24	20.8125	47.8125	67.75	97.125
34	12	12.5625	29.4375	42.75	62.0625	73	25	22.1875	51.1875	72.5625	104.0625
35	12	12.6875	29.5625	42.9375	62.5625	74	25	21.6875	50.5	72.5625	105.4375
36	12	12.5	29.4375	42.4375	61.875	75	25	21.6875	50.625	72.4375	104.625
37	13	12.5625	29.625	42.6875	62.1875						
38	13	12.4375	29.3125	42.3125	61.5625						
39	13	12.4375	29.4375	42.3125	61.625						

5.3.6 Results

For each collapse, the four length height ratios are averaged and transformed to a rotation via Eqn. 116. These averaged rotation values were then averaged with the three collapses to determine a single rotation angle value. The measurement error was propagated through the averaging calculations and compared with the variance in the three collapses. This comparison revealed the variance in

collapse dominated the error. Nonetheless, a minimum of 3 digits of precision was obtained for each hinge set. Table 6 presents the results.

Table 6. Calculated collapse angles, error and its source for the full-scale arch

Hinge Set	θ_t	±	source	Hinge Set	θ_t	±	source
1	7.68	0.08	stdv	**16**	26.0	0.1	stdv
2	7.38	0.08	stdv	**17**	24.9	0.1	stdv
3	7.04	0.08	stdv	**18**	24.5	0.1	stdv
4	6.84	0.08	stdv	**19**	25.0	0.1	stdv
5	6.99	0.08	stdv	**20**	25.4	0.1	meas
6	13.93	0.09	stdv	**21**	30.5	0.1	stdv
7	13.66	0.09	stdv	**22**	30.4	0.1	stdv
8	14.05	0.09	stdv	**23**	30.4	0.1	stdv
9	14.17	0.09	stdv	**24**	31.0	0.1	stdv
10	14.90	0.09	stdv	**25**	32.5	0.1	stdv
11	20.4	0.1	meas	* meas – measurement error stdv – standard deviation Note: Refer to Table 5 for hinge set details.			
12	20.4	0.1	stdv				
13	20.4	0.1	stdv				
14	19.7	0.1	stdv				
15	20.1	0.1	stdv				

The resulting rotation capacities of the experiment and their comparison with the black box analysis model are shown in Figure 155. The hinge sets are shown in a decision tree format with the minimum and maximum configurations identified. The black box analysis results are consistently greater than the experimental, but a capacity increase factor of 4.2 was experimentally obtained, nonetheless.

5.3.6.1 Experimental Observations

In the hinge set transition for hinge H_1 from J_2 to J_3 and from J_3 to J_4 base rotations were observed between the base block, N_1 and the platform. The reasoning for this was the cam strap anchoring was insufficient to create a rigid base. For both instances additional strapping was applied to the base blocks in an attempt to establish rigidity. The increased strapping reinforcement applied for the J_3 to J_4 was repeated for the remining transitions without any observed base deformations.

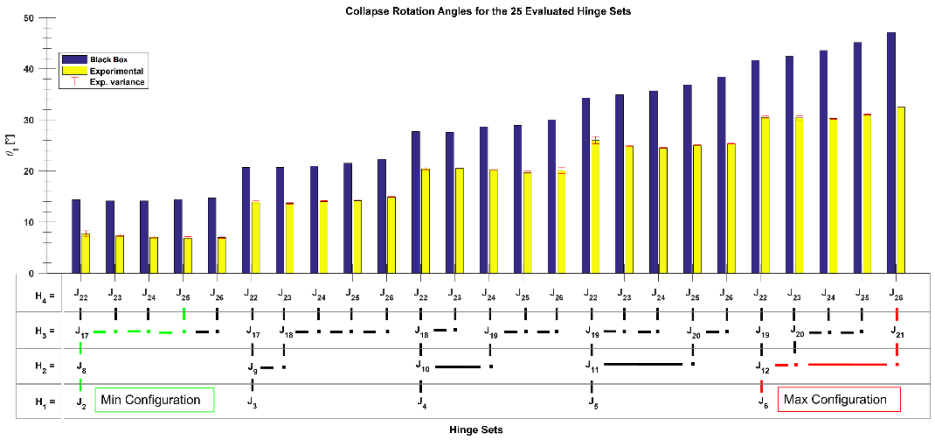

Figure 155. Theoretical and experimental results for the full-scale arch subjected to a tilting plane

5.3.7 Post-Processing

The observed capacity increase of 4.2 is greater than the theoretical potential of 3.3. One reason for this discrepancy was the existence of the observed base deformations under H_1. When H_1 was switched from J_2 to J_3 and from J_3 to J_4 deformations were observed and the base stiffening strategy was adjusted.

5.3.7.1 Capacity Adjustment

Following the same post-processing approach as for the in-scale arch tests of Section 5.2, the ratio between the experimental and the theoretical results for each hinge set were calculated. These ratios were then averaged for fixed hinge H_1 positions. Figure 156 shows this averaged ratio between the black box analysis and experimental results for each H_1 position.

From Figure 156 the insufficient stiffness between the base block and the platform can be directly observed in the significant reduction of capacity for hinge H_1 and joint J_1. The first readjustment can also be observed by the increase in relative capacity for hinge H_1 at joint J_2. The stabilization of the base stiffness is also observed in the developed consistency in the relative capacity for hinge H_1 greater than joint J_2. Therefore, the evaluation of the averaged relative capacities is able to capture these deficiencies in addition to establishing the capacity adjustment equation. Ignoring the data points for J_1 and J_2, the capacity adjustment equation,

$$C_{LA} = -0.0017 \cdot H_1 + 0.71 \quad (120)$$

is established. Applying Eqn. 120 to the black box model produces the results shown in Figure 157.

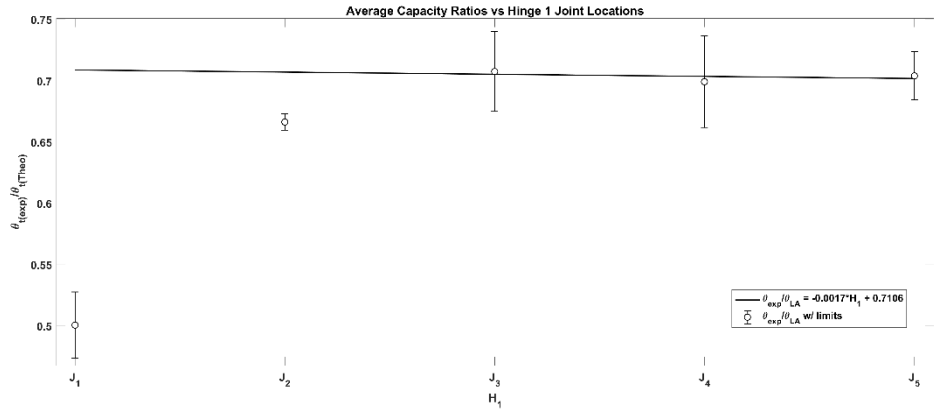

Figure 156. Averaged ratios and capacity adjustment equation for the full-scale arch subjected to a tilting plane

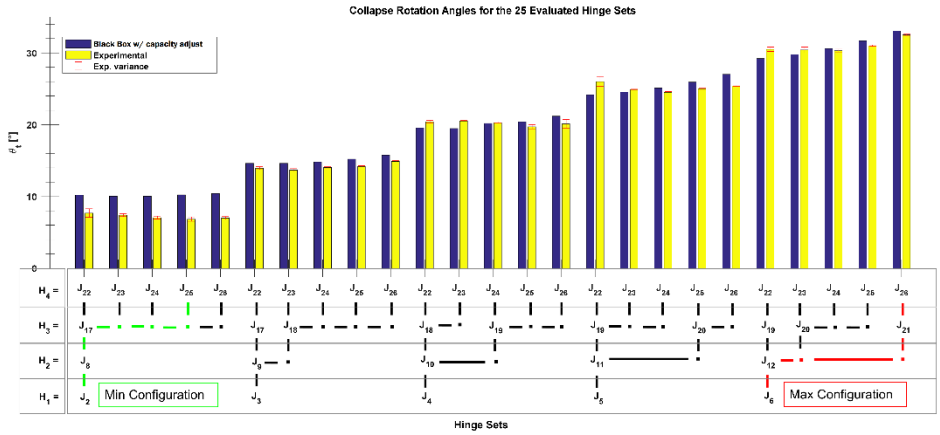

Figure 157. Capacity results comparison with capacity adjustment applied for the full-scale arch subjected to a tilting platform

5.3.8 Additional Remarks

The second experimental campaign focusing on hinge control and the characterization of dry-stack masonry arches revealed that the potential to control failure for a full-scale masonry arch exists and that the applied approach to characterize the analysis model to the experimental behavior is repeatable. As with the first experiment, the existence of base deformations was observed, but in this instance, these deformations were between the base block and the platform. With the first experiment, the base blocks were anchored to the platform with screws, and the deformations were observed in the first joint as a result of the Velcro's® stiffness. This experiment however corrected that issue with the application of the cam straps, but the anchoring of the arch to the platform was insufficient to resist deformations. Nonetheless, this deformation

was identified, and corrective measures implemented for hinge H_1 at and above joint J_3. This can be seen in the capacity adjustment equation (see Figure 156) which becomes almost constant after this correction is made. Also, the inclusion of the 36-grit sandpaper on the block joint surfaces successfully removed the inclusion of additional mechanisms types.

After the completion of the experimental testing the arch was disassembled, inspected and stored for future tests (see Figure 158). The inspection of the blocks revealed no observable damage and highlights a great benefit that arises from designing and defining mechanical failure as the system's limit.

Figure 158. Disassembled (a) arch and (b) reinforcing materials, and (c) the stored system

5.4 Concluding Remarks

The hinge-controlling of dry-stack arches and the examination of a family of admissible mechanisms allows for their characterization. The CLDs create a simple first-order assessment structure that can be utilized in project design and development. The CLDs go even further by establishing the general limits of admissible mechanisms that exist in an arch and provide a defined family of mechanisms that can exist with the implementation of hinge control.

Utilizing the defined family of mechanisms from the CLD to perform capacity testing of a physical arch then allows the characterization of the analysis model to the physical arch through the capacity adjustment equation. This capacity adjustment equation extends the capacity adjustment to all admissible mechanisms and can be directly incorporated into the black box structure that governs the analysis and the KCLC. Additionally, each of the two arches faced non-ideal conditions that effected their capacities, and the capacity adjustment equations were able to adjust the model without the direct knowledge or intervention of the non-ideal condition into the analysis. This highlights an incredible versatility potential to this analysis structure and design approach.

CHAPTER 6

2D SEISMIC MODELLING

List of Abbreviations and Symbols

- A_i — Polynomial fit constants for cartesian deformation path of the CM (Chapter 4)
- a_p — Acceleration pulse magnitude for two-step pulse test
- a_x — Horizontal component of applied acceleration
- a_y — Vertical component of applied acceleration
- α_i — Rotation angle of the i^{th} mechanical joint
- B_i — Polynomial fit constants for Element lever arm rotations versus horizontal CM position (Chapter 4)
- C_i — Polynomial fit constants for curve fitting work equation
- CM — Center of Mass
- COR — Coefficient of Restitution
- D_i — Polynomial fit constants for establishing the time domain function
- d/dt — Time derivative
- ΔKE — Change in kinetic energy
- ΔPE — Change in gravitational potential energy
- Δt — Timestep
- $F_{acc,x}$ — Net equivalent horizontal acceleration force
- F_{app} — Net applied acceleration force
- F_{min} — Minimum force requirement to maintain the kinematic condition
- F_x — Horizontal force
- F_y — Vertical force
- H_i — Identifier for the i^{th} hinge

$H(x)$	—	Spatial function for establishing the time domain
I_{Ej}	—	Moment of inertia of the j^{th} element
KE_i	—	Initial kinetic energy
KE_f	—	Final kinetic energy
l_{Ej}	—	Lever arm length between the arch and j^{th} element centroids
λ_a	—	Collapse multiplier for uniform acceleration
m_{Ej}	—	Total mass of the j^{th} element
m_T	—	Total mass of the arch
ω_{Ej}	—	Angular velocity of the j^{th} element's lever arm
SDOF	—	Single degree of freedom
t_0	—	Start time
t_1	—	First time value
t_2	—	Second time value
t_p	—	Acceleration pulse duration
τ_{Ej}	—	Torque from the j^{th} element applied at the CM from the element's centroid
θ_a	—	Polar angle of an acceleration vector
$\boldsymbol{v}$	—	Velocity vector
W	—	Work
W_{app}	—	Applied work
W_{min}	—	Minimum work
W_{req}	—	Required work
W_{rot}	—	Rotational work
W_{trans}	—	Translational work

It is imperative in modern structural engineering that a comprehensive analysis model be able to address dynamic conditions. In Chapter 3 the kinematic equilibrium approach to limit analysis was presented through the development of free-body diagrams and the corresponding equations of equilibrium for defining kinematic conditions. In Chapter 4, the inclusion of static mechanism deformations revealed that under constant horizontal acceleration the arch maintains a kinematically admissible condition as it propagates towards collapse. Maintaining kinematic equilibrium through this propagation of the kinematic condition requires an applied force. This required force coupled with the deformation generates a required work. The establishment of a deformation

description and the required work formulates a 2D spatial domain of the kinematic arch. In the context of dynamic modelling the remaining component necessary to describe the behavior is time domain.

The objective of this chapter is to establish a dynamic modelling methodology through the formation of the time domain from the application of kinematic equilibrium analysis to the static SDOF deformations of an arch. First the time domain is established for the standard Type I mechanism condition and constant horizontal acceleration in excess of the kinematic limit. The time domain formulation is expanded to constant 2D accelerations. Incorporating the time domain with the spatial domain then establishes the dynamic condition. This in turn allows for a more generalized analysis through the assumption of constant acceleration per time step sequence.

6.1 Time Domain for Constant Horizontal Acceleration

Utilizing the kinematic equilibrium evaluation of constant horizontal acceleration (Eqn. 6), the SDOF deformations of the standard mechanism (Eqns. 107-110), and the equivalent systems through parametric plotting (Section 4.4.3) for the arch shown in Figure 117, this section develops the time-displacement relationship through the path independence of conservative work. First, a work path is established and used to define the kinetic energy as a function of horizontal displacement. This time independent energy equation is then utilized with the velocity relationship of kinetic energy to formulate the time-displacement relationship.

6.1.1 Work Path

For conservative systems, the work required to travel from one position to another is path independent. The required work to mechanically deform an arch can be equated by the centroid equivalent deformations (Figure 119) and lever arm rotations (Figure 120) bound by α_1 rotations at hinge H_1 (see Section 4.4.3 for the deformation equivalents). Converting the horizontal acceleration collapse multiplier into an equivalent force, $F_{acc,x}$, applied to the total arch mass, m_T, at the centroid generates the force-displacement plot shown in Figure 159. Converting the collapse multiplier into equivalent forces at each element's centroid establishes the torque-rotation plots shown in Figure 160.

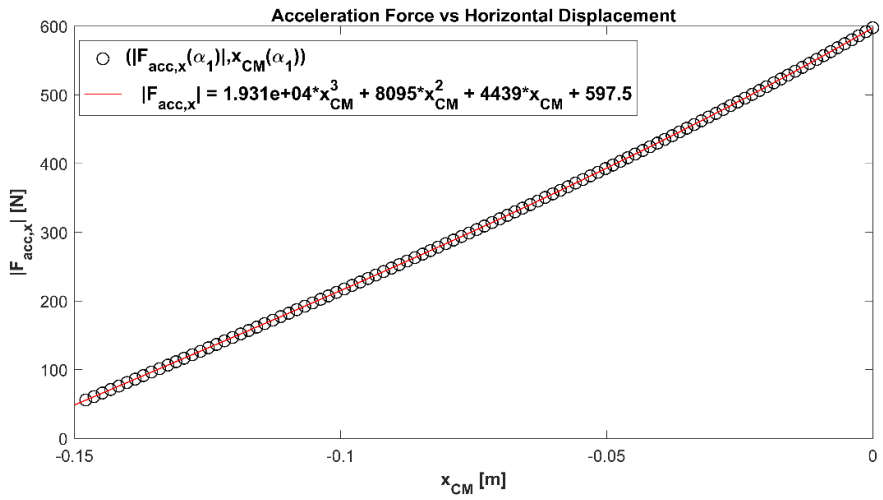

Figure 159. Parametric plot of acceleration force versus horizontal CM displacement and best fit polynomial

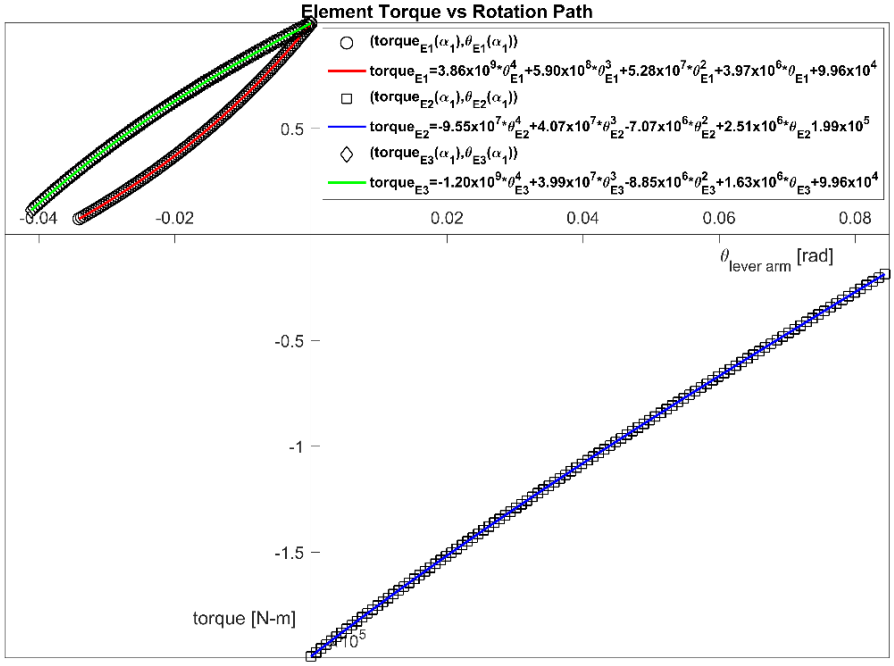

Figure 160. Parametric plot of the element induced torque at CM versus the respective lever arm rotation angles

Work can be expressed as the sum of the translational and rotational work

$$W = \int F dx + \int \tau_{E1} d\theta_{E1} + \int \tau_{E2} d\theta_{E2} + \int \tau_{E3} d\theta_{E3} \quad (121)$$

where τ_{Ej} is the torque from the j[th] element force equivalence. Integrating the force-displacement plot and torque-rotation plots generates the work path (see Figure 161). The potential energy curve established from

$$\Delta PE = m_T g \Delta y \tag{122}$$

is also shown in Figure 161. Note that the required work to carry the arch to collapse exceeds the change in potential energy. This difference is the result of the required thrust deformation necessary for the formation of the mechanism prior to and during the progression towards collapse. The required element rotations also add to this difference.

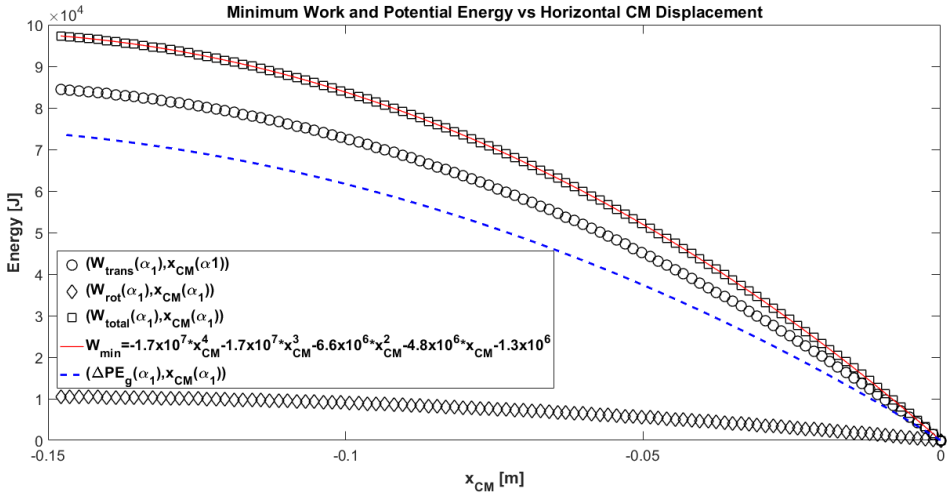

Figure 161. Parametric plot of minimum work and potential energy versus horizontal CM displacement with polynomial fit

The application of a polynomial fit evaluation to the work path identifies

$$W_{min}(x) = C_1 x^4 + C_2 x^3 + C_3 x^2 + C_4 x + C_5 \tag{123}$$

as a reasonable equation the with constants C_i identified in Figure 161.

6.1.2 Kinetic Energy

The work path in Figure 161 represents the required work to maintain kinematic equilibrium along the deformation path to collapse. An applied acceleration force, F_{app}, that exceeds the limit, F_{min}, established from the collapse multiplier, transitions the system from its stable state to its mechanical state. Maintaining the rigid element assumption and ideal hinges results in the excess energy from the applied work,

$$W_{app} = F_{app} \Delta x \tag{124}$$

be transformed into kinetic energy

$$\Delta KE = W_{app} - W_{req} \tag{125}$$

The required work, W_{req}, to travel from position x_1 to a position x is

$$W_{req} = W_{min}(x) - W_{min}(x_1) \tag{126}$$

Combining Eqns. 124-126 with the constant horizontal acceleration condition produces a final kinetic energy

$$KE_f(x) = KE_1 + F_{app}(x - x_1) - W_{min}(x) + W_{min}(x_1) \tag{127}$$

where KE_1 is the initial kinetic energy. Equation 127 therefore provides a spatial equation to the kinetic energy based upon the established work path of kinematic equilibrium (Figure 161 and Eqn. 123).

6.1.3 Time Domain

While Eqn. 127 establishes a displacement domain equation for kinetic energy, it can also be expressed as

$$KE = \frac{1}{2} m_T \boldsymbol{v}^2 + \frac{1}{2} I_{E1} \omega_{E1}^2 + \frac{1}{2} I_{E2} \omega_{E2}^2 + \frac{1}{2} I_{E3} \omega_{E3}^2 \tag{128}$$

where $\boldsymbol{v}$ is the velocity vector, and I_{Ej} and ω_{Ej} are the moment of inertia and lever arm angular velocity for the j[th] element respectively. The velocity vector is

$$\boldsymbol{v} = \frac{d\boldsymbol{r}}{dt} = \frac{dx}{dt} + \frac{dy}{dt} \tag{129}$$

and the angular velocities are

$$\omega_{Ei} = \frac{d\theta_{Ei}}{dt} \tag{130}$$

Utilizing the equivalent systems Eqns. 112-114 with Eqns. 128-130 generates

$$KE_f(x) = \frac{1}{2}\left[m_T \left(1 + \frac{1}{2} A_1 x + A_2\right)^2 + \sum_{i=1}^{3} m_{Ei} l_{Ei}^2 \left(\frac{1}{2} B_{1,Ei} x + B_{2,Ei}\right)^2\right] \left(\frac{dx}{dt}\right)^2 \tag{131}$$

where m_{Ei} and l_{Ei} are the i[th] elements mass and lever arm respectively, and the constants $B_{1,Ei}$ and $B_{2,Ei}$ are obtained from Eqn. 114 and Figure 120. Since the developed kinetic energy equation (Eqn. 127) is only dependent on position, the relationship between time and displacement is established by the integral

$$t - t_0 = \int H(x)\, dx \tag{132}$$

where

$$H(x) = \sqrt{\frac{m_T\left(1+\frac{1}{2}A_1 x + A_2\right)^2 + \sum_{i=1}^{3} m_{Ei} l_{Ei}^2 \left(\frac{1}{2} B_{1,Ei} x + B_{2,Ei}\right)^2}{2KE_f(x)}} \tag{133}$$

Figure 162 shows a plot of H(x) and the area representation of the numeric evaluation of Eqn. 132 for an applied acceleration of $1.14\lambda_a$. Both the initial time and kinetic energy are set to zero.

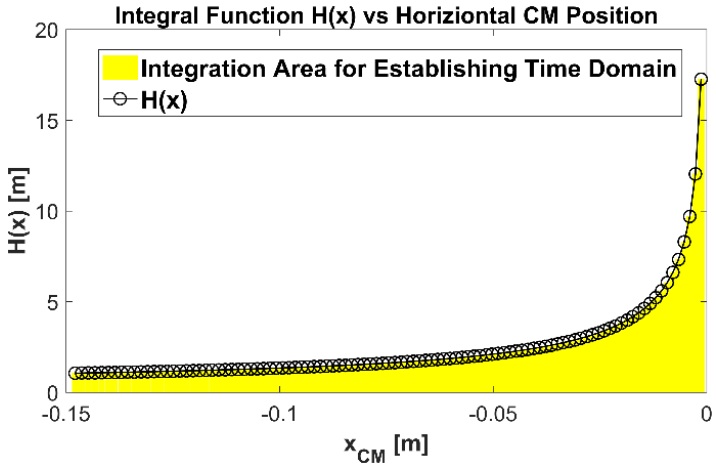

Figure 162. H(x) versus horizontal CM displacement and integration area

Figure 163 shows the solution to Eqn. 132, thus defining the relationship between horizontal CM position and time. A polynomial fit evaluation to the curve in Figure 163 reveals the relationship

$$x(t) = D_1 t^4 + D_2 t^3 + D_3 t^2 + D_4 t + D_5 \quad (134)$$

with the constants D_i shown in the figure. Therefore, given the initial conditions and the applied acceleration's magnitude and duration the horizontal CM displacement can be calculated. Once the displacement is known, the SDOF system is defined and the final energies and velocities can be obtained.

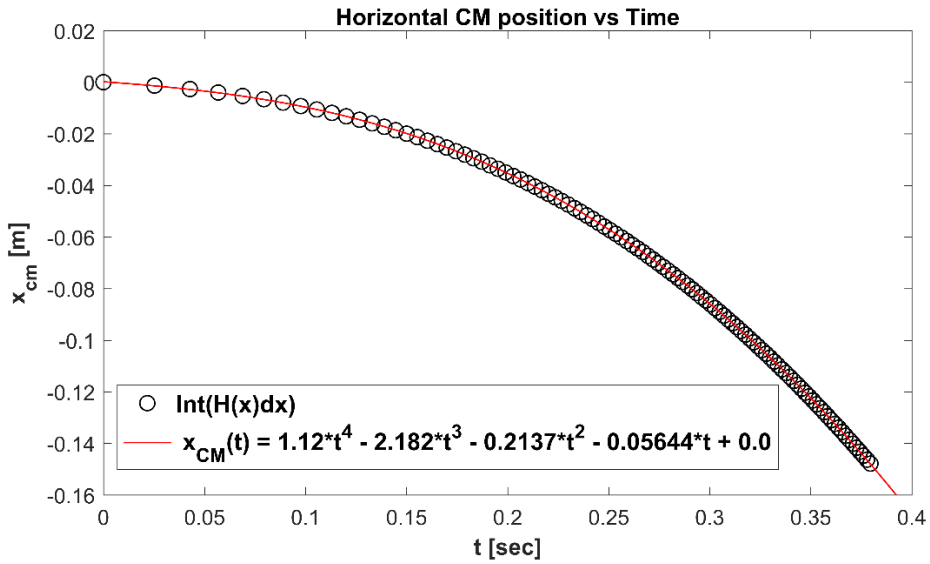

Figure 163. Horizontal position versus time with polynomial fit

6.2 2D Accelerations

For the non-horizontal acceleration condition the free-body diagram and equations of equilibrium used are shown in Figure 8 and Eqn. 7 of Section 3.2.1.2 respectively. For the generalization of acceleration direction, the limits of the potential acceleration against the defined mechanism must be established prior to establishing the work path.

6.2.1 Limit Line

Figure 164 shows the cartesian and polar plots of the collapse multiplier, λ_a versus the direction angle for the undeformed arch-hinge set shown in Figure 117. Note that a full 360° at 1° intervals with no admissibility evaluation was performed. From the cartesian plot the admissible angles (positive λ_a) are clearly defined between 87.5° and 267.5°. The polar plot establishes a clear line on which every calculated multiplier exists. This limit line creates a single boundary condition for the formation of the mechanism from any 2D acceleration applied to the arch-hinge condition. If the acceleration vector crosses the limit line, then the mechanism is initiated, and the kinematic system exists. Otherwise the arch is stable against the defined mechanism-loading condition.

Expanding upon this limit line observation, the same analysis was performed through the deformation process of the mechanism. Figure 165 shows the limit line plots for the α_1 at hinge H_1 deformations of 0°, 4°, 8° and 12°. These plots reveal that the defined SDOF deformation process of the arch-hinge condition causes the limit line to pivot towards vertical about the point 1 at 90°. This process even highlights the loss of admissibility through the crossing of vertical by the limit line at the 12° rotation of α_1 at hinge H_1 identified in the analysis shown in Figure 118. The pivot point is the shift from gravity's inclusion in the constants vector.

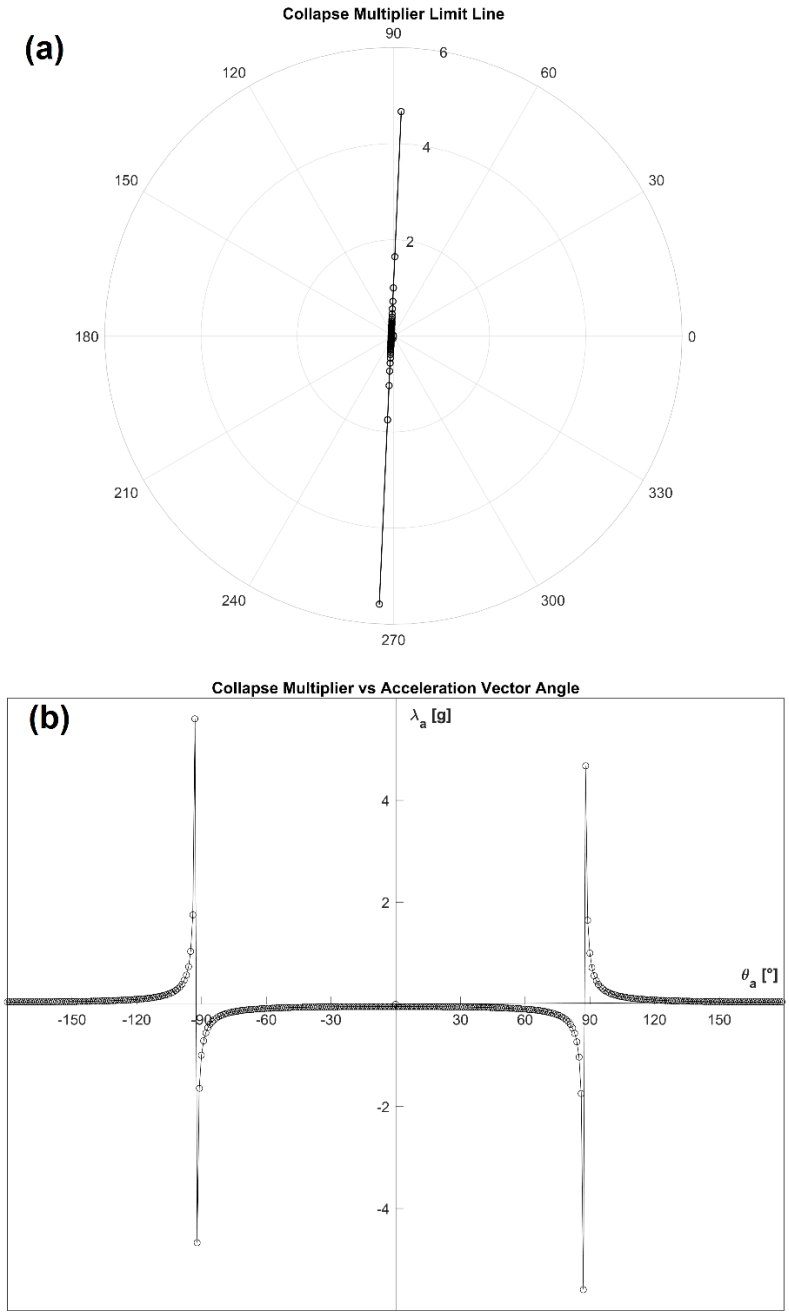

Figure 164. (a) Polar and (b) cartesian plots of λ_a versus θ_a

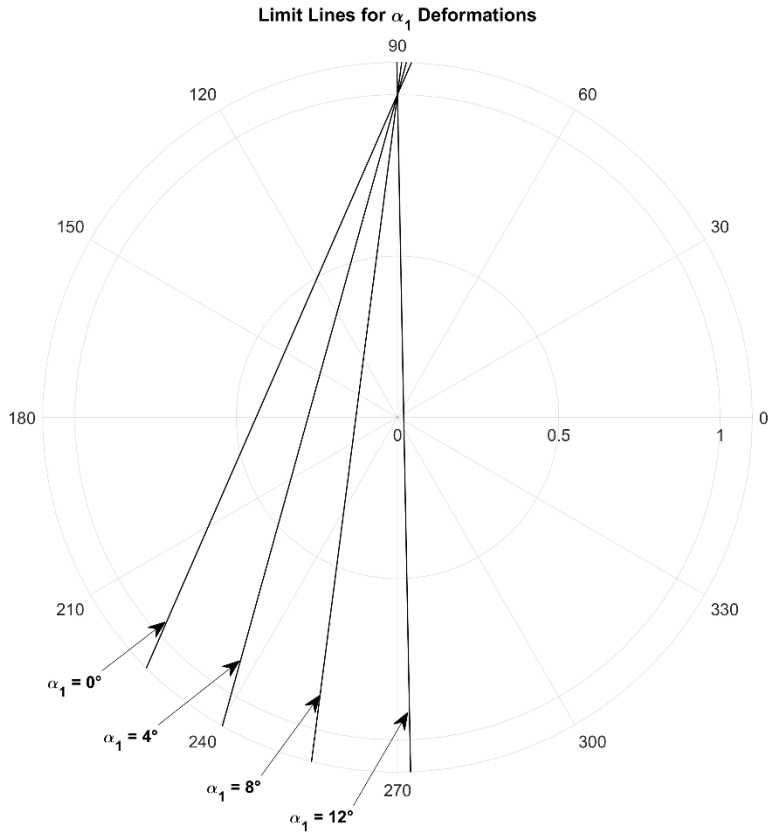

Figure 165. Acceleration limit lines for the α_1 at hinge H_1 deformations shown in Figure 118

6.2.2 Work Paths

The inclusion of a vertical force introduces a vertical work

$$W_{app} = \int F_x dx + \int F_y dy \tag{135}$$

but utilizing the deformation relationships of Eqns 112-114 allows the work to be rewritten solely in terms of x

$$W_{app} = \int \left[F_x + F_y \left(\frac{1}{2} B_1 x + B_2 \right) \right] dx \tag{136}$$

Figure 166 shows the calculated minimum work paths for various acceleration angles within the deformation limits identified in Figure 163. From Figure 166 there is an observed decrease in the required work with the polar angle increase. In cartesian coordinates, the more vertically negative the acceleration the greater the work. For the angle of 90°, the multiplier is 1.0 and the translational work required to carry the arch to collapse is identical to the change in potential energy (see Figure 167). This translational equivalence provides a validation of

the established work-path calculation under the applied conservative energy assumptions. The rotational work decreases with a vertically increasing acceleration vector and transitions to promoting collapse (see Figure 167b). This rotational work transformation results in the required work being less than the change in potential energy for acceleration angles between 90° and 97° for the arch-hinge set under evaluation (see Figure 166). Additionally, Eqn. 123 holds with varying constants for all work paths.

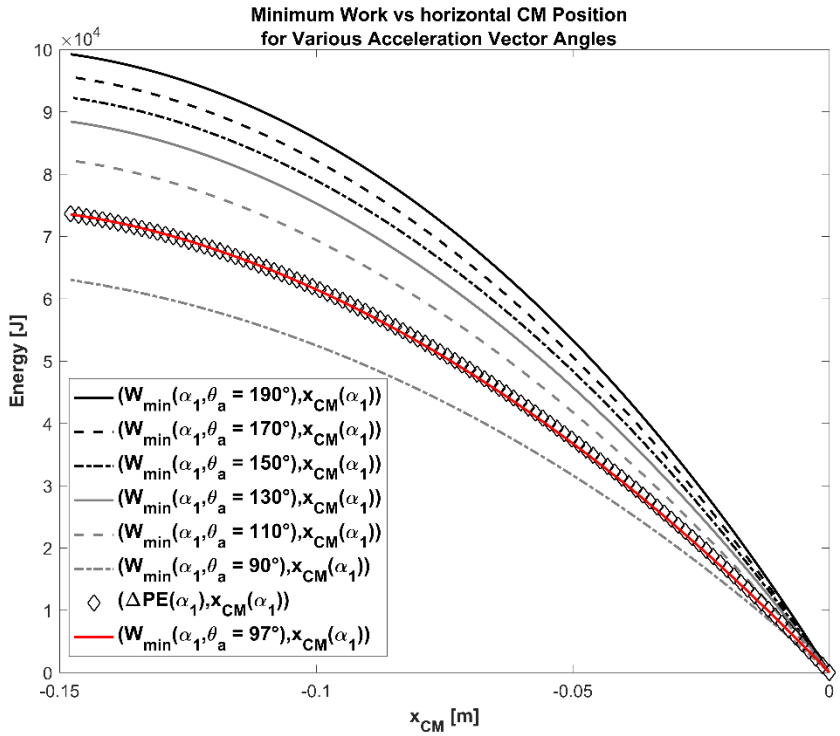

Figure 166. Parametric plots of minimum work versus horizontal displacement for acceleration vector angles, θ_a

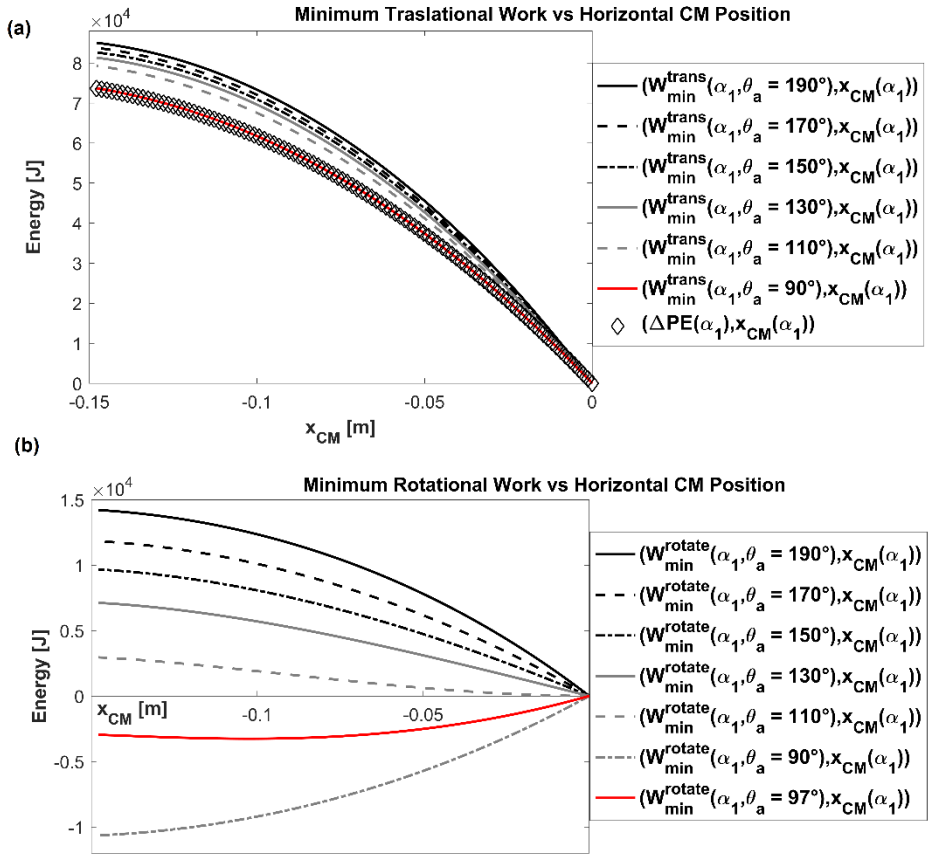

Figure 167. Parametric Plots of the minimum (a) translational and (b) rotational work for various acceleration angles

6.2.3 Kinetic Energies

With the inclusion of the vertical component of acceleration, the final displacement based kinetic energy equation becomes

$$KE_f(x) = KE_1 + F_x(x - x_1) + F_y\left[\frac{1}{2}B_1(x^2 - x_1^2) - B_2(x - x_1)\right] - W_{min}(x) + W_{min}(x_1) \quad (137)$$

Therefore, the polynomial behavior identified with the horizontal acceleration is maintained for any constant acceleration that exceeds the limit line.

6.2.4 Time Domain

The consistency with the polynomial structure of the work paths and spatial form of kinetic energy results in the time domain equations (Eqns. 132-133) to hold for all constant accelerations. Additionally, since Eqn. 120 holds for varying acceleration vector angles within the admissible limits, the time-displacement equation (Eqn. 134) and the procedure of obtaining its constants holds. This in turn establishes a simple methodology for evaluating the onset of a defined

mechanism and obtaining the resulting time-displacement domain for any constant 2D acceleration.

6.3 Time Incremental Analysis Procedure

Beginning at rest and undeformed, consider an arch subjected to a time dependent acceleration sequence that exceeds the limit line at time t_1. Assuming constant acceleration allows the formulation of the kinetic energy equation (Eqn. 137) and the time-displacement equation (Eqn. 134). At time t_2 the acceleration changes. Applying this timestep, Δt, to Eqn. 134 establishes the displacement x_2 at t_2. Applying the displacement position x_2 to Eqn. 137 determines the kinetic energy at time t_2. The final position and kinetic energy then become the initial conditions for the next constant acceleration condition. Repeating this time incremental calculation sequence therefore allows the arch to be dynamically propagated forward in a time.

6.3.1 Kinematic Condition and the Limit Line

If at time t_2 the displacement of the arch does not exceed the admissible kinematic equilibrium limit of the deformed state, then the arch has not collapsed. The arch has also entered a kinematic state. In this kinematic state, the limit line identifies whether kinetic energy is added or consumed in the deformation propagation. If the acceleration vector still exceeds the limit line then additional kinetic energy will accumulate in the system, otherwise the accumulated energy will be spent to propagate the arch forward.

6.3.2 Forward Facing Motion

In the kinematic state, the arch will continue to propagate along the deformation path until collapse or zero kinetic energy is reached. Reaching zero kinetic switches the direction of motion. If the acceleration remains below the limit line for the next time step, then the direction change results in the reversal of the motion and a negative final kinetic energy. The square root of Eqn. 133 requires the kinetic energy equation to be positive. Therefore, motion must always be forward facing. This is obtained by reversing the kinetic energy equation.

6.3.3 Crossing the Origin and the Coefficient of Restitution

The reversed motion propagates the arch back towards its original undeformed condition. Upon reaching that condition, the arch elements will experience an impact as the mechanical joints come into contact and the hinges switch joint limits. This impact will result in the dissipation of energy over a finite period of time. The standard parameter to define energy loss during impact is the Coefficient of Restitution (COR), and it is typically determined through one of three models: kinematic, kinetic and energetic [131]. The kinematic model developed by Newton

$$COR = \frac{KE_f}{KE_i} \tag{138}$$

is the model considered in this developed approach. The process of establishing a COR falls outside the scope of this work. For the development of the dynamic

analysis procedure, the motion is defined incrementally with the time steps. The impact can be isolated by the timesteps and the COR can be applied. The importance for the development of this dynamic analysis procedure is that the COR can be directly applied in the transition between the two hinge sets that define motion.

The hinge position switch reverses the mechanism. The limit line and deformation path are switched with the mechanism. The reduced kinetic energy and new constant acceleration are set, and the evaluation continues.

6.3.4 Combining Conditions

Figure 168 shows a flowchart representation of the dynamic analysis procedure developed from combining the described dynamic conditions. During each timestep in the defined acceleration sequence, the limit line is established and used to evaluate the work condition. Combining the identified work condition with the previous kinetic energy and position generate a final position and kinetic energy of the timestep. The reversal of final kinetic energy switches the motion. The arch's return to its undeformed configuration causes a COR reduction to the final kinetic energy of the timestep, and the hinge set is switched. This incremental process is repeated until the end of the acceleration sequence or a maximum displacement resulting in collapse is reached.

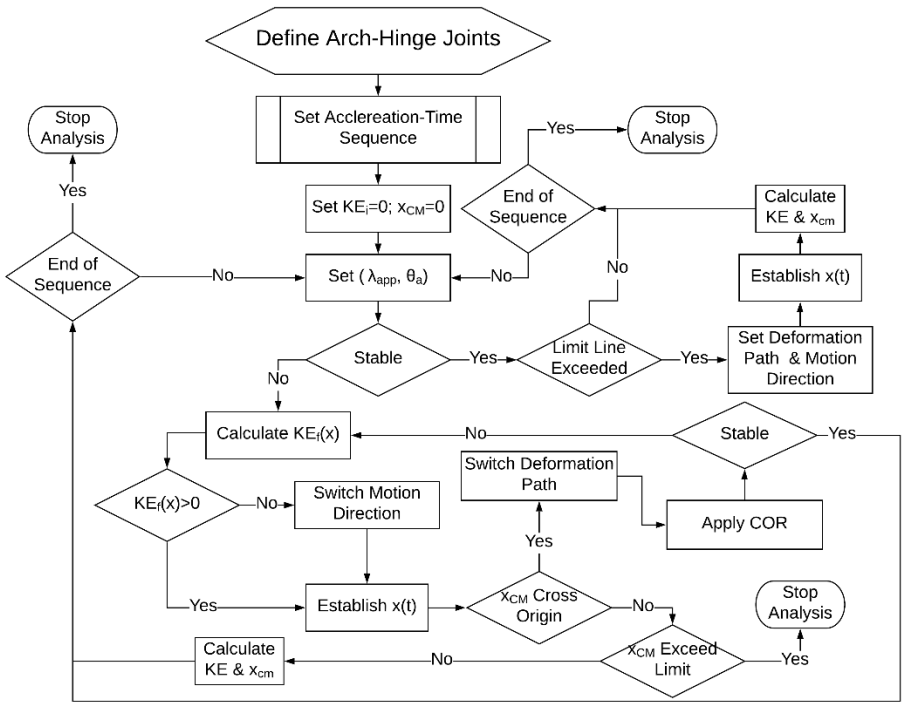

Figure 168. Dynamic analysis procedure flowchart

6.4 Half Cycle Collapse and Conservation of Energy

The developed incremental dynamic analysis procedure was constructed from the principles of energy conservation, the establishment of equivalent systems through parametric plots, and the path independence of conservative work. The equivalent systems were directly defined through the fixed rotations of hinge H_1 and utilized to establish the deformation paths and work paths of the mechanism. The work paths were validated by the equivalence of work and potential energy when the applied acceleration is directly opposed to gravity. The final validations remaining for this time incremental analysis structure are Oppenheim's half-cycle collapse line benchmark and the conservation of energy [132].

The Oppenheim arch geometry is shown in Figure 169 [132]. Note that the hinges switch joint limits, but the mechanical joints are defined as fixed. Examining the deformation sequence of the two configurations establishes the dynamic model for the arch.

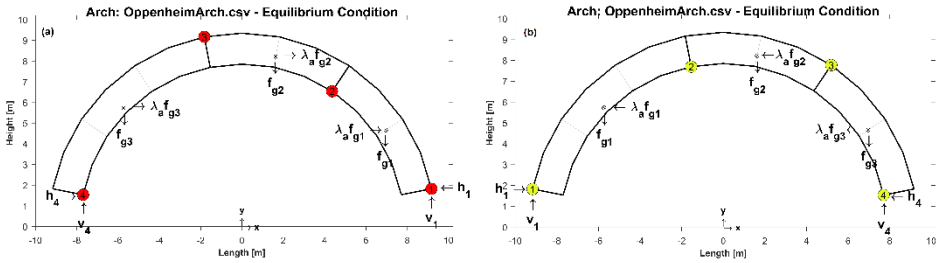

Figure 169. Oppenheim arch geometry with (a) original hinge geometry and (b) the hinge reversal from defined mechanical joints

Figure 170 shows a graphical display created for monitoring the propagation of a dynamic sequence. This graphical display consists of the three-element arch, the acceleration and limit line tracker, the CM position tracker and the applied acceleration timeline. The arch plot displays the geometric condition through the dynamic sequence. The acceleration and limit line tracker identify the polar position of the applied acceleration and the kinematic condition at each time step. The kinematic condition is identified by color; red indicates a condition promoting collapse and blue a condition promoting recovery. The acceleration tracker's color identifies the applied loads role and the limit line's color indicates the direction of motion.

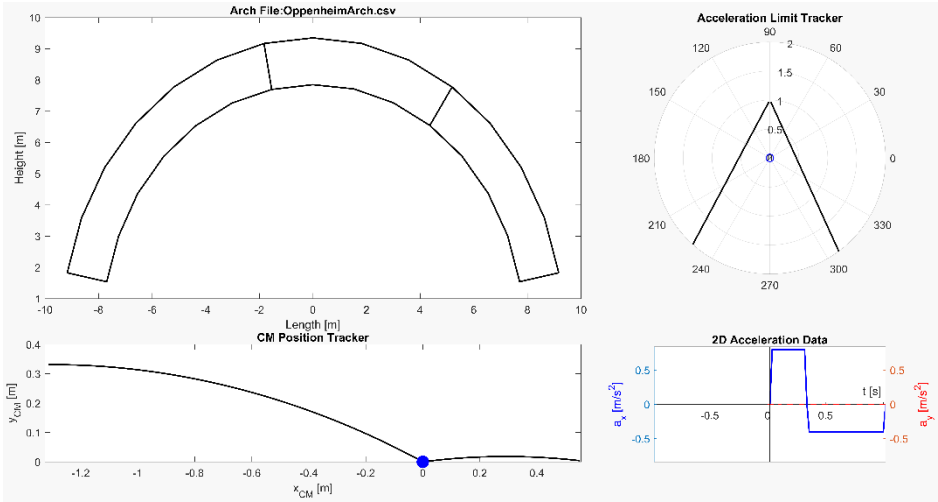

Figure 170. Dynamic monitoring display at time zero and a two-step acceleration pulse

Figure 171 shows three examples of the motion conditions through the propagation of the horizontal two-step acceleration pulse. The first has the acceleration and kinematic motion promoting and propagating towards collapse respectively. Then the acceleration drops below the limit line and the net work is against collapse, but the motion is still propagating towards collapse. Lastly in Figure 171, both motion and acceleration are driving the arch towards its undeformed configuration. If the deformation of the arch reaches or exceeds the kinematically admissible limit, then the arch geometry and CM tracker both turn red and the evaluation is stopped. Figure 172 shows this kinematic limit failure condition for a two-step pulse in excess of recovery.

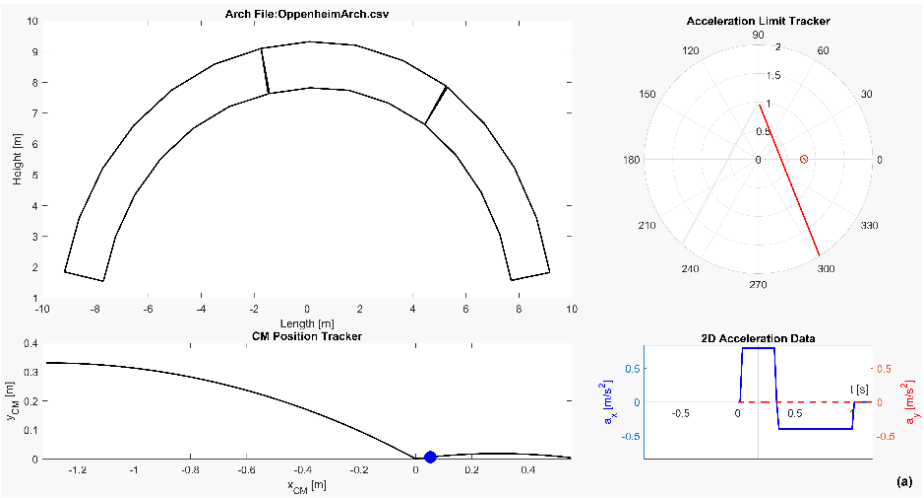

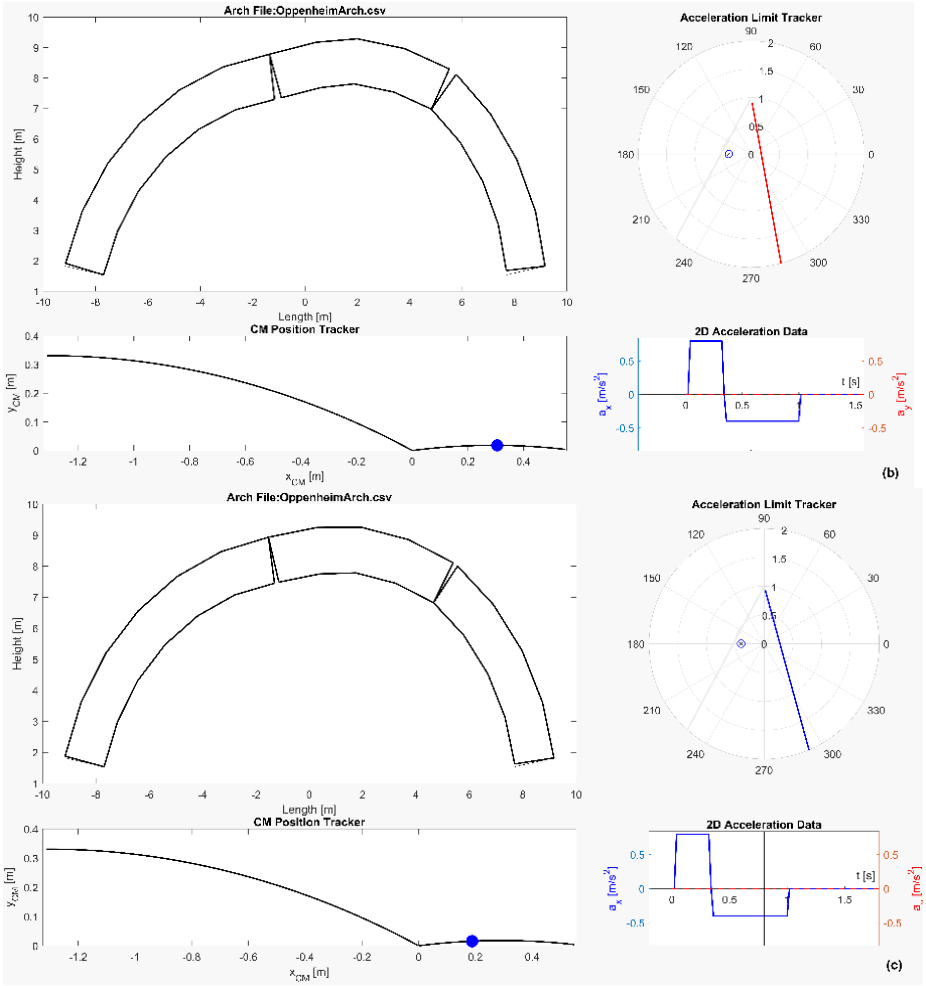

Figure 171. Dynamic propagation of the two-step pulse with (a) acceleration and motion propagating towards collapse, (b) acceleration working towards recovery, and (c) motion and acceleration towards recovery.

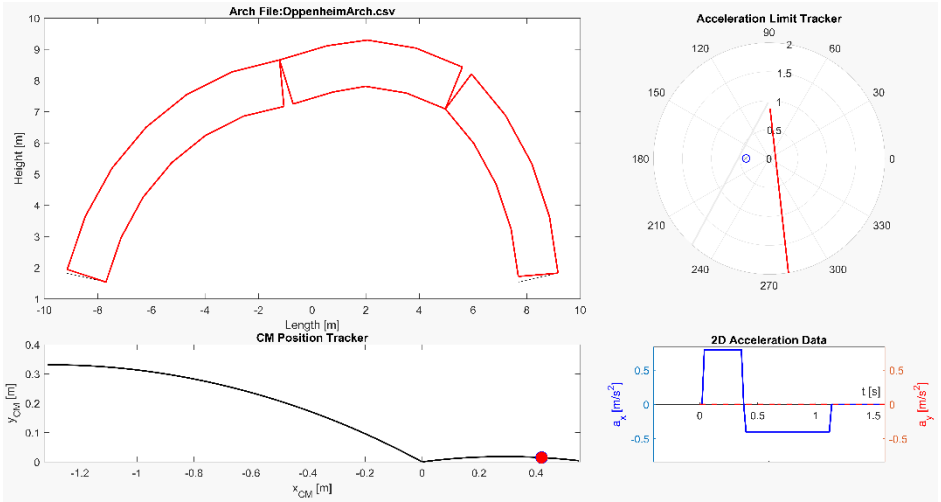

Figure 172. Identified collapse in the dynamic propagation

6.4.1 Half Cycle Collapse

In order to evaluate the half-cycle collapse, the Oppenheim two-step pulse was applied to a system with a COR set to zero for a perfectly plastic impact [131], [132]. The two-step pulse consists of applying an acceleration impulse of magnitude a_p for a duration t_p and followed by a reversed acceleration of half the magnitude applied for twice the duration. For each acceleration amplitude, the pulse time was continually increased by 0.02 seconds until a collapse was identified (see Figure 172). Figure 173 shows the resulting half-cycle failure domain developed from the described work-path approach as well as the original Oppenheim results. From Figure 173 it can be seen that the increase in static capacity from the upper bound limit is coupled with a small decrease in the recoverable impulse duration. The behavior of the arche's half-cycle failure is nonetheless captured by this time incremental work-path approach.

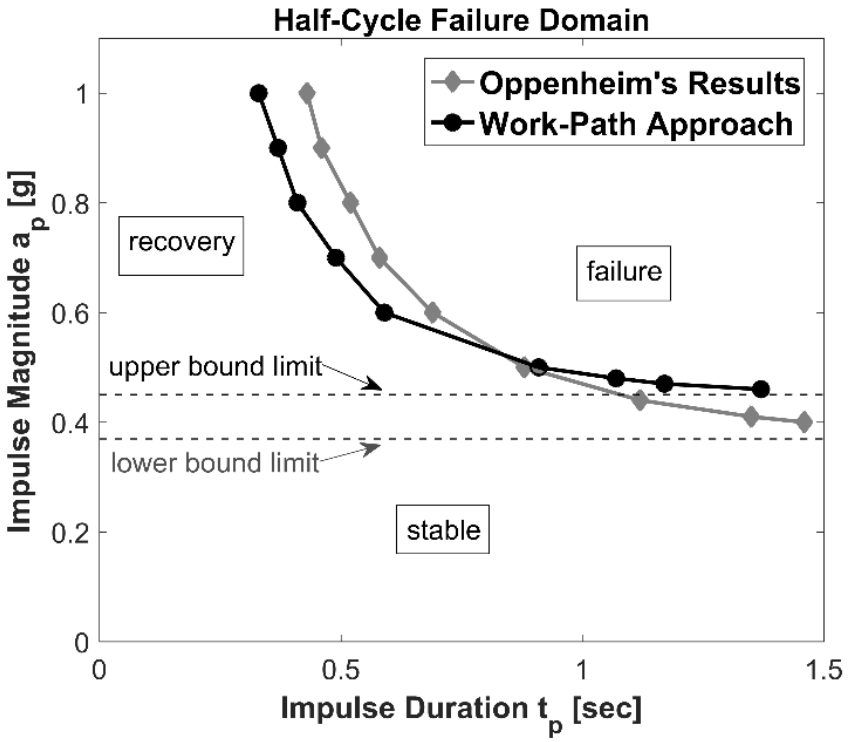

Figure 173. Half-cycle failure domain comparison for the two-step pulse analysis of the Oppenheim arch [132]

In order to examine the effects of a vertical component to the applied acceleration, the half-cycle collapse evaluation was repeated with the inclusion of constant vertical accelerations. This generates the failure domains shown in Figure 174. An applied vertical acceleration changes the static limit of its horizontal counterpart as expected. The behavior of the half-cycle failure is also maintained for all the shown conditions except for a vertical acceleration of 0.9g. As previously discussed, this strong vertical acceleration has the effect of reversing the rotational work. This reversal minimizes the window of recovery for weak horizontal pulses. This is consistent with the observations of the work paths shown in Figure 166 and it diminishes with the increase in the horizontal acceleration's magnitude.

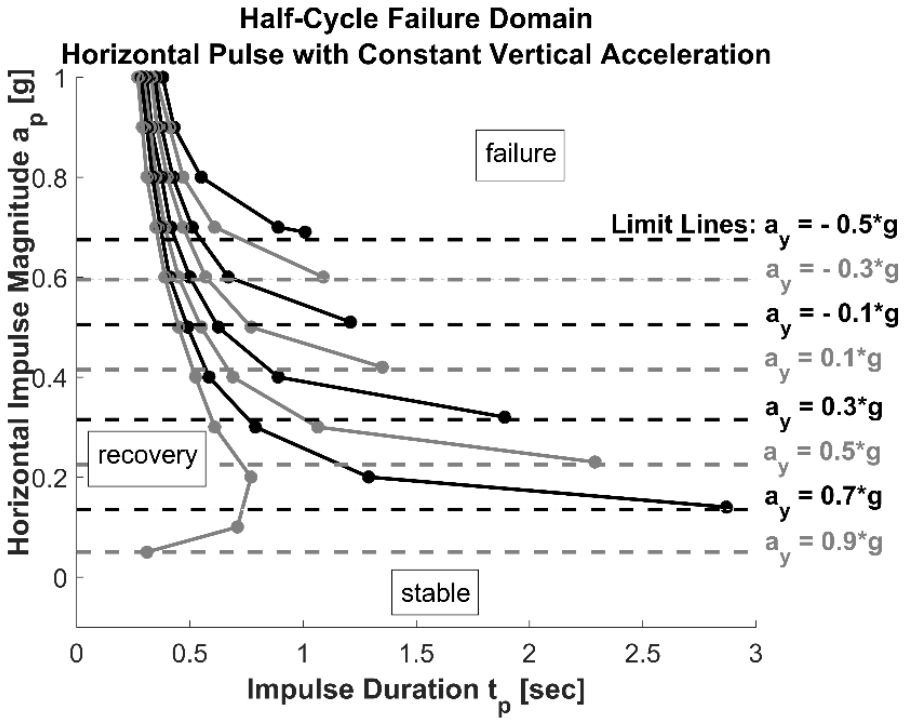

Figure 174. Half-cycle failure domains for various vertical accelerations with a horizontal pulse

6.4.2 Conservation of Energy

For the conservation of energy check, the COR was switched to unity to define a perfectly elastic instantaneous impacts. A 0.55g magnitude acceleration pulse was applied at various vector angles for a duration of 0.5 seconds. After the applied pulse, the analysis continued running for a total 20 seconds. The time-steps of the analysis were set at 0.02 seconds.

The rightward motion limit-line in Figure 170 identifies the admissible acceleration vector limits for a 0.55g magnitude as $-17° \leq \theta_a \leq 65°$. Therefore acceleration vector angles between -10° and 50° were selected for the evaluation of energy conservation. For each evaluation, the horizontal CM displacement and kinetic energy were recorded at each time increment. Figure 175 shows ten seconds of the displacement and kinetic energy plots for applied accelerations with vector angles of -10°, 0° and 10°. This figure shows the application of the acceleration and the resulting periodic nature of free motion with two distinct half-cycles resulting from the two mechanism geometries of left and right displacements. Additionally, as is expected the displacements and kinetic energies are out phase.

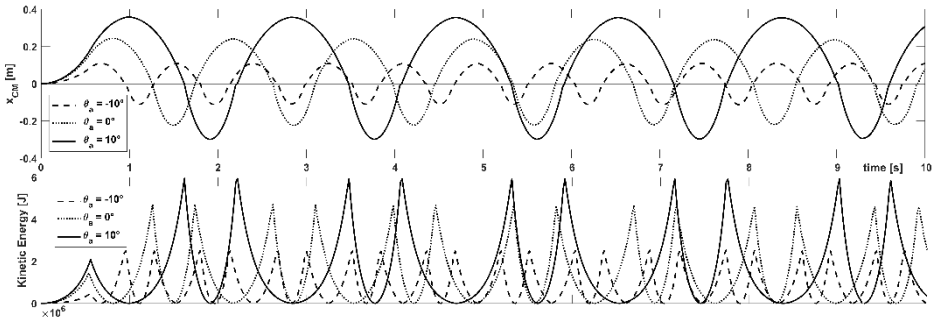

Figure 175. Horizontal CM displacement and kinetic energy versus time for applied 0.55g acceleration pulse with vector angles of -10°, 0°, and 10°

Figure 176 shows the percentage of kinetic energy loss between the first and last recorded energy peaks for each acceleration vector angle tested. The average energy loss is 4.4% over the 20 second evaluation for all the tests. Additionally, the energy loss never exceeded 10% for any single analysis. It can thus be reasonably argued that energy is conserved for the ideal conditions prescribed to the dynamic modelling approach.

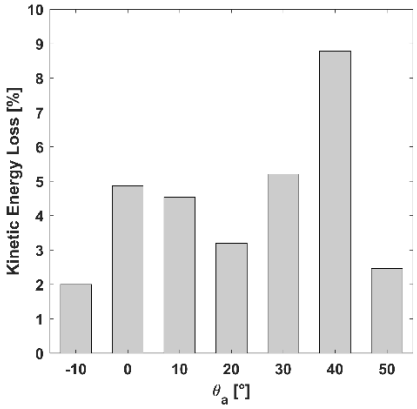

Figure 176. Percent kinematic energy loss versus applied acceleration with vector angle with a 0.55*g magnitude applied for 0.5 seconds

Figure 177 shows the peak horizontal displacement of the CM, the time duration when the peak displacement was reached, and the maximum kinetic energy for each of the applied acceleration vector angles with a 0.55g magnitude and a 0.5 second application. These plots reveal the sensitivity of the arch's response to the acceleration vector angle and the 20° vector angle is identified as the most kinematically significant angle for the single pulse applied to the given arch-hinge configuration.

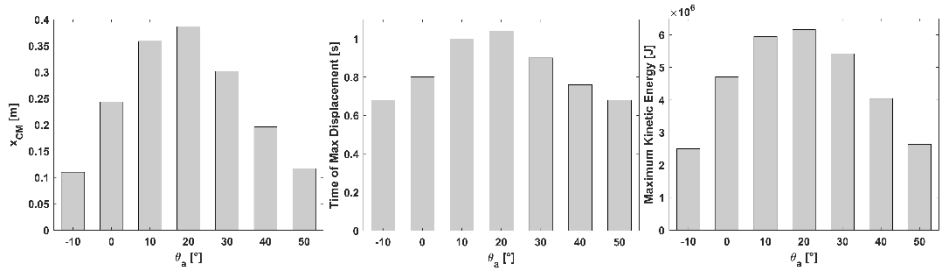

Figure 177. Maximum horizontal CM displacement, the time of maximum displacement, and the maximum kinetic energy versus the applied acceleration vector angle with a 0.55*g magnitude and applied for 0.5 seconds

6.5 Concluding Remarks

This chapter extends the application of kinematic equilibrium to the dynamic modelling of applied two-dimensional acceleration vectors. Using ideal conditions, the work path and time domain are formulated for applied 2D accelerations that exceed the stable limit of the arch-hinge configuration and they are used to construct the dynamic time incremental analysis structure from a defined constant acceleration at each time step of the analysis. The time domain and kinetic energy equations were finally coupled with a finite set of motions and impacts to establish the modelling structure.

The dynamic modelling approach was then evaluated for its half cycle collapse response and conservation of energy. The half-cycle collapse provided a benchmark test to the performance of the model and was also used to highlight the behavior change that arises when the applied accelerations are strongly vertical. The conservation of energy tests revealed that this dynamic model maintains an acceptable level of energy conservation when left under free motion, and the sensitivities of the acceleration vector angle are again highlighted.

With the inclusion of the dynamic modelling under the same kinematic equilibrium analysis structure, the foundation for a complete and comprehensive analysis approach has been formulated for hinge-controlled masonry arches.

CHAPTER 7

CONCLUSIONS

List of Abbreviations and Symbols

BVP — Boundary value problem

CLD — Collapse load diagram

KCLC — Kinematic collapse load calculator

LA — Limit analysis

RSBD — Reinforced stability-based design

SBD — Stability-based design

Structural masonry and the underlying SBD techniques have the potential to become an advantageous building method for future constructions. This requires architects to be versed in their application, engineers to be educated in their analysis, and practitioners to be trained in their construction. While the understanding of structural masonry has not been lost, the focus of that understanding has been applied to the preservation, restoration, and rehabilitation of historical structures. Consequently, fundamental gaps in the knowledge structure exist when considering the modernization of the structural system for new constructions. Limiting the focus to the analysis of masonry arches, the objective here has been to establish the foundation of a simplified structural analysis approach that bridges these engineering gaps for new constructions.

In Chapter 1, the motivation for the modernization of masonry was presented and followed with a discussion on a solution to removing sudden collapse and the joint slip potential through RSBD. Then it was highlighted how the objective of design versus assessment requires the evaluation of more than the minimum problem and the focus of stability instead of strength overlooks the conditions arising from controlling the mechanism. Lastly, SBD was described as a BVP whose solution is obtained through a singularity (kinematic equilibrium) calculation and an admissibility (thrust line geometry). This structure provides the typical input-output nature of a black-box analysis where the input is an arch

and mechanical joint configuration and the output is the loads, reactions and admissibility of the state's existence.

Chapter 2 presented a general schematic of the current understanding of unreinforced masonry and SBD as seen through the wealth of knowledge that exists and its consolidation. The mechanics of masonry and computational methods for vaults were discussed in this manner. From this discussion it is clear that most arch conditions can be analyzed. In the context of modernization for new constructions however, this information is not structured for the practicing engineer, the LA approaches are limited to the onset of mechanization, and the numerical approaches are computationally expensive.

The kinematic equilibrium problem and the construction of the free-body diagrams and corresponding equations of equilibrium were developed in Chapter 3. Through the representation of the arch as three rigid elements connected by four pins, the basic statics problem is derived as an infinite solution problem under self-weight. The inclusion of a loading geometry variable into the free body diagram of the traditional statics problem introduces the additional variable necessary to establish a determinant system. This determinate system is represented by the equations of equilibrium which are structured to obtain the solution through simple matrix manipulation. While the construction of the equations of equilibrium is quite simple, each loading condition requires its own, as well as each potential mechanism that arises from the inclusion of non-ideal slip joints. Therefore, the remainder of Chapter 3 was dedicated to establishing the free-body diagrams and equations of equilibrium for the basic loading conditions and the 69 additional mechanisms from the inclusion of static friction. The creation of these equations of equilibrium and free-body diagrams also establishes a database analysis structure as well as simplified formation strategies for the equations of equilibrium from conditions not yet addressed.

Chapter 4 developed the black box analysis structure. This analysis structure focuses on the assessment of kinematic admissibility primarily through the evaluation of the thrust line geometry against the kinematic boundary conditions of the arch. The thrust line geometry itself was established through thrust point position calculations established from the equilibrium evaluation between each block joint line and the first mechanical joint. After the discussion on kinematic admissibility, the KCLC was presented. The KCLC is a simplified interactive software analysis tool designed to carry out the black box analysis and display the results. The simplicity and adaptability of the KCLC was demonstrated through the inclusion of seven mechanism types and the corresponding limiting condition evaluation between the different mechanism capacities. The incorporation of non-circular arches into the KCLC was also developed through an AutoCAD® data extraction technique which simplifies the geometric development and links the analysis with one of the most widely used software in construction and engineering. Next, the capacity compensation for non-stable kinematically admissible conditions was developed and incorporated into the software structure. Capacity compensation is defined as the required joint reinforcement capacity necessary to maintain the thrust line within the material boundary of the arch, and it establishes the requirements for designing rigid

elements from a collection of rigid blocks. The last component of the black box analysis structure was the inclusion mechanical deformations. The SDOF nature of the defined kinematic condition produces a single variable requirement for defining a deformed state and the BVP nature of the analysis structure allows its synchronization. This synchronization was highlighted with the ability to evaluate the experimentally observed capacity reduction resulting from a finite hinge stiffness at a joint.

Chapters 3 and 4 presented the foundation of the developed SBD analysis for hinge-controlled masonry arches. They established an input-output structure of a calculator. Chapter 5 began the examination of the output through characterization strategies. First, the CLDs were developed for a first-order analysis strategy necessary for a design/analysis structure to compete in the modern market. Then two experimental campaigns were discussed in detail where the capacities of a family of mechanisms were tested. The experiments revealed the ability to capture the capacity behavior of an arch, develop simplified capacity adjustment equations, and directly address observed non-ideal conditions with the analysis structure. These non-ideal conditions were the inclusion of the slip-joint and static deformations resulting from a finite stiffness to the base blocks which were derived in Chapters 3 and 4.

Lastly, Chapter 6 utilized the link with mechanical deformations to incorporate the time domain and develop a 2D seismic modelling strategy. The link between the mechanical deformations and kinematic equilibrium was utilized to construct work path equations. These work paths in combination with the path independence of conservative work established a spatial description of kinetic energy for constant accelerations and allowed the formulation of the time domain. Then the assumption of constant acceleration per time increment was introduced to establish an incremental propagation of the position and kinetic energy of the arch. The examination of the dynamic modelling approach was compared against a half-cycle collapse benchmark and evaluated for the conservation of energy. These conditions revealed that the ideal conditions are upheld by the analysis model and that kinematic equilibrium can be utilized for both the static and dynamic analysis of arches.

This work establishes the foundation for a robust, efficient, adaptable, and accessible structural analysis model for the SBD analysis of dry-stack masonry arches, but it is by no means complete. The different loading conditions and all the mechanism types need to be incorporated into the software to form a single comprehensive KCLC. A simplified point grid measurement technique needs to be established to efficiently link theory and experiment to reduce the lag time between research and application. The dynamic modelling needs to expand to cover wind, traffic and potentially water loads as well. Lastly, a continued experimentation must be performed to further refine the non-ideal condition both for the analysis model and the development of construction techniques. While this list is long, this work has established the foundation (kinematic equilibrium) to determine the conditions requiring evaluation and the blueprint (black-box analysis, characterization, and dynamic modelling) to carry the condition through a comprehensive analysis. In essence, this work generates the minimum viable

product necessary to promote and advance the application of masonry in new constructions. Additionally, the developed analysis approach is structured to adapt and expand with time. So begins a new branch of structural analysis.

A

APPENDIX A – DEM ANALYSIS MODEL FOR THE IN-SCALE ARCH EXPERIMENT

List of Abbreviations and Symbols

DEM — Discrete element modelling

d — Unit weight of the voussoirs

In Section 5.2 the experimentation of an in-scale arch subjected to a tilting plane was presented in a format that focuses on the characterization of the arch and the experimental observations. As discussed in the text, a DEM model was developed and tested under that same hinge sets in order to create a validation trifecta. The reason for the trifecta was that both the experimentation of a family of mechanisms and the developed analysis model presented in this thesis are novel approaches that did not have any direct benchmarks for evaluation. The DEM model itself however lies outside the main scope of this work. Therefore, for the purpose of reproducibility and completeness the DEM model details are presented here in Appendix A, but they can also be found in existing literature [124]. Refer to Section 5.2 for the details of arch model geometry creation, hinge set selection, and the results of the DEM analysis.

For each of the 25 hinge sets tested an interdependent geometric model was created for the DEM evaluation of the experimental arch (see Figure 178). Each of the arch voussoirs were represented by rigid blocks. The joints were defined as zero-thickness interface elements behaving in accordance to the Coulomb failure criterion. The voussoir material properties of the arch are shown in Table 7. These material properties were obtained through experimental testing of the individual voussoirs. The required material parameter to model the voussoirs is the unit weight (d), which was taken as 550 kg/m^3. The joints between were presented by interfaces modelled using elastic-perfectly plastic coulomb slip joint area contact. Normal and shear stiffness were set high to prevent penetration between blocks at the joints. The interface cohesive, tensile strength and the dilatation angle were set to zero to represent dry-joints. Self-weight effects were incorporated as gravitational loads. Each analysis began by

establishing equilibrium under self-weight and then, a tilting plane analysis was undertaken until the observed collapse of the arch (Figure 178).

Table 7. Material properties used for the dry joints in the DEM model [124]

Joint Normal Stiffness [GPa/m]	Joint Shear Stiffness [GPa/m]	Joint Friction Angle [°]	Joint Cohesive Strength [kPa]	Joint Tensile Strength [MPa]	Joint Dilation Angle [°]
20	10	22	0	0	0

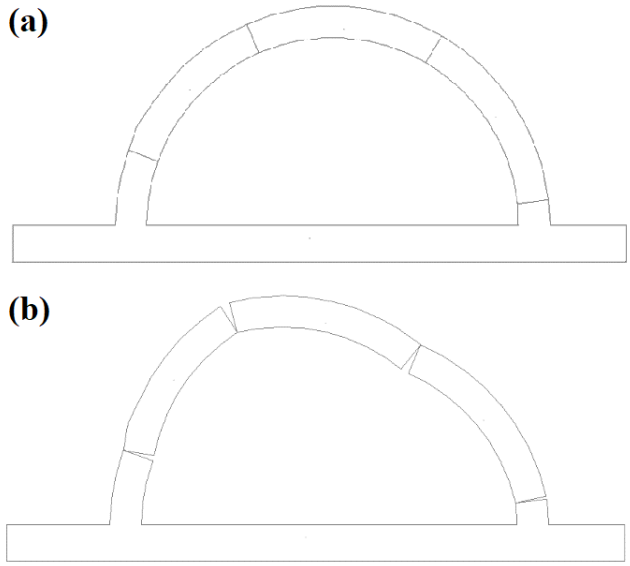

Figure 178. Typical geometry (Hinge Set 11, see Section 5.2) developed for (a) the DEM mode, and (b) the observed failure mode [124]

R

REFERENCES

[1] ACI (American Concrete Institute), *Building Code Requirements for Stuctural Concrete, ACI 318-14*. Farmington Hills, MI, USA, 2014.

[2] J. Heyman, *The Stone Skeleton*. Chambridge: Chambridge University Press, 1995.

[3] K. Culmann, *Die graphische Statik*. Zürich: Meyer und Zeller, 1866.

[4] P. Block, M. DeJong, and J. Ochsendorf, "As Hangs the Flexible Line: Equilibrium of Masonry Arches," *Nexus Netw. J.*, vol. 8, no. 2, pp. 13–24, Oct. 2006.

[5] G. L. Stockdale, "Reinforced stability-based design: a theoretical introduction through a mechanically reinforced masonry arch," *Int. J. Mason. Res. Innov.*, vol. 1, no. 2, pp. 101–142, 2016.

[6] G. L. Stockdale, "Generalized Processing of Fbg / Frp Strain Data for Structural Health Monitoring," University of Hawaii at Manoa, 2012.

[7] J. Z. Heydariha, H. Ghaednia, S. Nayak, S. Das, S. Bhattacharya, and S. C. Dutta, "Experimental and Field Performance of PP Band–Retrofitted Masonry: Evaluation of Seismic Behavior," *J. Perform. Constr. Facil.*, vol. 33, no. 1, p. 04018086, Feb. 2019.

[8] L. A. S. Kouris and T. C. Triantafillou, "State-of-the-art on strengthening of masonry structures with textile reinforced mortar (TRM)," *Constr. Build. Mater.*, vol. 188, pp. 1221–1233, Nov. 2018.

[9] E. Bertolesi, G. Milani, F. G. Carozzi, and C. Poggi, "Ancient masonry arches and vaults strengthened with TRM, SRG and FRP

composites: Numerical analyses," *Compos. Struct.*, vol. 187, pp. 385–402, Mar. 2018.

[10] F. G. Carozzi, C. Poggi, E. Bertolesi, and G. Milani, "Ancient masonry arches and vaults strengthened with TRM, SRG and FRP composites: Experimental evaluation," *Compos. Struct.*, vol. 187, pp. 466–480, Mar. 2018.

[11] F. Ceroni and P. Salzano, "Design provisions for FRCM systems bonded to concrete and masonry elements," *Compos. Part B Eng.*, vol. 143, pp. 230–242, Jun. 2018.

[12] S. De Santis, H. A. Hadad, F. De Caso y Basalo, G. de Felice, and A. Nanni, "Acceptance Criteria for Tensile Characterization of Fabric-Reinforced Cementitious Matrix Systems for Concrete and Masonry Repair," *J. Compos. Constr.*, vol. 22, no. 6, p. 04018048, Dec. 2018.

[13] S. De Santis, F. Roscini, and G. de Felice, "Full-scale tests on masonry vaults strengthened with Steel Reinforced Grout," *Compos. Part B Eng.*, vol. 141, pp. 20–36, May 2018.

[14] N. Gattesco, I. Boem, and V. Andretta, "Experimental behaviour of non-structural masonry vaults reinforced through fibre-reinforced mortar coating and subjected to cyclic horizontal loads," *Eng. Struct.*, vol. 172, pp. 419–431, Oct. 2018.

[15] C. Modena *et al.*, "Reinforced concrete and masonry arch bridges in seismic areas: typical deficiencies and retrofitting strategies," *Struct. Infrastruct. Eng.*, vol. 11, no. 4, pp. 415–442, Apr. 2015.

[16] S. Bhattacharya, S. Nayak, and S. C. Dutta, "A critical review of retrofitting methods for unreinforced masonry structures," *Int. J. Disaster Risk Reduct.*, vol. 7, pp. 51–67, Mar. 2014.

[17] C. Calderini and S. Lagomarsino, "Seismic Response of Masonry Arches Reinforced by Tie-Rods: Static Tests on a Scale Model," *J. Struct. Eng.*, vol. 141, no. 5, p. 04014137, May 2015.

[18] L. Anania and G. D'Agata, "Limit analysis of vaulted structures strengthened by an innovative technology in applying CFRP," *Constr. Build. Mater.*, vol. 145, pp. 336–346, Aug. 2017.

[19] A. Borri, G. Castori, and M. Corradi, "Intrados strengthening of brick masonry arches with composite materials," *Compos. Part B Eng.*, vol. 42, no. 5, pp. 1164–1172, Jul. 2011.

[20] I. Cancelliere, M. Imbimbo, and E. Sacco, “Experimental tests and numerical modeling of reinforced masonry arches,” *Eng. Struct.*, vol. 32, no. 3, pp. 776–792, Mar. 2010.

[21] D. V. Oliveira, I. Basilio, and P. B. Lourenço, “Experimental Behavior of FRP Strengthened Masonry Arches,” *J. Compos. Constr.*, vol. 14, no. 3, pp. 312–322, Jun. 2010.

[22] *CNR-DT 200 R1. Guide for the Design and Construction of Externally Bonded FRP Systems for Strengthening Existing Structures*. Rome: Italian National Research Counsil, 2014.

[23] R. C. Hibbeler, *Structural Analysis, Seventh Edition*. Singapore: Prentice Hall, 2009.

[24] M. Angelillo, Ed., *Mechanics of Masonry Structures*, vol. 551. Vienna: Springer Vienna, 2014.

[25] M. Angelillo, P. B. Lourenço, and G. Milani, “Masonry behaviour and modelling,” in *Mechanics of Masonry Structures*, Springer, Vienna, 2014, pp. 1–26.

[26] J. Heyman, “The stone skeleton,” *Int. J. Solids Struct.*, vol. 2, no. 2, pp. 249–279, Apr. 1966.

[27] M. Šilhavý, “Mathematics of the Masonry–Like model and Limit Analysis,” in *Mechanics of Masonry Structures*, Springer, Vienna, 2014, pp. 29–69.

[28] M. Lucchesi, “A numerical method for solving BVP of masonry-like solids,” in *Mechanics of Masonry Structures*, Springer, Vienna, 2014, pp. 71–108.

[29] M. Angelillo, “Practical applications of unilateral models to Masonry Equilibrium,” in *Mechanics of Masonry Structures*, Springer, Vienna, 2014, pp. 109–210.

[30] F. Lebon, “Modeling the interfaces in masonry structures,” in *Mechanics of Masonry Structures*, Springer, Vienna, 2014, pp. 213–240.

[31] E. Sacco, “Micro, Multiscale and Macro Models for Masonry Structures,” in *Mechanics of Masonry Structures*, Springer, Vienna, 2014, pp. 241–291.

[32] P. B. Lourenço and G. Milani, “Homogenization and Seismic Assessment: Review and Recent Trends,” in *Mechanics of*

Masonry Structures, Springer, Vienna, 2014, pp. 293–341.

[33] P. B. Lourenço, “Computations on historic masonry structures,” *Prog. Struct. Eng. Mater.*, vol. 4, no. 3, pp. 301–319, 2002.

[34] R. Marques and P. B. Lourenço, “Possibilities and comparison of structural component models for the seismic assessment of modern unreinforced masonry buildings,” *Comput. Struct.*, vol. 89, no. 21–22, pp. 2079–2091, Nov. 2011.

[35] P. B. Lourenço, N. Mendes, L. F. Ramos, and D. V. Oliveira, “Analysis of masonry structures without box behavior,” *Int. J. Archit. Herit.*, vol. 5, no. 4–5, pp. 369–382, 2011.

[36] A. Tralli, C. Alessandri, and G. Milani, “Computational Methods for Masonry Vaults: A Review of Recent Results,” *Open Civ. Eng. J.*, vol. 8, no. 1, pp. 272–287, Oct. 2014.

[37] S. Huerta, “Mechanics of masonry vaults: the equilibrium approach,” *Proc. 1st Int. Congr. Struct. Anal. Hist. Constr. Guimaraes*, pp. 47–70, 2001.

[38] S. Huerta, “The Analysis of Masonry Architecture: A Historical Approach,” *Archit. Sci. Rev.*, vol. 51, no. 4, pp. 297–328, Dec. 2008.

[39] E. Benvenuto, *An Introduction to the History of Structural Mechanics : Part I: Statics and Resistance of Solids*. Springer New York, 1991.

[40] M. Como, *Statics of Historic Masonry Constructions*, vol. 1. Berlin, Heidelberg: Springer Berlin Heidelberg, 2013.

[41] P. J. Fanning and T. E. Boothby, “Three-dimensional modelling and full-scale testing of stone arch bridges,” *Comput. Struct.*, vol. 79, no. 29–30, pp. 2645–2662, Nov. 2001.

[42] A. Page, “The Biaxial Compressive Strength of Brick Masonry.,” *Proc. Inst. Civ. Eng.*, vol. 71, no. 3, pp. 893–906, 1981.

[43] M. Dhanasekar, A. Page, and P. Kleeman, “The Failure of Brick Masonry Under Biaxial Stresses.,” in *Proceedings of the Institution of Civil Engineers*, 1985, vol. 79, no. 2, pp. 295–313.

[44] G. Milani, P. B. Lourenço, and A. Tralli, “Homogenised limit analysis of masonry walls, Part I: Failure surfaces,” *Comput. Struct.*, vol. 84, no. 3–4, pp. 166–180, Jan. 2006.

[45] G. Milani, P. B. Lourenço, and A. Tralli, "Homogenised limit analysis of masonry walls, Part II: Structural examples," *Comput. Struct.*, vol. 84, no. 3–4, pp. 181–195, Jan. 2006.

[46] P. B. Lourenço and J. G. Rots, "Multisurface Interface Model for Analysis of Masonry Structures," *J. Eng. Mech.*, vol. 123, no. 7, pp. 660–668, 1997.

[47] D. J. Sutcliffe, H. S. Yu, and A. W. Page, "Lower bound limit analysis of unreinforced masonry shear walls," *Comput. Struct.*, vol. 79, no. 14, pp. 1295–1312, Jun. 2001.

[48] G. Vasconcelos and P. B. Lourenço, "Assessment of the in-plane shear strength of stone masonry walls by simplified models," in *Structural Analysis of Historical Constructions*, 2006, vol. 2, pp. 837–844.

[49] D. Radenkovic, "Limit theorems for a Coulomb material with a non standard dilatation," *Comptes Rendus l'Académie des Sci. Paris*, vol. 252, pp. 4103–4104, 1961.

[50] J. Salencon, *Application of the theory of plasticity in soil mechanics*. Chichester, UK: John Wiley & Sons., 1977.

[51] E. Milani, G. Milani, and A. Tralli, "Limit analysis of masonry vaults by means of curved shell finite elements and homogenization," *Int. J. Solids Struct.*, vol. 45, no. 20, pp. 5258–5288, Oct. 2008.

[52] G. Milani, E. Milani, and A. Tralli, "Upper Bound limit analysis model for FRP-reinforced masonry curved structures. Part I: Unreinforced masonry failure surfaces," *Comput. Struct.*, vol. 87, no. 23–24, pp. 1516–1533, Dec. 2009.

[53] G. Milani, E. Milani, and A. Tralli, "Upper bound limit analysis model for FRP–reinforced masonry curved structures. Part II: Structural analyses," *Comput. Struct.*, vol. 87, no. 23–24, pp. 1534–1558, Dec. 2009.

[54] A. Carini and F. Genna, "Stability and strength of old masonry vaults under compressive longitudinal loads: Engineering analyses of a case study," *Eng. Struct.*, vol. 40, pp. 218–229, Jul. 2012.

[55] G. Milani and P. B. Lourenço, "3D non-linear behavior of masonry arch bridges," *Comput. Struct.*, vol. 110–111, pp. 133–150, Nov. 2012.

[56] A. J. S. Pippard, “The approximate estimation of safe loads on masonry bridges,” *Civ. Eng. War*, vol. 1, pp. 365–372, 1948.

[57] M. Gilbert and C. Melbourne, “Rigid-Block Analysis of Masonry Structures,” *Struct. Eng.*, vol. 72, no. 21, pp. 356–361, 1994.

[58] T. E. Boothby, “Collapse modes of masonry arch bridges,” *Mason. Int.*, vol. 9, no. 2, pp. 62–69, 1995.

[59] M. Gilbert, C. Casapulla, and H. M. Ahmed, “Limit analysis of masonry block structures with non-associative frictional joints using linear programming,” *Comput. Struct.*, vol. 84, no. 13–14, pp. 873–887, May 2006.

[60] G. de Felice and S. De Santis, “Experimental and Numerical Response of Arch Bridge Historic Masonry Under Eccentric Loading,” *Int. J. Archit. Herit.*, vol. 4, no. 2, pp. 115–137, Jan. 2010.

[61] A. Audenaert, P. Fanning, L. Sobczak, and H. Peremans, “2-D analysis of arch bridges using an elasto-plastic material model,” *Eng. Struct.*, vol. 30, no. 3, pp. 845–855, Mar. 2008.

[62] A. Cavicchi and L. Gambarotta, “Collapse analysis of masonry bridges taking into account arch–fill interaction,” *Eng. Struct.*, vol. 27, no. 4, pp. 605–615, Mar. 2005.

[63] A. Cavicchi and L. Gambarotta, “Two-dimensional finite element upper bound limit analysis of masonry bridges,” *Comput. Struct.*, vol. 84, no. 31–32, pp. 2316–2328, Dec. 2006.

[64] M. Gilbert, “RING: a 2D rigid-block analysis program for masonry arch bridges,” in *International Arch Bridges Conference*, 2001, pp. 459–464.

[65] D. O’Dwyer, “Funicular analysis of masonry vaults,” *Comput. Struct.*, vol. 73, no. 1–5, pp. 187–197, Oct. 1999.

[66] P. Block, T. Ciblac, and J. Ochsendorf, “Real-time limit analysis of vaulted masonry buildings,” *Comput. Struct.*, vol. 84, no. 29–30, pp. 1841–1852, Nov. 2006.

[67] P. Block and J. Ochsendorf, “Thrust Network Analysis: A New Methodology for Three-Dimensional Equilibrium,” in *International Association for Shell and Spatial Structures (IASS)*, 2007, vol. 48, no. 3, pp. 161–173.

[68] P. Block and L. Lachauer, “Three-Dimensional (3D) Equilibrium Analysis of Gothic Masonry Vaults,” *Int. J. Archit. Herit.*, vol. 8, no. 3, pp. 312–335, May 2014.

[69] A. Andreu, L. Gil, and P. Roca, “Computational Analysis of Masonry Structures with a Funicular Model,” *J. Eng. Mech.*, vol. 133, no. 4, pp. 473–480, Apr. 2007.

[70] A. Andreu, L. Gil, and P. Roca, “Analysis of masonry structures by funicular networks,” *Proc. Inst. Civ. Eng. - Eng. Comput. Mech.*, vol. 163, no. 3, pp. 147–154, Sep. 2010.

[71] F. Fraternali, “A thrust network approach to the equilibrium problem of unreinforced masonry vaults via polyhedral stress functions,” *Mech. Res. Commun.*, vol. 37, no. 2, pp. 198–204, Mar. 2010.

[72] F. Fraternali, M. Angelillo, and A. Fortunato, “A lumped stress method for plane elastic problems and the discrete-continuum approximation,” *Int. J. Solids Struct.*, vol. 39, no. 25, pp. 6211–6240, Dec. 2002.

[73] E. Babilio, A. Fortunato, and M. Lippiello, “A stress approach to the equilibrium of masonry domes: a case study,” in *Proceedings of the workshop “WonderMasonry*, 2007.

[74] M. Angelillo, E. Babilio, and A. Fortunato, “Singular stress fields for masonry-like vaults,” *Contin. Mech. Thermodyn.*, vol. 25, no. 2–4, pp. 423–441, Mar. 2013.

[75] E. Vouga, M. Höbinger, J. Wallner, and H. Pottmann, “Design of self-supporting surfaces,” *ACM Trans. Graph.*, vol. 31, no. 4, p. 87, Jul. 2012.

[76] A. Baratta and O. Corbi, “Stress analysis of masonry vaults and static efficacy of FRP repairs,” *Int. J. Solids Struct.*, vol. 44, no. 24, pp. 8028–8056, Dec. 2007.

[77] A. Baratta and O. Corbi, “On the equilibrium and admissibility coupling in NT vaults of general shape,” *Int. J. Solids Struct.*, vol. 47, no. 17, pp. 2276–2284, Aug. 2010.

[78] M. Lucchesi, C. Padovani, G. Pasquinelli, and N. Zani, “On the Collapse of Masonry Arches,” *Meccanica*, vol. 32, no. 4, pp. 327–346, 1997.

[79] P. B. Lourenço, “Computational Strategies for Masonry Structures,” TU Delft, Delft University of Technology, 1996.

[80] A. Bacigalupo, A. Brencich, and L. Gambarotta, “A simplified assessment of the dome and drum of the Basilica of S. Maria Assunta in Carignano in Genoa,” *Eng. Struct.*, vol. 56, pp. 749–765, Nov. 2013.

[81] D. F. D’Ayala and E. Tomasoni, “Three-Dimensional Analysis of Masonry Vaults Using Limit State Analysis with Finite Friction,” *Int. J. Archit. Herit.*, vol. 5, no. 2, pp. 140–171, Feb. 2011.

[82] D. Theodossopoulos, B. P. Sinha, A. S. Usmani, and A. J. Macdonald, “Assessment of the structural response of masonry cross vaults,” *Strain*, vol. 38, no. 3, pp. 119–127, 2002.

[83] G. Creazza, A. Saetta, R. Matteazzi, and R. Vitaliani, “of masonry vaulted structures by using a 3-D damage model,” in *European Congress on Computational Methods in Applied Sciences and Engineering*, 2000.

[84] G. Creazza, R. Matteazzi, A. Saetta, and R. Vitaliani, “Analyses of Masonry Vaults: A Macro Approach based on Three-Dimensional Damage Model,” *J. Struct. Eng.*, vol. 128, no. 5, pp. 646–654, May 2002.

[85] G. Milani and A. Tralli, “A simple meso-macro model based on SQP for the non-linear analysis of masonry double curvature structures,” *Int. J. Solids Struct.*, vol. 49, no. 5, pp. 808–834, Mar. 2012.

[86] S. De Santis and G. de Felice, “Overview of Railway Masonry Bridges with a Safety Factor Estimate,” *Int. J. Archit. Herit.*, vol. 8, no. 3, pp. 452–474, May 2014.

[87] V. Sarhosis, S. De Santis, and G. de Felice, “A review of experimental investigations and assessment methods for masonry arch bridges,” *Struct. Infrastruct. Eng.*, vol. 12, no. 11, pp. 1439–1464, 2016.

[88] V. Giamundo, V. Sarhosis, G. P. Lignola, Y. Sheng, and G. Manfredi, “Evaluation of different computational modelling strategies for the analysis of low strength masonry structures,” *Eng. Struct.*, vol. 73, pp. 160–169, Aug. 2014.

[89] V. Sarhosis and Y. Sheng, “Identification of material parameters

for low bond strength masonry," *Eng. Struct.*, vol. 60, pp. 100–110, Feb. 2014.

[90] E. Reccia, G. Milani, A. Cecchi, and A. Tralli, "Full 3D homogenization approach to investigate the behavior of masonry arch bridges: The Venice trans-lagoon railway bridge," *Constr. Build. Mater.*, vol. 66, pp. 567–586, Sep. 2014.

[91] I. Group, *3DEC version 5.00 distinct-element modeling of jointed and blocky material in 3D*. Minneapolis, 2015.

[92] R. Dimitri and F. Tornabene, "A parametric investigation of the seismic capacity for masonry arches and portals of different shapes," *Eng. Fail. Anal.*, vol. 52, pp. 1–34, Jun. 2015.

[93] V. Sarhosis, K. Bagi, J. V. Lemos, and G. Milani, *Computational modeling of masonry structures using the discrete element method*. 2016.

[94] V. Sarhosis, P. Asteris, T. Wang, W. Hu, and Y. Han, "On the stability of colonnade structural systems under static and dynamic loading conditions," *Bull. Earthq. Eng.*, vol. 14, no. 4, pp. 1131–1152, Apr. 2016.

[95] B. Conde, L. Díaz-Vilariño, S. Lagüela, and P. Arias, "Structural analysis of Monforte de Lemos masonry arch bridge considering the influence of the geometry of the arches and fill material on the collapse load estimation," *Constr. Build. Mater.*, vol. 120, pp. 630–642, Sep. 2016.

[96] Y. Zhang, L. Macorini, and B. A. Izzuddin, "Mesoscale partitioned analysis of brick-masonry arches," *Eng. Struct.*, vol. 124, pp. 142–166, Oct. 2016.

[97] T. Forgács, V. Sarhosis, and K. Bagi, "Minimum thickness of semi-circular skewed masonry arches," *Eng. Struct.*, vol. 140, pp. 317–336, Jun. 2017.

[98] A. Gaetani, P. B. Lourenço, G. Monti, and M. Moroni, "Shaking table tests and numerical analyses on a scaled dry-joint arch undergoing windowed sine pulses," *Bull. Earthq. Eng.*, vol. 15, no. 11, pp. 4939–4961, Nov. 2017.

[99] A. Formisano and A. Marzo, "Simplified and refined methods for seismic vulnerability assessment and retrofitting of an Italian cultural heritage masonry building," *Comput. Struct.*, vol. 180, pp.

13–26, Feb. 2017.

[100] B. Conde, L. F. Ramos, D. V. Oliveira, B. Riveiro, and M. Solla, "Structural assessment of masonry arch bridges by combination of non-destructive testing techniques and three-dimensional numerical modelling: Application to Vilanova bridge," *Eng. Struct.*, vol. 148, pp. 621–638, Oct. 2017.

[101] T. T. Bui, A. Limam, V. Sarhosis, and M. Hjiaj, "Discrete element modelling of the in-plane and out-of-plane behaviour of dry-joint masonry wall constructions," *Eng. Struct.*, vol. 136, pp. 277–294, Apr. 2017.

[102] E. Bertolesi, G. Milani, F. D. Lopane, and M. Acito, "Augustus Bridge in Narni (Italy): Seismic Vulnerability Assessment of the Still Standing Part, Possible Causes of Collapse, and Importance of the Roman Concrete Infill in the Seismic-Resistant Behavior," *Int. J. Archit. Herit.*, pp. 1–30, Jun. 2017.

[103] A. Chiozzi, G. Milani, and A. Tralli, "A Genetic Algorithm NURBS-based new approach for fast kinematic limit analysis of masonry vaults," *Comput. Struct.*, vol. 182, pp. 187–204, Apr. 2017.

[104] T. Forgács, V. Sarhosis, and K. Bagi, "Influence of construction method on the load bearing capacity of skew masonry arches," *Eng. Struct.*, vol. 168, pp. 612–627, Aug. 2018.

[105] A. Iannuzzo, F. De Serio, A. Gesualdo, G. Zuccaro, A. Fortunato, and M. Angelillo, "Crack patterns identification in masonry structures with a C° displacement energy method," *Int. J. Mason. Res. Innov.*, vol. 3, no. 3, p. 295, 2018.

[106] Y. Zhang, L. Macorini, and B. A. Izzuddin, "Numerical investigation of arches in brick-masonry bridges," *Struct. Infrastruct. Eng.*, vol. 14, no. 1, pp. 14–32, Jan. 2018.

[107] G. Brandonisio, E. Mele, and A. De Luca, "Closed form solution for predicting the horizontal capacity of masonry portal frames through limit analysis and comparison with experimental test results," *Eng. Fail. Anal.*, vol. 55, pp. 246–270, Sep. 2015.

[108] P. Zampieri, M. A. Zanini, and C. Modena, "Simplified seismic assessment of multi-span masonry arch bridges," *Bull. Earthq. Eng.*, vol. 13, no. 9, pp. 2629–2646, Sep. 2015.

[109] V. N. Moreira, J. Fernandes, J. C. Matos, and D. V. Oliveira, "Reliability-based assessment of existing masonry arch railway bridges," *Constr. Build. Mater.*, vol. 115, pp. 544–554, Jul. 2016.

[110] P. Zampieri, M. A. Zanini, and F. Faleschini, "Influence of damage on the seismic failure analysis of masonry arches," *Constr. Build. Mater.*, vol. 119, pp. 343–355, Aug. 2016.

[111] LimitState Ltd, *LimitState: RING Manul*. Scheffield, UK, 2016.

[112] N. Cavalagli, V. Gusella, and L. Severini, "Lateral loads carrying capacity and minimum thickness of circular and pointed masonry arches," *Int. J. Mech. Sci.*, vol. 115–116, pp. 645–656, Sep. 2016.

[113] V. N. Moreira, J. C. Matos, and D. V. Oliveira, "Probabilistic-based assessment of a masonry arch bridge considering inferential procedures," *Eng. Struct.*, vol. 134, pp. 61–73, Mar. 2017.

[114] G. Brandonisio, E. Mele, and A. De Luca, "Limit analysis of masonry circular buttressed arches under horizontal loads," *Meccanica*, vol. 52, no. 11–12, pp. 2547–2565, Sep. 2017.

[115] N. Cavalagli, V. Gusella, and L. Severini, "The safety of masonry arches with uncertain geometry," *Comput. Struct.*, vol. 188, pp. 17–31, Aug. 2017.

[116] M. Angelillo, A. Fortunato, A. Gesualdo, A. Iannuzzo, and G. Zuccaro, "Rigid block models for masonry structures," *Int. J. Mason. Res. Innov.*, vol. 3, no. 4, p. 349, 2018.

[117] C. Cennamo and C. Cusano, "The Gothic arcade of Santa Maria Incoronata in Naples: equilibrium of Gothic arches," *Int. J. Mason. Res. Innov.*, vol. 3, no. 2, p. 92, 2018.

[118] B. Ghiassi and G. Milani, Eds., *Numerical Modeling of Masonry and Historical Structures*. Elsevier, 2019.

[119] C. Wang, V. Sarhosis, and N. Nikitas, "Strengthening/Retrofitting Techniques on Unreinforced Masonry Structure/Element Subjected to Seismic Loads: A Literature Review," *Open Constr. Build. Technol. J.*, vol. 12, no. 1, pp. 251–268, Oct. 2018.

[120] B. Ghiassi and P. B. Lourenço, Eds., *Long-term Performance and Durability of Masonry Structures*. Woodhead Publishing, 2019.

[121] M. J. DeJong, L. De Lorenzis, S. Adams, and J. Ochsendorf, "Rocking Stability of Masonry Arches in Seismic Regions,"

Earthq. Spectra, vol. 24, no. 4, pp. 847–865, Nov. 2008.

[122] M. J. (Matthew J. DeJong, "Seismic assessment strategies for masonry structures," Massachusetts Institute of Technology, 2009.

[123] L. De Lorenzis, M. DeJong, and J. Ochsendorf, "Failure of masonry arches under impulse base motion," *Earthq. Eng. Struct. Dyn.*, vol. 36, no. 14, pp. 2119–2136, Nov. 2007.

[124] G. Stockdale, V. Sarhosis, and G. Milani, "Seismic capacity and multi-mechanism analysis for dry-stack masonry arches subjected to hinge control," *Bull. Earthq. Eng.*, no. 0123456789, 2019.

[125] G. L. Stockdale, V. Sarhosis, and G. Milani, "Increase in seismic resistance for a dry joint masonry arch subjected to hinge contro," in *10th IMC Conference Proceedings*, 2018, pp. 968–981.

[126] G. L. Stockdale *et al.*, "Kinematic collapse load calculator: Circular arches," *SoftwareX*, 2018.

[127] G. L. Stockdale and G. Milani, "Interactive MATLAB-CAD limit analysis of horizontally loaded masonry arches," in *10th IMC Conference Proceedings*, 2018, pp. 298–306.

[128] *AutoCAD 2013 Command Reference Guide*. Autodesk, Inc., 2012.

[129] ASCE (AmeicanSociety of Civil Engineers), *Minimum Design Loads and Associated Criteria for Buildings and Other Structures (7-16)*. Reston, Virginia: Americal Society of Civil Engineers, 2017.

[130] G. L. Stockdale and G. Milani, "Diagram based assessment strategy for first-order analysis of masonry arches," *J. Build. Eng.*, vol. 22, pp. 122–129, Mar. 2019.

[131] M. Ahmad, K. A. Ismail, and F. Mat, "IMPACT MODELS AND COEFFICIENT OF RESTITUTION: A REVIEW," *J. Eng. Appl. Sci.*, vol. 11, no. 10, pp. 6549–6555, 2016.

[132] I. J. Oppenheim, "The masonry arch as a four-link mechanism under base motion," *Earthq. Eng. Struct. Dyn.*, vol. 21, no. 11, pp. 1005–1017, Jan. 1992.